# Perturbative Approaches to Redshift Space Distortions

Dissertation
zur
Erlangung der naturwissenschaftlichen Doktorwürde
(Dr. sc. nat.)

vorgelegt der
Mathematisch-naturwissenschaftlichen Fakultät
der

Universität Zürich

von

Zvonimir Vlah

aus
Kroatien

Promotionskomitee
Prof. Dr. Thomas Gehrmann (Vorsitz)
Prof. Dr. Uros Seljak (Leitung der Dissertation)
Prof. Dr. Ben Moore

Zürich 2014

## Abstract

In this dissertation, we develop theoretical models and tools for describing the dark matter and galaxy distribution in the Universe. Importance of developing these models lies in our interest to reveal the structure of the Universe, its composition and initial conditions that seeded the evolution, using the data from large scale structure surveys.

In the first part we review the dark matter gravitational clustering and biasing models, which relate the galaxy distribution to the dark matter. We also review the redshift space distortion effects which take into account the effects of peculiar movement of particles relative to the Hubble flow. The second part consists of three studies. The first focuses on the accurate modeling of redshift space distortions effects in the dark matter power spectrum in the mildly-nonlinear regime, using the phase space distribution function approach as a newly developed tool. We generalize this approach in the second study to include the galaxy bias effects, i.e. to extend the validity of the model to include the observable objects. In the third study, we explore the Lagrangian perturbation theory results for dark matter and develop a novice parametric model which allows consistent modeling of the power spectrum and correlation function. We conclude by giving the guidelines for the potential follow up work along these lines.

## Zusammenfassung

In dieser Arbeit entwickeln wir die theoretische Modelle und Werkzeuge für die Dunkle-Materie- und Galaxienverteilung im Universum. Die Bedeutung der Entwicklung dieser Modelle liegt in unserem Interesse die Struktur des Universums, seine Zusammensetzung und seine Anfangs Bedingungen zu enthüllen, weshalb die Daten aus Beobachtungen der grossräumigen Strukturen im Universum benutzt werden.

Im ersten Teil besprechen wir die Dunkle-Materie-Gravitationsclustering- und die Biasing-Modelle, welche die Galaxienverteilung mit der Dunkle-Materie-Verteilung in Beziehung setzen. Wir besprechen auch die Rotverschiebungsraumverzerrungseffekte, welche die Auswirkungen der eigentümliche Bewegung von Teilchen relativ zum Hubble-Flow im Beziehung setzen. Der zweite Teil besteht aus drei Studien. Die erste konzentriert sich auf die genaue Modellierung der Rotverschiebungraumverzerrungseffekte im schwach nichtlinearen Regime des Dunklen-Materie-Leistungsspektrums, durch Verwendung des Phasenraumverteilungsfunktionansatz als ein neuentwickeltes Werkzeug. Wir verallgemeinern dieses Konzept in der zweiten Studie, um die Galaxiebiasingeffekte miteinzubeziehen. In der dritten Studie untersuchen wir die Ergebnisse der Lagrange-Störungstheorie für die Dunkle-Materie und entwickeln ein neues parametrisches Modell, das konsequente Modellierung von Leistungsspektrum und Korrelationsfunktion ermöglicht. Wir schliessen mit den Richtlinien für die potenziellen Folgearbeiten entlang dieser Linien.

For my parents, Nada and Zvonko

## Acknowledgements

I would like to thank Prof. Dr. Uroš Seljak for giving me the opportunity to work in his group and under his supervision. I would also like to thank Prof. Dr. Thomas Gehrmann for his supervision in the last year of my PhD.
I am also very grateful to my senior collaborators Teppei Okumura, Vincent Desjacques, Patrick Mcdonald, Jaiyul Yoo for their help and motivation.
Thanks to my colleagues Tobias Baldauf, Jonathan Blazek, Andreu Font, Nico Hamaus and Lucas Lombriser for many helpful discussions and debates. I am very grateful to Tobias Baldauf for sharing his thesis latex template on which this thesis is based.
I would also like to thank Swiss Federation and Euclid Consortium for funding me. I enjoyed time spent at the Institute for Theoretical Physics, Physik Institut and Institute for Computational Science at the University of Zurich. Thanks to EWHA Womans University, the Lawrence Berkeley Labratory and the University of California at Berkeley for their hospitality.
Finally, I want to thank Nina and my parents for their support and encouragement.

Zürich, August 2014

# Contents

# List of Figures

# Chapter 1

# Introduction[1]

In the last few decades cosmology has been experiencing a renaissance. Numerous observation endeavors have been confirming the cosmological concordance model and have been giving ever better constraints of the cosmological parameters. This enabled the formulation of clear and quantitative questions on the nature of the constituents of the concordance model. Among some of the most interesting of these theoretical challenges are certainly the nature of inflation, dark matter, and dark energy.

Inflation (see e.g. [6, 7] for the review), was a phase of accelerated expansion in the early stages of the universe, where in a short period of time the universe was enlarged by at least the factor of $10^{27}$ times. This expansion mechanism naturally provides solutions for so called problems of flatness, homogeneity and isotropy of the universe. At the same time, inflation continually stretches the fluctuations of quantum vacuum outside of the Hubble horizon (e.g. [8, 9, 10, 11], also e.g. [12] for the review ), seeding thus the Cosmic Microwave Background (CMB) temperature fluctuations as well as the formation of cosmic structures, i.e. galaxies clustering. While this is an elegant idea and it has become widely accepted as a standard paradigm in the last three decades, all the underlying theoretical details still remains to be determined and tested.

Dark energy (see e.g. [13, 14] for the review) on the other hand, effects the cosmic distances and the growth rate of cosmic structures and in this way controls the expansion history of the universe. Since it affects the observations of galaxies on the sky, where the positions of galaxies are determined by their angular positions and redshifts, it provides the relation between the coordinates and physical distances that depend on the expansion rate and angular diameter distance. Also the gravitational evolution of cosmic structure is slowed down by the expansion rate of the universe, and therefore, measuring the distances and growth of cosmic structures constraints the properties of dark energy.

The large scale structure (LSS) of the universe constitute thus a rich probe of both early and late periods of cosmic acceleration. Understanding the details of gravitational instability and the central role it plays in the formation of large scale structures seen in galaxy surveys is one of the main goals of modern cosmology. Extracting the wealth of information contained in galaxy clustering to learn about cosmology thus requires a good quantitative understanding of the dynamics of gravitational instability, as well as application of sophisticated statistical tools that can be used to test these theoretical models against the observations.

## 1.1 Background Cosmology

In this section we review the fundamental assumptions of physical cosmology and state the usual initial assumption that the observable part of our universe can be approximated as

[1] Contents of this Chapter is reproduced using standard cosmology textbooks [1, 2, 3] and review article [4, 5].

homogeneous and isotropic, expanding Friedmann-Robertson-Walker (FRW) universe. The postulate that the universe is homogeneous and isotropic on large scale is often called the cosmological principle. In conjunction with the general relativity (GR) theory it describes the evolution and structure of spacetime which we recognize at small-scales as the departures from homogeneity and isotropy. Thus, the paradigm is that we live in a perturbed FRW universe where the metric fluctuations are small on the horizon scale although density fluctuations itself are not necessarily small.

We introduce the metric characterization of the geometry of spacetime. The Robertson-Walker metric line element for a homogeneous and isotropic spacetime is given by

$$ds^2 = -c^2dt^2 + a(t)^2\left[\frac{dx^2}{1-kx^2/c^2} + x^2\left(d\theta^2 + \sin^2(\theta)d\phi^2\right)\right], \tag{1.1}$$

were $a(t)$ is the cosmic scale factor, and $\mathbf{x}$ is the comoving spatial coordinate, which multiplied by the scale factor $a(t)$ corresponds to the proper position $\mathbf{r} = a(t)\mathbf{x}$. Effects of curvature in the metric, where $k$ is the curvature constant, are well constrained and are small for distances much less than the horizon scale (e.g. [15]). We will restrict ourselves to structures much smaller than this, so that the curvature term may be neglected in the metric. The Robertson-Walker line element may now be written as flat Minkowski metric in the comoving coordinates.

From the metric and Einstein equations we get the Hubble expansion, in the absence of perturbations, described by the cosmic scale factor $a(t)$. We get the first Friedmann equation:

$$\mathcal{H}^2(t) \equiv \left(\frac{da}{dt}\right)^2 = a^2\frac{8\pi}{3}G\bar{\rho}(t) - k, \tag{1.2}$$

where $\bar{\rho}(t)$ is the total mean mass density that includes both the relativistic and nonrelativistic components alike. $\mathcal{H} = aH$ is the reduced Hubble parameter and present day Hubble parameter $H_0$ has value $H_0 = 100h$ kms$^{-1}$Mpc$^{-1}$; with $h$ well constrained in numerous recent surveys to be about $h \propto 0.7$ (see e.g.[15]). We will write the present values with a subscript 0, and will also take the present value of expansion factor to be $a_0 = 1$. Note that with this choice, the curvature constant has units and therefore is not equal to the canonical $-1, +1$ or 0 values. Form 1.2 it follows that

$$(\Omega_{tot}(t) - 1)\mathcal{H}^2(t) = k, \tag{1.3}$$

where $\Omega_{tot} = \frac{8\pi G\bar{\rho}(t)}{3H^2(t)}$ is the ratio of the total density divided by the critical density. The content of $\Omega_{tot}$ includes the vacuum energy $\rho_\Lambda = \Lambda/(8\pi G)$ along with the matter $\rho_{\rm m}$ and radiation $\rho_{\rm r}$. A positive cosmological constant $\Lambda$ also has associated with it a negative pressure, $p_\Lambda = -\rho_\Lambda c^2$. Second Friedmann equation thus reads

$$\frac{d\mathcal{H}}{d\tau} = -\frac{\Omega_{\rm m}}{2}\mathcal{H}^2(\tau) + \frac{\Lambda}{3}a^2(\tau) = \left(\Omega_\Lambda(\tau) - \frac{\Omega_{\rm m}}{2}\right)\mathcal{H}^2(\tau). \tag{1.4}$$

Note that we have changed the time coordinate from the proper time $t$ to the conformal time $\tau$ which we define as $d\tau = dt/a(t)$. In our fiducial, $\Lambda CDM$ universe (see [15]) the dominant component is the dark energy with $\Omega_\Lambda \simeq 0.68$ followed by the nonrelativistic matter $\Omega_{\mathbf{m}} \simeq 0.32$, in which the pressure is negligible compared with $\bar{\rho}c^2$ and expansion dilutes the mass density inversely with volume: $\rho(t) = \rho_0 a^{-3}(t)$.

## 1.2 Beyond the Homogeneous Universe and the Origin of Fluctuations

In this section we introduce the metric fluctuations arising from the fact that the universe is, as predicted by the inflation, not perfectly homogeneous and isotropic. As mentioned

earlier, the paradigm is that during the inflation period quantum fluctuations got stretched outside of the horizon and became the initial seeds for inhomogeneities we see today. In these inflationary models, from which the simplest one is the single-field model within the slow-roll approximation, all fluctuations originate from the scalar adiabatic perturbations. Throughout the inflationary phase the energy density is dominated by the density stored in the inflaton field. Quantum fluctuations of this field can be decomposed into the Fourier modes $\boldsymbol{k}$,

$$\Delta\varphi = \int d^3k \ \left[a_{\boldsymbol{k}}\psi_k(t)\exp(i\boldsymbol{k}\cdot\boldsymbol{x}) + a^\dagger_{\boldsymbol{k}}\ \psi^*_k(t)\exp(-i\boldsymbol{k}\cdot\boldsymbol{x})\right], \tag{1.5}$$

where we introduced the creation and annihilation operators $a^\dagger_{\boldsymbol{k}}$ and $a_{\boldsymbol{k}}$ which obey the standard commutator $[a_{\boldsymbol{k}}, a^\dagger_{-\boldsymbol{k}'}] = \delta^D(\boldsymbol{k}+\boldsymbol{k}')$ and the mode functions $\psi_k(t)$ are solutions of the Klein-Gordon equation in an expanding Universe. In a de-Sitter metric where the spatial sections are flat and Hubble expansion $H$ is constant, we have

$$\psi_k(t) = \frac{H}{(2k)^{1/2}k}\ \left(i + \frac{k}{aH}\right)\ \exp\left[\frac{ik}{aH}\right]. \tag{1.6}$$

For modes exiting the Hubble radius we have $k/(aH) \ll 1$, which then leads to

$$\varphi_{\boldsymbol{k}} \approx \frac{iH}{\sqrt{2}k^{3/2}}\left(a_{\boldsymbol{k}} + a^\dagger_{-\boldsymbol{k}}\right), \quad \Delta\varphi = \int d^3k\ \varphi_{\boldsymbol{k}}\, e^{i\boldsymbol{k}\cdot\boldsymbol{x}}. \tag{1.7}$$

We see that all the modes are proportional to $\left(a_{\boldsymbol{k}} + a^\dagger_{-\boldsymbol{k}}\right)$ operator, which means that the quantum nature of the fluctuations vanishes and all the combinations of $\varphi_{\boldsymbol{k}}$ commute with each other. The field $\varphi$ can then be turned into to the classic stochastic field where the vacuum expectation value is exchanged with the ensemble average $\langle 0|...|0\rangle = \langle ...\rangle$. When the inflationary phase finishes modes enter the Hubble radius again and leave energy fluctuations imprints in the gravitational potential. Thus the stochasticity that appears in the cosmic fields can be expressed in terms of the random variable $\varphi_{\boldsymbol{k}}$.

In the following, we restrict ourselves to the postrecombination universe and we assume that the fluctuations due to the radiation and any other relativistic components (e.g. neutrinos) are small compared to the density fluctuations of nonrelativistic matter, so that only the latter produce a significant gravitational effect. This allows for an uniform relativistic background energy density and pressure such as that provided by a cosmological constant, but we neglect the gravitational effect of the momentum density, of fluctuations in pressure and the relativistic component of energy density. This approximation is inappropriate in the early, radiation dominated universe, but it is allowed in our case (after the recombination) since the large-scale structure developed during a matter-dominated era. The metric fluctuations are then determined by one scalar field, which we can interpret as Newtonian gravitational potential perturbation $\phi$. Einstein field equations can then be solved by expanding into small $\phi$ field perturbations. The form of the results then depend on the way the coordinates are assigned to the perturbed space-time, i.e., on the choice of gauge. We adopt the conformal Newtonian gauge, in which the line element reads

$$ds^2 = a(\tau)^2\left[-\left(1+\frac{2\phi}{c^2}\right)c^2d\tau^2 + \left(1-\frac{2\phi}{c^2}\right)\left(dx^2+dy^2+dz^2\right)\right] \tag{1.8}$$

This is a solution to the Einstein field equations for a perturbed Friedmann-Robertson-Walker universe in the weak-field, slow-motion approximation of general relativity (neglecting gravitational radiation and the weak gravitational effects of vorticity). We continue the study of growth of structure in the Newtonian limit in the section 2.

Tests of these cosmological theories characterized by the primordial seeds are thus of the statistical nature rather than deterministic. The reasons for that is that there is no direct observational access to primordial fluctuations that would provide a definite initial conditions. Additionally, cosmological evolution time-scale is much longer than that over

which observations can be made. This is in effect making it impossible to follow the evolution of single systems. What we observe in our the past light cone is different objects at different times of their evolution and therefore testing the evolution of structure leads to the statistical approach.

Thus, we model the observable universe as a stochastic realization of a statistical ensemble of possibilities, where the goal is to make the statistical predictions. These predictions are then dependent on the properties of the primordial perturbations responsible for the formation of structures.

## 1.3 Current Status and LSS Surveys

We live in locally highly non-linear part of the universe filled with the rich structures like galaxies and clusters of galaxies. Galaxies and clusters of galaxies thus constitute one of the most-important observational probes of large scale structure (LSS) formation. Primary reason for this is the fact that by measuring the three-dimensional distribution of galaxies we can in principle extract the information of the three-dimensional distribution of the underlying dark matter. Distribution of dark matter is sensitive to many of cosmological parameters and models. Through the growth of dark matter structures, we can obtain the constraints of the inflationary models and the alternatives, as well on the composition of the universe like the amount and nature of the dark matter and the dark energy (see e.g. [16, 17, 18, 19]. Furthermore, it enables us to determine the role of the neutrinos in structure formation and put constraints on their mass and number of species, modifications of gravity (e.g. [20, 21]), as well as the effects of string theories in cosmology.

In recent years there have been many ongoing and planned galaxy redshift surveys like the Sloan Digital Sky Survey (SDSS), the CfA survey [22], the 2dF Survey [23], Hobby-Eberly Telescope Dark Energy Experiment (HETDEX) [24], etc. Even though not limited to any specific survey, methods presented in this thesis are likely to be first applied to the observations from the Baryon Oscillation Spectroscopic Survey (BOSS) which is part of Sloan Digital Sky Survey III (SDSS-III) (see e.g. [25, 26]). In addition to these there are more currently planned observational missions like DES[1], LSST[2], Euclid [3], BigBOSS[4].

Galaxy redshift surveys provide also additional information because the observed redshift is a sum of the radial distance to the galaxy and its peculiar velocity (Doppler shift) which leads to the clustering strength that depends on the angle between the galaxy pairs and the line of sight, which is referred to as the redshift space distortions (RSD) [27]. These distortions thus make the galaxy clustering in redshift space more complex, but at the same time provide an opportunity to extract important information on the dark matter clustering directly from the redshift surveys. In recent years several studies have been performed investigating these effects and trying to combine it in order to model galaxy clustering (e.g. [28, 29, 30, 31]).

## 1.4 Motivation and Overview

Achievements of the observational surveys have led to the new frontiers in understanding of the formation of structures. Obtained new insights about the origin and evolution of the universe have opened new questions about the processes seeding and mechanism's leading to the structures like galaxies and clusters of galaxies that are observed at present. Large scale structures offer a potentially promising way to answer some of these questions. Numerous proposals have been made where using the LSS gives constraints to the total neutrino mass, offers a way to rule out modifications of gravity, constrains models of inflation as well as dark

[1] Dark Energy Survey, www.darkenergysurvey.org
[2] Large Synoptic Survey Telescope, www.lsst.org
[3] sci.esa.int/euclid
[4] bigboss.lbl.gov

energy. In order to use galaxy surveys to achieve these goals, we need a better understanding of a number of physical effects and develop robust tools for analyzing and extracting the information from obtained data. This thesis will focus on three primary steps needed in order to use the information stored in the data from LSS surveys. These are non-linear evolution and clustering of dark matter overdensities, connection of galaxies as the imperfect tracers to the underlying non-linear matter distribution (so-called problem of galaxy biasing), and redshift space distortions effects arising from the Doppler shift contributions to the Hubble flow.

This dissertation is organized as follows. In the first part, we start by reviewing the perturbative approach to the nonlinear dark matter clustering (in chapter 2), and continue by shortly introducing the halo biasing concept (chapter 3). We continue by introduction of the redshift space distortions and reviewing the current status in the field (chapter 4). The next part of the thesis consists of the three papers published during the period of the author's PhD program. In chapter 5 we present the phase space distribution function approach to modeling the redshift space distortions of dark matter. We then continue by generalizing this formalism for the biased tracers (like galaxies) in chapter 6. In chapter 7 we focus on the Lagrangian perturbation theory in order to study the details of dark matter clustering, and the connection of the Fourier and configuration space statistics. Finely, in chapter 8 we summarize our findings and give prospective directions for further development of the presented ideas.

# Bibliography


[1] S. Dodelson, *Modern cosmology*. Academic Press, 2003.

[2] P. J. E. Peebles, *The large-scale structure of the universe*. Princeton University Press, 1980.

[3] J. A. Peacock, *Cosmological Physics*. Cambridge University Press, 1999.

[4] F. Bernardeau, S. Colombi, E. Gaztanaga, and R. Scoccimarro, **Large scale structure of the universe and cosmological perturbation theory**, *Phys.Rept.* **367** (2002) 1–248, [astro-ph/0112551].

[5] E. Bertschinger, *Large-scale structures and motions: Linear theory and statistics*, vol. 408 of *Lecture Notes in Physics*. Springer Berlin Heidelberg, 1992.

[6] A. Riotto, **Inflation and the theory of cosmological perturbations**, hep-ph/0210162.

[7] D. Baumann, **TASI Lectures on Inflation**, arXiv:0907.5424.

[8] A. H. Guth and S. Pi, **Fluctuations in the New Inflationary Universe**, *Phys.Rev.Lett.* **49** (1982) 1110–1113.

[9] S. Hawking, **The Development of Irregularities in a Single Bubble Inflationary Universe**, *Phys.Lett.* **B115** (1982) 295.

[10] A. A. Starobinsky, **Dynamics of Phase Transition in the New Inflationary Universe Scenario and Generation of Perturbations**, *Phys.Lett.* **B117** (1982) 175–178.

[11] J. M. Bardeen, P. J. Steinhardt, and M. S. Turner, **Spontaneous Creation of Almost Scale - Free Density Perturbations in an Inflationary Universe**, *Phys.Rev.* **D28** (1983) 679.

[12] V. F. Mukhanov, H. Feldman, and R. H. Brandenberger, **Theory of cosmological perturbations. Part 1. Classical perturbations. Part 2. Quantum theory of perturbations. Part 3. Extensions**, *Phys.Rept.* **215** (1992) 203–333.

[13] J. Frieman, M. Turner, and D. Huterer, **Dark Energy and the Accelerating Universe**, *Ann.Rev.Astron.Astrophys.* **46** (2008) 385–432, [arXiv:0803.0982].

[14] M. J. Mortonson, D. H. Weinberg, and M. White, **Dark Energy: A Short Review**, arXiv:1401.0046.

[15] **P**lanck Collaboration Collaboration, P. Ade et al., **Planck 2013 results. XVI. Cosmological parameters**, arXiv:1303.5076.

[16] S. Cole, K. B. Fisher, and D. H. Weinberg, **Fourier analysis of redshift space distortions and the determination of Omega**, *MNRAS* **267** (1994) 785, [astro-ph/9308003].

[17] L. Guzzo, M. Pierleoni, B. Meneux, E. Branchini, O. L. Fevre, et al., **A test of the nature of cosmic acceleration using galaxy redshift distortions**, *Nature* **451** (2008) 541–545, [arXiv:0802.1944].

[18] Y.-S. Song and W. J. Percival, **Reconstructing the history of structure formation using Redshift Distortions**, *JCAP* **0910** (2009) 004, [arXiv:0807.0810].

[19] M. White, Y.-S. Song, and W. Percival, **Forecasting Cosmological Constraints from Redshift Surveys**, *MNRAS* **397** (2008) 1348–1354, [arXiv:0810.1518].

[20] P. McDonald and U. Seljak, **How to measure redshift-space distortions without sample variance**, *JCAP* **0910** (2009) 007, [arXiv:0810.0323]. * Brief entry *.

[21] G. M. Bernstein and Y.-C. Cai, **Cosmology without cosmic variance**, arXiv:1104.3862.

[22] J. Huchra, M. Davis, D. Latham, and J. Tonry, **A survey of galaxy redshifts: 4. The data.**, *Astrophys.J.Suppl.* **52** (1983) L89–L119.

[23] **2**dFGRS Collaboration Collaboration, W. J. Percival et al., **The 2dF Galaxy Redshift Survey: The Power spectrum and the matter content of the Universe**, *Mon.Not.Roy.Astron.Soc.* **327** (2001) 1297, [astro-ph/0105252].

[24] G. Hill, K. Gebhardt, E. Komatsu, N. Drory, P. MacQueen, et al., **The Hobby-Eberly Telescope Dark Energy Experiment (HETDEX): Description and Early Pilot Survey Results**, *ASP Conf.Ser.* **399** (2008) 115–118, [arXiv:0806.0183].

[25] **S**DSS-III Collaboration Collaboration, D. Schlegel, M. White, and D. Eisenstein, **The Baryon Oscillation Spectroscopic Survey: Precision measurements of the absolute cosmic distance scale**, arXiv:0902.4680.

[26] **S**DSS Collaboration Collaboration, C. P. Ahn et al., **The Ninth Data Release of the Sloan Digital Sky Survey: First Spectroscopic Data from the SDSS-III Baryon Oscillation Spectroscopic Survey**, *Astrophys.J.Suppl.* **203** (2012) 21, [arXiv:1207.7137].

[27] N. Kaiser, **Clustering in real space and in redshift space**, *Mon. Not. Roy. Astron. Soc.* **227** (1987) 1–27.

[28] R. Scoccimarro, **Redshift-space distortions, pairwise velocities and nonlinearities**, *Phys.Rev.* **D70** (2004) 083007, [astro-ph/0407214].

[29] A. Taruya, T. Nishimichi, and S. Saito, **Baryon Acoustic Oscillations in 2D: Modeling Redshift-space Power Spectrum from Perturbation Theory**, *Phys.Rev.* **D82** (2010) 063522, [arXiv:1006.0699].

[30] B. A. Reid and M. White, **Towards an accurate model of the redshift space clustering of halos in the quasilinear regime**, arXiv:1105.4165.

[31] J. Carlson, B. Reid, and M. White, **Convolution Lagrangian perturbation theory for biased tracers**, arXiv:1209.0780.

# Chapter 2

# Dynamics of Gravitational Instabilities and Statistics of Cosmic Fields[1]

In the last chapter we have presented the picture of the cold dark matter (CDM) particles as non-relativistic at scales much smaller than the Hubble radius. This allows us to reduce the equations of motion to those of Newtonian gravity in expanding background. Manifestation of expansion of the background appears in a redefinition of the variables used to describe the position and momentum of particles, as well as a redefinition of the gravitational potential.

We start by introducing the equations of motions of the CDM particle fluctuations field and continue by looking at the collisionless fluid approximation. We also consider the two standard pictures in describing these systems: Eulerian and Lagrangian. Further on, we look at the perturbative solutions of these equations that yield the results known as Standard (SPT) and Lagrangian Perturbation Theory (LPT). We consider the statistical properties of large scale structure, i.e. power spectrum and correlation function. We show the one and two loop power spectrum results in SPT as well as the power spectrum and correlation function in the Zel'dovich approximation.

## 2.1 Newtonian Particle Dynamics in the Expanding Background

We start by considering the system of particles of mass $m$ interacting gravitationally in the Newtonian limit. This assumes distances $x \ll H^{-1}$ and small velocities $v \ll c$. The equation of motion for a particle in physical coordinates (position $\boldsymbol{r}$ and time $t$) is

$$\frac{d^2\mathbf{r}}{d^2t} = -\nabla_r \Phi, \tag{2.1}$$

where $\Phi$ is the Newtonian potential. In the limit of large number of particles we can assume that gravitational potential is smooth and given in terms of the smooth density distribution of particles $\rho(\mathbf{x})$

$$\Phi(\mathbf{r}) = G \int d^3r' \frac{\rho(\mathbf{r}')}{|\mathbf{r} - \mathbf{r}'|}. \tag{2.2}$$

We are interested in studying the gravitational instabilities in terms of a departure from the homogeneous background expansion. For this reason, it is convenient to move to the

[1] This chapter is based on the material presented in cosmological perturbation theory review paper [1] and thesis [2].

comoving coordinates; position $\mathbf{x} = \mathbf{r}/a$ and time $d\tau = dt/a$, that were defined in the last chapter. It is also useful to define the density contrast $\delta(\mathbf{x})$ by

$$\rho(\mathbf{x}, \tau) = \bar{\rho}(\tau)\left(1 + \delta(\mathbf{x})\right), \tag{2.3}$$

where $\bar{\rho}$ is the mean background density. We can define the peculiar velocity relative to the background Hubble flow

$$\mathbf{u} = \frac{d\mathbf{r}}{dt} - \mathcal{H}\mathbf{x}, \tag{2.4}$$

where $\mathcal{H} = d\ln a/d\tau = Ha$ is the conformal expansion rate, already introduced in the previous chapter. In similar way potential $\Phi$ can be separated into the background part sourced by the mean density $\bar{\rho}$ and the contribution sourced by the overdensity fluctuations $\delta$

$$\Phi(\mathbf{x}, \tau) = -\frac{1}{2}\frac{d\mathcal{H}}{d\tau}x^2 + \phi(\mathbf{x}, \tau). \tag{2.5}$$

Using the Friedmann equations and density decomposition 2.3 we get the Poisson equation relating the fluctuations $\delta$ and the newly defined potential

$$\nabla_x^2\phi(\mathbf{x}) = \frac{3}{2}\mathcal{H}^2\Omega_{\mathrm{m}}(a)\delta(\mathbf{x}). \tag{2.6}$$

We are assuming that dark energy density is homogeneous, thus at late times this energy density fluctuations are dominated by the fluctuations in the matter density.

Canonical momentum corresponding to the position $\mathbf{x}$ is given by

$$\mathbf{p} = am\mathbf{u}, \tag{2.7}$$

where $\boldsymbol{u} = d\mathbf{x}/d\tau$. From equation 2.1 it follows that the equation of motion in the comoving coordinates is

$$\frac{d\mathbf{p}}{d\tau} = -am\nabla_{\mathbf{x}}\phi. \tag{2.8}$$

## 2.2 Eulerian Dynamics

We have described the system of many particles moving in the expanding background without the collisions and effected only by the gravitational potential $\phi$ sourced by the smooth overdensity fluctuations $\delta$. We can introduce the distribution function of particles in phase space

$$dN = f(\mathbf{x}, \mathbf{p}, \tau)d^3x d^3p. \tag{2.9}$$

By the Liouville's theorem distribution function is constant along the particle trajectories in the phase space so it follows

$$\frac{\mathrm{d}f}{\mathrm{d}\tau} = \frac{\partial f}{\partial \tau} + \frac{\boldsymbol{p}}{ma}\cdot\frac{\partial f}{\partial \boldsymbol{x}} - am\boldsymbol{\nabla}\phi\cdot\frac{\partial f}{\partial \boldsymbol{p}} = 0 \tag{2.10}$$

where we have used the equation of motion (2.8). This equation is known as the collisionless *Boltzmann equation* or the *Vlasov equation*. Vlasov equation provides the full description of our system but obtaining the full non-linear solution is a very difficult task. Non-linearity is introduced through the integral dependence in the Poisson equation on the distribution function.

We are mostly interested in distribution of the particles in the configuration space rather than in obtaining the full phase space information. It is thus convenient to take integral moments of the distribution function. In this way, we get the hierarchy of moments where the first few are the mass density field,

$$\rho(\boldsymbol{x}, \tau) = ma^{-3}\int d^3p\ f(\boldsymbol{x}, \boldsymbol{p}, \tau), \tag{2.11}$$

mean streaming velocity field

$$v_i(\boldsymbol{x},\tau) = \frac{\int d^3p \ \frac{p_i}{am} f(\boldsymbol{x},\boldsymbol{p},\tau)}{\int d^3p \ f(\boldsymbol{x},\boldsymbol{p},\tau)}, \tag{2.12}$$

and velocity dispersion

$$\sigma_{ij}(\boldsymbol{x},\tau) = \frac{\int d^3p \ \frac{p_i}{am}\frac{p_j}{am} f(\boldsymbol{x},\boldsymbol{p},\tau)}{\int d^3p \ f(\boldsymbol{x},\boldsymbol{p},\tau)} - v_i(\boldsymbol{x})v_j(\boldsymbol{x}). \tag{2.13}$$

The velocity dispersion is also called the anisotropic stress tensor, and it describes the deviation from a single coherent flow. The equations of motion for these newly introduced quantities are obtained by taking moments of the Vlasov equation. In this way, we get the continuity equation by taking the zeroth moment of the Vlasov equation

$$\frac{\partial\delta(\boldsymbol{x},\tau)}{\partial\tau} + \nabla\cdot\big[(1+\delta(\boldsymbol{x},\tau))\boldsymbol{v}(\boldsymbol{x},\tau)\big] = 0. \tag{2.14}$$

By taking the first moment we obtain the Euler equation

$$\frac{\partial v_i(\boldsymbol{x},\tau)}{\partial\tau} + \mathcal{H}v_i(\boldsymbol{x},\tau) + \boldsymbol{v}(\boldsymbol{x},\tau)\cdot\nabla v_i(\boldsymbol{x},\tau) = -\nabla_i\phi(\boldsymbol{x},\tau) - \frac{1}{\rho(\boldsymbol{x},\tau)}\nabla_i(\rho(\boldsymbol{x},\tau)\sigma_{ij}(\boldsymbol{x},\tau)). \tag{2.15}$$

Taking the higher moments of the Vlasov equation, we would get the hierarchy of equations which couple the equation of motion for $n$-th momentum moment of the phase space distribution function to the $n+1$-th moment. Here, in order to close the hierarchy we assume that the anisotropic stress tensor can be dropped out. This approximation is also known as the *pressureless perfect fluid* regime. This approximation is well established on large scales where linear solution of equations holds. As one starts to approach the nonlinear scales and structures collapse, virialize and shell crossing occurs, anisotropic stress and the higher moments start to play a more important role.

### 2.2.1 Linear Theory Solution

On large scales, we expect the Universe to be smooth, and thus, fluctuations to be small compared to the background fields. Thus, we can neglect the quadratic terms in the continuity and Euler equation. We get linearized equations

$$\begin{aligned}\frac{\partial\delta(\boldsymbol{x},\tau)}{\partial\tau} + \theta(\boldsymbol{x},\tau) &= 0,\\ \frac{\partial\boldsymbol{v}(\boldsymbol{x},\tau)}{\partial\tau} + \mathcal{H}\boldsymbol{v}(\boldsymbol{x},\tau) &= -\nabla\phi(\boldsymbol{x},\tau),\end{aligned} \tag{2.16}$$

where we have introduced the scalar component of the velocity field $\theta = \nabla\cdot\boldsymbol{v}$. Velocity field can be decomposed into a scalar $\theta$ contribution and a vector (vorticity) $\boldsymbol{w} = \boldsymbol{\nabla}\times\boldsymbol{v}$ contribution.

It follows for the vorticity contribution $\boldsymbol{w} \propto a^{-1}$, i.e. any initially present vorticity decays at linear level. Furthermore, even in the non-linear regime vorticity does not get generated if there is no anisotropic stress contribution. This means we can neglect the vorticity contribution altogether and focus on the evolution of density and velocity divergence components. This leaves us with the equation for the velocity divergence

$$\frac{\partial}{\partial\tau}\theta(\boldsymbol{x},\tau) + \mathcal{H}\theta(\boldsymbol{x},\tau) = -\nabla^2\phi(\boldsymbol{x},\tau). \tag{2.17}$$

Combining this with the linearized continuity equation and the Poisson equation and Fourier transforming we get the equation for the evolution of the linear overdensity field

$$\frac{\partial^2}{\partial\tau^2}\delta(\boldsymbol{k},\tau) + \mathcal{H}(\tau)\frac{\partial}{\partial\tau}\delta(\boldsymbol{k},\tau) = \frac{3}{2}\Omega_{\rm m}(\tau)\mathcal{H}^2(\tau)\delta(\boldsymbol{k},\tau). \tag{2.18}$$

This equation we can solve by the separation of variables $\delta(\boldsymbol{k},\tau) = D(\tau)\delta_L(\boldsymbol{k})$. The interesting solution is the mode growing in time which we call the growth rate $D(\tau)$. Growth rate can be expressed in the integral form

$$D(\tau) = D_0 H \int_0^a \frac{da'}{(a'H)^3}, \tag{2.19}$$

where $D_0$ is a normalization factor defined to give $D(a=1)=1$. In a Einstein-de-Sitter (EdS) Universe, where matter is dominating we have $H = a^{-3/2}$ and thus growth rate is equal to the scale factor $D = a$. In ΛCDM model the growth rate corresponds to the EdS at early times but then slows down at later times when the cosmological constant starts to dominate.

Neglecting the curl of the velocity field as we discussed above we have for the velocity field $\boldsymbol{v}(\boldsymbol{k}) = i\frac{\boldsymbol{k}}{k^2}\theta(\boldsymbol{k})$. From the linearized continuity equation it follows

$$\frac{\partial\delta(\boldsymbol{k})}{\partial\tau} = -\theta(\boldsymbol{k}) = f\mathcal{H}\delta(\boldsymbol{k}), \tag{2.20}$$

where we introduced the logarithmic growth factor $f = d\ln D/d\ln a$. In EdS case logarithmic growth factor is unity. For the ΛCDM model, it is straightforward to get the logarithmic growth factor from the expression for the growth rate. The good approximation valid up to a few percent is $f \approx \Omega_m^{5/9}$. At the late time cosmological constant starts to play a more significant role and $f$ start to decay from the EdS value, and finely drops to $f(a=1)\approx 0.48$ at present time.

### 2.2.2 Non-Linear Perturbation Theory

We now go beyond the linear solution of the fluid equations in order to probe mildly non-linear regime. Since the Fourier modes are decoupled in the linear theory, it is natural to do the perturbative expansion in the Fourier space. Continuity and Euler equations are then given as

$$\begin{aligned}
\frac{\partial}{\partial\tau}\delta(\boldsymbol{k}) + \theta(\boldsymbol{k}) &= -\int \frac{\mathrm{d}^3q}{(2\pi)^3}\frac{\mathrm{d}^3q'}{(2\pi)^3}\delta^D(\boldsymbol{k}-\boldsymbol{q}-\boldsymbol{q}')\alpha(\boldsymbol{q},\boldsymbol{q}')\theta(\boldsymbol{q})\delta(\boldsymbol{q}'),\\
\frac{\partial}{\partial\tau}\theta(\boldsymbol{k}) + \mathcal{H}\theta(\boldsymbol{k}) + \frac{3}{2}\Omega_{\mathrm{m}}(a)\mathcal{H}^2\delta(\boldsymbol{k}) &= -\int \frac{\mathrm{d}^3q}{(2\pi)^3}\frac{\mathrm{d}^3q'}{(2\pi)^3}\delta^D(\boldsymbol{k}-\boldsymbol{q}-\boldsymbol{q}')\beta(\boldsymbol{q},\boldsymbol{q}')\theta(\boldsymbol{q})\theta(\boldsymbol{q}'),
\end{aligned} \tag{2.21}$$

where we have defined the gravity coupling kernels as

$$\alpha(\boldsymbol{k}_1,\boldsymbol{k}_2) = \frac{\boldsymbol{k}_1\cdot(\boldsymbol{k}_1+\boldsymbol{k}_2)}{k_1^2}, \qquad \beta(\boldsymbol{k}_1,\boldsymbol{k}_2) = \frac{1}{2}\frac{\boldsymbol{k}_1\cdot\boldsymbol{k}_2}{k_1k_2}\left(\frac{k_2}{k_1}+\frac{k_1}{k_2}\right) + \frac{(\boldsymbol{k}_1\cdot\boldsymbol{k}_2)^2}{k_1^2k_2^2}. \tag{2.22}$$

We resort to the perturbation theory in order to solve these equations, note that this assumes $\delta \ll 1$ and $\theta \ll 1$.

In Standard Perturbation Theory (SPT) we assume the solution for non-linear fields $\delta$ and $\theta$ is given in the form of the power law expansion in the linear field $\delta_L$. We start with the ansatz

$$\begin{aligned}
\delta(\boldsymbol{k},\tau) &= \sum_{n=1}^{\infty} D^n(\tau)\int \frac{d^3q_1\ldots d^3q_n}{(2\pi)^{3n}}\delta_L(\boldsymbol{q}_1)\ldots\delta_L(\boldsymbol{q}_n)F_n(\boldsymbol{q}_1,\ldots,\boldsymbol{q}_n)\delta^D(\boldsymbol{k}-\boldsymbol{q}|_1^n),\\
\theta(\boldsymbol{k},\tau) &= -f(\tau)\mathcal{H}(\tau)\sum_{n=1}^{\infty} D^n(\tau)\int \frac{d^3q_1\ldots d^3q_n}{(2\pi)^{3n}}\delta_L(\boldsymbol{q}_1)\ldots\delta_L(\boldsymbol{q}_n)G_n(\boldsymbol{q}_1,\ldots,\boldsymbol{q}_n)\delta^D(\boldsymbol{k}-\boldsymbol{q}|_1^n),
\end{aligned} \tag{2.23}$$

where $\boldsymbol{q}|_i^j = \sum_{m=i}^{j} \boldsymbol{q}_l$. Inserting this ansatz into the equations above and assuming that the time dependence of the gravity kernels $F$ and $G$ can be neglected (see e.g. [3]) we obtain the following recursive solution

$$F_n(\boldsymbol{q}_1,\ldots,\boldsymbol{q}_n) = \sum_{m=1}^{n-1} \frac{G_m(\boldsymbol{q}_1,\ldots,\boldsymbol{q}_m)}{(2n+3)(n-1)} \Big[(2n+1)\alpha\left(\boldsymbol{q}|_1^m, \boldsymbol{q}|_{m+1}^n\right) F_{n-m}\left(\boldsymbol{q}_{m+1},\ldots,\boldsymbol{q}_n\right) + 2\beta\left(\boldsymbol{q}|_1^m, \boldsymbol{q}|_{m+1}^n\right) G_{n-m}\left(\boldsymbol{q}_{m+1},\ldots,\boldsymbol{q}_n\right)\Big] \tag{2.24}$$

$$G_n(\boldsymbol{q}_1,\ldots,\boldsymbol{q}_n) = \sum_{m=1}^{n-1} \frac{G_m(\boldsymbol{q}_1,\ldots,\boldsymbol{q}_m)}{(2n+3)(n-1)} \Big[3\alpha\left(\boldsymbol{q}|_1^m, \boldsymbol{q}|_{m+1}^n\right) F_{n-m}\left(\boldsymbol{q}_{m+1},\ldots,\boldsymbol{q}_n\right) + 2n\beta\left(\boldsymbol{q}|_1^m, \boldsymbol{q}|_{m+1}^n\right) G_{n-m}\left(\boldsymbol{q}_{m+1},\ldots,\boldsymbol{q}_n\right)\Big]. \tag{2.25}$$

We are primarily interested in the second and third order solution since these, as we will see later, contribute to the one loop power spectra result. The second order density and velocity kernels are given by

$$\begin{aligned} F_2(\boldsymbol{k}_1,\boldsymbol{k}_2) &= \frac{5}{7}\alpha(\boldsymbol{k}_1,\boldsymbol{k}_2) + \frac{2}{7}\beta(\boldsymbol{k}_1,\boldsymbol{k}_2) = \frac{5}{7} + \frac{1}{2}\frac{\boldsymbol{k}_1\cdot\boldsymbol{k}_2}{k_1 k_2}\left(\frac{k_2}{k_1}+\frac{k_1}{k_2}\right) + \frac{2}{7}\frac{(\boldsymbol{k}_1\cdot\boldsymbol{k}_2)^2}{k_1^2 k_2^2}, \\ G_2(\boldsymbol{k}_1,\boldsymbol{k}_2) &= \frac{3}{7}\alpha(\boldsymbol{k}_1,\boldsymbol{k}_2) + \frac{4}{7}\beta(\boldsymbol{k}_1,\boldsymbol{k}_2) = \frac{3}{7} + \frac{1}{2}\frac{\boldsymbol{k}_1\cdot\boldsymbol{k}_2}{k_1 k_2}\left(\frac{k_2}{k_1}+\frac{k_1}{k_2}\right) + \frac{4}{7}\frac{(\boldsymbol{k}_1\cdot\boldsymbol{k}_2)^2}{k_1^2 k_2^2} \end{aligned} \tag{2.26}$$

These relations are symmetrized over the momenta. Also, it is useful to note that

$$F_2(\boldsymbol{q}_1,\boldsymbol{q}_2) - G_2(\boldsymbol{q}_1,\boldsymbol{q}_2) = \frac{2}{7}\big[\alpha(\boldsymbol{q}_1,\boldsymbol{q}_2) - \beta(\boldsymbol{q}_1,\boldsymbol{q}_2)\big]. \tag{2.27}$$

Futrher on, explicit expressions for $F_3$ and $G_3$ are given by

$$\begin{aligned} F_3(\boldsymbol{q}_1,\boldsymbol{q}_2,\boldsymbol{q}_3) =& \frac{1}{18}\left(7\alpha(\boldsymbol{q}_1,\boldsymbol{q}_2+\boldsymbol{q}_3)F_2(\boldsymbol{q}_2,\boldsymbol{q}_3) + 2\beta(\boldsymbol{q}_1,\boldsymbol{q}_2+\boldsymbol{q}_3)G_2(\boldsymbol{q}_2,\boldsymbol{q}_3)\right) \\ &+ \frac{1}{18}G_2(\boldsymbol{q}_1,\boldsymbol{q}_2)\left(7\alpha(\boldsymbol{q}_1+\boldsymbol{q}_2,\boldsymbol{q}_3) + 2\beta(\boldsymbol{q}_1+\boldsymbol{q}_2,\boldsymbol{q}_3)\right), \\ G_3(\boldsymbol{q}_1,\boldsymbol{q}_2,\boldsymbol{q}_3) =& \frac{1}{18}\left(3\alpha(\boldsymbol{q}_1,\boldsymbol{q}_2+\boldsymbol{q}_3)F_2(\boldsymbol{q}_2,\boldsymbol{q}_3) + 6\beta(\boldsymbol{q}_1,\boldsymbol{q}_2+\boldsymbol{q}_3)G_2(\boldsymbol{q}_2,\boldsymbol{q}_3)\right) \\ &+ \frac{1}{18}G_2(\boldsymbol{q}_1,\boldsymbol{q}_2)\left(3\alpha(\boldsymbol{q}_1+\boldsymbol{q}_2,\boldsymbol{q}_3) + 6\beta(\boldsymbol{q}_1+\boldsymbol{q}_2,\boldsymbol{q}_3)\right). \end{aligned} \tag{2.28}$$

These kernels are not yet symmetrized over the arguments yet, and one should account for both the 2 cyclic permutations of the momentum arguments in the kernels.

## 2.3 Lagrangian Dynamics

In this section we look at Lagrangian Perturbation Theory (LPT). We start from the initial Lagrangian particle position $\boldsymbol{q}$ and follow the trajectory to the final position $\boldsymbol{x}$. The goal is to describe the mapping $\boldsymbol{\Psi}$ from the initial, Lagrangian coordinates to the Eulerian coordinates

$$\boldsymbol{x}(\boldsymbol{q},\tau) = \boldsymbol{q} + \boldsymbol{\Psi}(\boldsymbol{q},\tau). \tag{2.29}$$

Continuity relation connects the density in the Lagrangian and Eulerian coordinates $(1+\delta(\boldsymbol{x}))d^3x = d^3q$, which then gives the Jacobian

$$J = \left|\frac{d^3x}{d^3q}\right| = \det\left[\delta_{ij}^K + \Psi_{i,j}\right]. \tag{2.30}$$

Using the fact that $1+\delta(\boldsymbol{x}) = 1/J$ and taking the divergence of the equation of motion of a particle 2.8 and using the Poisson equation we get

$$J\ \nabla\cdot\left[\frac{d^2\boldsymbol{x}}{d\tau^2}+\mathcal{H}\frac{d\boldsymbol{x}}{d\tau}\right] = \frac{3}{2}\Omega_{\rm m}(a)\mathcal{H}^2(J-1). \tag{2.31}$$

In order to express all the parts in Lagrangian coordinates we need to replace $\nabla_i = (\delta_{ij}+\Psi_{i,j})^{-1}\nabla_{q_i}$. Perturbative approach in solving this equation suggests the expansion of displacement field and Jacobian $\Psi = \sum_n \Psi^{(n)}$, and $J = \sum_n J^{(n)}$. This gives the contributions to the Jacobian (see e.g. [4, 2])

$$J^{(1)} = L^{(1)} = \sum_i \Psi^{(1)}_{i,i} \tag{2.32}$$

$$J^{(2)} = L^{(2)} + K^{(2)} = \sum_i \Psi^{(2)}_{i,i} + \frac{1}{2}\sum_{i\neq j}\left\{\Psi^{(1)}_{i,i}\Psi^{(1)}_{j,j} - \Psi^{(1)}_{i,j}\Psi^{(1)}_{j,i}\right\} \tag{2.33}$$

$$J^{(3)} = L^{(3)} + K^{(3)} + M^{(3)} = \sum_i \Psi^{(3)}_{i,i} + \frac{1}{2}\sum_{i\neq j}\left\{\Psi^{(1)}_{i,i}\Psi^{(2)}_{j,j} - \Psi^{(2)}_{i,j}\Psi^{(1)}_{j,i}\right\} + \det\Psi^{(1)}_{i,j} \tag{2.34}$$

At leading order, we have for the equation of motion becomes

$$\left[\frac{d^2\Psi^{(1)}_{i,i}}{d\tau^2}+\mathcal{H}\frac{d\Psi^{(1)}_{i,i}}{d\tau}\right] = \frac{3}{2}\Omega_{\rm m}(a)\mathcal{H}^2\Psi^{(1)}_{i,i}. \tag{2.35}$$

### 2.3.1 Zel'dovich Approximation

Displacement field $\Psi(\mathbf{q},\tau)$ can be determined as is the velocity field integral along the world-line of the particle:

$$\Psi(\mathbf{q},\tau) = \int^{\tau} d\tau' \mathbf{v}[\mathbf{r}(\mathbf{q},\tau'),\tau']. \tag{2.36}$$

From continuity equation and assumption thet we have uniform initial densety field we have

$$(1+\delta(\mathbf{r}))d^3r = d^3q \quad\rightarrow\quad 1+\delta(\mathbf{r}) = \int d^3q\ \delta^D[\mathbf{r}-\mathbf{q}-\Psi(\mathbf{q})]. \tag{2.37}$$

In Fourier space this gives the closed relation for the density and the displacement field

$$\delta(\mathbf{k}) = \int d^3q\ e^{i\mathbf{k}\cdot\mathbf{q}}\left(e^{i\mathbf{k}\cdot\Psi}-1\right). \tag{2.38}$$

Using the linear equation for the displacement field 2.35 and implying the separation of variables we get the solution for the displacement field in the *Zel'dovich approximation*

$$\Psi^{(1)}(\mathbf{k}) = -i\frac{\mathbf{k}}{k^2}\delta_L(\mathbf{k}). \tag{2.39}$$

## 2.4 Statistical Measurements of Structure

We want to describe the statistical properties of the fields that can either be the cosmic density field, $\delta(\mathbf{x})$, the cosmic gravitational potential, the velocity divergence field or any other field of interest.

A random field is considered statistically homogeneous if all the joint multipoint probability distribution functions $p(\delta_1,\delta_2,\dots)$ or its moments, ensemble averages of local density products, remain the same under translation of the coordinates $\mathbf{x}_1,\mathbf{x}_2,\dots$ in space, here

$\delta_i = \delta(\mathbf{x}_i)$. The probabilities, thus, depend only on the relative positions. Similarly, stochastic field is called statistically isotropic if the probability distribution functions $p(\delta_1, \delta_2, \dots)$ is invariant under the spatial rotations. We assume that cosmic fields we are considering are statistically homogeneous and isotropic. This assumption is in principle supported by the current observational data, but observational effects like redshift space distortions in galaxy redshift surveys introduce significant deviations from statistical isotropy and homogeneity. These effects we can take into account, and they are the topics of interest in the rest of this thesis.

### 2.4.1 Two Point Correlation Function and Power Spectrum

The two-point *correlation function* is defined as the ensemble average of the density field at two different locations,

$$\xi(r) = \langle \delta(\boldsymbol{x}) | \delta(\boldsymbol{x} + \boldsymbol{r}) \rangle \,. \tag{2.40}$$

Because of the statistical homogeneity and isotropy correlation function depends only on the norm of $\mathbf{r}$. Fourier transform of the real overdensity field $\delta(\mathbf{x})$ is then complex random variable, and we have $\delta(\boldsymbol{k}) = \delta^*(-\boldsymbol{k})$. Correlation in Fourier space is given by

$$\langle \delta(\boldsymbol{k}) | \delta(\boldsymbol{k}') \rangle = \int d^3x \; d^3r \;\; \langle \delta(\boldsymbol{x}) | \delta(\boldsymbol{x} + \boldsymbol{r}) \rangle \, e^{-i(\boldsymbol{k}+\boldsymbol{k}')\cdot\boldsymbol{x} - i\boldsymbol{k}'\cdot\boldsymbol{r}}. \tag{2.41}$$

Using the statistical homogeneity and isotropy of the correlation function then gives,

$$\langle \delta(\boldsymbol{k}) | \delta(\boldsymbol{k}') \rangle = (2\pi)^3 \delta^D(\boldsymbol{k} + \boldsymbol{k}') \int d^3\boldsymbol{r} \; \xi(r) e^{i\boldsymbol{k}\cdot\boldsymbol{r}} = (2\pi)^3 \delta^D(\boldsymbol{k} + \boldsymbol{k}') P(k), \tag{2.42}$$

where we have defined the density *power spectrum* $P(k)$. In our convention $k^3 P(k)/(2\pi^2)$ represents the contribution per logarithmic wavenumber to the variance.

### 2.4.2 Gaussian Random Fields and Wick Theorem

Power spectrum becomes especially useful quantity once we consider a *Gaussian field* for which any joint distribution of local densities has a Gaussian distribution. Ensemble average of the product of random variables can then be expressed as the product of pair ensemble averages. In Fourier space we can write this as

$$\langle \delta(\boldsymbol{k}_1) \dots \delta(\boldsymbol{k}_{2p+1}) \rangle = 0, \qquad \langle \delta(\boldsymbol{k}_1) \dots \delta(\boldsymbol{k}_{2p}) \rangle = \sum_{\text{pairings}} \prod_{\text{pairs}(i,j)} \langle \delta(\boldsymbol{k}_i) \delta(\boldsymbol{k}_j) \rangle \tag{2.43}$$

This is known as the *Wick theorem*. This means that the statistical properties of the random variable $\delta(\mathbf{k})$ is then entirely determined by the shape and normalization of the power spectra $P(k)$. In inflationary scenario the initial energy density fluctuations are expected to have Gaussian random distribution which is a consequence of the commutation rules for creation and annihilation operators for a free quantum field

$$\left[ \left( a_{\boldsymbol{k}} + a^\dagger_{-\boldsymbol{k}} \right), \left( a_{\boldsymbol{k}'} + a^\dagger_{-\boldsymbol{k}'} \right) \right] = \delta^D(\boldsymbol{k} + \boldsymbol{k}'). \tag{2.44}$$

This implies that the Wick theorem is valid for all modes of $\varphi_{\mathbf{k}}$ that exit the Hubble radius and afterwords come back in as classical stochastic perturbations.

### 2.4.3 Higher Order Correlations

Going beyond the two-point function, we can also define higher-order correlations. We define them as the connected part of the ensemble average of the density in an arbitrary number of locations. In the case of Gaussian random field, all connected correlation functions are zero except the two-point correlation function $\xi_2$ as a consequence of Wick's theorem.

This means that any field, not necessarily linear, built from a Gaussian field $\delta$ can be written in terms of the combinations of two-point functions of $\delta$. Connected part has the important property that it vanishes when one or more points are separated by infinite separation. Additionally it provides a useful way of characterizing the statistical properties since unlike unconnected correlation, each connected correlation provides independent information.

In Fourier space this leads to the expression for the multi-spectra

$$\langle \delta(\boldsymbol{k}_1) \dots \delta(\boldsymbol{k}_N) \rangle_c = \delta^D(\boldsymbol{k}_1 + \dots + \boldsymbol{k}_N)\, P_N(\boldsymbol{k}_1, \dots, \boldsymbol{k}_N). \tag{2.45}$$

where the delta function is the consequence of the homogeneity of space. A particular case of these multi-spectra is the $N = 3$, the bispectrum, which usually is denoted by $B(\mathbf{k}_1, \mathbf{k}_2, \mathbf{k}_3)$.

## 2.5 Perturbation Theory Results for Power Spectrum and Correlation Function

In the previous sections, we expressed the non-linear density and velocity fields as a sum of products of linear density fields. We are interested in the obtaining the two-point spectra of these fields. Thus, we need to correlate two of these non-linear fields with each other. Using the Wick theorem we can express the non-linear power spectra in terms of linear power spectra

$$(2\pi)^3 P_L(k) \delta^D(\mathbf{k} + \mathbf{k}') = \langle \delta_L(\mathbf{k}) | \delta_L(\mathbf{k}') \rangle. \tag{2.46}$$

Linear power spectrum is determined by the initial conditions and is usually given as the output of the Boltzmann codes like CAMB [1].

The leading order correction to the linear power spectrum the so called one loop power spectra. Here we show the one and two loop SPT results as well as Zel'dovich result as the leading corrections in LPT.

### 2.5.1 One-loop Eulerian Power Spectrum

In order to obtain the one-loop result for the power spectrum in Eulerian scheme we correlate the terms in the expansion given in 2.23, and keep the terms up to the fourth order in the fields. We get

$$\begin{aligned} \langle \delta(\boldsymbol{k}) | \delta(\boldsymbol{k}') \rangle =& \left\langle \delta^{(1)}(\boldsymbol{k}) | \delta^{*(1)}(\boldsymbol{k}') \right\rangle + 2 \left\langle \delta^{(1)}(\boldsymbol{k}) | \delta^{*(3)}(\boldsymbol{k}') \right\rangle + \left\langle \delta^{(2)}(\boldsymbol{k}) | \delta^{*(2)}(\boldsymbol{k}') \right\rangle, \\ P_{1\mathrm{loop}}(k) =& P_{\mathrm{L}}(k) + 2P_{13}(k) + P_{22}(k), \end{aligned} \tag{2.47}$$

where the one-loop terms are given as the integrals over the gravity kernels and linear power spectra

$$\begin{aligned} P_{\delta\delta}^{(2,2)}(k) &= 2 \int \frac{d^3q}{(2\pi)^3} \left[ F_2^{(s)}(\mathbf{q}, \mathbf{k} - \mathbf{q}) \right]^2 P_L(q) P_L(|\mathbf{k} - \mathbf{q}|) \\ P_{\delta\delta}^{(1,3)}(k) &= 3 P_L(k) \int \frac{d^3q}{(2\pi)^3} F_3^{(s)}(\mathbf{k}, \mathbf{q}, -\mathbf{q})\, P_L(q). \end{aligned} \tag{2.48}$$

$P_{\delta\delta}^{(2,2)}$ term represents the correction due to the non-linear mode coupling, and $P_{\delta\delta}^{(1,3)}$ is so called propagator term which represents the correction to the linear mode propagation.

[1] http://camb.info

### 2.5.2 Two-loop Eulerian Power Spectrum

Going further in the perturbative expansion, we get the two loop contribution which gives additional terms by correlating first order field with the fifth, second order field with the fourth and autocorrelation of third order fields:

$$\begin{aligned}\langle\delta(\boldsymbol{k})|\delta(\boldsymbol{k}')\rangle = &\left\langle\delta^{(1)}(\boldsymbol{k})|\delta^{*(1)}(\boldsymbol{k}')\right\rangle + 2\left\langle\delta^{(1)}(\boldsymbol{k})|\delta^{*(3)}(\boldsymbol{k}')\right\rangle + \left\langle\delta^{(2)}(\boldsymbol{k})|\delta^{*(2)}(\boldsymbol{k}')\right\rangle \\ &+ \left\langle\delta^{(3)}(\boldsymbol{k})|\delta^{*(3)}(\boldsymbol{k}')\right\rangle + 2\left\langle\delta^{(2)}(\boldsymbol{k})|\delta^{*(4)}(\boldsymbol{k}')\right\rangle + \left\langle\delta^{(1)}(\boldsymbol{k})|\delta^{*(5)}(\boldsymbol{k}')\right\rangle\end{aligned} \tag{2.49}$$

In terms of the power spectrum, we get three new correction terms

$$P_{\delta\delta}(\mathbf{k},\tau) = P_{\delta\delta}^{(1,1)}(\mathbf{k}) + P_{\delta\delta}^{(2,2)}(\mathbf{k},\tau) + 2P_{\delta\delta}^{(1,3)}(\mathbf{k},\tau) + 2P_{\delta\delta}^{(1,5)}(\mathbf{k},\tau) + 2P_{\delta\delta}^{(2,4)}(\mathbf{k},\tau) + P_{\delta\delta}^{(3,3)}(\mathbf{k},\tau), \tag{2.50}$$

where the correction terms are explicitly given

$$\begin{aligned}P_{\delta\delta}^{(1,5)}(k) =& 15P_L(k,\tau)\int\frac{d^3q_1}{(2\pi)^3}\frac{d^3q_2}{(2\pi)^3}F_5^{(s)}\left(\mathbf{k},\mathbf{q}_1,-\mathbf{q}_1,\mathbf{q}_2,-\mathbf{q}_2\right)P_L(q_1)P_L(q_2) \\ P_{\delta\delta}^{(2,4)}(k) =& 12\int\frac{d^3q_1}{(2\pi)^3}\frac{d^3q_2}{(2\pi)^3}F_2^{(s)}\left(\mathbf{q}_1,\mathbf{k}-\mathbf{q}_1\right)F_4^{(s)}\left(-\mathbf{q}_1,\mathbf{q}_1-\mathbf{k},\mathbf{q}_2,-\mathbf{q}_2\right) \\ &\times P_L(q_1)P_L(q_2)P_L\left(|\mathbf{k}-\mathbf{q}_1|\right) \\ P_{\delta\delta}^{(3,3)}(k) =& \int\frac{d^3q_1}{(2\pi)^3}\frac{d^3q_2}{(2\pi)^3}\Big[9F_3^{(s)}\left(\mathbf{k},-\mathbf{q}_1,\mathbf{q}_1\right)F_3^{(s)}\left(-\mathbf{k},\mathbf{q}_2,-\mathbf{q}_2\right)P_L(k)P_L(q_1)P_L(q_2) \\ &+ 6F_3^{(s)}\left(\mathbf{q}_1,\mathbf{q}_2,\mathbf{k}-\mathbf{q}_1-\mathbf{q}_2\right)F_3^{(s)}\left(-\mathbf{q}_1,-\mathbf{q}_2,\mathbf{q}_1+\mathbf{q}_2-\mathbf{k}\right) \\ &\times P_L(q_1)P_L(q_2)P_L\left(|\mathbf{k}-\mathbf{q}_1-\mathbf{q}_2|\right)\Big]\end{aligned} \tag{2.51}$$

where the integration is performed over $\mathbf{q}_1$ and $\mathbf{q}_2-$ momenta.

### 2.5.3 Power Spectrum in Zel'dovich Approximation

Using the equation 2.38 we get the expression for the power spectra (see e.g. [5])

$$P(k) = \int d^3q e^{i\mathbf{k}\cdot\mathbf{r}}\left(\langle\exp(i\mathbf{k}\cdot\Delta\Psi)\rangle - 1\right). \tag{2.52}$$

Here $\langle\exp(i\mathbf{k}\Delta\Psi)\rangle$ is the generating function of differential displacement field, $\Delta\Psi(\mathbf{q})$, of the two points separated by $\mathbf{q} = \mathbf{q}_1 - \mathbf{q}_2$:

$$\Delta\Psi(\mathbf{q}) = \Psi(\mathbf{q}_1) - \Psi(\mathbf{q}_2). \tag{2.53}$$

Using the Zel'dovich approximation for the displacement field, we have

$$\Psi(\mathbf{q},\tau) = D(\tau)\Psi_L(\mathbf{q}) = D(\tau)\int\frac{d^3p}{(2\pi)^3}\frac{i\mathbf{p}}{p^2}\delta_L(\mathbf{p})\exp(-i\mathbf{q}\cdot\mathbf{p}). \tag{2.54}$$

By construction, the Lagrangian coordinates preserve the mass but in Zel'dovich approximation at the expense of not satisfying the Euler equation. If we assume the Gaussian initial condition, we see from the last equation that the displacement field remains Gaussian for all time. For Gaussian fields, we can use the cumulant expansion theorem

$$\begin{aligned}\langle\exp(i\mathbf{k}\cdot\Delta\Psi)\rangle &= \exp\left(-ik_ik_j\left\langle\Delta\Psi_i\Delta\Psi_j\right\rangle/2\right) \\ &= \exp\left(-ik_ik_j\left[\psi_{ij}(0) - \psi_{ij}(\mathbf{q})\right]\right),\end{aligned} \tag{2.55}$$

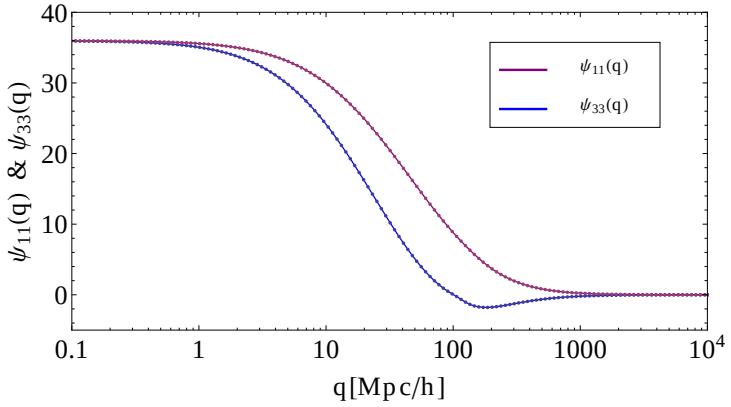


**Figure 2.1:** $q$ dependence of $\psi_{11}(q)$ (purple line) and $\psi_{33}(q)$ (blue line). At low $q$ limit both $\psi_{11}(q)$ and $\psi_{33}(q)$ values converge to $\sigma_v^2$.

where $\psi_{ij}(\mathbf{q}) = \langle \Psi_i(\mathbf{q}_1)\Psi_j(\mathbf{q}_2)\rangle$ is the displacement correlation function. In Zel'dovich approximation we have

$$\psi_{Lij}(\mathbf{q}) = D(\tau)^2 \int \frac{d^3p}{(2\pi)^3}\frac{p_i p_j}{p^4} P_L(\mathbf{p}) \exp(-i\mathbf{q}\cdot\mathbf{p}), \tag{2.56}$$

and for which the zero separation is

$$\psi_{Lij}(0) = D(\tau)^2 \frac{\delta_{ij}}{3}\int \frac{d^3p}{(2\pi)^3} p^{-2} P_L(p) = D(\tau)^2 \delta_{ij}\sigma_v^2. \tag{2.57}$$

Power spectrum is then given as

$$P(\mathbf{k}) = \int d^3q\; e^{i\mathbf{k}\cdot\mathbf{q}} \left(e^{-k_i k_j[\psi_{ij}(0)-\psi_{ij}(\mathbf{q})]} - 1\right). \tag{2.58}$$

We evaluate $\psi_{ij}(\mathbf{q})$ in the frame where $\mathbf{q}$ is oriented along the $\hat{z}$ direction

$$\begin{aligned}\psi_{11}(q) = \psi_{22}(q) &= 2D(\tau)^2 \int \frac{dp}{(2\pi)^2} P_L(p)\frac{j_1(pq)}{pq}.\\ \psi_{33}(q) &= 2D(\tau)^2 \int \frac{dp}{(2\pi)^2} P_L(p)\left(j_0(pq) - 2\frac{j_1(pq)}{pq}\right),\end{aligned} \tag{2.59}$$

where $j_n(x)$ is the spherical Bessel function of the $n-$th order. In figure 2.1 we show the scale dependence of the functions $\psi_{11}$ and $\psi_{33}$, which for low $q$ converge to $\sigma_v^2$ value. We want to evaluate the power spectrum in the frame where $\mathbf{k}$ is oriented along the $\hat{z}$ direction, so we have to rotate $\psi_{ij}$ results above. Preforming the $\hat{z}\to\mathbf{q}$ rotation $\mathbf{q} = R(\phi,\theta)\hat{z} = R_z(\phi)R_y(\theta)\hat{z}$ accomplishes this. The exponent term in power spectrum then reads

$$\exp(k_i k_j \psi_{ij}(\mathbf{q})) = \exp(k_3 k_3 R_{3i} R_{3j}\psi_{ij}(\mathbf{q})) = \exp\left(k^2\left[(1-\mu^2)\psi_{11}(q) + \mu^2\psi_{33}(q)\right]\right). \tag{2.60}$$

Finally, we get the explicit power spectrum expression

$$P(k) = \int d^3q\; e^{i\mathbf{k}\cdot\mathbf{q}} \left(e^{-k^2\sigma_v^2 + k^2\psi_{11} - k^2\mu^2(\psi_{11}-\psi_{33})} - 1\right). \tag{2.61}$$

In the figure 2.2 we show results for Zel'dovich power spectrum at four different redshifts $z = 0,\ 0.5,\ 1.0,\ 2.0$. We also show the results of one-loop SPT as well as two other methods: Closure two-loop theory presented in [6] and phenomenological model presented in [7]. These

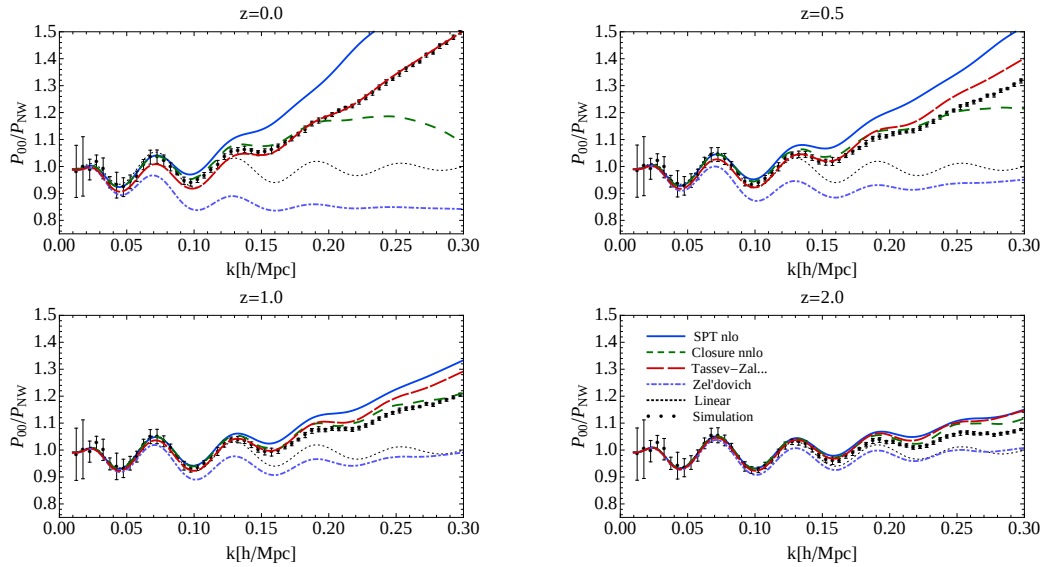


**Figure 2.2:** We compare the result of Zel'dovich approximation (purple, dot-dashed) in equation 2.61, Tassev-Zaldarriaga model (red, long-dashed) from [7], one-loop SPT result (blue, solid), Closure PT (green, dashed) from [6] and simulation data (black, dots). We also show the linear theory result (black, dotted line) results. Four different redshifts are $z = 0,\ 0.5,\ 1.0,\ 2.0$. Results are divided by no-wiggle power spectrum [8].

results are shown relative to the linear theory result where baryon acoustic wiggles have been flattened, so called no-wiggle result (see e.g. [8]). All the results are compared to the N-body simulations. We see that the Zel'dovich result is suppressed relative to the other methods.

Let us show that Zel'dovich power spectra recovers the linear theory on large scales. By expanding the exponential term with $\psi_{11}$ and $\psi_{33}$ fields we have

$$\begin{aligned} e^{k^2\psi_{33}} - 1 &\simeq k^2\psi_{33} + \dots, \\ e^{k^2\psi_{33}}\left(\psi_{11} - \psi_{33}\right) &\simeq \psi_{11} - \psi_{33} + \dots. \end{aligned} \tag{2.62}$$

It follows that the Zel'dovich power spectrum in equation 2.61 reduces to

$$\begin{aligned} P(k) =& 4\pi \int dp\ P_L(p) \left[ \frac{k^2}{2\pi^2} \int dq\ q^2 j_0(kq) j_0(pq) \right. \\ & - \frac{k^2}{\pi^2} \int dq\ q \left( \frac{1}{p} j_0(kq) j_1(pq) + \frac{1}{k} j_0(pq) j_1(kq) \right) \\ & \left. + \frac{k^2}{\pi^2} \int dq\ \frac{3}{pk} j_1(kq) j_1(pq) \right] \\ =& P_L(k) \end{aligned} \tag{2.63}$$

Where in the second relation we have used the fact that the first, $j_0 j_0$, term gives $\frac{\pi}{2k^2}\delta^D(k-p)$ contribution and the latter two terms exactly cancel.

# Bibliography


[1] F. Bernardeau, S. Colombi, E. Gaztanaga, and R. Scoccimarro, **Large scale structure of the universe and cosmological perturbation theory**, *Phys.Rept.* **367** (2002) 1–248, [astro-ph/0112551].

[2] D. Jeong, **Cosmology with high (z $>$ 1) redshift galaxy surveys**, (2010) PhD Thesis.

[3] R. Takahashi, **Third Order Density Perturbation and One-loop Power Spectrum in a Dark Energy Dominated Universe**, *Prog.Theor.Phys.* **120** (2008) 549–559, [arXiv:0806.1437].

[4] F. Bouchet, S. Colombi, E. Hivon, and R. Juszkiewicz, **Perturbative Lagrangian approach to gravitational instability**, *Astron.Astrophys.* **296** (1995) 575, [astro-ph/9406013].

[5] A. Taylor and A. Hamilton, **Nonlinear cosmological power spectra in real and redshift space**, *Mon. Not. Roy. Astron. Soc.* (1996) [astro-ph/9604020].

[6] A. Taruya and T. Hiramatsu, **A Closure Theory for Non-linear Evolution of Cosmological Power Spectra**, arXiv:0708.1367.

[7] S. Tassev and M. Zaldarriaga, **The Mildly Non-Linear Regime of Structure Formation**, arXiv:1109.4939.

[8] D. J. Eisenstein and W. Hu, **Baryonic Features in the Matter Transfer Function**, *Astrophys. J.* **496** (1998) 605, [astro-ph/9709112].

# Chapter 3

# Clustering of Biased Objects: Dark Matter Halos [1]

In the last chapter, we have reviewed the clustering of dark matter. Since dark matter is dark, i.e. interacts weakly if at all, we have no means of direct observation of its clustering. What we typically can observe are tracers of dark matter, such as e.g. galaxies. Even though the formation of galaxies is itself a complex subject, involving highly nonlinear processes, as well as baryonic physics, we can resort to a simplified but still very useful picture. In this picture galaxies are formed in the potential wells of virialized clumps of dark matter, called dark matter halos. Thus, the key in relating the dark matter clustering to the observations lies in understanding the connection of dark matter distribution to the distribution of dark matter halos, and secondly the population of these halos with galaxies, depending on their types as well as the properties of a hosting halo.

This chapter contains a short review of the halo mass function and peak background split formalism. We then introduce the Eulerian and Lagrangian bias, and show how they are related. Finally, we write down the more general biasing formalism of relating the dark matter halos to the non-linear dark matter density field taking into account the non-locality of this relation in the Eulerian framework.

## 3.1 Halo Mass Function and Abundance of Haloes

In the simplest picture obtained from the spherical collapse model halos form at a given position in space whenever the linear overdensity field reaches a threshold of $\delta_{\rm c} = 1.69$. We apply this concept to estimate the mean number density of halos at a given time. We denote the number density of halos of mass $M$ at position $x$ and time $\tau$ by $n_{\rm h}(x, M, \tau)$ and the corresponding mean density by $\bar{n}_{\rm h}(M) = \langle n_{\rm h}(x, M)\rangle$. We also introduce the density field $\delta_M$ smoothed over a given mass $M = \frac{4\pi}{3} R^3 \bar{\rho}$.

Press and Schechter [6] proposed the model where if $\delta_M$ at a given point is larger than the threshold $\delta_{\rm c}$ this point is contained within a halo of mass $> M$. Since we assume that $\delta_M$ is a zero mean Gaussian random field with variance $\sigma_M^2$ , the probability that at a random point $\delta_M$ exceeds the threshold $\delta_{\rm c}$ is given by

$$p(\sigma_M) = \frac{1}{\sqrt{2\pi}\sigma_M} \int_{\delta_{\rm c}}^{\infty} dx \ \exp\left(-\frac{x^2}{2\sigma_M^2}\right) = \frac{1}{2}\left[1 - {\rm erf}\left(\frac{\nu}{\sqrt{2}}\right)\right], \tag{3.1}$$

where $\nu = \delta_{\rm c}/\sigma_M$ is the peak height and erf is the error function. For $\Lambda$CDM universe $\sigma(M)$ is decreasing, i.e. inhomogeneities at the small scale have a larger rms amplitude and are thus the first to cross the critical collapse density. This leads to the bottom up scenario of structure formation, where small scale objects form first and then merge to form more

[1] The material presented in this chapter is based on following review articles and textbooks: [1, 2, 3, 4, 5].

massive objects. For hot dark matter universes, the structure formation follows a top down scenario, where large objects form first and subsequently disintegrate into smaller objects.

Since a halo of mass M effectively collects the mass within a comoving volume $V(M) = M/\bar{\rho}$, we consider $\delta_c$ at random positions $x_i$, so that the volumes V(M) associated with these positions do not overlap. The fraction of points with $\delta_M > \delta_c$ for masses within range from $M$ to $M + dM$ is given by $(dp/dM)dM$. The mass function or multiplicity function is the mean number of halos of mass $M$ per unit of comoving volume and unit mass, and it is given by

$$\frac{d\bar{n}_h}{dM}(M) = -\frac{2}{V(M)}\frac{dp}{dM} = -2\frac{\bar{\rho}_0}{M}\frac{dp}{d\sigma_M}\frac{d\sigma_M}{dM} = -\sqrt{\frac{2}{\pi}}\frac{\bar{\rho}_0}{M\sigma_M}\frac{d\sigma_M}{dM}\nu e^{-\nu^2/2} \tag{3.2}$$

Here we multiplied the whole expression by the factor 2 in order to be consistent with simulations. This result is called the *Press-Schechter* (PS) mass function, first presented in [6]. If we redefine the peak height $\nu \to \sqrt{\nu}$ the PS mass function reads

$$\frac{d\bar{n}_h}{dM}(M) = \sqrt{\frac{\nu}{2\pi}}\frac{\bar{\rho}_0}{M^2}e^{-\frac{\nu}{2}}\frac{d\ln\nu}{d\ln M}. \tag{3.3}$$

PS mass function is underestimating the abundance of massive halos relative to what is found in $N$-body simulations. In order to improve this result, we can construct a bit more complicated mass function

$$\frac{d\bar{n}_h}{dM}(M) = \sqrt{\frac{q\nu}{2\pi}}\left(1 + \frac{1}{(q\nu)^p}\right)\frac{\bar{\rho}_0}{M^2}e^{-\frac{q\nu}{2}}\frac{d\ln\nu}{d\ln M} \tag{3.4}$$

where the introduced parameters are $q = 0.707$ $p = 0.3$ (note that $q = 1$ $p = 0$ gives the PS result). This result is known as the *Sheth-Tormen* mass function [7], and the normalization is given by the constraint that all mass in the universe is to be contained in halos of some mass $\int dM M n(M) = \bar{\rho}$.

Press-Schechter result presented here is a 'phenomenological' approach based on simplistic assumptions. These initial assumptions to a large extent neglect the nonlinear evolution of the density field. It also assumes that spherical collapse models a spherically symmetric process while in reality the halos can have complex three-axial shapes. In addition, there is the 'peaks-within-peaks problem' asserting that the Press-Schechter approach does not take into account whether a halo of a certain mass is included in a halo of some larger mass. Despite all of this, a comparison between the PS approach and numerical simulations gives roughly the right shape of the mass function and is correct up to an order of magnitude.

Much work has been done since the PS result that is trying to improve the previously mentioned drawbacks. For reviews of the most significant improvements see e.g. [8]. Nowadays, simulation calibrated models or fitting formulas are used to describe halo mass function (e.g., [7, 9, 10, 11, 12]). It has been suggested that there might exist a 'universal mass function,' i.e. same functional form and numerical parameters for different cosmologies and over a range of redshifts. However, recent studies have shown that if one aims at a precision better than 5% such a universal mass function cannot be found, neither for different cosmologies nor a broad redshift range.

## 3.2 Peak-Background Split and Lagrangian Bias

As shown in the previous section, Press-Schechter mode enables an analytical calculation of the mean number density of dark matter halos. Moreover, it gives an insight into the correlation of these halos in space. This leads to the concept of 'bias', i.e. the connection of the auto-correlation function or the power spectra of halos of mass M to the underlying dark matter density fluctuations. We define the overdensity of halos of mass M in terms of their comoving number density $n_h(x, M)$ as follows

$$\delta_h(\mathbf{x}, M) = \frac{n_h(\mathbf{x}, M) - \bar{n}_h(M)}{\bar{n}_h(M)}. \tag{3.5}$$

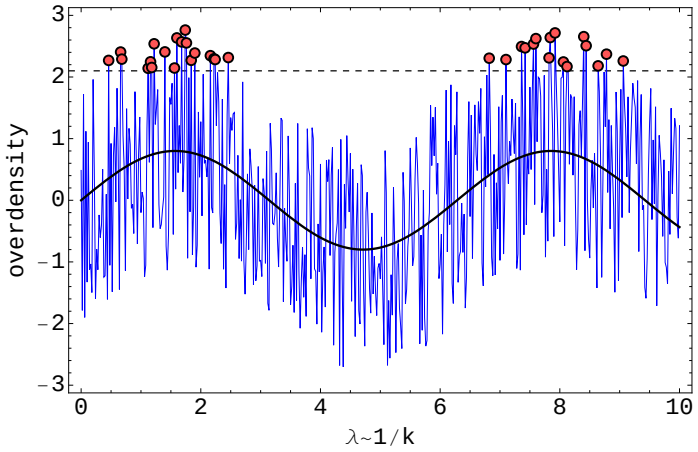


**Figure 3.1:** Peak-background split: a schematic picture of short wavelength fluctuations $\delta_{\rm h}$ (blue solid line) superposed on to a mode of long wavelength background fluctuation $\delta_{\rm b}$ (black solid line). In Press-Schechter model, virialized halos (schematically shown as red points) form in regions exceeding the density threshold of the spherical collapse $\delta_{\rm c} = 1.69$.

This leads to the corresponding halo auto-correlation function;

$$\xi_{\rm hh}(r, M) = \langle \delta_{\rm h}(\mathbf{x}, M) | \delta_{\rm h}(\mathbf{x}', M) \rangle = \frac{\langle n_{\rm h}(\mathbf{x}, M) | n_{\rm h}(\mathbf{x}', M) \rangle}{\bar{n}_{\rm h}^2(M)} - 1, \tag{3.6}$$

where $r = |\mathbf{x}' - \mathbf{x}|$. The equation can be interpreted as a measure of the excess of halo-pairs at separations $r$ compared to the mean number density of the halos. Halo power spectrum is then given as the Fourier transform of the correlation function.

In addition to the mean number density of halos $\bar{n}_{\rm h}(M)$ obtained for the mass function, we are also interested in the variations of the number density of halos in space and cosmic environment. The simplest way to show how the local number of halos depends on the environment is the *peak-background* split. In this picture halos form in the peaks of short wavelength fluctuations $\delta_{\rm h}$ (small scale perturbations) in the Lagrangian density field, which are effected by the presence of the long wavelength fluctuations $\delta_b$. The total overdensity is thus given as a sum of these two contributions, $\delta = \delta_{\rm h} + \delta_{\rm b}$. Long wavelength perturbation $\delta_{\rm b}$ represents the smooth background density in the linear regime in Lagrangian space. In this way $\delta_{\rm b}$ is effectively perturbing the critical threshold that $\delta_{\rm h}$ needs to reach in order to collapse and form virialized halo. Once the $\delta_{\rm h}$ reaches the effective threshold $\tilde{\delta}_{\rm c} = \delta_{\rm c} - \delta_{\rm b}$ the total perturbation $\delta$ reaches threshold $\delta_{\rm c}$ needed for a structure to collapse. Since the effective threshold $\tilde{\delta}_{\rm c}$ depends on the background field $\delta_{\rm b}$ and causes the fluctuation of different amplitudes to collapse at different places and times, and causes the local number density $n_{\rm h}$ to vary in space depending on $\delta_{\rm b}$. Since $\delta_{\rm b} \ll 1$, local number density $n_{\rm h}$ can be expanded in Taylor series

$$\frac{dn_{\rm h}}{dM}(\mathbf{q}) = \frac{d\bar{n}_{\rm h}}{dM} + \sum_{l=1}^{\infty} \frac{\partial^l}{\partial \delta_{\rm b}^l} \frac{d\bar{n}_{\rm h}}{dM} \left( \delta_{\rm b}^l(\mathbf{q}) - \langle \delta_{\rm b}^l \rangle \right), \tag{3.7}$$

which gives the overdensity in Lagrangian space

$$\delta_{\rm h}^{\rm (L)}(\mathbf{q}) = \frac{n_{\rm h}(\mathbf{q})}{\bar{n}_{\rm h}} - 1 = \sum_{l=1}^{\infty} \frac{b_l^{\rm (L)}}{l!} \left( \delta_{\rm b}^l(\mathbf{q}) - \langle \delta_{\rm b}^l \rangle \right), \tag{3.8}$$

where we have defined Lagrangian bias parameters

$$b_l^{\rm (L)} = \frac{1}{d\bar{n}_{\rm h}/dM} \frac{\partial^l}{\partial \delta_{\rm b}^l} \frac{d\bar{n}_{\rm h}}{dM}. \tag{3.9}$$

If we assume universality of the mass function the derivative in $\delta_{\rm b}$ can be replaced by the derivative with respect to $\nu$. Using these expressions above we can determine the Lagrangian bias parameters for a given mass function. For example in case of the Sheth-Tormen mass function the first three bias parameters are

$$b_1^{(\rm L)} = \frac{2p}{\delta_{\rm c}\left((\nu q)^p + 1\right)} + \frac{\nu q - 1}{\delta_{\rm c}}, \tag{3.10}$$

$$b_2^{(\rm L)} = \frac{2\left(2p^2 + 2\nu pq - p\right)}{\delta_{\rm c}^2\left((\nu q)^p + 1\right)} + \frac{\nu q(\nu q - 3)}{\delta_{\rm c}^2}, \tag{3.11}$$

$$b_3^{(\rm L)} = \frac{2\left(4p^3 + 6\nu p^2 q + 3\nu^2 pq^2 - 6\nu pq - p\right)}{\delta_{\rm c}^3\left((\nu q)^p + 1\right)} + \frac{\nu q\left(\nu^2 q^2 - 6\nu q + 3\right)}{\delta_{\rm c}^3}. \tag{3.12}$$

Here we assume the linearly evolution of the long wavelength perturbations. Otherwise, if the Lagrangian density amplitudes had been used, the bias parameters would have been rescaled by the growth factor $D(z)$ at the given redshift $z$.

## 3.3 Local Eulerian Bias

Eulerian perturbation theory has been extensively used in describing the dark matter clustering. The goal of the biasing models it to relate the distribution of dark matter in Eulerian space to the distribution of dark matter halos in terms of the underlying linear or non-linear density fluctuations. Most generally, this relation can be described as a functional dependence of halo overdensity, where the smoothed halo overdensity at a certain position is given in terms of the matter overdensity in the nearby region. For practical purposes, this general functional dependence is not very instructive, and it has become common to assume local dependence in space and time of the halo overdensity field on the dark matter overdensity. As suggested in [13] this allows for the Taylor expansion, local both in space and time

$$\delta_{\rm h}^{(\rm E)}(\boldsymbol{x}) = \sum_{i=1}^{\infty} \frac{b_i^{(\rm E)}}{i!}\left(\delta^i(\boldsymbol{x}) - \left\langle\delta^i\right\rangle\right). \tag{3.13}$$

here $b_i^{(\rm E)}$ are the Eulerian bias coefficients. Initial proposition was to relate the halo overdensity field to the smoothed dark matter field, which we have omitted in the relation above. This we can think of as being implicitly achieved through the Taylor expansion. Since the halo spectrum is the observable quantity, we expect it to be independent of the explicit smoothing scale on large enough scales.

The Eulerian biasing model can be interpreted as an effective model where the coefficients are free parameters incorporating the physics on small scales, which need to be measured from the data. In order to get the rough estimate of the magnitude of these coefficients we consider a mapping of the halo formation in Lagrangian space to the final evolved halos. As seen in last chapter the mapping from the Lagrangian space to the Eulerian space is given by $(1 + \delta(\mathbf{x}))\, d^3x = d^3q$. Since we can assume that the number of halos is conserved it follows that we can relate the halo overdensities in Lagrangian and Eulerian space

$$\left(1 + \delta_{\rm h}^{(\rm E)}(\mathbf{x})\right) d^3x = \left(1 + \delta_{\rm h}^{(\rm L)}(\mathbf{q})\right) d^3q, \tag{3.14}$$

form which then follows

$$\delta_{\rm h}^{(\rm E)}(\mathbf{x}) = \delta(\mathbf{x}) + (1 + \delta(\mathbf{x}))\, \delta_{\rm h}^{(\rm L)}(\mathbf{q}), \tag{3.15}$$

where positions in Eulerian space $\mathbf{x}$ and Lagrangian space $\mathbf{q}$ are related through the displacement field $\Psi$. The standard way to relate the Lagrangian and Eulerian overdensities is to employ the relation between linear and non-linear overdensity in the spherical collapse model

(see e.g. [1]). In addition to the spherical collapse assumption we can use the perturbative expansion of the non-linear density field $\delta$ in terms of the linear $\delta_L$. This gives

$$\delta_{sc} = \sum_n \int d^3q_1 \dots d^3\ q_n F_n\left(\mathbf{q}_1, \dots, \mathbf{q}_n\right) \delta_L(|\mathbf{q}_1|) \dots \delta_L(|\mathbf{q}_n|) = \sum_n \frac{\nu_n}{n!}\epsilon^n, \tag{3.16}$$

where $\epsilon = \int d^3q\ \delta_L(|\mathbf{q}|)$, and the first three coefficients are $\nu_1 = 1$, $\nu_2 = -\frac{34}{21}$, $\nu_3 = \frac{682}{189}$, etc. Combining all this we get the relation of biasing coefficients,

$$\begin{aligned} b_1^{(\mathrm{E})} =& 1 + b_1^{(\mathrm{L})}, \\ b_2^{(\mathrm{E})} =& b_2^{(\mathrm{L})} + \frac{8}{21} b_1^{(\mathrm{L})}, \\ b_3^{(\mathrm{E})} =& -\frac{236}{189} b_1^{(\mathrm{L})} - \frac{13}{7} b_2^{(\mathrm{L})} + b_3^{(\mathrm{L})}. \end{aligned} \tag{3.17}$$

Assumption of spherical collapse turns out to be an oversimplification of the problem, and the consistent coevolution of halos and dark matter introduces a non-local terms at higher orders.

## 3.4 Non-Local Eulerian Bias

As noted in the previous section, local biasing model does not rise up to the challenge of consistently various statistics like halo cross and auto power spectra of densities and momenta. Generalizations where non-local contributions are added have been suggested in the literature (see [3, 14]). In this approach all non-local terms allowed by the symmetries are added to the Eulerian biasing model. Halo overdensity field is thus related to the underlying dark matter overdensity field as

$$\begin{aligned} \delta_{\mathrm{h}}(\mathbf{x}) =& c_\delta \delta(\mathbf{x}) \\ &+ \frac{1}{2} c_{\delta^2} \delta^2(\mathbf{x}) + \frac{1}{2} c_{s^2} s^2(\mathbf{x}) \\ &+ \frac{1}{3!} c_{\delta^3} \delta)^3(\mathbf{x} + \frac{1}{2} c_{\delta s^2} \delta(\mathbf{x}) s^2(\mathbf{x}) + c_\psi \psi(\mathbf{x}) + c_{st} s(\mathbf{x}) t(\mathbf{x}) + \frac{1}{3!} c_{s^3} s^3(\mathbf{x}) \\ &+ c_\epsilon \epsilon + \dots, \end{aligned} \tag{3.18}$$

where each independent variable is defined as

$$s_{ij}(\mathbf{x}) = \partial_i \partial_j \phi(\mathbf{x}) - \frac{1}{3}\delta^{\mathrm{K}}_{ij}\delta(\mathbf{x}) = \left[\partial_i\partial_j\partial^{-2} - \frac{1}{3}\delta^{\mathrm{K}}_{ij}\right]\delta(\mathbf{x}), \tag{3.19}$$

$$t_{ij}(\mathbf{x}) = \partial_i v_j - \frac{1}{3}\delta^{\mathrm{K}}_{ij}\theta(\mathbf{x}) - s_{ij}(\mathbf{x}) = \left[\partial_i\partial_j\partial^{-2} - \frac{1}{3}\delta^{\mathrm{K}}_{ij}\right][\theta(\mathbf{x}) - \delta(\mathbf{x})], \tag{3.20}$$

$$\psi(\mathbf{x}) = [\theta(\mathbf{x}) - \delta(\mathbf{x})] - \frac{2}{7}s(\mathbf{x})^2 + \frac{4}{21}\delta(\mathbf{x})^2, \tag{3.21}$$

where $\phi$ is the gravitational potential due to the overdensity $\delta$, and we introduced the white noise variable $\epsilon$ in order to allow for the stochasticity and shotnoise. Note that $t_{ij}$ is zero at the first order, and $\psi$ is zero up to the second order. In order to obtain the prediction of the observables like power spectra the halo overdensity contrast can is Fourier transformed into the momentum space. Since this yield somewhat lengthy expressions, we refer to the e.g. [3] for the explicit form in momentum space.

### 3.4.1 Halo-matter and halo-halo power spectrum

Here we summarize the consequences of non-local contributions to the matter-halo and halo-halo power spectra. After some calculation and employing the renormalization schemes

suggested in [15] it follows that the matter-halo power spectrum at one loop is given by

$$P^{\rm mh}(k) = b_1 P^{\rm NL}_{\delta\delta}(k) + b_2 P_{b2,\delta}(k) + b_{s^2} P_{bs2,\delta}(k) + b_{\rm 3nl}\,\sigma_3^2(k) P(k), \tag{3.22}$$

where $P^{\rm NL}_{\delta\delta}$ is the nonlinear matter density power spectra, and the terms associated with renormalized bias parameters are defined as

$$\begin{aligned} P_{b2,\delta}(k) &= \int \frac{d^3q}{(2\pi)^3}\, P_L(q) P_L(|\mathbf{k}-\mathbf{q}|) F_2(\mathbf{q}, \mathbf{k}-\mathbf{q}), \\ P_{bs2,\delta}(k) &= \int \frac{d^3q}{(2\pi)^3}\, P_L(q) P_L(|\mathbf{k}-\mathbf{q}|) F_2(\mathbf{q}, \mathbf{k}-\mathbf{q}) S_2(\mathbf{q}, \mathbf{k}-\mathbf{q}), \end{aligned} \tag{3.23}$$

and we have a second order non-local kernel defined as

$$S_2(\mathbf{q}_1, \mathbf{q}_2) = \left(\frac{\mathbf{q}_1 \cdot \mathbf{q}_2}{q_1 q_2}\right)^2 - \frac{1}{3}. \tag{3.24}$$

The third order non-local contribution associated with the bias coefficient $b_{\rm 3nl}$ gives the contribution

$$\sigma_3^2(k) = k^3 \int \frac{r^2 dr}{2\pi^2} P_L(kr) I_{\rm R}(r), \tag{3.25}$$

where

$$I_R(r) = \frac{5}{128 r^4}(1+r^2)(-3+14r^2-3r^4) + \frac{3(r^2-1)^4}{256 r^5} \ln\left|\frac{1+r}{1-r}\right|. \tag{3.26}$$

Halo-halo power spectrum is similarly given as

$$\begin{aligned} P^{\rm hh}(k) = {} & b_1^2 P^{\rm NL}_{\delta\delta}(k) + 2 b_1 b_2 P_{b2,\delta}(k) + 2 b_1 b_{s^2} P_{bs2,\delta}(k) + 2 b_1 b_{\rm 3nl} \sigma_3^2(k) P(k) \\ & + b_2^2 P_{b22}(k) + 2 b_2 b_{s^2} P_{b2s2}(k) + b_{s^2}^2 P_{s22}(k) + N, \end{aligned} \tag{3.27}$$

where the additional terms associated with renormalized bias parameters are

$$P_{b22}(k) = \frac{1}{2}\int \frac{d^3q}{(2\pi)^3}\, P(q) \left\{P_L(|\mathbf{k}-\mathbf{q}|) - P_L(q)\right\}, \tag{3.28}$$

$$P_{b2s2}(k) = \frac{1}{2}\int \frac{d^3q}{(2\pi)^3}\, P(q) \left\{P_L(|\mathbf{k}-\mathbf{q}|) S_2(\mathbf{q}, \mathbf{k}-\mathbf{q}) - \frac{2}{3} P_L(q)\right\}, \tag{3.29}$$

$$P_{bs22}(k) = \frac{1}{2}\int \frac{d^3q}{(2\pi)^3}\, P(q) \left\{P_L(|\mathbf{k}-\mathbf{q}|) S_2(\mathbf{q}, \mathbf{k}-\mathbf{q})^2 - \frac{4}{9} P_L(q)\right\}. \tag{3.30}$$

Here we subtract the constant terms like $\int d^3q\, P(q)^2$ to keep nonlinear corrections vanishing in the limit of $k \to 0$. In the lowest order $N$ is the usual galaxy shot-noise contribution.

Later on, in chapter 6 we will use the biasing schemes presented in this chapter to model the halo power spectrum in redshift space.

# Bibliography


[1] F. Bernardeau, S. Colombi, E. Gaztanaga, and R. Scoccimarro, **Large scale structure of the universe and cosmological perturbation theory**, *Phys.Rept.* **367** (2002) 1–248, [astro-ph/0112551].

[2] C. Knobel, **An introduction into the theory of cosmological structure formation**, arXiv:1208.5931.

[3] P. McDonald and A. Roy, **Clustering of dark matter tracers: generalizing bias for the coming era of precision LSS**, *JCAP* **0908** (2009) 020, [arXiv:0902.0991].

[4] D. Jeong, **Cosmology with high (z $>$ 1) redshift galaxy surveys**, (2010) PhD Thesis.

[5] T. Baldauf, **Modelling Large Scale Structure Statistics for Precision Cosmology**, (2013) PhD Thesis.

[6] W. H. Press and P. Schechter, **Formation of galaxies and clusters of galaxies by selfsimilar gravitational condensation**, *Astrophys.J.* **187** (1974) 425–438.

[7] R. K. Sheth and G. Tormen, **Large scale bias and the peak background split**, *Mon.Not.Roy.Astron.Soc.* **308** (1999) 119, [astro-ph/9901122].

[8] A. R. Zentner, **The Excursion Set Theory of Halo Mass Functions, Halo Clustering, and Halo Growth**, *Int.J.Mod.Phys.* **D16** (2007) 763–816, [astro-ph/0611454].

[9] A. Jenkins, C. Frenk, S. D. White, J. Colberg, S. Cole, et al., **The Mass function of dark matter halos**, *Mon.Not.Roy.Astron.Soc.* **321** (2001) 372, [astro-ph/0005260].

[10] R. K. Sheth, H. Mo, and G. Tormen, **Ellipsoidal collapse and an improved model for the number and spatial distribution of dark matter haloes**, *Mon.Not.Roy.Astron.Soc.* **323** (2001) 1, [astro-ph/9907024].

[11] D. Reed, J. Gardner, T. R. Quinn, J. Stadel, M. Fardal, et al., **Evolution of the mass function of dark matter haloes**, *Mon.Not.Roy.Astron.Soc.* **346** (2003) 565, [astro-ph/0301270].

[12] J. L. Tinker, A. V. Kravtsov, A. Klypin, K. Abazajian, M. S. Warren, et al., **Toward a halo mass function for precision cosmology: The Limits of universality**, *Astrophys.J.* **688** (2008) 709–728, [arXiv:0803.2706].

[13] J. N. Fry and E. Gaztanaga, **Biasing and hierarchical statistics in large scale structure**, *Astrophys.J.* **413** (1993) 447–452, [astro-ph/9302009].

[14] V. Assassi, D. Baumann, D. Green, and M. Zaldarriaga, **Renormalized Halo Bias**, arXiv:1402.5916.

[15] P. McDonald, **Clustering of dark matter tracers: Renormalizing the bias parameters**, *Phys.Rev.* **D74** (2006) 103512, [astro-ph/0609413].

# Chapter 4

# Redshift Space Distortions. Part I: Linear Theory [1]

In large scale structures, we look at the three-dimensional distributions of galaxies in the sky. It is important to note that in addition to the two-dimensional angular position, galaxy redshifts are used as an indicator of radial distance from the observer. From the Hubble law, it follows that the velocity of an object is proportional to its distance from us. However, due to the dynamics of clustering, the observed velocity has an additional contribution called the peculiar velocity. This contribution is unrelated to the Hubble expansion and thus gives rise to the degeneracy in distance information. Since the clustering pattern is now different then the actual one in real space distribution, we end up with so-called redshift space distortion (RSD) effect.

In this chapter, we first look how redshift space distortions effect the dark matter (and galaxy) density field. We show the results in linear theory, so-called Kaiser limit [4]. We also shortly review some of the results that take nonlinear clustering effects into account.

## 4.1 Introduction

Let us first take a look at two different regimes where the RSD yield very different effects. At large scales, objects fall into the overdense regions. When looking at these objects, that are located between us and some larger cluster, we need to add their infall velocities to the Hubble flow, and thus, they appear to be farther away in redshift space. On the other hand, objects falling from the far side of the cluster have their peculiar velocities subtracting from the Hubble flow, and thus, appear closer to us than they would in real space. As a consequence, we get a picture in the redshift space where structures on the largest of scales appear flattened or squashed along the line of sight.

On the other hand, on scales smaller than the size of a typical cluster the main contribution to peculiar velocities come from the velocity dispersion from the virialization. In redshift space, this gives rise to an elongation along the line of sight of structures and leads to the so-called finger of God (FoG) effect. Name is motivated by the fact that these structures have a tendency to point towards the observer. We show these effect schematically in figure 4.1.

Let us also mention that galaxies are expected to be almost unbiased tracers of the dark matter velocities, and so by measuring the RSD one can measure dark matter density field. The reason for that is the direct connection of velocity and density field through the continuity equation. This allows direct measurement of growth rate of structure and in this way provides us with one of the most-interesting ways to test the general relativity theory and its potential modifications.

[1] The material in this Chapter is based on following review articles and textbooks: [1, 2, 3].

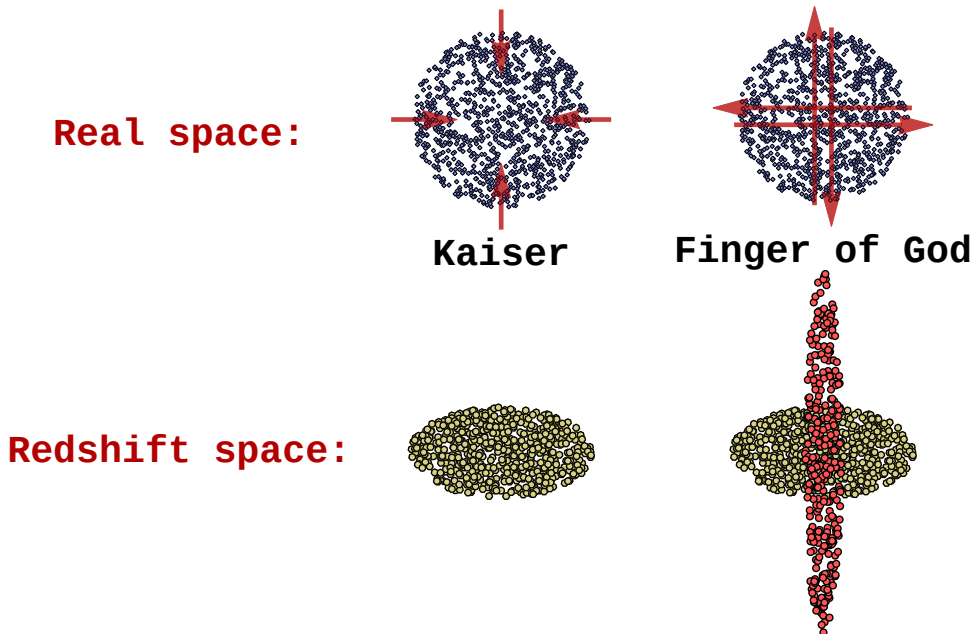


**Figure 4.1:** Schematic picture of two regimes of redshift space distortions: linear or Kaiser on the left side and highly nonlinear (fingers of God) on the right. Upper part represents the configuration in real space while lower part is the mapping in redshift space. Line of sight direction is to be imagined pointing from the bottom to the top of the figure. Red arrows denote direction and magnitudes of velocities. In case of nonlinear collapse, velocities are large, so that they invert the picture along the line of sight (e.g. points on the bottom of the upper picture get mapped on the top of the finger in the bottom picture, and vice versa).

## 4.2 Density Field in Redshift Space

In order to investigate the redshift distortions effects on clustering statistics such as the power spectrum, the bispectrum and higher-order moments let us start by looking how RSD effect the density field itself. In redshift space, the radial coordinate $\mathbf{s}$ of an object is given by its observed radial velocity, a combination of its Hubble flow plus distortions due to peculiar velocities caused by the fact that the object is feeling the local gravitational potential. We restrict our analysis to the plane-parallel approximation, which means that the line of sight is taken as a fixed direction usually taken to be along the $\hat{z}$ direction. Big advantage of the plane-parallel approximation is that statistical homogeneity remains valid, and Fourier modes remain the natural basis also in redshift-space. Statistical isotropy is, on the other hand, no longer valid since clustering along the line of sight is different from that in the perpendicular directions (see the figure 4.1).

However, going beyond the plane-parallel approximation means taking into account the radial character of redshift distortions and then the picture changes. Radial distortions respect statistical isotropy, since it means they represent the rotation around the observer, but, on the other hand, break the statistical homogeneity, since the preferred location is the observer's position. In this case Fourier modes are no longer special, in particular, the power spectrum is no longer diagonal. We will stick to the plane-parallel approximation here, which has been tested in N-body simulation studies and it is valid for most of the current surveys.

Mapping from real-space position $\mathbf{x}$ to redshift space in the plane-parallel approximation is given by :

$$\mathbf{s} = \mathbf{x} - f u_z(\mathbf{x})\hat{z}, \tag{4.1}$$

where $\hat{z}$ is the unit vector pointing along the observer's line of sight, $u_z \equiv -v_z/(f\mathcal{H})$ where $\mathbf{v}$ is the peculiar velocity field (note the differences in notation from the chapter 2), projected along the line of sight $v_z = \hat{z} \cdot \mathbf{v}$. $\mathcal{H}(\tau) \equiv (1/a)(da/d\tau) = Ha$ is the conformal Hubble parameter and $f$ the logarithmic growth rate (see 2.20).

### 4.2.1 Linear approximation - Kaiser formula

Since fingers of god are highly nonlinear they present fairly challenging computational issue, but on the other hand, linear perturbation theory allows us to address the Kaiser regime in fairly simple manner.

The density field in redshift space, $\delta(\mathbf{s})$, is obtained from the real-space density field $\delta(\mathbf{x})$ by requiring that the redshift-space mapping conserves the mass, i.e.

$$(1 + \delta_s)\delta^3 s = (1 + \delta)\delta^3 x. \tag{4.2}$$

Using the relation $d^3\boldsymbol{s} = J(\mathbf{x})d^3\mathbf{x}$, where $J(\mathbf{x}) = |1 - f\nabla_z u_z(\mathbf{x})|$ is the full Jacobian of the mapping in the plane-parallel approximation, we have

$$1 + \delta_s(\mathbf{s}) = \frac{1 + \delta(\mathbf{x})}{J(\mathbf{x})}. \tag{4.3}$$

This relation is very interesting since it points towards the possible caustics in redshift space, i.e. zeros of the Jacobian, which give rise to the apparent infinities in the density field. This surface is characterized in real space by those points which are undergoing a turnaround in the gravitational collapse, i.e. there is an exact cancellation between the peculiar velocities and the Hubble flow.

From these expressions, it follows (see e.g. [1, 5]) that the density field in redshift space is given by

$$\delta_s(\mathbf{k}) = \int d^3x \; e^{i\boldsymbol{k}\cdot\boldsymbol{x}} e^{-if k_z u_z(\mathbf{x})} \Big(\delta(\boldsymbol{x}) + f\nabla_z u_z(\mathbf{x})\Big), \tag{4.4}$$

where it is assumed that only $f\nabla_z u_z(\mathbf{x}) < 1$ points contribute in this expression. The only other approximation in this expression is the use of the plane-parallel approximation, i.e. this is a fully non-linear expression. By expanding the second exponential, we are able to preform the Fourier transform, and we end up with the expression;

$$\delta_s(\mathbf{k}) = \sum_{n=1}^{\infty} \int \frac{d^3k_1}{(2\pi)^3} \cdots \frac{d^3k_n}{(2\pi)^3} \left[\delta_n^D\right] \Big(\delta(\mathbf{k}_1) + f\mu_1^2 \bar{\theta}(\mathbf{k}_1)\Big) \frac{(f\mu k)^{n-1}}{(n-1)!} \frac{\mu_2}{k_2} \bar{\theta}(\mathbf{k}_2) \ldots \frac{\mu_n}{k_n} \bar{\theta}(\mathbf{k}_n), \tag{4.5}$$

where $\left[\delta_n^D\right] = \delta_{\mathrm{D}}(\mathbf{k} - \mathbf{k}_1 - \ldots - \mathbf{k}_n)$, the velocity divergence $\bar{\theta}(\mathbf{k}) = -i\mathbf{k}\cdot\mathbf{u}(\mathbf{k})$, and $\mu_i = \mathbf{k}_i \cdot \hat{z}/k_i$ is the cosine of the angle between the line-of-sight and the wave-vector. In linear PT only the $n = 1$ term survives, and we recover the well-known Kaiser formula [4]:

$$\delta_s(\mathbf{k}) = \delta(\mathbf{k})(1 + f\mu^2). \tag{4.6}$$

### 4.2.2 Non-linear Eulerian approach

From the former relation we can extract the higher order redshift space kernels. For the redshift space density field we can formally write

$$\delta_s(\mathbf{k}) = \sum_{n=1}^{\infty} \int \frac{d^3k_1}{(2\pi)^2} \cdots \frac{d^3k_n}{(2\pi)^3} \left[\delta_n^D\right] Z_n(\mathbf{k}_1, \ldots, \mathbf{k}_n) \delta_L(\mathbf{k}_1) \cdots \delta_L(\mathbf{k}_n), \tag{4.7}$$

where $\delta_L$ is the linear density field. In case of Galaxies or biased object the idea is that we can treat the local deterministic and non-linear bias in an equal footing as non-linear dynamics. Thus, it is possible to obtain the kernels $Z_n$ including biasing and redshift-distortions. We

write down first three kernels $Z_n$ in redshift space in case where we take only linear biasing, $b_1$ into account. We have

$$\begin{aligned}
Z_1(\mathbf{k}) &= (b_1 + f\mu^2), \\
Z_2(\mathbf{k}_1, \mathbf{k}_2) &= b_1 F_2(\mathbf{k}_1, \mathbf{k}_2) + f\mu^2 G_2(\mathbf{k}_1, \mathbf{k}_2) + \frac{f\mu k}{2}\Big[\frac{\mu_1}{k_1}(b_1 + f\mu_2^2) + \frac{\mu_2}{k_2}(b_1 + f\mu_1^2)\Big] + \frac{b_2}{2}, \\
Z_3(\mathbf{k}_1, \mathbf{k}_2, \mathbf{k}_3) &= b_1 F_3(\mathbf{k}_1, \mathbf{k}_2, \mathbf{k}_3) + f\mu^2 G_3(\mathbf{k}_1, \mathbf{k}_2, \mathbf{k}_3) \\
&\quad + f\mu k\Big[b_1 F_2(\mathbf{k}_1, \mathbf{k}_2) + f\mu_{12}^2 G_2(\mathbf{k}_1, \mathbf{k}_2)\Big]\frac{\mu_3}{k_3} + f\mu k(b_1 + f\mu_1^2)\frac{\mu_{23}}{k_{23}} G_2^{(s)}(\mathbf{k}_2, \mathbf{k}_3) \\
&\quad + \frac{(f\mu k)^2}{2}(b_1 + f\mu_1^2)\frac{\mu_2}{k_2}\frac{\mu_3}{k_3} + 3b_2 F_2^{(s)}(\mathbf{k}_1, \mathbf{k}_2) + \frac{b_3}{6},
\end{aligned} \tag{4.8}$$

where $\mu = \mathbf{k} \cdot \hat{z}/k$, with $\mathbf{k} = \mathbf{k}_1 + \ldots + \mathbf{k}_n$, and $\mu_i = \mathbf{k}_i \cdot \hat{z}/k_i$. As was described in chapter 2, $F_2$ and $G_2$ and similarly for $F_3$ and $G_3$ are the second and third order gravity kernels for the real-space density and velocity-divergence fields. Similarly one can obtain the PT kernels $Z_n$ in redshift space to arbitrary higher order.

The process above involves two levels of approximations: first we expand the exponential term in master equation 4.5, and secondly we use the PT expansion of nonlinear density $\delta(\mathbf{k})$ and velocity $\theta(\mathbf{k})$ fields in terms of the linear fluctuations $\delta_L(\mathbf{k})$ in equation 4.7. The performance due to the second of these approximations in describing the RSD statistics falls into the domain of the PT methods of nonlinear clustering, and it has been addressed in chapter 2. The first approximation though comes in addition and has been a matter of debate. Worries that expanding the exponent in 4.5 might lead to the poorer performance have been put forward (e.g. [1]). In chapters 5 and 6 we show that this is unjustified and that a very good agreement with numerical simulation results can be achieved by doing the expansion in velocity field moments, and taking appropriate care of the zero lag contributions. This has also been indicated by the work in e.g. [6, 7], where nonlinear effects in RSD are also treated in Eulerian picture.

### 4.2.3 Non-linear Lagrangian approach

Motivated by the failure of straightforward performance of the kernels 4.8 in calculating the one-loop power spectrum in redshift space, other approaches have been proposed to deal with the mentioned approximations. These alternatives are mostly based on the Lagrangian picture (for some of the developments look at e.g. [8, 9, 10, 11] ).

In Lagrangian picture particles with initial position $\mathbf{q}$ are mapped to the position $\mathbf{x} = \mathbf{q} + \Psi(\mathbf{q})$, where $\Psi(\mathbf{q})$ is the displacement vector at Lagrangian position $\mathbf{q}$. Mapping to the redshift space we obtain by substituting the displacement field

$$\Psi(\mathbf{q}) \to \Psi_s(\mathbf{q}) = \Psi(\mathbf{q}) + \frac{\hat{z} \cdot \dot{\Psi}(\mathbf{q})}{\mathcal{H}}\hat{z} = R\Psi(\mathbf{q}) \tag{4.9}$$

Density field in redshift space is then given by the continuity relation

$$1 + \delta_s(\mathbf{x}) = \int d^3q \; \delta^D\left(\mathbf{x} - \mathbf{q} - \Psi_s)\right), \tag{4.10}$$

Later on we will look at the implication of this approach for the power spectrum and the correlation function.

## 4.3 Power Spectrum and Correlation Function in Redshift Space

In this section, we show the results of redshift-space statistics focusing on the power spectrum and its Fourier transform, the correlation function. Generally, it is a common

practice to decompose the angular dependence of the power spectra in redshift space into the Legendre polynomial $\mathcal{P}_l(\mu)$. It follows

$$P_s(\mathbf{k}) = \sum_{l=0}^{\infty} P_l^s(k)\mathcal{P}_l(\mu), \tag{4.11}$$

where multipole coefficients are given by

$$P_l^s(k) = (2l+1)\int_0^1 P^s(k,\mu)\mathcal{P}_l(\mu)d\mu \ . \tag{4.12}$$

Usually the first three non-vanishing multipoles are of the highest interest. These are given explicitly by $\mathcal{P}_0(\mu) = 1$, $\mathcal{P}_2(\mu) = (3\mu^2-1)/2$ and $\mathcal{P}_4(\mu) = (35\mu^4 - 30\mu^2 + 3)/8$. Because in the plane-parallel approximation RSD are invariant under the mirroring relative to the line of sight, only the even powers of $\mu$ contribute. In this way the non-trivial measurement of the dipole signal would correspond to the deviations from the plane-parallel approximation (in addition to the survey window effects and relativistic effects on large scales).

By Fourier transforming these results, we get the Rayleigh expansion of the correlation function

$$\xi(\mathbf{x}) = \sum_{l=0}^{\infty} \xi_l^s(x)\mathcal{P}_l(\nu), \tag{4.13}$$

where the coefficients are given by

$$\xi_l^s(x) = i^l \int \frac{k^2 dk}{2\pi^2} P_l^s(k) j_l(kr), \tag{4.14}$$

where $j_l$ are the spherical Bessel functions.

General expression for the redshift space power spectrum can be obtained from the equation 4.5, we have

$$P_s(\mathbf{k}) = \int d^3r \ e^{i\mathbf{k}\cdot\mathbf{r}} \Big\langle e^{-ifk\mu\Delta u_z}\Big[\delta(\mathbf{x}) + f\nabla_z u_z(\mathbf{x})\Big]\Big[\delta(\mathbf{x}') + f\nabla'_z u_z(\mathbf{x}')\Big]\Big\rangle, \tag{4.15}$$

where $\Delta u_z = u_z(\mathbf{x}) - u_z(\mathbf{x}')$, $\mathbf{r} = \mathbf{x} - \mathbf{x}'$. This is the Fourier space analog of the so-called 'streaming model' result (see e.g. [12, 1]). Up to the plane-parallel approximation, it is fully non-linear expression. The factors in the square brackets describe the amplification of the power spectrum in redshift space due to the infall. They are the only contribution in linear theory (see below). This gives a positive contribution to the quadrupole ($l = 2$) and hexacadupole ($l = 4$) anisotropies. On the small scales, as we approach higher $k$ values, presence of the exponential factor starts to play a more important role, decreasing the contributions from the pairwise velocity along the line of sight. This leads to the suppression of the monopole and quadrupole power spectra relative to the linear contribution.

### 4.3.1 Linear theory result

At the leading, linear, order, from equation 4.6, it follows for the power spectrum :

$$P_s(\mathbf{k}) = P_g(k)\ (1+\beta\mu^2)^2 \tag{4.16}$$

this is so called Kaiser power spectrum. $P_g(k) = b_1^2 P(k)$ is the real-space galaxy power spectrum in the approximation of linear biasing $b_1$. $P(k)$ is the linear mass power spectrum, and $\beta = f/b_1$, where $f$ is logarithmic growth rate. Expressed in terms of multipoles this result reads:

$$\frac{P_s(\mathbf{k})}{P_g(k)} = \left(1 + \frac{2}{3}\beta + \frac{1}{5}\beta^2\right)\mathcal{P}_0 + \left(\frac{4}{3}\beta + \frac{4}{7}\beta^2\right)\mathcal{P}_2 + \frac{8}{35}\beta^2\mathcal{P}_4 \tag{4.17}$$

and all other multipoles vanish. These equations are considered a standard tool for measuring $\Omega_m$ since $f \approx \Omega_m^{0.55}$ from redshift distortions of the power spectrum. Ratio of quadrupole to monopole, $R_{2,0} = P_2^s/P_0^s$ is predicted to be constant at large scale the limit as $k \to 0$. However, $\Omega_m$ appears here only through the $\beta$ parameter, so a degeneracy between $\Omega_m$ and the linear bias factor $b_1$ appears.

### 4.3.2 Modelling of Fingers of God

In order to describe the highly non-linear contributions to the redshift-space power spectrum arising from the exponential factor describing the velocity dispersion effects in equation 4.15, it has become a common practice to introduce the phenomenological models in order to take that into account. These contributions are known as Finger of God (FoG) effects. These FoG are described by the damping factor that is generated by the pairwise-velocity distribution function. In the case of linear power spectrum, we would have

$$P_s(\mathbf{k}) = \mathrm{FoG}(k_z, \sigma_v)(1 + \beta\mu^2)^2 P_g(k) \tag{4.18}$$

where FoG term is modeled either by the Lorentzian

$$\mathrm{FoG}(k_z, \sigma_v) = \left(\frac{1}{1 + (k\mu\sigma_v)^2/2}\right)^2, \tag{4.19}$$

or the Gaussian form

$$\mathrm{FoG}(k_z, \sigma_v) = \exp\left[-(k\mu\sigma_v)^2\right]. \tag{4.20}$$

where $\sigma_v$ is characterizing the velocity dispersion along the line of sight, and is in practice treated as a free parameter. Empirically, comparing the results to the numerical N-body simulations, Lorentzian form tends to be preferred over the Gaussian one. Although $\sigma_v$ fit can be used to provide a given statistics on an individual basis relatively well, e.g. monopole or quadrupole, it has proven difficult to make the modeling work simultaneously on multiple of these statistics. Nevertheless, accuracy in describing the shape of the multipoles and their ratios as a function of scale is of great interest since it enables a direct determination of $\beta$ from the clustering surveys.

### 4.3.3 PT based extensions and approximations

Achieving a good RSD modeling based on the equation 4.15 has proven to be a challenging undertaking. As mentioned above, one of the main reasons for this can be traced to the highly nonlinear effects from small scales that can be mapped to the linear scales in redshift space. Modeling of this comes on top of the mildly non-linear clustering effects that can be addressed by the PT. Middle ground approaches have been proposed (e.g. [13, 6]), where part of the contribution is treated in PT and for the highly nonlinear effect we once again resort to the phenomenological FoG kernels. One of such models proposed in [13] as an empirical upgrade of the Kaiser model is given by:

$$P_s(\mathbf{k}) = \mathrm{FoG}(k_z, \sigma_v)\left(b_1^2 P_{\delta\delta} + 2f b_1 \mu^2 P_{\delta\theta} + f^2\mu^4 P_{\theta\theta}\right), \tag{4.21}$$

where $P_{\delta\delta}$, $P_{\theta\delta}$, $P_{\theta\theta}$ are non-linear (for example one-loop SPT) density and velocity cross and auto spectra. Going beyond this requires and evaluation of the pairwise velocity PDF which can be non-Gaussian even on large scales. In [6] this model was extended by adding two additional terms (that are treated in PT) in the brackets corresponding to the $\langle\delta|\delta\theta\rangle$ and $\langle\delta\theta|\delta\theta\rangle$ terms in equation 4.15.

In chapter 5 we develop a robust formalism that enables us to deal with mentioned problems in more efficient and rigorous manner. We show that it is possible to make clear separations between purely perturbative contributions that can then be addressed by the PT techniques

of choice, and on the other hand, non-linear velocity dispersion contributions. The latter are by definition the zero-lag quantities and as such get contributions from all scales, and so as expected substantial velocity contributions come from small scales. These terms are thus of intrinsically non-perturbative character, and in the light of the effective field theory formalism can be treated as the effective coefficients.

### 4.3.4 Zel'dovich approximation

We have mentioned earlier that Lagrangian formalism offers an alternative way of resumming some of the contributions we are considering. Fourier transforming the corresponding expression 4.10 in redshift space, we get the power spectrum form

$$P_s(\mathbf{k}) = \int d^3q\ e^{i\mathbf{k}\cdot\mathbf{q}} \left(\langle \exp(i\mathbf{k}\cdot\Delta_s)\rangle - 1\right), \tag{4.22}$$

where $\Delta_s = \Psi_s(\mathbf{q}_1) - \Psi_s(\mathbf{q}_2)$ and $\mathbf{q} = \mathbf{q}_1 - \mathbf{q}_2$. Using the Zel'dovich approximation (i.e. use the linear theory displacement) and Gaussian initial conditions, this equation can be evaluated in terms of the two-point correlator of $\Psi_s(\mathbf{q})$. We have

$$P_s(\mathbf{k}) = \int d^3q\ e^{i\mathbf{k}\cdot\mathbf{q}} \exp\left[-\frac{1}{2}k_i k_j \left(\psi_{s,ij}(0) - \psi_{s,ij}(\mathbf{q})\right)\right], \tag{4.23}$$

where $\psi_{s,ij} = \langle \Psi_{s,i}(\mathbf{q}_1) | \Psi_{s,j}(\mathbf{q}_2)\rangle$. As the simplest case of this approach we can leave the zero-lag part in the exponent and expand the rest. Using

$$k_i k_j R_{in} R_{jm} \delta^K_{nm} = k^2 \left(1 + f(f+2)\mu^2\right), \tag{4.24}$$

we get

$$P_s(\mathbf{k}) = \exp\left[-(1 + f(f+2)\mu^2)k^2\sigma_v^2\right] (1 + f\mu^2)^2 P_L(k) \tag{4.25}$$

This result clearly stresses the importance of the FoG term and shows that bare Kaiser limit is valid only when $k^2\sigma_v^2 \ll 1$. FoG term also shows that the Zel'dovich damping is increased in redshift space relative to the real space along the line of sight by the factor $f(f+2)$. This results again leads to a reasonable description of the quadrupole to monopole ratio provided that the zero-crossing scale is fixed to agree with numerical simulations. Furthermore, although the shape of the quadrupole to monopole ratio resembles that in the simulations, the monopole and quadrupole do not agree as well as their ratio. This can be improved by using higher-order Lagrangian PT (e.g. [10]).

## 4.4 Higher Order Statistics and Cosmological Distortions

So far we have looked at the RSD effects in two-point function in Fourier as well as the configuration space. As shown above, alongside the cosmological opportunities that RSD offer, they also bring non-trivial computational barriers. This trend continues even more substantially when higher order statistics is considered. Never the less, bispectrum and the corresponding three-point function are the quantities of great potential as the sources of cosmological information. In the following, we take a short look at the RSD effects on the tree level bispectrum based on the redshift space kernels 4.8.

Finally, we shortly address the geometrical distortions effects (like Alcock-Paczynski [14]). In addition to the RSD, these effects arise in galaxy clustering measures because of the incorrect fiducial cosmology assumptions that can as well lead to apparent anisotropies in the clustering statistics.

### 4.4.1 Bispectrum in Redshift Space

Above we have written the PT kernels in redshift-space, which alongside the pure gravity kernels and biasing have contributions that arise from the redshift space mapping. It follows that the leading-order, tree-level bispectrum in redshift-space is given as

$$B_s(\mathbf{k}_1, \mathbf{k}_2, \mathbf{k}_3) = 2Z_2(\mathbf{k}_1, \mathbf{k}_2)Z_1(\mathbf{k}_1)Z_1(\mathbf{k}_2)P(k_1)P(k_2) + \text{'perm'}, \tag{4.26}$$

where 'perm' denotes a sum over all permutations of $\{k_1, k_2, k_3\}$, and we have $\mathbf{k}_1 + \mathbf{k}_2 + \mathbf{k}_3 = 0$. At leading order, the triangle configuration depends separately on $f$, $b_1$, and $b_2$ which allows us to break the degeneracy between $\Omega_m$ and $b_1$ present in measurement of the power spectrum multipoles in redshift space. Dependence of the monopole in equilateral configurations on $\Omega_m$ brought by redshift-space distortions is rather small, typically about 10%, but the quadrupole, on the other hand, shows a strong $\Omega_m$ dependence.

At small scales, PT models break down in similar fashion as in power spectrum case and again phenomenological models motivated by the power spectrum modeling have been proposed in order to account for FoG effects. [1] suggests for the bispectrum form

$$B_s(\mathbf{k}_1, \mathbf{k}_2, \mathbf{k}_3) = \frac{B_s^{PT}(\mathbf{k}_1, \mathbf{k}_2, \mathbf{k}_3)}{\left[1 + \alpha^2 \left[(k_1\mu_1)^2 + (k_2\mu_2)^2 + (k_3\mu_3)^2\right]^2 \sigma_v^2/2\right]^2}, \tag{4.27}$$

where $B_s^{PT}(\mathbf{k}_1, \mathbf{k}_2, \mathbf{k}_3)$ is the tree level PT redshift-space bispectrum. The assumption here is that one can write the triplet velocity dispersion along the line of sight in terms of the velocity dispersion $\sigma_v$ and some constant $\alpha$ which reflects the configuration dependence of the triplet velocity dispersion. $\sigma_v$ can be determined from the power spectrum analysis so that the parameter $\alpha$ is then fitted for a given bispectrum configuration.

### 4.4.2 Cosmological Distortions

In galaxy clustering surveys distortions related to the geometrical or Alcock-Paczynski (AP) effects can arise because the assumption of an incorrect cosmology leads to an apparent anisotropy effects. For example, structures can get flattened along the line of sight in similar way as in case of RSD. This can cause additional anisotropic effects in power spectrum and correlation functions. AP effects usually have smaller effect in magnitude compared to RSD, thus measuring them also requires an accurate treatment of redshift distortions.

Lastly, let us mention the light cone effects that arise from the fact that we do not observe a constant time slices. Our observation is made along the past light cone in redshift space. Thus, our line of sight contains the continuous clustering evolution effects (e.g. [15]). For more general treatment of all relativistic effects we refer to e.g. [16]. Estimates of these effects in the very wide surveys like SDSS and EUCLID can amount to 5% effects in the power spectrum and higher order statistics, and can become even larger for deep surveys.

# Bibliography


[1] F. Bernardeau, S. Colombi, E. Gaztanaga, and R. Scoccimarro, **Large scale structure of the universe and cosmological perturbation theory**, *Phys.Rept.* **367** (2002) 1–248, [astro-ph/0112551].

[2] A. Hamilton, **Linear redshift distortions: A Review**, astro-ph/9708102. Published in The Evolving Universe. Edited by D. Hamilton, Kluwer Academic, 1998, p. 185-275.

[3] S. Dodelson, *Modern cosmology.* Academic Press, 2003.

[4] N. Kaiser, **Clustering in real space and in redshift space**, *Mon. Not. Roy. Astron. Soc.* **227** (1987) 1–27.

[5] R. Scoccimarro, H. Couchman, and J. A. Frieman, **The Bispectrum as a signature of gravitational instability in redshift-space**, *Astrophys.J.* **517** (1999) 531–540, [astro-ph/9808305].

[6] A. Taruya, T. Nishimichi, and S. Saito, **Baryon Acoustic Oscillations in 2D: Modeling Redshift-space Power Spectrum from Perturbation Theory**, *Phys.Rev.* **D82** (2010) 063522, [arXiv:1006.0699].

[7] A. Taruya, T. Nishimichi, and F. Bernardeau, **Precision modeling of redshift-space distortions from multi-point propagator expansion**, arXiv:1301.3624.

[8] T. Matsubara, **Resumming Cosmological Perturbations via the Lagrangian Picture: One-loop Results in Real Space and in Redshift Space**, *Phys.Rev.* **D77** (2008) 063530, [arXiv:0711.2521].

[9] T. Matsubara, **Nonlinear perturbation theory with halo bias and redshift-space distortions via the Lagrangian picture**, *Phys.Rev.* **D78** (2008) 083519, [arXiv:0807.1733].

[10] J. Carlson, B. Reid, and M. White, **Convolution Lagrangian perturbation theory for biased tracers**, arXiv:1209.0780.

[11] M. White, **The Zeldovich approximation**, arXiv:1401.5466.

[12] P. J. E. Peebles, *The large-scale structure of the universe.* Princeton University Press, 1980.

[13] R. Scoccimarro, **Redshift-space distortions, pairwise velocities and nonlinearities**, *Phys.Rev.* **D70** (2004) 083007, [astro-ph/0407214].

[14] C. Alcock and B. Paczynski, **An evolution free test for non-zero cosmological constant**, *Nature* **281** (1979).

[15] T. Matsubara, **The Correlation function in redshift space: General formula with wide angle effects and cosmological distortions**, *Astrophys.J.* (1999) [astro-ph/9908056].

[16] J. Yoo, A. L. Fitzpatrick, and M. Zaldarriaga, **A New Perspective on Galaxy Clustering as a Cosmological Probe: General Relativistic Effects**, *Phys.Rev.* **D80** (2009) 083514, [arXiv:0907.0707].

# Chapter 5

# Redshift Space Distortions. Part II: Dark Matter [1]

We develop a perturbative approach to redshift space distortions (RSD) using the phase space distribution function approach and apply it to the dark matter redshift space power spectrum and its moments. RSD can be written as a sum over density weighted velocity moments correlators, with the lowest order being density, momentum density and stress energy density. We use standard and extended perturbation theory (PT) to determine their auto and cross correlators, comparing them to N-body simulations. We show which of the terms can be modeled well with the standard PT and which need additional terms that include higher order corrections which cannot be modeled in PT. Most of these additional terms are related to the small scale velocity dispersion effects, the so called finger of god (FoG) effects, which affect some, but not all, of the terms in this expansion, and which can be approximately modeled using a simple physically motivated ansatz such as the halo model. We point out that there are several velocity dispersions that enter into the detailed RSD analysis with very different amplitudes, which can be approximately predicted by the halo model. In contrast to previous models our approach systematically includes all of the terms at a given order in PT and provides a physical interpretation for the small scale dispersion values. We investigate RSD power spectrum as a function of $\mu$, the cosine of the angle between the Fourier mode and line of sight, focusing on the lowest order powers of $\mu$ and multipole moments which dominate the observable RSD power spectrum. Overall we find considerable success in modeling many, but not all, of the terms in this expansion. This is similar to the situation in real space, but predicting power spectrum in redshift space is more difficult because of the explicit influence of small scale dispersion type effects in RSD, which extend to very large scales.

## 5.1 Introduction

Galaxy clustering surveys are one of the most important venues to extract cosmological information today. This is because by measuring the 3 dimensional distribution of galaxies we can in principle relate it to the 3 dimensional distribution of the underlying dark matter. The dark matter distribution is sensitive to many of the cosmological parameters. The growth of dark matter structures in time also provides important constraints on the models, such as the nature and amount of dark energy.

Since galaxies are not perfect tracers of dark matter, their clustering is biased relative to the dark matter. This means that galaxy surveys cannot determine the rate of growth of structure unless this biasing is determined. Fortunately, galaxy redshift surveys provide

[1] This chapter is based on a paper by Z. Vlah, U. Seljak, P. McDonald, T. Okumura, T. Baldauf published in the JCAP, Vol. 1211, [1].

additional information, because the observed redshift is a sum of the radial distance to the galaxy and its peculiar velocity (Doppler shift). Galaxies are expected to follow the same gravitational potential as the dark matter and thus they are expected to have the same velocity (in a large-scale average at least). This leads to a clustering strength that depends on the angle between the galaxy pairs and the line of sight, which is referred to as redshift space distortions (RSD). In linear theory it can be easily related to the dark matter clustering [2, 3]. These distortions thus make the galaxy clustering in redshift space more complex, but at the same time provide an opportunity to extract important information on the dark matter clustering directly from the redshift surveys. To what extent this is possible is a matter of considerable debate: there are significant nonlinear effects that spoil this simple picture, once one goes beyond very large scales, as will also be seen in this paper.

It is worth pursuing how far we can understand RSD for the simple reason that RSD offer a unique way to measure growth rate of structure formation [4], and also can provide tests of dark energy models and general relativity [5, 6, 7]. Generically, if one had a good understanding of the nonlinear effects, RSD would be the most powerful technique for these studies because redshift surveys provide 3-dimensional information, while other methods, such as weak lensing, provide 2-dimensional information (or slightly more if the so-called tomographic information is used [8, 9]). The most problematic part of RSD studies are the nonlinear effects, which have proved to be difficult to model, and which can extend to rather large scales, making their modeling essential for using the RSD as a tool.

In recent years several studies have been performed investigating these effects [10, 11, 12, 13]. Some of these studies included galaxies or halos, [14, 15, 16, 17]. Some of these methods use analysis and modeling based on perturbation theory (PT) [18], but none attempt to rely entirely on PT to explain all of the effects. Instead, they rely on ansatzes with free parameters, so that if the ansatz are accurate one can model the effects accurately. Separately, there have been several approaches trying to improve perturbation methods and to increase their ranges of validity [19, 20, 21, 22, 23, 24, 25, 26, 27, 28]. All of these approaches adopt a single stream approximation, which we know breaks down on small scales inside the virialized halos and which is particularly problematic for modeling of RSD.

The goal of this paper is to present a systematic PT approach to all of the lowest order terms contributing to RSD. Our goal is to identify which can be modeled well with PT, which can be modeled with extended PT methods mentioned above, and which require phenomenological additions to account for the small scale physics which cannot be modeled with traditional PT that does not include velocity dispersion. This approach is enabled by the recently developed distribution function approach to RSD [29], which decomposes RSD contributions into separate correlations between moments of distribution function. As such it allows us to investigate individual contributions to RSD and develop different PT or other approximation schemes for these terms. Whether this is ultimately useful for modeling RSD remains to be seen: our primary goal is to develop better physical understanding of dominant contributions to RSD.

The paper is organized as follows: we begin in Sec. 6.2 by presenting a more detailed derivation of the angular decomposition of redshift space power spectra than given in [29]. We then use in Sec. 5.3 the perturbative methods to model the lowest contributing terms in this expansion, augmented by simple phenomenological models and/or beyond the lowest order contributions to improve the model when necessary. Results are also compared to numerical simulation measurements presented in [30]. We summarize and conclude in Sec. 6.5. In Appendices 5.5, 5.6, 5.7, 5.8 we show some details of the calculations and write explicit forms of the terms contributing to the power spectra.

For this work, flat ΛCDM model is assumed $\Omega_{\rm m} = 0.279$, $\Omega_\Lambda = 0.721$, $\Omega_{\rm b}/\Omega_{\rm m} = 0.165$, $h = 0.701$, $n_s = 0.96$, $\sigma_8 = 0.807$. The primordial density field is generated using the matter transfer function by CAMB. The positions and velocities of all the dark matter particles are given at the redshifts $z = 0,\ 0.509,\ 0.989$, and 2.070, which are for simplicity quoted as $z$ =0, 0.5, 1, and 2.

## 5.2 Redshift-space distortions form the distribution function

### 5.2.1 Generation of velocity moments

Evolution of collisionless particles is described by the Vlasov equation [31]

$$\frac{df}{d\tau} = \frac{\partial f}{\partial \tau} + \frac{\mathbf{p}}{am} \cdot \nabla_x f - am \nabla\phi \cdot \nabla_p f = 0, \tag{5.1}$$

where the gravitational potential $\phi$ is given by

$$\nabla_x^2 \phi = 4\pi G a^2 \bar{\rho}\delta = \frac{3}{2}\mathcal{H}^2 \Omega_m \delta. \tag{5.2}$$

Here $f(\mathbf{x}, \mathbf{p}, \tau)$ is the particle distribution function at a phase space point $(\mathbf{x}, \mathbf{p})$, where $\mathbf{x}$ is the comoving position, $\mathbf{p}$ is the corresponding canonical particle momentum defined by $\frac{d\mathbf{p}}{d\tau} = -am\nabla\phi$. $\tau = \int dt/a$ is the conformal time, $m$ is the particle mass, and $\mathcal{H} \equiv d\ln a/d\tau = Ha$ is the conformal expansion rate, where $H$ is the Hubble parameter.
Note that in this paper we will use the canonical momentum $\mathbf{p}$ rather then comoving $\mathbf{q} = \mathbf{p}/a$ defined in [29]. The reason is that the comoving momenta $\mathbf{q}$ is not the canonical coordinate to comoving position $\mathbf{x}$, and this would lead to additional terms in the Vlasov equation (because of coordinate transformations), i.e. taking corresponding q-moments of usual form of Vlasov equation 5.1 would not give the standard form of continuity equation, Euler equation, and higher moment equations. This is not a inconvenience when the symmetries are to be considered, but in order to avoid this we will use the canonical momenta $\mathbf{p}$.
In the following we will drop explicitly writing the time dependence, i.e we will write $f(\mathbf{x}, \mathbf{p})$. The density field in real space is obtained by integrating the distribution function over the momentum space

$$\rho(\mathbf{x}) \equiv ma^{-3} \int d^3p f(\mathbf{x}, \mathbf{p}), \tag{5.3}$$

and mean (bulk) velocity $\mathbf{v}$ and higher moment fields can be similarly obtained by multiplying the distribution function by corresponding number of particle momentum $\mathbf{p} = am\mathbf{u}$ ($\mathbf{u}$ is here a particle peculiar velocity) and then integrating over it. The mean velocity field of a particles is then given by

$$\mathbf{v}(\mathbf{x}) \equiv \frac{\int d^3p \frac{\mathbf{p}}{ma} f(\mathbf{x}, \mathbf{p})}{\int d^3p f(\mathbf{x}, \mathbf{p})}, \tag{5.4}$$

and the velocity dispersion tensor is

$$\sigma^{ij}(\mathbf{x}) \equiv \frac{\int d^3p \frac{p_i p_j}{m^2 a^2} f(\mathbf{x}, \mathbf{p})}{\int d^3p f(\mathbf{x}, \mathbf{p})} - v^i v^j, \tag{5.5}$$

i.e. $\sigma^{ij}(\mathbf{x}) \equiv \left\langle \partial v^i \partial v^j \right\rangle_p$ with $\partial v^i$ being the deviation of a particle's velocity from the local mean velocity, and the average is taken over all particles at position $\mathbf{x}$. Note the difference between the particle velocity $\mathbf{u}$ and mean velocity $\mathbf{v}$. The first one is the velocity of a single particle that corresponds to the canonical momentum $\mathbf{p}$, which is one coordinate in the phase space. On the other hand $\mathbf{v}$ is a field defined at every coordinate $\mathbf{x}$ and is averaged over all the phase space. In the similar way higher order moments can also be considered.
Taking a arbitrary constant unit vector $\mathbf{h}$, we can construct a following object

$$T_{\mathbf{h}}^L(\mathbf{x}) \equiv \frac{ma^{-3}}{\bar{\rho}} \int d^3p f(\mathbf{x}, \mathbf{p}) \left( \frac{\mathbf{h} \cdot \mathbf{p}}{ma} \right)^L, \tag{5.6}$$

i.e. velocity moments projected on the direction of vector $\mathbf{h}$, and where $\bar{\rho}$ is the mean mass density. If we introduce approximations in which we neglect velocity dispersion and anisotropic stress, i.e. we neglect all the contributions from this second rank stress tensor, and similar higher rank tensors ($\sigma^{ij} = 0, \ldots$) it can be shown (App. 5.5) that 5.6 is reduced to

$$T^L_{\mathbf{h}}(\mathbf{x}) = (1 + \delta(\mathbf{x})) \left(\mathbf{h} \cdot \mathbf{v}(\mathbf{x})\right)^L, \tag{5.7}$$

where $\delta$ is a usual overdensity field ($\delta \equiv \rho/\bar{\rho} - 1$).
In this paper we omit the following Fourier transform ($\mathcal{F}$) conventions

$$\begin{aligned} \tilde{f}(\mathbf{k}) &= \mathcal{F}\left[f(\mathbf{x})\right](\mathbf{k}) = \int d^3x \, \exp(i\mathbf{k}\cdot\mathbf{x}) f(\mathbf{x}), \\ f(\mathbf{x}) &= \mathcal{F}^{-1}\left[\tilde{f}(\mathbf{k})\right](\mathbf{x}) = \int \frac{d^3k}{(2\pi)^3} \, \exp(-i\mathbf{k}\cdot\mathbf{x}) \tilde{f}(\mathbf{k}). \end{aligned} \tag{5.8}$$

### 5.2.2 Redshift-space distortions

In redshift space the position of a particle is distorted by its peculiar velocity, thus the comoving redshift-space coordinate for this particle is given by

$$\mathbf{s} = \mathbf{x} + \hat{r}\frac{u_\parallel}{\mathcal{H}}, \tag{5.9}$$

where $\hat{r}$ is the unit vector pointing along the observer's line of sight, $u_\parallel$ is radial comoving velocity, $amu_\parallel = p_\parallel = \mathbf{p} \cdot \hat{r}$. The mass density in redshift space is then given by

$$\rho_s(\mathbf{s}) = ma^{-3} \int d^3p \; d^3x \; f\left(\mathbf{x}, \mathbf{p}\right) \delta^D \left(\mathbf{s} - \mathbf{x} - \hat{r}\frac{u_\parallel}{\mathcal{H}}\right) = ma^{-3} \int d^3p \; f\left(\mathbf{s} - \hat{r}\frac{u_\parallel}{\mathcal{H}}, \mathbf{p}\right). \tag{5.10}$$

By Fourier transforming equation 5.10, we get

$$\begin{aligned} \rho_s(\mathbf{k}) &= ma^{-3} \int d^3x \; d^3p \; f\left(\mathbf{x}, \mathbf{p}\right) e^{(i\mathbf{k}\cdot\mathbf{x} + ik_\parallel u_\parallel/\mathcal{H})} \\ &= ma^{-3} \int d^3x \; e^{i\mathbf{k}\cdot\mathbf{x}} \int d^3p \; f(\mathbf{x}, \mathbf{p}) e^{ik_\parallel u_\parallel/\mathcal{H}}, \end{aligned} \tag{5.11}$$

were $\mathbf{k}$ is the wavevector in redshift space, corresponding to redshift-space coordinate $\mathbf{s}$. Expanding the second integral in equation 5.11 as a Taylor series in $k_\parallel u_\parallel / m\mathcal{H}$,

$$\begin{aligned} ma^{-3} \int d^3p \; f\left(\mathbf{x}, \mathbf{p}\right) e^{ik_\parallel u_\parallel/\mathcal{H}} &= ma^{-3} \int d^3q \; f\left(\mathbf{x}, \mathbf{p}\right) \sum_{L=0} \frac{1}{L!} \left(ik_\parallel u_\parallel/\mathcal{H}\right)^L \\ &= \bar{\rho} \left[\sum_{L=0} \frac{1}{L!} \left(\frac{ik_\parallel}{\mathcal{H}}\right)^L T^L_\parallel(\mathbf{x})\right] \end{aligned} \tag{5.12}$$

where in the last part we have used equation 5.6 setting the vector $\mathbf{h}$ to be the unit vector pointing along the observer's line of sight $\mathbf{h} = \hat{r}$. Using that in equation 5.7 we have, in the case with no velocity dispersion or other second or higher rank tensors (which we will *not* generally assume)

$$T^L_\parallel(\mathbf{x}) = (1 + \delta(\mathbf{x})) v^L_\parallel(\mathbf{x}). \tag{5.13}$$

The Fourier component of the density fluctuation in redshift space is

$$\delta_s(\mathbf{k}) = \sum_{L=0} \frac{1}{L!} \left(\frac{ik_\parallel}{\mathcal{H}}\right)^L T^L_\parallel(\mathbf{k}), \tag{5.14}$$

were $T^L_\parallel(\mathbf{k})$ is the Fourier transform of the $T^L_\parallel(\mathbf{x})$. For L=0 we drop the unmeasurable $k = 0$ mode, and we are left with the density fluctuation $T^0_\parallel(\mathbf{k}) = \delta(\mathbf{k})$.

### 5.2.3 Angular decomposition of the moments of distribution function

In order to make the context of this paper more clear we repeat angular decomposition of the moments of distribution function from [29], providing more detailed derivation. The object $T^L_{\mathbf{h}}(\mathbf{x})$ introduced in equation 5.6 can be obtained as taking all components of moments of distribution function in $\mathbf{h}$ direction, which are the rank $L$ tensors,

$$T^L_{i_1,i_2,\ldots i_L} = \frac{ma^{-3}}{\bar{\rho}} \int d^3p f(\mathbf{x},\mathbf{p}) u_{i_1} u_{i_2} \ldots u_{i_L}. \tag{5.15}$$

The real-space density field corresponds to $L = 0$, i.e. zeroth moment 5.3, the $L = 1$ moment corresponds to the momentum density 5.4, $L = 2$ gives the stress energy density tensor 5.5 etc. These objects are symmetric under exchange of any two indices and have (L + 1)(L + 2)/2 independent components. They can be decomposed into helicity eigenstates under rotation around $\mathbf{k}$.
The full detailed derivation of this decomposition is done in (App. 5.6) and here we give the final result taking $\mathbf{h} = \hat{r}$;

$$T^L_{\parallel}(\mathbf{k}) = \sum_{(l=L,L-2,\ldots)} \sum_{m=-l}^{m=l} n^L_l T^{L,m}_l(k) Y_{lm}(\theta,\phi), \tag{5.16}$$

where coefficients $n^L_l$ are defined in equation 5.106, and spherical tensors $T^{L,m}_l$ in equation 5.104, and evaluated in frame where $z \parallel \mathbf{k}$, so it does not contain any angular dependence.

### 5.2.4 Redshift power spectrum

In our analysis we will adopt a plane-parallel approximation, were only the angle between the line of sight and the Fourier mode needs to be specified. The redshift-space power spectrum is defined as $\left\langle \delta_s(\mathbf{k}) | \delta^*_s(\mathbf{k}') \right\rangle = (2\pi)^3 P^{ss}(\mathbf{k}) \delta^D(\mathbf{k} - \mathbf{k}')$. Equation 5.14 gives,

$$P^{ss}(\mathbf{k}) = \sum_{L=0} \sum_{L'=0} \frac{(-1)^{L'}}{L!L'!} \left(\frac{ik_\parallel}{\mathcal{H}}\right)^{L+L'} P_{LL'}(\mathbf{k}), \tag{5.17}$$

where we define

$$(2\pi)^3 P_{LL'}(\mathbf{k}) \delta^D(\mathbf{k} - \mathbf{k}') = \left\langle T^L_{\parallel}(\mathbf{k}) \left| T^{*L'}_{\parallel}(\mathbf{k}') \right\rangle \right. . \tag{5.18}$$

Note that $P_{LL'}(\mathbf{k}) = P_{L'L}(\mathbf{k})^*$ so that the total result is real valued (what is explicitly shown in PT approach in App. 5.7). Thus only the terms $P_{LL'}(\mathbf{k})$ with $L \leq L'$ need to be considered, each of which comes with a factor of 2 if $L \neq L'$ and 1 if $L = L'$. If we introduce $\mu = k_\parallel/k = \cos\theta$, we can write,

$$P^{ss}(\mathbf{k}) = \sum_{L=0} \frac{1}{(L!)^2} \left(\frac{k\mu}{\mathcal{H}}\right)^{2L} P_{LL}(\mathbf{k}) + 2Re \sum_{L=0} \sum_{L'>L} \frac{(-1)^{L'}}{L!L'!} \left(\frac{ik\mu}{\mathcal{H}}\right)^{L+L'} P_{LL'}(\mathbf{k}). \tag{5.19}$$

Next we insert the helicity decomposition of equation 5.16 and consider the implications of rotational symmetry on the power spectrum. Each term $P_{LL'}(\mathbf{k})$ contains products of multipole moments

$$T^{L,m}_l(\mathbf{k}) Y_{lm}(\theta,\phi) \left(T^{L',m'}_{l'}(\mathbf{k}) Y_{l',m'}(\theta,\phi)\right)^* \propto e^{i(m-m')\phi}. \tag{5.20}$$

Upon averaging over the azimuthal angle $\phi$ of Fourier modes all the terms with $m \neq m'$ vanish. Another way to state this is that upon rotation by angle $\psi$ the correlator picks up a

term $e^{i(m-m')\psi}$ and in order for the power spectrum to be rotationally invariant we require $m = m'$. Putting all these together we find

$$P_{LL'}(\mathbf{k}) = \sum_{(l=L,L-2,\ldots)} \sum_{(l'=L',L'-2,\ldots)} \sum_{m=0}^{l} P_{l,l'}^{L,L',m}(k) P_l^m(\mu) P_{l'}^m(\mu), \tag{5.21}$$

where $P_l^m(\mu = \cos\theta)$, are the associated Legendre polynomials, which determine the $\theta$ angular dependence of the spherical harmonics. We absorb all of the terms that depend on $l$ and $m$ and various constants into the definition of power spectra $P_{l,l'}^{L,L',m}(k)$. Note once again that these spectra depend only on amplitude of k. We have

$$P_{l,l'}^{L,L',m}(k) \propto \left\langle T_l^{L,m}(k) \left| \left( T_{l'}^{L',m'}(k) \right)^* \right\rangle \right. . \tag{5.22}$$

We also replaced the two helicity states $\pm m$ by a single one with $m > 0$, since their $\theta$ angular dependencies are the same, and we absorbed the appropriate factors into the definition of $P_{l,l'}^{L,L',m}(k)$.

### 5.2.5 Perturbation theory approach

The parameter of the expansion in equation 5.19 can roughly be defined as $k\mu v/\mathcal{H}$, where $v$ is related to a typical gravitational velocity of the system. This velocity should be of order of a few hundred $km/s$, but note that higher and higher powers of these velocities enter the series. The expansion series is expected to be convergent if expansion parameter is less then unity.

The main goal of these paper is to use perturbation theory to compute and assess contributing terms in expansion formula 5.19 in next to leading order (one loop). There is a close, but not one to one, relation between the PT expansion and expansion in distortions function moments. Assuming that $\delta$ and $kv/\mathcal{H}$ make the same order of expansion in one loop (except $P_{04}$ where leading term is two loop quantity) regime we obtain

$$\begin{aligned} P^{ss}(\mathbf{k}) = P_{00}(\mathbf{k}) + \left(\frac{k\mu}{\mathcal{H}}\right)^2 P_{11}(\mathbf{k}) + \frac{1}{4}\left(\frac{k\mu}{\mathcal{H}}\right)^4 P_{22}(\mathbf{k}) + 2\mathrm{Re}\left[\left(\frac{-ik\mu}{\mathcal{H}} P_{01}(\mathbf{k})\right)\right. \\ + \left(-\frac{1}{2}\left(\frac{k\mu}{\mathcal{H}}\right)^2 P_{02}(\mathbf{k})\right) + \left(\frac{i}{6}\left(\frac{k\mu}{\mathcal{H}}\right)^3 P_{03}(\mathbf{k})\right) + \left(-\frac{i}{2}\left(\frac{k\mu}{\mathcal{H}}\right)^3 P_{12}(\mathbf{k})\right) \\ \left. + \left(-\frac{1}{6}\left(\frac{k\mu}{\mathcal{H}}\right)^4 P_{13}(\mathbf{k})\right) + \left(\frac{1}{24}\left(\frac{k\mu}{\mathcal{H}}\right)^4 P_{04}(\mathbf{k})\right)\right]. \end{aligned} \tag{5.23}$$

Neglecting all the velocity dispersion and anisotropic stress contributions we can use simplified form of $T_\parallel^L$ (equation 5.13). After preforming the Fourier transformation we obtain

$$T_\parallel^L(\mathbf{k}) = \mathcal{F}\left[(1+\delta(\mathbf{x}))\, v_\parallel^L(\mathbf{x})\right](\mathbf{k}). \tag{5.24}$$

In one loop PT regime only first three momenta are needed, so we can write

$$\begin{aligned} T_\parallel^1(\mathbf{k}) &= v_\parallel(\mathbf{k}) + \left(v_\parallel \circ \delta\right)(\mathbf{k}), \\ T_\parallel^2(\mathbf{k}) &= \left(v_\parallel \circ v_\parallel\right)(\mathbf{k}) + \left(v_\parallel \circ v_\parallel \circ \delta\right)(\mathbf{k}), \\ T_\parallel^3(\mathbf{k}) &= \left(v_\parallel \circ v_\parallel \circ v_\parallel\right)(\mathbf{k}), \end{aligned} \tag{5.25}$$

where we have used the following convention for convolution

$$(f \circ g)(\mathbf{k}) = \int \frac{d^3q}{(2\pi)^3} f(\mathbf{q}) g(\mathbf{k}-\mathbf{q}). \tag{5.26}$$

From the approximations we have adopted it also follows that curls of velocity field can be neglected, i.e. $\nabla \times \mathbf{v}(\mathbf{x}) = 0$. Thus velocity field can be fully described by its divergence field $\theta(\mathbf{x}) = \nabla \cdot \mathbf{v}(\mathbf{x})$. So it follows $v_\parallel(\mathbf{k}) = i\frac{k_\parallel}{k^2}\theta(\mathbf{k})$.
At this point it is useful to observe that if working in linear perturbation regime well known Kaiser result [2] can be easily obtained directly from equation 5.17. It follows

$$P^{ss}(\mathbf{k}) = P_{00}(\mathbf{k}) + 2\mathrm{Re}\left(\frac{-ik\mu}{\mathcal{H}}\right)P_{01}(\mathbf{k}) + \left(\frac{k\mu}{\mathcal{H}}\right)^2 P_{11}(\mathbf{k}), \tag{5.27}$$

and after using the facts that $P^{(1,1)}_{\delta\theta}(\mathbf{k}) = -f\mathcal{H}P_L(\mathbf{k})$ and that $P^{(1,1)}_{\theta\theta}(\mathbf{k}) = (f\mathcal{H})^2 P_L(\mathbf{k})$ we obtain

$$P^{ss}(\mathbf{k}) = \left(1 + f\mu^2\right)^2 P_{\delta\delta}(\mathbf{k}), \tag{5.28}$$

hence, the Kaiser formula.

## 5.3 Perturbation theory results and comparison to the N-body simulations

All of the N-body results used here have been presented in [30]. Briefly, for all of the power spectra of the derivative expansion one needs mass-weighted velocity moments, which can be straightforwardly measured from simulations. In [30] a series of $N$-body simulations of the $\Lambda$CDM cosmology seeded with Gaussian initial conditions has been used [32]. We employ $1024^3$ particles of mass $3.0 \times 10^{11} h^{-1} M_\odot$ in a cubic box of side $1600 h^{-1} Mpc$. We use 12 independent realizations in order to reduce the statistical scatters. For the details of the simulations measurements we refer to the [32] and here we shortly repeat the basics.

### 5.3.1 $P_{00}$: the isotropic term

At the lowest order in $kv/\mathcal{H}$ expansion we have auto correlation of density field $T^0_\parallel(\mathbf{k}) = \delta(\mathbf{k})$. Power spectrum, $P_{00}(k)\delta^D(\mathbf{k} - \mathbf{k}') = \left\langle \delta(\mathbf{k})|\delta^*(\mathbf{k}')\right\rangle$, is well known and has been intensively studied, e.g. [33, 18]. This first term does not have any $\mu$ dependence since it is independent of red shift space distortions, it dominants for small values of $\mu$ and in the limit $\mu = 0$ the transverse power spectrum becomes overdensity power spectrum $P_{00}(k)$. On scales smaller than $k^{-1} \sim 10 Mpc/h$, nonlinear corrections increase the power over the linear.
Familiar one loop PT result for overdensity power spectrum is [18]

$$P_{00}(\mathbf{k},\tau) = P_{\delta\delta}(\mathbf{k},\tau) = D^2(\tau)P^{(1,1)}_{\delta\delta}(\mathbf{k}) + D^4(\tau)\left[P^{(2,2)}_{\delta\delta}(\mathbf{k}) + 2P^{(1,3)}_{\delta\delta}(\mathbf{k})\right], \tag{5.29}$$

where we have restored time dependence, with $D(\tau)$ being linear cosmological growth factor. $P^{(1,1)}_{\delta\delta}(\mathbf{k})$ is the linear power spectrum $P_L(\mathbf{k})$, and one loop contributions are

$$\begin{aligned} P^{(2,2)}_{\delta\delta}(k) &= 2\int \frac{d^3q}{(2\pi)^3} P_L(q)P_L\left(|\mathbf{k}-\mathbf{q}|\right)\left[F_2^{(s)}\left(\mathbf{q}, \mathbf{k}-\mathbf{q}\right)\right]^2 \\ &= 2I_{00}(k), \\ P^{(1,3)}_{\delta\delta}(k) &= 3P_L(k)\int \frac{d^3q}{(2\pi)^3} P_L(q)F_3^{(s)}\left(\mathbf{k}, \mathbf{q}, -\mathbf{q}\right) \\ &= 3k^2 P_L(k)J_{00}(k). \end{aligned} \tag{5.30}$$

Explicit form of all integrals of the $I_{mn}(k)$ and $J_{mn}(k)$ type can be found in App 5.8. In figure 5.1 one loop PT results for power spectrum have been presented, along with some of the other approaches, such as the closure theory approach [25] obtained from the Copter code [33] and the semi-fitting method [34], based on power spectrum obtained from Zel'dovich approximation. Note that if one wants to impose consistency in expansion 5.23 and PT

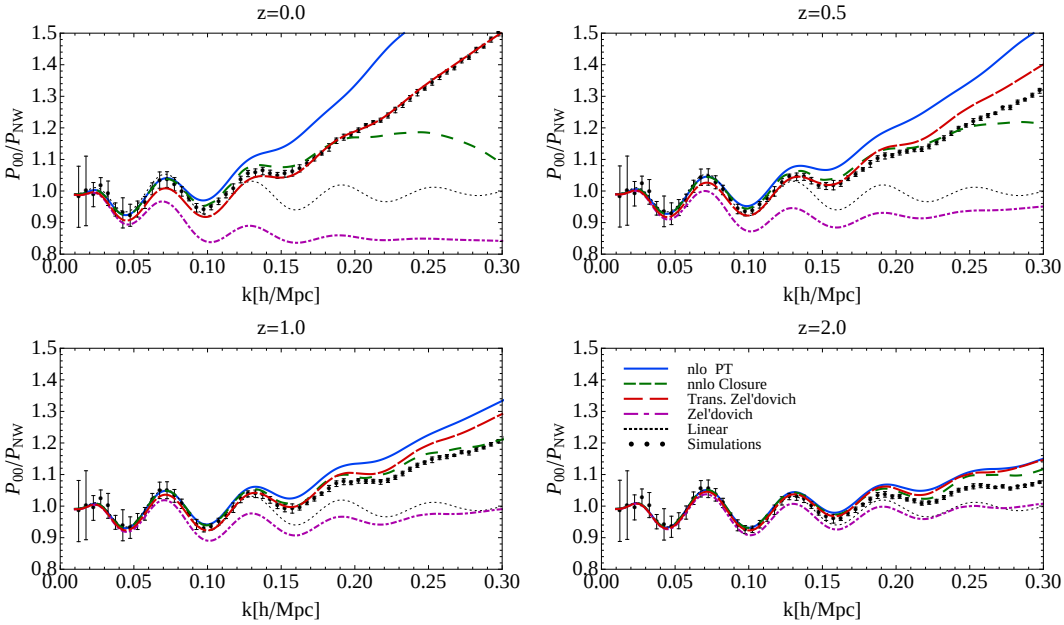


**Figure 5.1:** $P_{00}(k)$ power spectrum term is plotted at four redshifts $z = 0.0,\ 0.5,\ 1.0$ and 2.0. We show linear result (black, dotted), one loop PT (blue, solid), two loop closure (green, dashed), corrected Zel'dovich (red, long-dashed) of [34] , simple Zel'dovich (magenta, dot-dashed) and simulation measurements (black dots). The error bars show the variance among realizations in simulations. The power spectrum is divided by no-wiggle fitting formula from [35], to reduce the dynamic range.

approach, only one loop regime PT result should be considered. All the power spectra on the figures are divided by the linear power spectrum fitting formula from [35] without BAO wiggles. We see that none of the methods give perfect agreement across all range of scales. SPT (one loop PT) actually gives the best results for $k < 0.05h/Mpc$, but predicts too much power at higher $k$.

### 5.3.2 $P_{01}$

The next term to consider correlates the overdensity field $T^0_{\parallel}(\mathbf{k}) = \delta(\mathbf{k})$ and radial component of momentum density $T^1_{\parallel}(\mathbf{k})$. This is the dominant RSD term sensitive to velocities. As we can see from equation 5.16, momentum density can be decomposed into a scalar ($m = 0$) $T_1^{1,0}$ and two vector ($m = \pm 1$) components $T_1^{1,\pm 1}$. Only the scalar part correlates with the density $T_0^{0,0}$, which is a scalar field. Thus only non-vanishing contribution comes from $P_{0,1}^{0,1,0}(k) \propto \left\langle T_0^{0,0}(k) \left| \left(T_1^{1,0}(k)\right)^* \right\rangle \right.$, what gives the simple angular dependence

$$P_{01}(\mathbf{k}) = P_{0,1}^{0,1,0}(k) P_1^0(\mu) = \mu P_{0,1}^{0,1,0}(k). \tag{5.31}$$

On the other hand, correlating directly $\left\langle \delta(\mathbf{k}) | T^{*1}_{\parallel}(\mathbf{k}', \tau) \right\rangle$, from the equation 5.25 one gets power spectra

$$P_{01}(\mathbf{k}) = -i\frac{\mu}{k} P_{\delta\theta}(\mathbf{k}) - iA_{01}(\mathbf{k}), \tag{5.32}$$

where the first term is also well studied correlation function of overdensity field and divergence of velocity field

$$\begin{aligned} (2\pi)^3 P_{\delta\theta}(\mathbf{k}) \delta^D(\mathbf{k} - \mathbf{k}') &= \left\langle \delta(\mathbf{k}) | \theta(\mathbf{k}') \right\rangle, \\ (2\pi)^3 A_{01}(\mathbf{k}) \delta^D(\mathbf{k} - \mathbf{k}') &= \int \frac{d^3\mathbf{q}}{(2\pi)^3} \frac{q_{\parallel}}{q^2} \left\langle \delta(\mathbf{k}) | \theta^*(\mathbf{q}) \delta^*(\mathbf{k}' - \mathbf{q}) \right\rangle. \end{aligned} \tag{5.33}$$

For the first term, correlation function of overdensity and divergence of velocity field, one loop PT gives

$$P_{\delta\theta}(k,\tau) = D^2(\tau)P_{\delta\theta}^{(1,1)}(k) + D^4(\tau)\left[P_{\delta\theta}^{(2,2)}(k) + 2P_{\delta\theta}^{(1,3)}(k)\right], \tag{5.34}$$

where $P_{\delta\theta}^{(1,1)}(k) = -f\mathcal{H}P_L(k)$ is the contribution in the linear regime, and one loop contribution is

$$\begin{aligned}
P_{\delta\theta}^{(2,2)}(k) &= -2f\mathcal{H}\int \frac{d^3q}{(2\pi)^3}P_L(q)P_L\left(|\mathbf{k}-\mathbf{q}|\right)F_2^{(s)}\left(\mathbf{q},\mathbf{k}-\mathbf{q}\right)G_2^{(s)}\left(\mathbf{q},\mathbf{k}-\mathbf{q}\right) \\
&= -2f\mathcal{H}I_{01}(k), \\
P_{\delta\theta}^{(1,3)}(k) &= -3f\mathcal{H}P_L(k)\int \frac{d^3q}{(2\pi)^3}P_L(q)\frac{1}{2}\left[F_3^{(s)}\left(\mathbf{k},\mathbf{q},-\mathbf{q}\right) + G_3^{(s)}\left(\mathbf{k},\mathbf{q},-\mathbf{q}\right)\right] \\
&= -3f\mathcal{H}k^2P_L(k)J_{01}(k) \\
&= -\frac{1}{2}f\mathcal{H}\left(P_{\delta\delta}^{(1,3)}(k) + \frac{P_{\theta\theta}^{(1,3)}(k)}{(f\mathcal{H})^2}\right).
\end{aligned} \tag{5.35}$$

Here we have introduced logarithmic growth rate $f = f(\tau) = d\ln D/d\ln a$.
For the second term in equation 5.31, we expand all the fields to the second order, i.e., one loop in the correlation function. Schematically, this gives

$$\langle\delta\theta\delta\rangle = \left\langle\delta^{(2)}\theta^{(1)}\delta^{(1)}\right\rangle + \left\langle\delta^{(1)}\theta^{(2)}\delta^{(1)}\right\rangle + \left\langle\delta^{(1)}\theta^{(1)}\delta^{(2)}\right\rangle,$$

or in terms of power spectrum

$$A_{01}(\mathbf{k},\tau) = D^4(\tau)\left(A_{01}^{(211)}(\mathbf{k}) + A_{01}^{(112)}(\mathbf{k}) + A_{01}^{(112)}(\mathbf{k})\right). \tag{5.36}$$

Again, using one loop PT we obtain the contributions from each of the terms

$$\begin{aligned}
A_{01}^{(211)}(\mathbf{k}) &= -2f\mathcal{H}\int \frac{d^3q}{(2\pi)^3}\ \frac{q_\parallel}{q^2}F_2^{(s)}(\mathbf{q},\mathbf{k}-\mathbf{q})P_L(q)P_L(|\mathbf{k}-\mathbf{q}|) \\
&= -2f\mathcal{H}\frac{\mu}{k}I_{10}(k), \\
A_{01}^{(121)}(\mathbf{k}) &= -2f\mathcal{H}\ P_L(\mathbf{k})\int \frac{d^3q}{(2\pi)^3}\ \frac{(\mathbf{k}-\mathbf{q})_\parallel}{(\mathbf{k}-\mathbf{q})^2}G_2^{(s)}(-\mathbf{q},\mathbf{k})P_L(q) \\
&= -2f\mathcal{H}\mu kP_L(k)\left[3J_{10}(k) + \frac{1}{2}\left(\sigma_v^2 + \frac{\sigma_0^2}{3k^2}\right)\right], \\
A_{01}^{(112)}(\mathbf{k}) &= 2f\mathcal{H}\ P_L(\mathbf{k})\int \frac{d^3q}{(2\pi)^3}\ \frac{q_\parallel}{q^2}F_2^{(s)}(\mathbf{q},\mathbf{k})P_L(q) \\
&= f\mathcal{H}\mu kP_L(k)\left(\sigma_v^2 + \frac{\sigma_0^2}{3k^2}\right).
\end{aligned} \tag{5.37}$$

where the $\sigma_v^2 = \frac{1}{3}\int \frac{d^3q}{(2\pi)^3}\frac{P_L(q)}{q^2}$ is the one-dimensional velocity dispersion at linear order, and $\sigma_0^2 = \int \frac{d^3q}{(2\pi)^3}P_L(q)$. Note that all three terms give the same angular dependence, so $A_{01} \sim \mu$, and then follows that $P_{01} \sim \mu$, as was expected form the symmetry consideration on the beginning. Finally, collecting all the terms 5.32, 5.33, 5.36, 5.37 one loop PT prediction for the $P_{01}$ follows. Now the total contribution to the redshift power spectrum $P^{ss}$ from the $P_{01}$ term is

$$\begin{aligned}
P_{01}^{ss}(\mathbf{k},\tau) &= 2\frac{-ik\mu}{\mathcal{H}}P_{01}(\mathbf{k},\tau) \\
&= 2f(\tau)D^2(\tau)\mu^2\left(P_L(k) + 2D^2(\tau)\left[I_{01}(k) + I_{10}(k) + 3k^2\big(J_{01}(k) + J_{10}(k)\big)P_L(k)\right]\right).
\end{aligned} \tag{5.38}$$

In this form result is naturally separated in linear and one loop contribution part. Note that linear part here is the second term of Kaiser formula.
Alternatively, the scalar mode of momentum can be obtained from the divergence of momentum and related to $\dot{\delta}$ using the continuity equation $\dot{\delta} - ikp_s = 0$, which is in terms of quantities defined previously

$$\dot{T}_0^{0,0} - ikT_0^{1,0} = 0. \tag{5.39}$$

Note that the vector part of momentum field does not contribute, since it vanishes upon taking the divergence (i.e., vector components are orthogonal to $\mathbf{k}$ and the dot product is zero).
It follows

$$P_{01}(\mathbf{k},\tau) = i\frac{\mu}{k}P_{\delta\dot{\delta}}(k,\tau) = i\frac{\mu}{2k}\frac{dP_{00}(k,\tau)}{d\tau}, \tag{5.40}$$

and the total contribution to $P^{ss}(k,\tau)$ is

$$P_{01}^{ss}(\mathbf{k},\tau) = \mu^2\mathcal{H}^{-1}\frac{dP_{00}(k,\tau)}{d\tau} = \mu^2\frac{dP_{00}(k,a)}{d\ln a}. \tag{5.41}$$

This result, first obtained in [29], is exact for dark matter, valid also in the nonlinear regime. It shows that this term can be obtained directly from the redshift evolution of the dark matter power spectrum $P_{00}(k)$, so if we have an accurate PT model for $P_{00}$ then we should also have the same for $P_{01}$. On large scales it agrees with the linear theory predictions. If we write $P_{00}(k,\tau) = D(\tau)^2P_L(k,\tau)$, we find Kaiser part $P_{01}^{ss} = 2f\mu^2P_{lin}(k)$. On smaller scales we expect the term to deviate from the linear one, just as for $P_{00}(k)$. Using one loop PT we simply need to calculate the derivatives of growth factor $\dot{D}(\tau) = f(\tau)\mathcal{H}D(\tau)$, and from equation 5.29 we get

$$P_{\delta\dot{\delta}}(\mathbf{k},\tau) = f(\tau)\mathcal{H}D^2(\tau)\left[P_{\delta\delta}^{(1,1)}(k) + 2D^2(\tau)\left(P_{\delta\delta}^{(2,2)}(k) + 2P_{\delta\delta}^{(1,3)}(k)\right)\right]. \tag{5.42}$$

Finely, plugging that in equation 5.41 we get

$$P_{01}^{ss}(\mathbf{k}) = 2f(\tau)D^2(\tau)\mu^2\left[P_L(k) + 4D^2(\tau)\left(I_{00}(k) + 3k^2J_{00}(k)P_L(k)\right)\right]. \tag{5.43}$$

After some integral transformations and calculations it can be shown that this result is equivalent to the on in equation 5.38. Obtained $P_{01}^{ss}$ results are presented in Figure 5.2. We show the one loop PT results, along with semi-fitting method [34] based on power spectrum in Zel'dovich approximation, and simulation measurements. The power spectra are now divided by second term in Kaiser formula where no-wiggle linear power spectrum has been used.

### 5.3.3 $P_{11}$

The next term we are to consider is the autocorrelation of momentum density $T_\parallel^1(\mathbf{k})$ field. In this case scalar ($m = 0$) $T_1^{1,0}(k)$ correlates with itself, and the vector ($m = \pm 1$) components $T_1^{1,\pm1}(k)$ also correlate with itself, so both components of momentum contribute,

$$P_{11}(k) = P_{1,1}^{1,1,0}(k)\left[P_1^0(\mu)\right]^2 + P_{1,1}^{1,1,1}(k)\left[P_1^1(\mu)\right]^2. \tag{5.44}$$

Contributions to redshift space power spectrum is then given with

$$P_{11}^{ss}(k) = \mathcal{H}^{-2}k^2\mu^2\left[P_{1,1}^{1,1,0}(k)\mu^2 + P_{1,1}^{1,1,1}(k)(1-\mu^2)\right]. \tag{5.45}$$

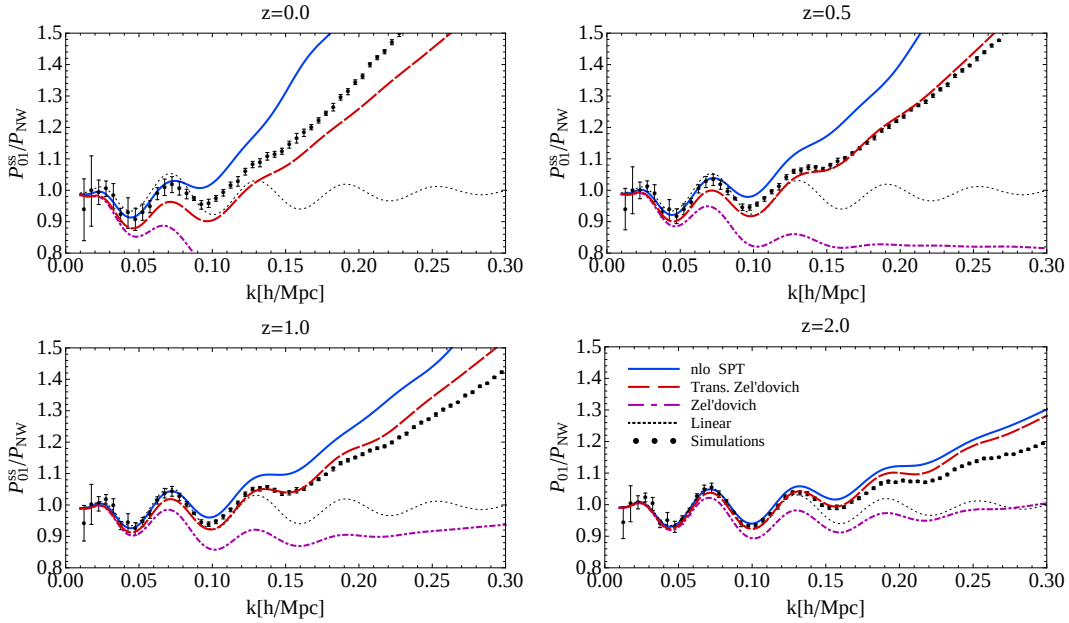


**Figure 5.2:** $k$-dependence of $P^{ss}_{01}$ term of redshift power spectrum is plotted at four redshifts $z = 0.0,\ 0.5,\ 1.0$ and $2.0$. This term has simple $\mu^2$ dependence in all nonlinear orders. Here we show linear Kaiser result (black, dotted), one loop PT (blue, solid), corrected Zel'dovich (red, dashed) model from [34], simple Zel'dovich (magenta, dot-dashed), and simulation measurements (black dots). The error bars show the variance among realizations in simulations. The power spectra are divided by second, no-wiggle, term of Kaiser formula to reduce the dynamic range.

The scalar part is the autocorrelation of the of the momentum that contributes to the continuity equation 5.39. In linear PT only the scalar contribution in non-zero and $P^{1,1,0}_{1,1}(k) = f^2 P_L(k)$, which is the last term in Kaiser formula. There is another contribution to both $\mu^2$ and $\mu^4$ terms from the vector part of momentum correlator $P^{1,1,1}_{1,1}(k) \propto \left\langle |T^{1,1}_1(k)|^2 \right\rangle$, which comes in at the second order in power spectrum, and can be computed using one loop PT. This vector part is often called the vorticity part of the momentum, because vorticity of momentum does not vanish, even if vorticity of velocity vanishes for a single streamed fluid [36]. From equation 5.45 can be seen that this term always adds power to $\mu^2$ term and subtracts it in $\mu^4$ term, but is combined with a positive contribution from the scalar part in $\mu^4$ term.

Now using expressions 5.25 we can straightforwardly expand the correlator in density $\delta$ and velocity divergence $\theta$ fields. In terms of power spectra we have

$$P_{11}(\mathbf{k}) = \frac{\mu^2}{k^2} P_{\theta\theta}(\mathbf{k}) + 2\frac{\mu}{k} B_{11}(\mathbf{k}) + C_{11}(\mathbf{k}), \tag{5.46}$$

where we have introduced:

$$\begin{aligned}
(2\pi)^3 P_{\theta\theta}(\mathbf{k})\delta^D(\mathbf{k}-\mathbf{k}') &= \left\langle \theta(\mathbf{k}) | \theta^*(\mathbf{k}') \right\rangle, \\
(2\pi)^3 B_{11}(\mathbf{k})\delta^D(\mathbf{k}-\mathbf{k}') &= \int \frac{d^3q}{(2\pi)^3} \frac{q_\parallel}{q^2} \left\langle \theta(\mathbf{q})\delta(\mathbf{k}-\mathbf{q}) | \theta^*(\mathbf{k}') \right\rangle, \\
(2\pi)^3 C_{11}(\mathbf{k})\delta^D(\mathbf{k}-\mathbf{k}') &= \int \frac{d^3q}{(2\pi)^3} \frac{d^3q'}{(2\pi)^3} \frac{q_\parallel}{q^2} \frac{q'_\parallel}{q'^2} \left\langle \theta(\mathbf{q})\delta(\mathbf{k}-\mathbf{q}) | \theta^*(\mathbf{q}')\delta^*(\mathbf{k}'-\mathbf{q}') \right\rangle.
\end{aligned} \tag{5.47}$$

Using one loop PT to evaluate these power spectra. First term gives familiar velocity divergence autocorrelation

$$P_{\theta\theta}(\mathbf{k},\tau) = D(\tau)^2 P^{(1,1)}_{\theta\theta}(\mathbf{k}) + D^4(\tau)\left(P^{(2,2)}_{\theta\theta}(\mathbf{k}) + 2P^{(1,3)}_{\theta\theta}(\mathbf{k})\right), \tag{5.48}$$

where $P_{\theta\theta}^{(1,1)}(k)$ is the linear power spectrum $(f\mathcal{H})^2 P_L(k)$ and rest is one loop contribution to velocity divergence power spectrum $P_{\theta\theta}(k)$,

$$\begin{aligned} P_{\theta\theta}^{(2,2)}(k) &= 2(f\mathcal{H})^2 \int \frac{d^3q}{(2\pi)^3} P_L(q) P_L\left(|\mathbf{k}-\mathbf{q}|\right) \left[G_2^{(s)}\left(\mathbf{q}, \mathbf{k}-\mathbf{q}\right)\right]^2 \\ &= 2(f\mathcal{H})^2 I_{11}(k) \\ P_{\theta\theta}^{(1,3)}(k) &= 3(f\mathcal{H})^2 P_L(k) \int \frac{d^3q}{(2\pi)^3} P_L(q) G_3^{(s)}\left(\mathbf{k}, \mathbf{q}, -\mathbf{q}\right) \\ &= 3(f\mathcal{H})^2 k^2 P_L(k) J_{11}(k) \end{aligned} \tag{5.49}$$

Second term can be expanded in the fields to the second order; schematically we have

$$\langle \theta\delta\theta \rangle = \left\langle \theta^{(2)}\delta^{(1)}\theta^{(1)} \right\rangle + \left\langle \theta^{(1)}\delta^{(2)}\theta^{(1)} \right\rangle + \left\langle \theta^{(1)}\delta^{(1)}\theta^{(2)} \right\rangle .$$

This gives in terms of the power spectrum $B_{11}(\mathbf{k})$

$$B_{11}(\mathbf{k}, \tau) = D^4(\tau) \left( B_{11}^{(211)}(\mathbf{k}) + B_{11}^{(112)}(\mathbf{k}) + B_{11}^{(112)}(\mathbf{k}) \right). \tag{5.50}$$

where contributing terms are

$$\begin{aligned} B_{11}^{(211)}(\mathbf{k}) &= 2(f\mathcal{H})^2 P_L(\mathbf{k}) \int \frac{d^3q}{(2\pi)^3} \frac{(\mathbf{k}-\mathbf{q})_\parallel}{(\mathbf{k}-\mathbf{q})^2} G_2^{(s)}(\mathbf{k}, -\mathbf{q}) P_L(\mathbf{q}) \\ &= 2(f\mathcal{H})^2 \mu k P_L(k) \left[ 3J_{10}(k) + \frac{1}{2}\left( \sigma_v^2 + \frac{\sigma_0^2}{3k^2} \right) \right], \\ B_{11}^{(121)}(\mathbf{k}) &= 2(f\mathcal{H})^2 P_L(\mathbf{k}) \int \frac{d^3q}{(2\pi)^3} \frac{q_\parallel}{q^2} F_2^{(s)}(\mathbf{k}, -\mathbf{q}) P_L(\mathbf{q}) \\ &= -(f\mathcal{H})^2 \mu k P_L(k) \left( \sigma_v^2 + \frac{\sigma_0^2}{3k^2} \right), \\ B_{11}^{(112)}(\mathbf{k}) &= 2(f\mathcal{H})^2 \int \frac{d^3q}{(2\pi)^3} \frac{q_\parallel}{q^2} G_2^{(s)}(\mathbf{k}-\mathbf{q}, \mathbf{q}) P_L(\mathbf{k}-\mathbf{q}) P_L(\mathbf{q}) \\ &= 2(f\mathcal{H})^2 \frac{\mu}{k} I_{22}(k). \end{aligned} \tag{5.51}$$

Similarly, for the last term in equation 5.46, we have

$$\begin{aligned} C_{11}^{(1111)}(\mathbf{k}) &= (f\mathcal{H})^2 \int \frac{d^3q}{(2\pi)^3} \frac{q_\parallel}{q^2} \left( \frac{q_\parallel}{q^2} + \frac{(\mathbf{k}-\mathbf{q})_\parallel}{(\mathbf{k}-\mathbf{q})^2} \right) P_L(\mathbf{k}-\mathbf{q}) P_L(\mathbf{q}) \\ &= (f\mathcal{H})^2 k^{-2} \left( I_{31}(k) + \mu^2 I_{13}(k) \right). \end{aligned} \tag{5.52}$$

Combining all that, we can write the contribution to redshift space power spectrum $P^{ss}$ from $P_{11}$ term

$$\begin{aligned} P_{11}^{ss}(\mathbf{k}) = \left( \frac{k\mu}{\mathcal{H}} \right)^2 P_{11}(\mathbf{k}) &= f^2(\tau) D^2(\tau) \mu^2 \left( \mu^2 P_L(k) + D^2(\tau) I_{31}(k) \right) \\ &+ f^2(\tau) D^4(\tau) \mu^4 \left[ 2I_{11}(k) + 4I_{22}(k) + I_{13}(k) + 6k^2 \big( J_{11}(k) + 2J_{10}(k) \big) P_L(k) \right]. \end{aligned} \tag{5.53}$$

As can be seen we obtained $\mu^2$ and $\mu^4$ angular dependence from this term, as was argued from symmetry consideration in [29]. Vector contribution can be identified as the part multiplying $\mu^2$ [29].

On the other hand, we could have started directly from equation 5.44. If we chose to work in the frame where $z \parallel \mathbf{k}$ one can write the decomposition 5.16 of momentum density $T_\parallel^1(\mathbf{k}) = p_\parallel(\mathbf{k}) = \hat{r} \cdot \mathbf{p}(\mathbf{k}) = p_s \cos\theta + p_v \sin\theta \cos\phi$, where we have chosen, without loss of generality,

for $\hat{r}$ to be in $x-z$ plane, and $p_s$ and $p_v$ represent scalar and vector part of decomposition, respectively. After averaging over $\phi$ angle, this enables us to write $P_{1,1}^{1,1,0} = P_{p_s,p_s}$ and $P_{1,1}^{1,1,1} = P_{p_v,p_v}$. Just as before, scalar part can be determined directly from continuity equation 5.39. We can again use one loop PT to evaluate scalar and vector contributions

$$\begin{aligned} P_{p_s,p_s} = k^{-2}P_{\dot{\delta},\dot{\delta}} &= (f\mathcal{H})^2 D(\tau)^2 k^{-2}\left(P_{\delta\delta}^{(1,1)}(\mathbf{k}) + D^2(\tau)\left[4P_{\delta\delta}^{(2,2)}(\mathbf{k}) + 6P_{\delta\delta}^{(1,3)}(\mathbf{k})\right]\right) \\ &= (f\mathcal{H})^2 D(\tau)^2 k^{-2}\left(P_L(k) + D(\tau)^2\left[8I_{00}(k) + 18k^2 J_{00}(k)P_L(k)\right]\right), \\ P_{p_v,p_v} &= (f\mathcal{H})^2 \int \frac{d^3q}{(2\pi)^3}\frac{\left|\hat{k}\times\mathbf{q}\right|^2}{q^4}\frac{k^2 - 2\mathbf{k}\cdot\mathbf{q}}{(\mathbf{k}-\mathbf{q})^2}P_L(k)P_L(|\mathbf{k}-\mathbf{q}|) \\ &= (f\mathcal{H})^2 D^4(\tau)k^{-2}I_{31}(k). \end{aligned} \tag{5.54}$$

Thus, the contribution to the total red shift power spectrum from $P_{11}$ term is

$$P_{11}^{ss} = f^2(\tau)D^2(\tau)\mu^2\left[\mu^2 P_L(k) + \mu^2 D(\tau)^2\big(8I_{00}(k) + 18J_{00}(k)P_L(k)\big) + (1-\mu^2)D(\tau)^2 I_{31}(k)\right]. \tag{5.55}$$

Again, after some coordinate transformations and algebra it can be shown that this result is equivalent to the one we obtained earlier in equation 5.53.
In order to improve our prediction for the vector part we can take into consideration the most relevant higher order loop contributions. Starting from definition of $C_{11}$ (equation 5.47), which gives raise to the vector part of $P_{11}$, and generalizing our one loop prediction in equation 5.52 we can write

$$C_{11}(\mathbf{k}) = \int \frac{d^3q}{(2\pi)^3}\,\frac{q_\parallel^2}{q^4}P_{\theta\theta}(\mathbf{q})P_{\delta\delta}(\mathbf{k}-\mathbf{q}) + \int \frac{d^3q}{(2\pi)^3}\,\frac{q_\parallel}{q^2}\frac{(\mathbf{k}-\mathbf{q})_\parallel}{(\mathbf{k}-\mathbf{q})^2}P_{\delta\theta}(\mathbf{q})P_{\delta\theta}(\mathbf{k}-\mathbf{q}). \tag{5.56}$$

In low $k$ limit this gives back the previous result from equation 5.52, and in high $k$ limit the first term dominates what is giving $(f\mathcal{H}D)^2 P_{00}(k)\sigma_v^2$ for the vector part.
In figure 5.3 we show scalar part of $P_{11}^{ss}$ which comes from scalar contributions. It has a simple $\mu^4$ angular dependence, and corresponds to the third Kaiser term. We divide the plots by this Kaiser limit, using the no-wiggle linear power spectrum. One loop PT results are compared to the simulation measurements. We see that PT is quite successful in reproducing the nonlinear evolution of this term.
In figure 5.4 we show the vector $\mu^2(1-\mu^2)$ part. We see that one loop PT is successful in reproducing the simulations for $k < 0.2h/Mpc$ (the disagreement for $k < 0.03h/Mpc$ is likely numerical), and adding two loop corrections increases these rage to larger $k$. We also see that this vector contribution is considerably smaller than the scalar part for $\mu = 1$ for most of the $k$-range shown here, becoming comparable only at $k \sim 0.5h/Mpc$. However, because this vector term scales as $\mu^2$ while the linear scalar term scales as $\mu^4$, the vector terms always dominates for sufficiently small $\mu$. So for $\mu = 0.1$ the nonlinear vector part exceeds linear scalar part already at $k \sim 0.05h/Mpc$.

### 5.3.4 $P_{02}$

At orders higher than $P_{11}(k)$ there are no linear contributions, hence these terms are usually not of interest for extracting the cosmological information. However, these terms are known to be important on surprisingly large scales. These terms have usually been modeled phenomenologically in terms of adopting a simple functional form for $k$ and $\mu$ dependence and are related to the so called Fingers-of-God (FoG) effect. We begin with the dominant $P_{02}$ term, which, as we will see, is the last term to contribute to $\mu^2$ dependence.
We correlate the scalar density filed $T_0^{0,0} = \delta$ with the tensor field $T_l^{2,m}$. Since scalars only correlate with scalars, there are only two different terms that contribute [29],

$$P_{02}(\mathbf{k}) = P_{0,0}^{0,2,0}(k)\left[P_0^0(\mu)\right]^2 + P_{0,2}^{0,2,0}(k)P_0^0(\mu)P_2^0(\mu). \tag{5.57}$$

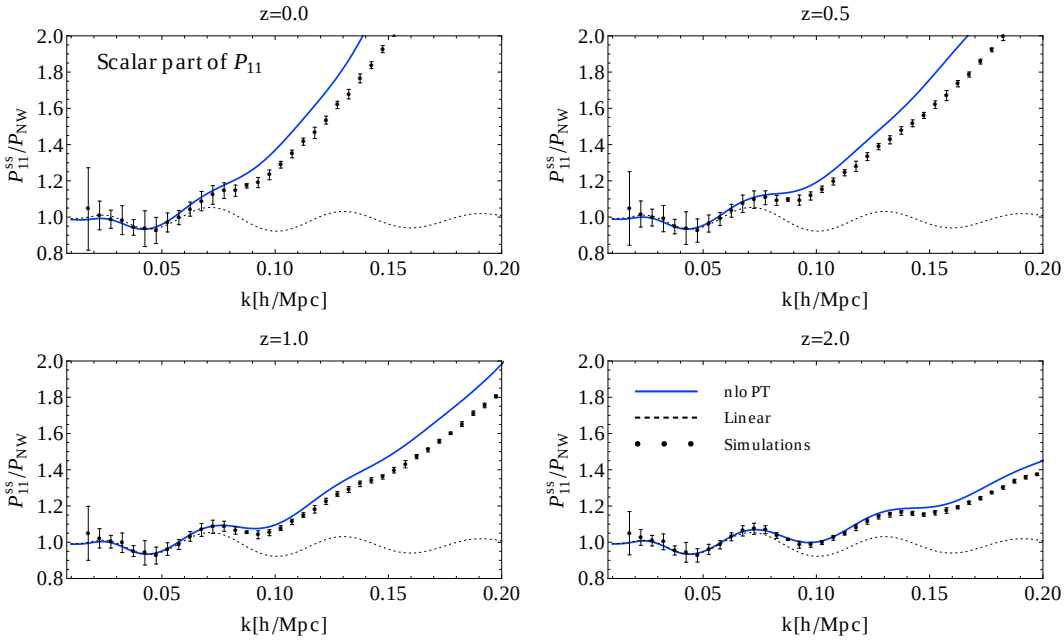


**Figure 5.3:** $k$-dependence of the scalar part of $P_{11}^{ss}$ term. Power spectrum is plotted at four redshifts $z = 0.0,\ 0.5,\ 1.0$ and 2.0. This term has a simple $\mu^4$ dependence. Here we show linear Kaiser (black, dotted) and one loop PT (blue, solid) result, and compare it to simulation measurements (black dots). The error bars show the variance among realizations in simulations. The power spectra are divided by the no-wiggle linear term.

In terms of the contribution to the redshift space power spectrum this gives

$$P_{02}^{ss} = -\left(\frac{k\mu}{\mathcal{H}}\right)^2 \left[P_{0,0}^{0,2,0}(k) + \frac{1}{2}P_{0,2}^{0,2,0}(k)(3\mu^2-1)\right]. \tag{5.58}$$

The first term is the correlation between the isotropic part of the mass weighted square of velocity, i.e. the energy density $T_0^{2,0} = (1+\delta)v^2$, and the density field $T_0^{0,0} = \delta$, and the second term comes from the scalar part of the anisotropic stress $T_2^{2,0}$, correlated with the density $T_0^{0,0} = \delta$.

Before using PT to model these terms let us consider what we can expect from physical grounds. As argued in [29], in systems with a large rms velocity, the first, isotropic part $P_{0,0}^{0,2,0}$ should scale as $P_{00}(k)\sigma^2$, where $\sigma^2$ has units of velocity square and includes the small scale velocity dispersion generated inside nonlinear halos. Some of this contribution cannot be modeled with simple fluid based PT, since not all of velocity dispersion is captured in this approach. As a result, we should not even hope that PT can be reliable for this term: we will need to add an extra contribution to account for the small scale velocity dispersion. Expanding the fields we can write the contributing terms as following

$$P_{02}(\mathbf{k},\tau) = -D^4(\tau)(A_{02}(\mathbf{k}) + B_{02}(\mathbf{k})), \tag{5.59}$$

where we have

$$\begin{aligned}
(2\pi)^3 A_{02}(\mathbf{k})\delta^D(\mathbf{k}-\mathbf{k}') &= \int \frac{d^3q}{(2\pi)^3}\,\frac{q_\parallel}{q^2}\frac{(\mathbf{k}'-\mathbf{q})_\parallel}{(\mathbf{k}'-\mathbf{q})^2}\left\langle\delta(\mathbf{k})|\theta^*(\mathbf{q})\theta^*(\mathbf{k}'-\mathbf{q})\right\rangle, \\
(2\pi)^3 B_{02}(\mathbf{k})\delta^D(\mathbf{k}-\mathbf{k}') &= \int \frac{d^3q}{(2\pi)^3}\frac{d^3q'}{(2\pi)^3}\,\frac{q_\parallel}{q^2}\frac{q'_\parallel}{q'^2}\left\langle\delta(\mathbf{k})|\theta^*(\mathbf{q})\theta^*(\mathbf{q}')\delta^*(\mathbf{k}'-\mathbf{q}-\mathbf{q}')\right\rangle.
\end{aligned} \tag{5.60}$$

Using the one loop PT to evaluate this terms we expand these terms in the following way

$$A_{02}(\mathbf{k}) = A_{02}^{(211)}(\mathbf{k}) + A_{02}^{(121)}(\mathbf{k}) + A_{02}^{(112)}(\mathbf{k}),$$

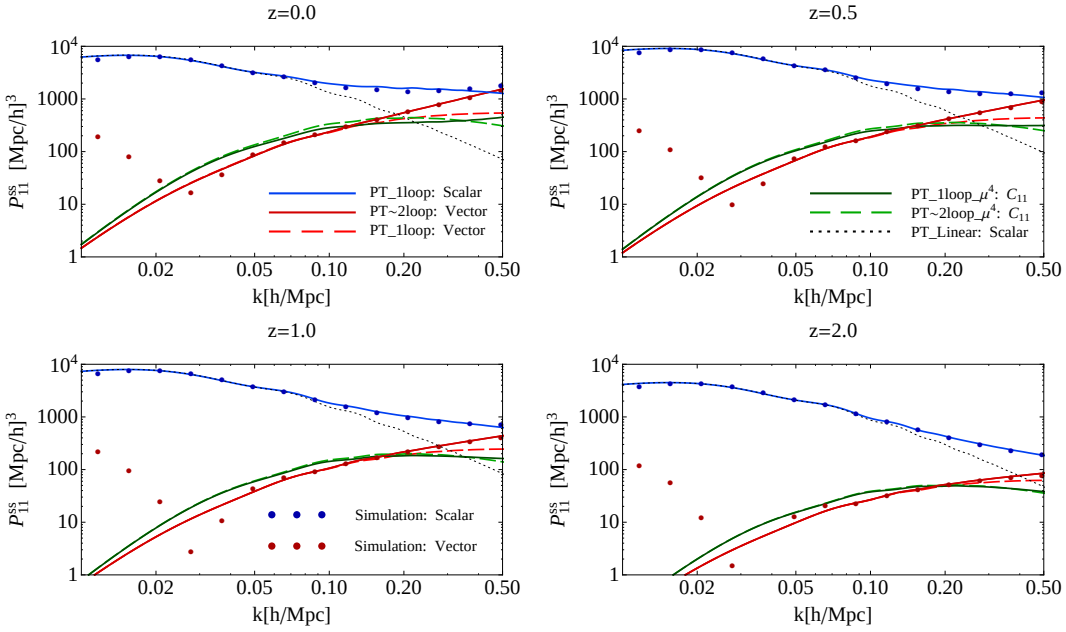


**Figure 5.4:** $k$-dependence of scalar and vector part of $P_{11}^{ss}$ term of the redshift power spectrum is plotted at four redshifts $z = 0.0,\ 0.5,\ 1.0$ and $2.0$, assuming $\mu = 1$. Scalar part has simple $\mu^4$ angular dependence while the vector part has $\mu^2(1-\mu^2)$ angular dependence at all (nonlinear) orders. We show linear/Kaiser result (black, dotted), one loop PT result for scalar part (blue, solid), one loop PT result for vector part (lighter red, dashed), relevant part of two loop PT for vector part (red, solid) and simulations for scalar (blue points) and vector (red points) part. We also show scalar contributions of $C_{11}$ term at one (lighter green, dashed) and two (green, solid) loop order.

$$B_{02}(\mathbf{k}) = B_{02}^{(1111)}(\mathbf{k}), \tag{5.61}$$

which after some computation give

$$\begin{aligned}
A_{02}^{(211)}(\mathbf{k}) &= 2(f\mathcal{H})^2 \int \frac{d^3q}{(2\pi)^3}\,\frac{q_\parallel}{q^2}\frac{(\mathbf{k}-\mathbf{q})_\parallel}{(\mathbf{k}-\mathbf{q})^2}F_2^{(s)}(\mathbf{q},\mathbf{k}-\mathbf{q})P_L(\mathbf{q})P_L(\mathbf{k}-\mathbf{q}) \\
&= (f\mathcal{H})^2 k^{-2}\left(I_{02}(k)+\mu^2 I_{20}(k)\right), \\
A_{02}^{(121)}(\mathbf{k}) &= A_{20}^{(112)}(\mathbf{k}) = 2(f\mathcal{H})^2 P_L(k)\int \frac{d^3q}{(2\pi)^3}\,\frac{q_\parallel}{q^2}\frac{(\mathbf{k}-\mathbf{q})_\parallel}{(\mathbf{k}-\mathbf{q})^2}G_2^{(s)}(\mathbf{q},-\mathbf{k})P_L(\mathbf{q}) \\
&= (f\mathcal{H})^2 P_L(k)\left(J_{02}(k)+\mu^2 J_{20}(k)\right), \\
B_{02}^{(1111)}(\mathbf{k}) &= -(f\mathcal{H})^2 P_L(k)\int \frac{d^3q}{(2\pi)^3}\,\frac{q_\parallel^2}{q^4}P_L(\mathbf{q}) \\
&= -(f\mathcal{H})^2 P_L(k)\sigma_v^2.
\end{aligned} \tag{5.62}$$

Putting together all of the above we obtain for the $P_{02}$ contribution to the total redshift power spectrum

$$\begin{aligned}
P_{02}^{ss}(\mathbf{k},\tau) &= -\left(\frac{k\mu}{\mathcal{H}}\right)^2 P_{02}(\mathbf{k}) \\
&= f^2(\tau)D^4(\tau)\mu^2\left[I_{02}(k)+k^2\Big(2J_{02}(k)-\sigma_v^2\Big)P_L(k)+\mu^2\Big(I_{20}(k)+2k^2J_{20}(k)P_L(k)\Big)\right].
\end{aligned} \tag{5.63}$$

As we mentioned above, we have the contribution of form $-\mu^2k^2\sigma^2P_L(k)$, which suppresses the linear power spectrum with a $k^2$ like effect, increasing towards higher $k$. This is the

lowest order FoG term, which we see contributes as $(k\mu)^2$ and so effects the $\mu^2$ term of total $P_{ss}$. Because small scale velocity dispersion effects cannot be modeled by PT, which is restricted to the weakly non-linear regime, we will consider a model where we add to the PT predicted value for velocity dispersion $\sigma_v^2$ the contributions coming from small scales. In the equations above we can then replace $\sigma_v^2 \to \sigma_v^2 + \sigma_{02}^2/(f\mathcal{H}D)^2$, where $\sigma_{02}^2$ is the small scale addition to the velocity dispersion, and which we treat here as a free parameter. List of values used here for these parameters (depending on redshift), is given in the table 5.1, in section 5.3.8. In these section we also consider the explanation of these values using the halo model, see for example [37]. In addition to small scale velocity dispersion model, we also include the most relevant higher order PT terms. If we consider higher order contributions to $\left\langle \delta | \delta v_\parallel^2 \right\rangle$ term we see that it has subsets of diagrams where $\langle\delta|$ is not connected to any of the velocity fields, so we can write $\left\langle \delta | \delta v_\parallel^2 \right\rangle = \langle\delta|\delta\rangle \left\langle v_\parallel^2 \right\rangle$. Formally, in one loop computation only the leading term of this subset contributes in equation 5.62. Collecting these we see that we can model $B_{02}$ term by replacement

$$D^4(\tau)B_{02}(k) = -\left(f\mathcal{H}D^2\right)^2 \sigma_v^2 P_L(k) \;\to -(f\mathcal{H}D)^2\left(\sigma_v^2 + \sigma_{02}^2/(f\mathcal{H}D)^2\right) P_{00}(k,\tau). \quad (5.64)$$

In order to discuss the results let us first rewrite equation 5.63 in form of isotropic and anisotropic part as for $P_{02}$. We have $P_{02}^{ss} = \mu^2\left(P_{02}^{ss,I} + \frac{1}{2}(3\mu^2-1)P_{02}^{ss,A}\right)$, where

$$\begin{aligned} P_{02}^{ss,I}(\mathbf{k},\tau) =& \frac{f^2(\tau)D^4(\tau)}{3}\Big[3I_{02}(k) + I_{20}(k) + 2k^2\big(3J_{02}(k) + J_{20}(k)\big)P_L(k)\Big] \\ & - f^2(\tau)D^2(\tau)k^2\left(\sigma_v^2 + \sigma_{02}^2/(f\mathcal{H}D)^2\right)P_{00}(k,\tau), \\ P_{02}^{ss,A}(\mathbf{k},\tau) =& \frac{2f^2(\tau)D^4(\tau)}{3}\Big[I_{20}(k) + 2k^2 J_{20}(k)P_L(k)\Big]. \end{aligned} \quad (5.65)$$

In figure 5.5 we show isotropic and anisotropic part of the $P_{02}$ contribution to the total redshift power spectrum. All power spectrum contributions are divided by the $(fDk)^2\sigma_v^2 P_L^{\rm nw}(k)$, where we again used the no-wiggle power spectrum. We can see that the contribution to $\mu^2$ is always negative, while the corresponding vector term from $P_{11}$ always adds power and the two partially cancel out [29]. As we see the scalar anisotropic stress-density correlator $P_{0,2}^{0,2,0}$ contributes to the $\mu^2$ angular term, as well as to the $\mu^4$ term. The anisotropic term is reasonably well modeled with PT and has smaller magnitude than the isotropic term, as expected, since the velocity dispersion in virialized objects is essentially isotropic. The isotropic term is poorly modeled with just PT: we need a significant contribution from the small scale velocity dispersion, which can be seen to essentially double the amplitude of this term at low $k$, and far more than that at high $k$. In figure 5.5 we can see that this term helps the model considerably, but of course it has one free parameter.
We can also write this result in powers of $\mu$,

$$\begin{aligned} P_{02}^{ss}[\mu^2] &= f^2(\tau)D^4(\tau)\Big(I_{02}(k) + 2k^2 J_{02}(k)P_L(k)\Big) - f^2(\tau)D^2(\tau)k^2\left(\sigma_v^2 + \sigma_{02}^2/(f\mathcal{H}D)^2\right)P_{00}(k,\tau), \\ &= \bar{P}_{02}^{ss}[\mu^2] - f^2(\tau)D^2(\tau)k^2\left(\sigma_v^2 + \sigma_{02}^2/(f\mathcal{H}D)^2\right)P_{00}(k,\tau), \\ P_{02}^{ss}[\mu^4] &= \bar{P}_{02}^{ss}[\mu^4] = f^2(\tau)D^4(\tau)\Big(I_{20}(k) + 2k^2 J_{20}(k)P_L(k)\Big), \end{aligned} \quad (5.66)$$

where we have implicitly defined $\bar{P}_{02}^{ss}$ by omitting the velocity dispersion part from $P_{02}^{ss}$.

### 5.3.5 $P_{12}$

As we can see the lowest order in $\mu$ with which correlators contribute is the $L + L'$ or $L + L' + 1$. So contributions to $\mu^2$ comes only from terms $P_{01}$, $P_{11}$ and $P_{02}$. The next order in powers of $\mu^2$ will be $\mu^4$ terms. As we have seen $P_{11}$ and $P_{02}$ also have contributions to $\mu^4$, with $P_{11}$ having the linear order term which dominates on large scales.

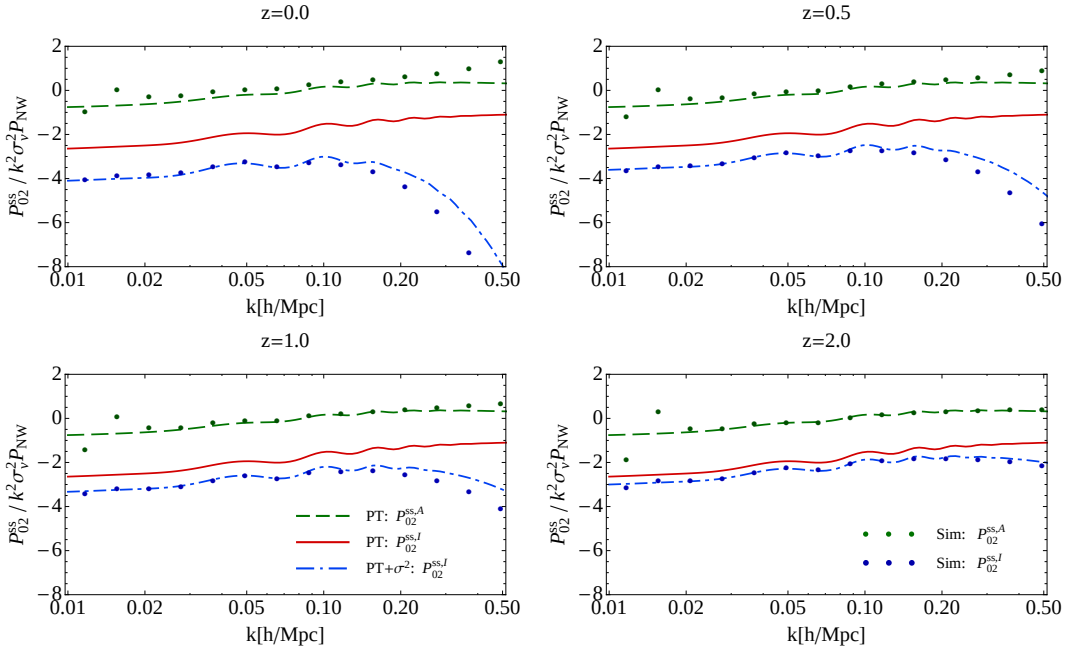


**Figure 5.5:** $k$-dependence of isotropic and anisotropic part of $P_{02}^{ss}$ term of redshift power spectrum is plotted at four redshifts $z = 0.0,\ 0.5,\ 1.0$ and $2.0$. Isotropic part $P_{02}^{ss,I}$, computed in one loop PT (red, solid) is plotted, as well as using the model presented above (blue, dot-dashed). Isotropic part has simple $\mu^2$ angular dependence while the anisotropic part $P_{02}^{ss,A}$ (green, dashed) has $\mu^2(3\mu^2-1)/2$ angular dependence. Simulation measurements (dots) for the corresponding terms are also presented. The power spectra are divided by $k^2\sigma_v^2 P_L^{\rm nw}$ without the wiggles.

Here we correlate the momentum filed $T_l^{1,m}$ with the tensor field $T_l^{2,m}$. Because of rotational invariance we can correlate only scalar to scalar field and vector to vector field

$$P_{12}(\mathbf{k}) = P_{1,0}^{1,2,0}(k)\left[P_0^0(\mu)P_1^0(\mu)\right] + P_{1,2}^{1,2,0}(k)\left[P_1^0(\mu)P_2^0(\mu)\right] + P_{1,2}^{1,2,1}(k)\left[P_1^1(\mu)P_2^1(\mu)\right] \tag{5.67}$$

In terms of the contribution to the redshift space power spectrum this gives

$$P_{12}^{ss}(\mathbf{k}) = -i\left(\frac{k\mu}{\mathcal{H}}\right)^3\left[P_{1,0}^{1,2,0}(k)\mu + \frac{1}{2}P_{1,2}^{1,2,0}(k)\mu(3\mu^2-1) + 3P_{1,2}^{1,2,1}(k)\mu(1-\mu^2)\right]. \tag{5.68}$$

Using the one loop PT we get both $\mu^4$ and $\mu^6$ angular terms, but since there are 3 terms we cannot distinguish between them in equation 5.68. Using equation 5.25 and one loop PT we get

$$P_{12}(\mathbf{k}) = -D^4(\tau)\frac{i}{k^2}\left(k_\parallel A_{12}(\mathbf{k}) + k^2 B_{12}(\mathbf{k}) + k_\parallel C_{12}(\mathbf{k})\right), \tag{5.69}$$

where the contributing terms are

$$\begin{aligned}
(2\pi)^3 A_{12}(\mathbf{k})\delta^D(\mathbf{k}-\mathbf{k}') &= \int \frac{d^3q}{(2\pi)^3}\,\frac{q_\parallel}{q^2}\,\frac{(\mathbf{k}'-\mathbf{q})_\parallel}{(\mathbf{k}'-\mathbf{q})^2}\left\langle\theta(\mathbf{k})|\theta^*(\mathbf{q})\theta^*(\mathbf{k}'-\mathbf{q})\right\rangle,\\
(2\pi)^3 B_{12}(\mathbf{k})\delta^D(\mathbf{k}-\mathbf{k}') &= \int \frac{d^3q\ d^3q'}{(2\pi)^6}\,\frac{q_\parallel}{q^2}\,\frac{q'_\parallel}{q'^2}\,\frac{(\mathbf{k}'-\mathbf{q}')_\parallel}{(\mathbf{k}'-\mathbf{q}')^2}\left\langle\theta(\mathbf{q})\delta(\mathbf{k}-\mathbf{q})|\theta^*(\mathbf{q}')\theta^*(\mathbf{k}'-\mathbf{q}')\right\rangle,\\
(2\pi)^3 C_{12}(\mathbf{k})\delta^D(\mathbf{k}-\mathbf{k}') &= \int \frac{d^3q\ d^3q'}{(2\pi)^6}\,\frac{q_\parallel}{q^2}\,\frac{q'_\parallel}{q'^2}\left\langle\theta(\mathbf{k})|\theta^*(\mathbf{q})\theta^*(\mathbf{q}')\delta^*(\mathbf{k}'-\mathbf{q}-\mathbf{q}')\right\rangle.
\end{aligned} \tag{5.70}$$

The first of these terms we can be expanded further

$$A_{12}(\mathbf{k}) = A_{12}^{(211)}(\mathbf{k}) + A_1^{(121)}(\mathbf{k}) + A_1^{(112)}(\mathbf{k}), \tag{5.71}$$

and computing these terms gives;

$$\begin{aligned}
A_{12}^{(211)}(\mathbf{k}) &= -2(f\mathcal{H})^3 \int \frac{d^3q}{(2\pi)^3}\ \frac{q_\parallel}{q^2}\frac{(\mathbf{k}-\mathbf{q})_\parallel}{(\mathbf{k}-\mathbf{q})^2} G_2^{(s)}(\mathbf{q},\mathbf{k}-\mathbf{q}) P_L(\mathbf{q}) P_L(\mathbf{k}-\mathbf{q}) \\
&= -(f\mathcal{H})^3 k^{-2}\left(I_{12}(k)+\mu^2 I_{21}(k)\right), \\
A_{12}^{(121)}(\mathbf{k}) &= A_{12}^{(112)}(\mathbf{k}) = -2(f\mathcal{H})^3 P_L(\mathbf{k}) \int \frac{d^3q}{(2\pi)^3}\ \frac{q_\parallel}{q^2}\frac{(\mathbf{k}-\mathbf{q})_\parallel}{(\mathbf{k}-\mathbf{q})^2} G_2^{(s)}(\mathbf{q},-\mathbf{k}) P_L(\mathbf{q}) \\
&= -(f\mathcal{H})^3 P_L(\mathbf{k})\left(J_{02}(k)+\mu^2 J_{20}(k)\right), \\
B_{12}(\mathbf{k}) &= -2(f\mathcal{H})^3 \int \frac{d^3q}{(2\pi)^3}\ \frac{q_\parallel^2}{q^4}\frac{(\mathbf{k}-\mathbf{q})_\parallel}{(\mathbf{k}-\mathbf{q})^2} P_L(\mathbf{q}) P_L(\mathbf{k}-\mathbf{q}) \\
&= (f\mathcal{H})^3 \mu k^{-3}\left(I_{03}(k)+\mu^2 I_{30}(k)\right), \\
C_{12}(\mathbf{k}) &= (f\mathcal{H})^3 P_L(\mathbf{k}) \int \frac{d^3q}{(2\pi)^3}\ \frac{q_\parallel^2}{q^4} P_L(\mathbf{q}), \\
&= (f\mathcal{H})^3 \sigma_v^2 P_L(\mathbf{k}).
\end{aligned} \tag{5.72}$$

All this gives us the contribution to total redshift space power spectrum

$$\begin{aligned}
P_{12}^{ss}(\mathbf{k},\tau) = -i\left(\frac{k\mu}{\mathcal{H}}\right)^3 P_{12}(\mathbf{k},\tau) =& f(\tau)^3 D(\tau)^4 \mu^4 \Big[ I_{12}(k) - I_{03}(k) + 2k^2 J_{02}(k) P_L(k) - k^2\sigma_v^2 P_L(k) \\
&+ \mu^2\Big(I_{21}(k) - I_{30}(k) + 2k^2 J_{20} P_L(k)\Big)\Big].
\end{aligned} \tag{5.73}$$

We can again add the small scale velocity dispersion in by hand, as was done and explained in case of $P_{02}$. Considering the relevant higher order contributions we see that the isotropic part of $\left\langle T_\parallel^1 |\delta v_\parallel^2\right\rangle$ can be modeled by

$$-iD^4(\tau)\frac{\mu}{k} C_{12}(k) = -iD^4(\tau)\frac{\mu}{k}(f\mathcal{H})^3\sigma_v^2 P_L(k) \to -(f\mathcal{H}D)^2\left(\sigma_v^2 + \sigma_{12}^2/(f\mathcal{H}D)^2\right) P_{01}(\mathbf{k},\tau),$$

where we again treat small scale velocity dispersion $\sigma_{12}^2$ as a free parameter with values for different redshifts given in table 5.1. These values are the same as for $P_{02}$ case, and the reasons and explanation in term of halo model is given in section 5.3.8.
As mentioned earlier, since we have only $\mu^4$ and $\mu^6$ angular dependence we can not determine all three terms in equation 5.68 separately. Let us instead separate the angular dependences itself and collect the terms

$$\begin{aligned}
P_{12}^{ss}\left[\mu^4\right] &= \left[P_{12}^{ss}\right]_{1,0}^{1,2,0} - \frac{1}{2}\left(\left[P_{12}^{ss}\right]_{1,2}^{1,2,0} - 6\left[P_{12}^{ss}\right]_{1,2}^{1,2,1}\right) \\
&= f(\tau)^3 D(\tau)^4\Big[I_{12}(k) - I_{03}(k) + 2k^2 J_{02}(k) P_L(k)\Big] \\
&\quad - \frac{1}{2} f(\tau)^2 D(\tau)^2 k^2\left(\sigma_v^2 + \sigma_{12}^2/(f\mathcal{H}D)^2\right) P_{01}^{ss}(k,\tau), \\
&= \bar{P}_{12}^{ss}\left[\mu^4\right] - \frac{1}{2} f(\tau)^2 D(\tau)^2 k^2\left(\sigma_v^2 + \sigma_{12}^2/(f\mathcal{H}D)^2\right) P_{01}^{ss}(k,\tau) \\
P_{12}^{ss}\left[\mu^6\right] &= \bar{P}_{12}^{ss}\left[\mu^6\right] = \frac{3}{2}\left(\left[P_{12}^{ss}\right]_{1,2}^{1,2,0} - 2\left[P_{12}^{ss}\right]_{1,2}^{1,2,1}\right) \\
&= f(\tau)^3 D(\tau)^4\Big[I_{21}(k) - I_{30}(k) + 2k^2 J_{20} P_L(k)\Big],
\end{aligned} \tag{5.74}$$

where we again implicitly define $\bar{P}_{12}^{ss}$, by omitting the velocity dispersion part.
In figure 5.6 we show $P_{12}^{ss}\left[\mu^4\right]$ and $P_{12}^{ss}\left[\mu^6\right]$ parts to the total redshift power spectrum. Power spectrum contributions are divided by the $(fDk)^2\sigma^2 P_L^{\rm nw}(k)$, where we again used no-wiggle power spectrum.

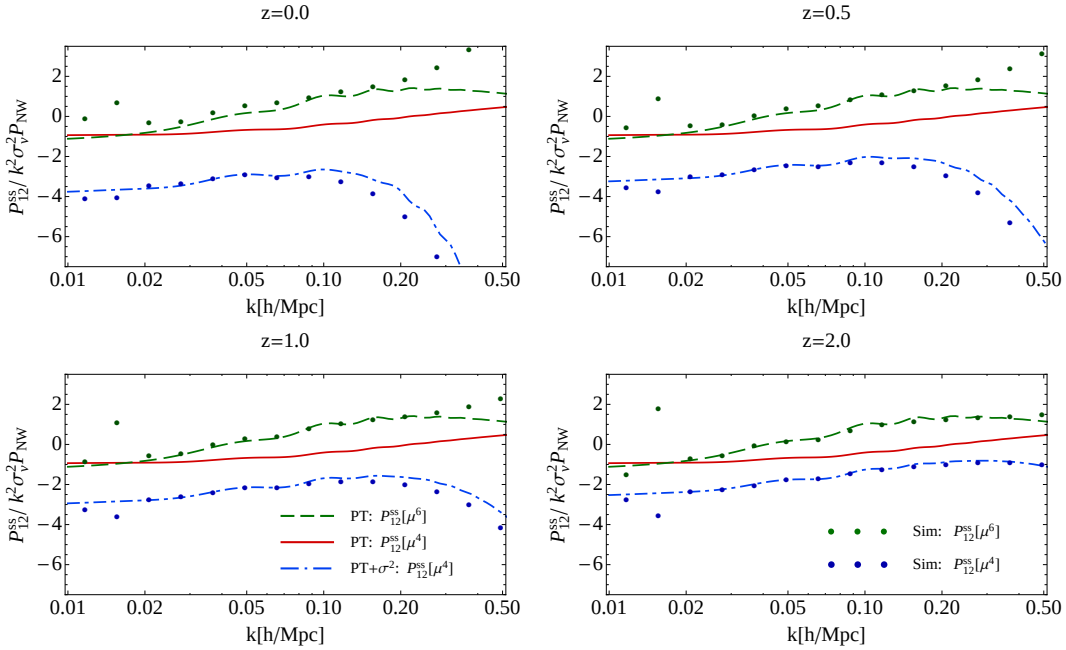


**Figure 5.6:** $k$-dependence of $\mu^4$ and $\mu^6$ part of $P_{12}^{ss}$ term of redshift power spectrum is plotted at four redshifts, $z = 0.0,\ 0.5,\ 1.0$ and $2.0$. $\mu^4$ part $P_{02}^{ss}[\mu^4]$ is computed in one loop PT (red, solid) regime, and using model presented above (blue, dot-dashed). We show $\mu^6$ part $P_{02}^{ss}[\mu^6]$ computed in one loop PT (green, dashed), and simulation measurements (dots) for the corresponding terms. All power spectra are divided by $k^2\sigma_v^2 P_L^{\rm nw}$ without the wiggles.

### 5.3.6 $P_{22}$

Next we consider correlator of tensor $T_l^{2,m}$ field with itself. This term will give $\mu^4$, $\mu^6$ and $\mu^8$ contributions. One loop PT gives first order contributions to all of these angular terms. From the expansion of power spectrum 5.21 we can see that the constant contribution to $P_{22}$ is coming from the scalar term, $P_{0,0}^{2,2,0}$ and partially from $P_{0,2}^{2,2,0}$ and $P_{2,2}^{2,2,0}$. This will give $\mu^4$ as the lowest order contribution to the total $P_{22}^{ss}$, and all of the other terms will come as $\mu^6$, $\mu^8$. Let us now assess these contributions using one loop PT

$$\begin{aligned}\bar{P}_{22}(\mathbf{k},\tau) &= 2(f\mathcal{H}D)^4 \int \frac{d^3q}{(2\pi)^3} \left[\frac{q_\parallel}{q^2}\frac{(\mathbf{k}-\mathbf{q})_\parallel}{(\mathbf{k}-\mathbf{q})^2}\right]^2 P_L(\mathbf{q})P_L(\mathbf{k}-\mathbf{q}) \\ &= (f\mathcal{H}D)^4 \frac{1}{4}k^{-4}\Big(I_{23}(k) + 2\mu^2 I_{32}(k) + \mu^4 I_{33}(k)\Big), \end{aligned} \tag{5.75}$$

which gives rise to the total red shift power spectrum contribution

$$P_{22}^{ss}(\mathbf{k},\tau) = \frac{1}{4}\left(\frac{k\mu}{\mathcal{H}}\right)^4 \bar{P}_{22}(\mathbf{k},\tau) = \frac{1}{16}f^4(\tau)D^4(\tau)\mu^4\Big(I_{23}(k)+2\mu^2 I_{32}(k)+\mu^4 I_{33}(k)\Big). \tag{5.76}$$

These are the leading order contributions to the angular dependence of this term. Now let us also investigate the most important contributions from the higher orders. For that purpose let us write the full correlator in terms of the density and velocity fields

$$\left\langle T_\parallel^2 \left| T_\parallel^2 \right.\right\rangle = \left\langle v_\parallel^2 \left| v_\parallel^2 \right.\right\rangle + 2\left\langle v_\parallel^2 \left| \delta v_\parallel^2 \right.\right\rangle + \left\langle \delta v_\parallel^2 \left| \delta v_\parallel^2 \right.\right\rangle. \tag{5.77}$$

In equation 5.76 we have considered only the first of these three terms, but we should also include some of the most important contributions from the remaining terms. From two loop considerations first we improve the first term 5.75 by exchanging linear power spectrum $P_L$

with one loop $P_{\theta\theta}$. The most important contributions of the other two terms can be modeled as

$$\left\langle v_\parallel^2 \left| \delta v_\parallel^2 \right\rangle \sim (f\mathcal{H}D)^2 \sigma_v^2 \bar{P}_{02},$$
$$\left\langle \delta v_\parallel^2 \left| \delta v_\parallel^2 \right\rangle \sim (f\mathcal{H}D)^4 (\sigma_v^2)^2 P_{00} + \bar{P}_{22} \circ P_{00}.$$

These are of course not the only higher order term, but after a detailed analysis these terms turn out to be the most relevant and the rest can be neglected. We can again include the small scale velocity dispersion extending $\sigma_v^2 \to \sigma_v^2 + \sigma_{22}^2/(f\mathcal{H}D)^2$ as we did previously for $P_{02}$ and $P_{12}$. Combining all we obtain a model

$$\begin{aligned} P_{22}(k,\mu) =& \bar{P}_{22}(k,\mu) - 2(f\mathcal{H}D)^2 \left(\sigma_v^2 + \sigma_{22}^2/(f\mathcal{H}D)^2\right) \bar{P}_{02}(k,\mu) \\ &+ (f\mathcal{H}D)^4 \left(\sigma_v^2 + \sigma_{22}^2/(f\mathcal{H}D)^2\right)^2 P_{00}(k) + (\bar{P}_{22} \circ P_{00})(k). \end{aligned} \tag{5.78}$$

In high $k$ limit last (convolution) term corresponds to $2(f\mathcal{H}D)^4 \sigma_v^4 P_{00}(k)$. In figure 5.7 we show the individual angular contributions for one loop PT calculus and for the improved model suggested above, and compare them to simulation measurements. We see that using the proposed model improves results in comparison to the one loop PT contributions, but still only qualitatively agrees with the simulations. One would find much better agreement if not imposing $\sigma_{22} = \sigma_{02}$, i.e. with more free parameters. We mention that most of the correction to the $\mu^4$ term comes from the isotropic modeling of the last $\left\langle \delta v_\parallel^2 \left| \delta v_\parallel^2 \right\rangle \right.$ terms. Term $\left\langle v_\parallel^2 \left| \delta v_\parallel^2 \right\rangle \right.$ also contributes to $\mu^4$ but less than the previous term. Corrections to the $\mu^6$ come from the angular dependency of $A_{02}$ term and we see that it can explain the change of sign and scale growth trends. The additional terms do not affect the $\mu^8$ term, which is well predicted (at least relative to $\mu^4$ and $\mu^6$) with two loop PT model of first term.

### 5.3.7 $P_{03}$, $P_{13}$ and $P_{04}$

Our goal is to consider all terms at the $\mu^4$ order. There are 3 left. First we consider terms $P_{03}$ and $P_{13}$. We correlate overdensity field or momentum field with rank three tensor field $T_\parallel^3(\mathbf{x})$. Angular decomposition for $P_{03}$ is relatively simple since it has only scalar contributions, but $P_{13}$ has scalar and vector contributions. Using the angular expansion we get the following angular dependence

$$\begin{aligned} P_{03}(\mathbf{k}) &= P_{0,1}^{0,3,0}(k)\mu + P_{0,3}^{0,3,0}(k)\frac{1}{2}\mu\left(5\mu^2 - 3\right), \\ P_{13}(\mathbf{k}) &= P_{1,1}^{1,3,0}(k)\mu^2 + P_{1,1}^{1,3,1}(k)\left(1-\mu^2\right) + P_{1,3}^{1,3,0}(k)\frac{1}{2}\mu^2\left(5\mu^2-3\right) - P_{1,3}^{1,3,1}(k)\frac{3}{2}\left(5\mu^4 - 6\mu^2 + 1\right). \end{aligned} \tag{5.79}$$

In one loop PT these terms are

$$\begin{aligned} P_{03}(\mathbf{k}) &= i3(f\mathcal{H})^3 D^4(\tau)\mu k^{-1} P_L(k) \int \frac{d^3q}{(2\pi)^3} \left(\frac{q_\parallel}{q^2}\right)^2 P_L(q) \\ &= i3(f\mathcal{H})^3 D^4(\tau)\mu k^{-1} P_L(k)\sigma_v^2, \\ P_{13}(\mathbf{k}) &= 3(f\mathcal{H}D(\tau))^4 \mu^2 k^{-2} P_L(k) \int \frac{d^3q}{(2\pi)^3} \left(\frac{q_\parallel}{q^2}\right)^2 P_L(q) \\ &= 3(f\mathcal{H})^4 D^4(\tau)\mu^2 k^{-2} P_L(k)\sigma_v^2. \end{aligned} \tag{5.80}$$

From angular decomposition of $P_{03}$ we have scalar terms, $P_{0,1}^{0,3,0}$ and $P_{0,3}^{0,3,0}$, contributing with angular dependence $\mu^4$ and $\mu^6$. One could evaluate these terms in PT, but at least two loop order is required for $\mu^6$, since in one loop order gives just $\mu^4$ dependence. For $P_{13}$

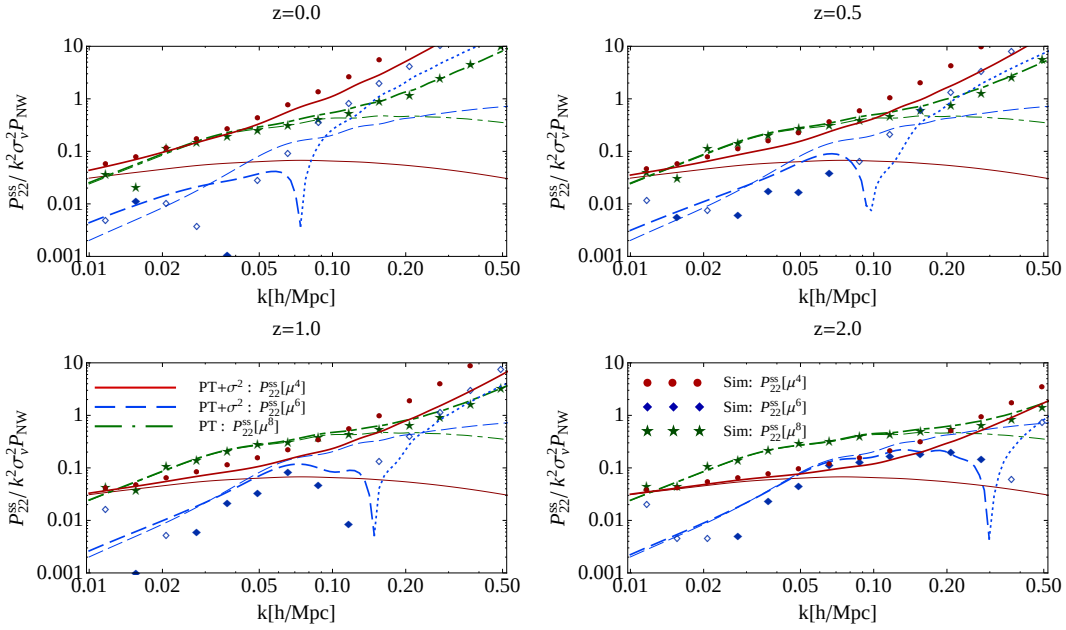


**Figure 5.7:** $k$-dependence of $\mu^4$, $\mu^6$ and $\mu^8$ parts of $P_{22}^{ss}$ term of redshift power spectrum is plotted at four redshifts, $z = 0.0,\ 0.5,\ 1.0$ and $2.0$. $\mu^4$ part $P_{22}^{ss}[\mu^4]$ is shown for one loop PT (red, solid, thin) regime, and for improved two loop PT model with small scale velocity dispersion (red, solid, thick), as well as for simulations (red dots). Similarly, $P_{22}^{ss}[\mu^6]$ part is shown using one loop PT (blue, dashed, thin) result, improved two loop PT model with small scale velocity dispersion (blue, dashed/dotted, thick), and simulations (blue, empty/full, diamonds). Dashed/full results present positive values of $\mu^6$ dependence and dotted/empty negative values. $\mu^8$ contribution is shown for one (thin, green, dot-dashed) and two loop PT (thick, green, dot-dashed), with the corresponding simulations (green stars). All power spectra are divided by $k^2\sigma_v^2 P_L^{\rm nw}$ without the wiggles.

we see that the lowest angular dependence comes from the vector contribution and not the scalar, although the scalar has lower perturbative order. Similar case was discussed for $P_{11}$, where the vector part, which is of one loop order, contributes to $\mu^2$, while the leading linear order scalar part has $\mu^4$ dependence.
One loop PT contribution to total $P^{ss}$ give

$$P_{03}^{ss}(\mathbf{k},\tau) = \frac{i}{3}\left(\frac{k\mu}{\mathcal{H}}\right)^3 P_{03}(\mathbf{k}) = -f^3(\tau)D^4(\tau)\mu^4 k^2\sigma_v^2 P_L(k),$$
$$P_{13}^{ss}(\mathbf{k},\tau) = -\frac{1}{3}\left(\frac{k\mu}{\mathcal{H}}\right)^4 P_{13}(\mathbf{k}) = -f^4(\tau)D^4(\tau)\mu^6 k^2\sigma_v^2 P_L(k). \qquad (5.81)$$

We can again include some higher order terms based on small scale velocity dispersion type arguments. For example, let us asses contributions to each of the terms above as if fully coming from

$$\left\langle T_\parallel^0 \middle| T_\parallel^3 \right\rangle = 3\sigma_v^2 \left\langle T_\parallel^0 \middle| T_\parallel^1 \right\rangle,$$
$$\left\langle T_\parallel^1 \middle| T_\parallel^3 \right\rangle = 3\sigma_v^2 \left\langle T_\parallel^1 \middle| T_\parallel^1 \right\rangle,$$

and neglecting other two loop contribution. Taking this into account we can model terms above by replacing $P_{03} \to 3(f\mathcal{H}D)^2\sigma_v^2 P_{01}$ and $P_{13} \to 3(f\mathcal{H}D)^2\sigma_v^2 P_{11}$. In figure 5.8 we show results for both $\mu^4$ part of $P_{03}$ and for $\mu^6$ part of $P_{13}$. On the same plot we show one loop PT prediction for both terms (keeping in mind that in the overall contribution they differ relative to each other by the factor of $-\mu^2 f(\tau)$. We compare model results presented

above to simulations. The specific shape in simulations is explained by the proposed model, while it is not in one loop PT result. This effect arises from substitution of $P_L$ with $P_{01}$ or $P_{11}$. We can again add the small scale velocity dispersion $\sigma_v^2 \to \sigma_v^2 + \sigma_{03}^2/(f\mathcal{H}D)^2$ (or equivalently $\sigma_{13}^2$) which is not included in PT analysis. In the model we suggest for $P_{13}$ we get, in addition to the $\mu^6$ dependence, also $\mu^4$ dependence, which comes from the vector part of $P_{11}$. In figure 5.9 we show that this can explain the trends and amplitude seen in simulations for this term. In the case of the leading contributions $P_{03}[\mu^4]$ and $P_{13}[\mu^6]$ we found that lower value for small scale velocity dispersion $\sigma_{03}$ and $\sigma_{13}$ is needed (table 5.1). This can be describer using the halo model and we return to that in section 5.3.8. Note that this value only affects the total amplitude, i.e. translates whole result up and down, but does not affect the shape.
In a similar fashion we can estimate contribution of $P_{04}$ term, which is the last term we need to consider at $\mu^4$ order. Formally this term does not even contribute at the one loop order in PT, but we can do two loop considerations as we did before. Considering the most relevant two loop contributions (from partially disconnected diagrams) this term can be modeled as

$$\left\langle T_\parallel^0 \;\middle|\; T_\parallel^4 \right\rangle = 6(f\mathcal{H}D)^2\sigma_v^2 \left\langle \delta \left| v_\parallel^2 \right.\right\rangle + 3(f\mathcal{H}D)^4\sigma_v^4 \langle \delta \,|\delta\rangle + \langle \delta \,|\delta\rangle \left\langle v_\parallel^2 \left| v_\parallel^2 \right.\right\rangle_c ,$$

where we used subscript $c$ to label the connected part of the correlator. Here we again include the small scale velocity dispersion using $\sigma_v^2 \to \sigma_v^2 + \sigma_{04}^2/(f\mathcal{H}D)^2$, just as in $P_{02}$ case. We can write the $P_{04}^{ss}$ contribution

$$\begin{aligned} P_{04}^{ss}\left[\mu^4\right] =& -\frac{1}{2} f(\tau)^2 D(\tau)^2 k^2 \left(\sigma_v^2 + \sigma_{04}^2/(f\mathcal{H}D)^2\right) \bar{P}_{02}^{ss}\left[\mu^2\right] \\ &+ \frac{1}{4} f(\tau)^4 D(\tau)^4 k^4 \left(\sigma_v^2 + \sigma_{04}^2/(f\mathcal{H}D)^2\right)^2 P_{00}^{ss}(k,\tau) + \frac{1}{12} P_{00}^{ss}(k,\tau) \int \frac{d^3q}{(2\pi)^3} \bar{P}_{22}(\mathbf{q},\tau) \\ P_{04}^{ss}\left[\mu^6\right] =& -\frac{1}{2} f(\tau)^2 D(\tau)^2 k^2 \left(\sigma_v^2 + \sigma_{04}^2/(f\mathcal{H}D)^2\right) \bar{P}_{02}^{ss}\left[\mu^4\right]. \end{aligned} \tag{5.82}$$

### 5.3.8 Halo model and small scale velocity dispersion

In our analysis of correlators that contribute in expansion of the RSD power spectrum we find that some of them have terms proportional to velocity dispersion of dark matter particles. Particles moving in the gravitational potential can have large velocities even on the small scales, so they have significant contribution to the total velocity dispersion. Using PT we can evaluate velocity dispersion

$$(f\mathcal{H}D\sigma_v)^2 = \frac{1}{3}\int \frac{d^3q}{(2\pi)^3} \frac{P_{\theta\theta}(q,\tau)}{q^2}. \tag{5.83}$$

Linear theory gives $\sigma_v \simeq 600 km/s$, but this does not properly take into account small scale contributions, which come from within virialized halos where PT cannot be used. Thus to take into account all nonlinear contributions we have to add this to our model in order to match the simulation predictions. In table 5.1 we show the values used for small scale velocity dispersion for modeled terms. These values are obtained by fitting our PT model using the free parameter for small scale dispersion ($\sigma_{02},\ \sigma_{12},\ \ldots$) in order to match simulation predictions. We see that we can classify these into a few groups which have approximately the same value.
We can understand the fact that some terms have equal velocity dispersion to others, and some do not, using the halo model [38, 39, 37, 40, 41]. We can distinguish between three types of contributions to velocity dispersion. For terms $P_{02},\ P_{12},\ P_{13}(vec)$ and $P_{22}$ we find that the same value is needed. In these terms $v_\parallel^2$ always comes weighted by $1+\delta$. In a halo model we divide all the mass into halos, such that the integral over the halo mass function times mass gives the mean density of the universe,

$$\int dM \frac{dn}{dM} M = \bar{\rho}, \tag{5.84}$$

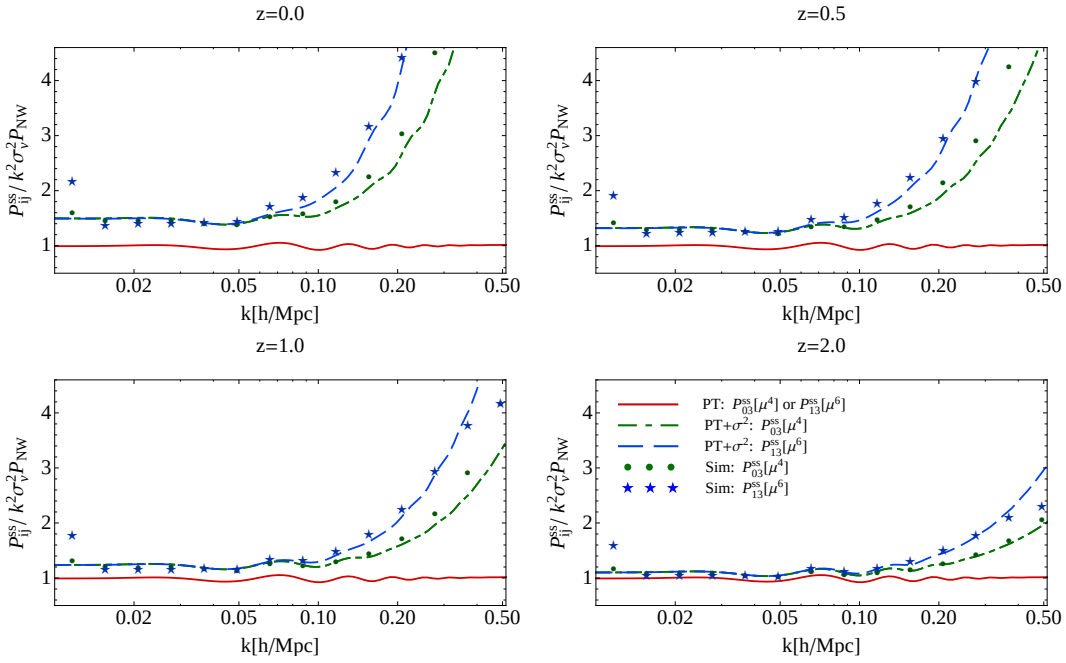


**Figure 5.8:** $\mu^4$ dependence of $P^{ss}_{03}$ and $\mu^6$ dependence of $P^{ss}_{13}$ is plotted at four redshifts, $z = 0.0,\ 0.5,\ 1.0$ and 2.0. One loop PT result is plotted (red, solid), as well as results of improved model discussed in the text for $P^{ss}_{03}[\mu^4]$ (blue, dashed) and $P^{ss}_{13}[\mu^6]$ (green, dot-dashed). Results are compared to the simulation measurements; $P^{ss}_{03}[\mu^4]$ (blue, stars) and $P^{ss}_{13}[\mu^6]$ (green, dots). All the plots are divided by no-wiggle $-f^3(D\mu)^4k^2\sigma_v^2P_L^{\rm nw}$ for $P^{ss}_{03}$ and $f\mu^2$ times this for the $P^{ss}_{13}$ term.

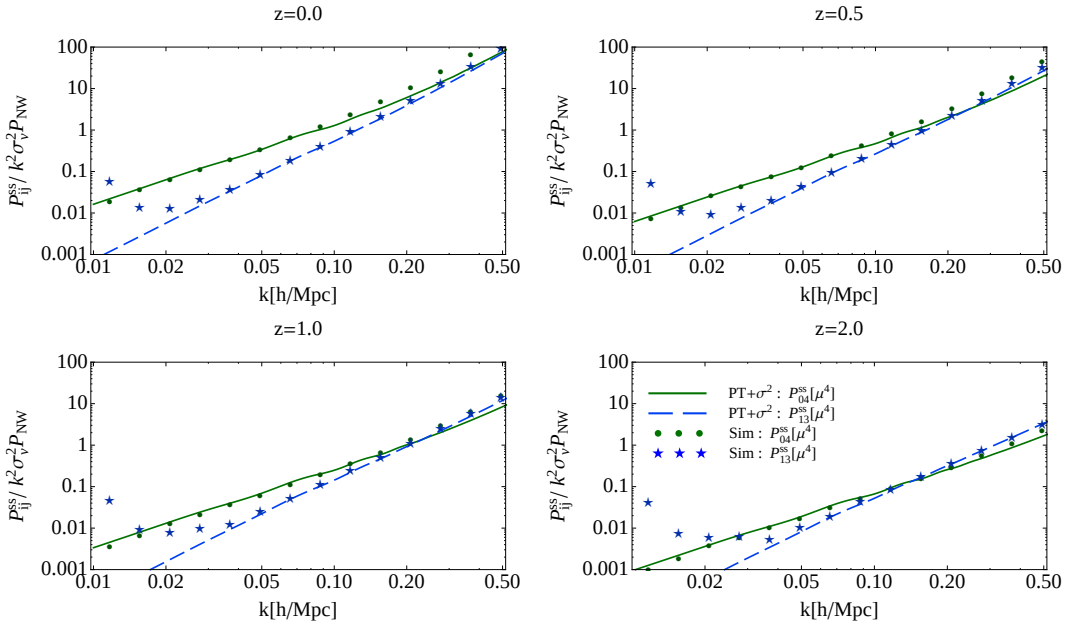


**Figure 5.9:** $\mu^4$ dependence of $P^{ss}_{13}$ and $P^{ss}_{04}$ term is plotted at four redshifts, $z = 0.0,\ 0.5,\ 1.0$ and 2.0. Simple modeled results for $P^{ss}_{13}$ (blue, dashed), and $P^{ss}_{04}$ (green, solid) are shown and compared to corresponding simulation measurements; $P^{ss}_{13}$ (blue, stars), and $P^{ss}_{04}$ (green, dots). Both, simulations and model results for $P^{ss}_{13}$ have negative values. All the plots are divided by no-wiggle $(fD\mu)^4k^2\sigma_v^2P_L^{\rm nw}$.

**Table 5.1:** Small scale velocity dispersions as described in the paper (in km/s).

| z | 0.0 | 0.5 | 1.0 | 2.0 | z | 0.0 | 0.5 | 1.0 | 2. |
|---|---|---|---|---|---|---|---|---|---|
| $\sigma_{02}$, $\sigma_{12}$, $\sigma_{13}$ (vec), $\sigma_{22}$ | 375 | 356 | 282 | 144 | $\sigma_{bv^2}$ | 377 | 267 | 190 | 105 |
| $\sigma_{03}$, $\sigma_{13}$ (sca) | 209 | 198 | 159 | 80 | $\sigma_{v^2}$ | 221 | 154 | 106 | 56 |
| $\sigma_{04}$ | 432 | 382 | 315 | 144 | $\sigma_{bv^4}$ | 510 | 371 | 270 | 153 |
| $\sigma_{FoG}$ | 346 | 322 | 249 | 133 | $(\bar{\sigma}^2)^{1/2}$ | 387 | 278 | 200 | 111 |

where $dn/dM$ is halo mas function. Each halo has a bias $b(M)$, which describes how strongly the halo clusters relative to the mean, since

$$\delta(\mathbf{k}) = \frac{1}{\bar{\rho}} \int dM \frac{dn}{dM} M b(M) \delta(\mathbf{k}). \tag{5.85}$$

Each halo also has a small scale 1-d velocity dispersion $v_\parallel^2(M) \propto M^{2/3}$, where the latter relation is only approximate and does not take into account effects such as halo profile dependence on the halo mass etc.
We now decompose the terms into halos of different mass, accounting for small scale velocity dispersion $v_\parallel^2(M)$, and accounting for biasing whenever this is multiplied by density $\delta$. For example for term $P_{02}$ schematically we can write

$$P_{02} = \left\langle \delta | (1+\delta) v_\parallel^2 \right\rangle \sim \left\langle \delta | \delta v_\parallel^2 \right\rangle = \langle \delta | \delta \rangle \frac{1}{\bar{\rho}} \int dM \frac{dn}{dM} M b(M) v_\parallel^2(M) \equiv P_{00} \sigma_{bv^2}^2, \tag{5.86}$$

i.e. we find that the velocity dispersion is weighted by bias. Note that we should have written the term $\delta$ in halo model as well, but since the bias integrates to unity (equation 5.85) we do not have a contribution from the left hand side. Note also that we only include the small scale velocity dispersion effects here that come on top of the PT calculations above. Same quantity enters also in $P_{12}$, $P_{13}(vector)$ and $P_{22}$.
For terms $P_{03}$ and $P_{13}(scalar)$ we have a different contribution to small scale velocity dispersion because one of the velocity field in $v_\parallel^3$ correlates with the density field and we can approximate $1+\delta$ with 1 at the lowest order. As a result $v_\parallel^2$ is not density weighted. For example for $P_{03}$ we have contributions from term

$$P_{03} = \left\langle \delta | (1+\delta) v_\parallel^3 \right\rangle \sim \left\langle \delta | v_\parallel^3 \right\rangle = 3 \left\langle \delta | v_\parallel \right\rangle \frac{1}{\bar{\rho}} \int dM \frac{dn}{dM} M v_\parallel^2(M) \equiv 3 P_{\delta v_\parallel} \sigma_{v^2}^2. \tag{5.87}$$

Since there is no biasing and since $b(M) > 1$ at high mass halos which dominate the velocity dispersion these terms have a smaller value of velocity dispersion than we had in the first case. This is precisely what we find when fitting to the simulations.
Finally, for the term $P_{04}$ we find contribution

$$P_{04} = \left\langle \delta | (1+\delta) v_\parallel^4 \right\rangle \sim \left\langle \delta | \delta v_\parallel^4 \right\rangle = \langle \delta | \delta \rangle \frac{1}{\bar{\rho}} \int dM \frac{dn}{dM} M b(M) v_{\parallel,s}^4(M) \equiv P_{00} \sigma_{bv^4}^2. \tag{5.88}$$

This term gives a value bigger then previous two because higher mass halos give a larger weight and they are more biased, which is also consistent with what we observe in simulations, and is presented in table 5.1. To convert $v_\parallel$ into velocity dispersion we use the relation

$$v_{\parallel,s}^2(M) = (235 \mathrm{km/s})^2 \left( \frac{M}{h 10^{13} M_\odot} \right)^{2/3}, \tag{5.89}$$

see for example [42]. We use standard Sheth-Tormen model for halo mass function and halo bias [43]. We see that predictions from the halo model presented in 5.1 agree qualitatively but not quantitatively. This could be a consequence of the simplifying assumptions, such as

ignoring the internal structure of the halo and its mass dependence. Note also that there are no errors in the analysis: it is possible that the sampling variance errors are large, specially for $\sigma^2_{bv^4}$, which receives dominant contributions from the very high mass halos which may or may not be present in our simulations, depending on the realization. We do not go into a more detailed modeling here, but it is possible that with a more detailed model the agreement would improve. Even at this level the halo model gives an insight in hierarchy of the contributions $\sigma^2_{v^2} < \sigma^2_{bv^2} < \sigma^2_{bv^4}$, and offers a qualitative picture why different terms in expansion need different values for velocity dispersion.

### 5.3.9 Putting it all together: $\mu^{2j}$ terms, finger of god resummation and Legendre moments

There are a finite number of velocity moment terms at each order of $\mu^{2j}$, in contrast to the Legendre multipoles expansion (monopole, quadrupole, hexadecapole etc), which receive contributions from all orders in moments of distribution function. We will thus investigate $\mu^{2j}$ expansion, with the lowest 3 orders containing cosmological information, while the rest can be treated as nuisance parameters to be marginalized over. Even in that case a good prior for these higher order angular terms would be very useful, although given the large number of terms that contribute to it it seems easier to be guided by the simulations rather than the PT. In this section we collect all the previous terms with $\mu^2$ and $\mu^4$ dependence. At $\mu^2$ level the contributions come from $P_{01}$, $P_{02}$ and $P_{11}$ terms, and for $\mu^4$ from $P_{11}$, $P_{02}$, $P_{12}$, $P_{22}$, $P_{03}$, $P_{13}$ and $P_{04}$ terms. In figures 5.10 and 5.11 we show $\mu^2$ and $\mu^4$ dependence of these terms divided by the corresponding no-wiggle Kaiser term. We show both the simplest PT model and the improved model that includes velocity dispersion effects. For modeling some of the terms we have been using the model for velocity dispersion $\sigma_v^2 \to \sigma_v^2 + \sigma_{ij}^2$, where the added value $\sigma_{ij}^2$ for term $P_{ij}$ is given by the table 5.1. These model was optimized to fit corresponding terms primarily on large scales, where the dominant contributions comes from $P_{01}$ for $\mu^2$ and $P_{11}$ form $\mu^4$ terms. To improve the model further for $P_{01}$ and scalar part of $P_{11}$, instead of PT predictions, we use exact values obtained from the simulations. We expect that ongoing activities in the modeling of nonlinear power spectrum will result in a successful model of these terms (note that $P_{01}$ is given by the time derivative of the nonlinear power spectrum $P_{00}$). Although we have introduced a free parameters in our model note that $P_{01}$ and $P_{11}$ terms do not contain any free parameters, so we can use simulation results as well as any other method to predict these terms.

The leading order in RSD is the $\mu^2$ term. On large scales it is given by the Kaiser expression, but note that the deviations from the linear theory are of the order of 10% at $z = 0$ already at $k \sim 0.05$h/Mpc. These nonlinear effects are dominated by the small scale velocity dispersion effects, which cannot be modeled by PT (a smaller effect, of the order of 2% at these scales, is caused by nonlinear effects in $P_{01}$ which are modeled in PT). This is a serious challenge for the RSD models and the ability to extract cosmological information from RSD: any additional free parameter that needs to be determined from the data will reduce the statistical power of the data set. Note however that we do not observe dark matter, but galaxies, so to address this concern in a proper way one will need to repeat this study with galaxies. We plan to pursue this in the near future. At higher redshifts these nonlinear effects are smaller: at $z = 1$ the 10% nonlinear suppression happens at $k \sim 0.1$h/Mpc. In all cases the dominant nonlinear effect is to suppress the small scale power, as expected by the phenomenological models like [10], where a Gaussian smoothing is added to the extension of Kaiser formula.

The $\mu^4$ terms show considerably more structure in the nonlinear effects: the overall power is initially suppressed relative to the linear term, stays flat for a while and then increases again (above $k \sim 0.1$h/Mpc at $z = 0$). The effects are large: 20% suppression of power at $k \sim 0.05$h/Mpc for $z = 0$ relative to linear. The model has some success in predicting some of these details, but is far from perfect and again it relies on the free parameters. The nonlinear effects are smaller at higher redshift, but remain significant. These $\mu^4$ terms

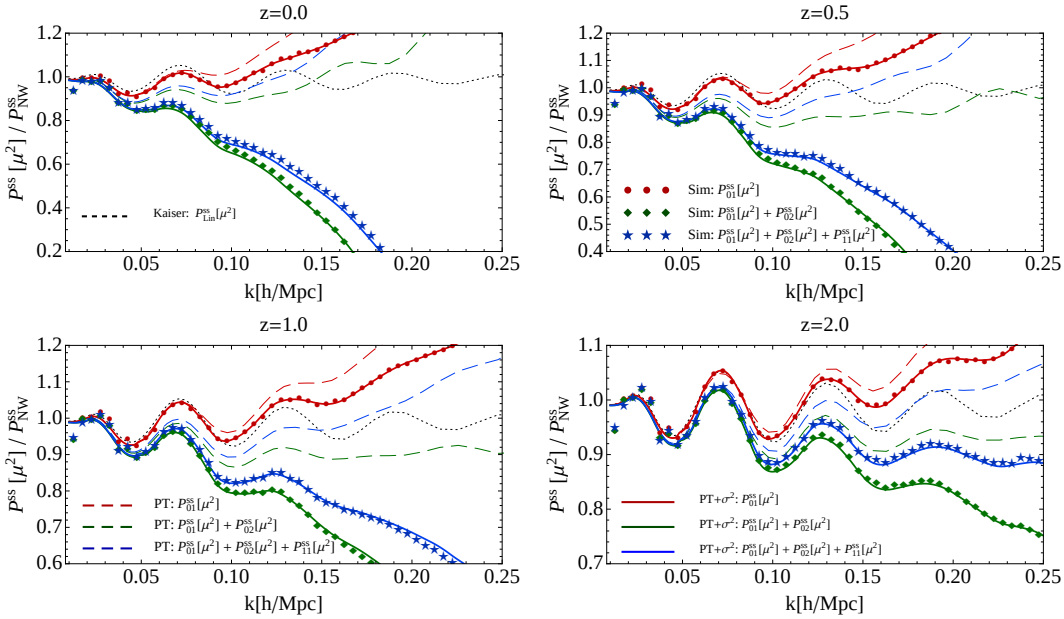


**Figure 5.10:** $\mu^2$ dependence of $P^{ss}$ at four redshifts, $z = 0.0,\ 0.5,\ 1.0$ and 2.0. We show separately contributions of the PT (dashed lies), the improved velocity dispersion model (solid lines), and simulation measurements (points). The leading term is $P^{ss}_{01}$ (red), to which we add $P^{ss}_{02}$ (green), and to which we add $P^{ss}_{11}$ to get the total (blue). Kaiser $\mu^2$ term (black, dotted) is also shown. All the lines are divided by no-wiggle $\mu^2$ Kaiser term.

have an important contribution to RSD. For example, at higher redshift (where $f \sim 1$) they contribute about 30% to the quadrupole on large scales, with the dominant 70% contribution coming from $\mu^2$ term. As for the $\mu^2$ term, it remains to be seen how well we can model these terms such that we can extract the maximal information from the data, but the fact that the nonlinear effects are so large already on very large scales is a cause for concern.
Our result for the RSD power spectrum $P^{ss}$ can be compactified in so called finger of good resummation. Following the ideas presented in [30] we can show explicitly that up to $\mu^4$ order our result in equation 5.23 can be written in the following way

$$P^{ss}_{\rm FoG}(k,\mu) = \exp\left[-k^2\mu^2\sigma^2_{\rm FoG}\right]\Big(A(k) + \mu^2 B(k) + \mu^4 C(k) + \dots\Big), \tag{5.90}$$

where we have defined

$$\begin{aligned} A(k) &= P_{00}, \\ B(k) &= P^{ss}[\mu^2] + k^2\sigma^2_{\rm FoG}P_{00}, \\ C(k) &= P^{ss}[\mu^4] + k^2\sigma^2_{\rm FoG}P^{ss}[\mu^2] + \frac{1}{2}\big(k^2\sigma^2_{\rm FoG}\big)^2 P_{00}, \end{aligned} \tag{5.91}$$

i.e. there is no change to $\mu^2$, and $\mu^4$ terms, since the terms $P^{ss}[\mu^2]$ and $P^{ss}[\mu^4]$ contain all the terms discussed previously and the FoG terms cancel by construction of $B(k)$ and $C(k)$. If we set the value of $\sigma^2_{\rm FoG} = (fD)^2\sigma^2_v$ this reduces to simple form where $\sigma^2_v$ is now present only in the exponent in equation 5.90 and not in the brackets, i.e.

$$\begin{aligned} A(k) &= P_{00}, \\ B(k) &= P^{ss}_{01} + \bar{P}^{ss}_{02}[\mu^2] + P^{ss}_{01}[\mu^2], \\ C(k) &= P^{ss}_{11}[\mu^4] + \bar{P}^{ss}_{02}[\mu^4] + \bar{P}^{ss}_{12}[\mu^4] + \bar{P}^{ss}_{22}[\mu^4], \end{aligned} \tag{5.92}$$

where all the $P^{ss}$ and $\bar{P}^{ss}$ terms here, as defined in previous sections, do not contain velocity dispersion contributions. This argument also generalizes to the case where we replace $\sigma^2_{\rm FoG} =$

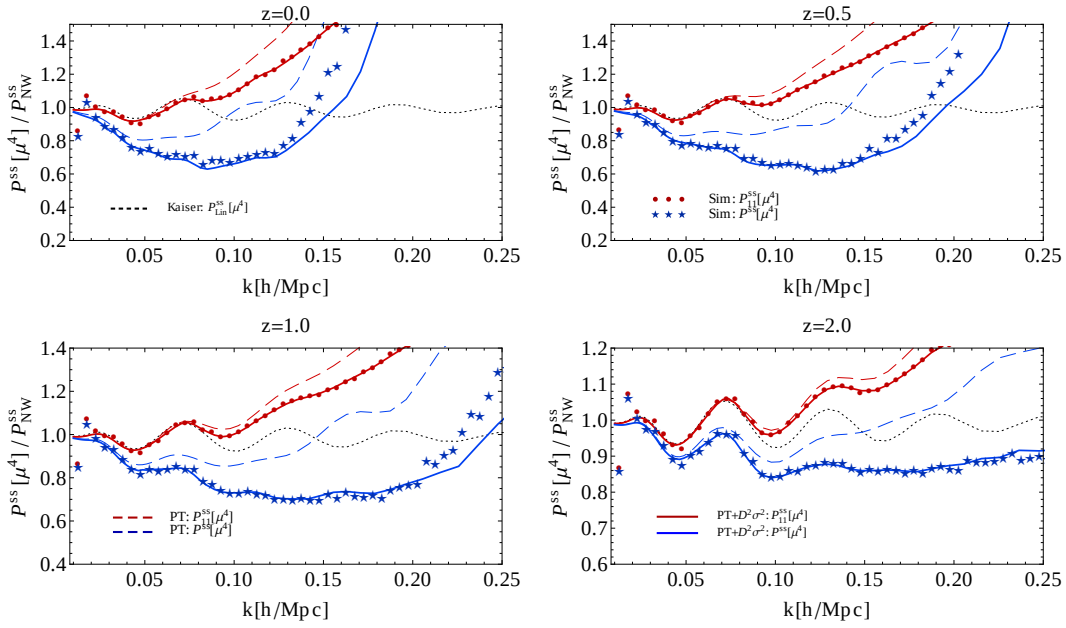


**Figure 5.11:** $\mu^4$ dependence of $P^{ss}$ at four redshifts, $z = 0.0,\ 0.5,\ 1.0$ and 2.0. We show the PT (blue, dashed line) results, the improved velocity dispersion model presented in this paper (blue, solid line), and simulation measurements (blue, stars). Also, the leading $P^{ss}_{11}$ term is shown in red. Kaiser $\mu^4$ term (black, dotted) is also shown. All the lines are divided by no-wiggle $\mu^4$ Kaiser term.

$(fD)^2\sigma_v^2 + \sigma^2$, where $\sigma^2$ is the small scale velocity dispersion. This is the basic justification for using the FoG model.

Unfortunately, the fact that $\sigma_v^2$ cancels out is of limited use, since in practice the velocity dispersion is not dominated by linear $\sigma_v^2$, but by small scale velocity dispersions, and as argued above, there is no single $\sigma^2$, but instead there are several different velocity dispersions entering in the detailed RSD analysis at $\mu^2$ and $\mu^4$ order, $\sigma_{bv^2}$, $\sigma_{v^2}$ and $\sigma_{bv^4}$. In fact, in our analysis we include these terms already so one can argue that it is the next term that we do not include that should enter in $\sigma^2_{\rm FoG}$. At $\mu^6$ order there are again several velocity dispersions that can be defined and that have a wide range of values, so we cannot simply write down a value without explicitly evaluating all the terms at this order. It is however likely that their values will be of the same order as $\sigma_{bv^2}$, $\sigma_{v^2}$ and $\sigma_{bv^4}$. In table 5.1 we compare the root mean square average of these velocity dispersion values to the best fit value for $\sigma_{\rm FoG}$, showing that indeed the value of $\sigma^2_{\rm FoG}$ is indeed related to these other values.

It is customary to expand the redshift-space power spectrum in terms of Legendre multipole moments. The motivation for this is that when using the full angular information Legendre moments are uncorrelated on scales small relative to the survey size. Using ordinary Legendre polynomials $\mathcal{P}_l(\mu)$, we have

$$P^{ss}(k,\mu) = \sum_{l=0,2,4,\cdots} P^{ss}_l(k)\mathcal{P}_l(\mu), \tag{5.93}$$

where multipole moments, $P^{ss}_l$, are given by

$$P^{ss}_l(k) = (2l+1)\int_0^1 P^{ss}(k,\mu)\mathcal{P}_l(\mu)d\mu\ . \tag{5.94}$$

where $\mathcal{P}_l(\mu)$ are the ordinary Legendre polynomials, $\mathcal{P}_0(\mu) = 1$, $\mathcal{P}_2(\mu) = (3\mu^2-1)/2$ and $\mathcal{P}_4(\mu) = (35\mu^4 - 30\mu^2 + 3)/8$. In the RSD analyses we are usually limited to modeling the monopole ($l = 0$) and quadrupole ($l = 2$) terms, although some information is also contained in hexadecapole term ($l = 4$).

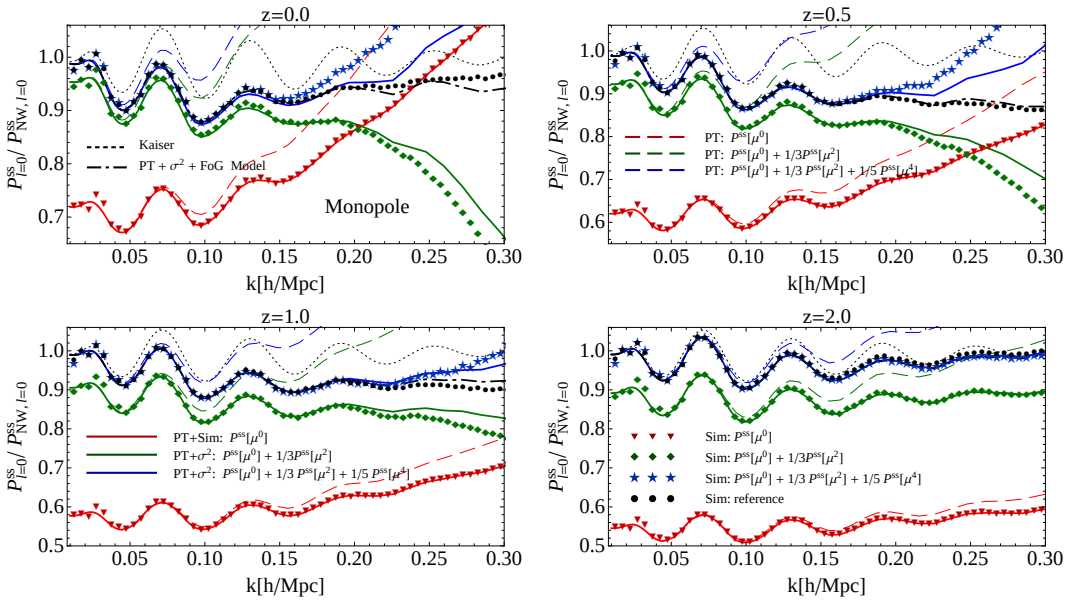


**Figure 5.12:** Monopole moment $P_0^{ss}$ is plotted at four redshifts, $z = 0.0,\ 0.5,\ 1.0$ and 2.0. To the first isotropic term (red) of $P^{ss}$ expansion we first add $\mu^2$ (green) term and then also $\mu^4$ term (blue). We show PT (dashed lines) results, improved velocity dispersion model presented in this paper (solid lines), simulations up to $\mu^4$ contributions (triangles, diamonds and stars), and reference simulation results (points). Resummed FoG model from equation 5.90 (black dot-dashed line) and linear Kaiser model (black dotted line) are also shown. All the results shown are divided by monopole contributions of the no-wiggle Kaiser model.

In figures 5.12 and 5.13 we show monopole and quadrupole power spectra predictions of improved velocity dispersion model presented in the paper, as well as one loop PT result. We also show resummed FoG result choosing for $\sigma_{\rm FoG}$ values given in the last line in table 5.1. We compare this to the reference multipole results obtained from full simulation redshift space power spectra. We also show simulation results where only terms up to $\mu^4$ are considered. In case of monopole we see that these two simulation results agree on scales larger then $k \sim (0.15-0.20)$h/Mpc (depending on redshift) but then start to deviate one from an other. In the case of the quadrupole these deviations start to be more then 1% for $k > 0.15$h/Mpc. This trend is due to the $\mu^6$ term which is weighted by $1/7$ for the monopole but $11/21$ for the quadrupole, which is almost the same weight $(4/7)$ as for $\mu^4$ term. At higher $k$ higher $\mu$ terms ($\mu^6$, $\mu^8$, ...) start to be relevant and contribute significantly to the total redshift power spectrum. These higher $\mu$ contributions have large amplitudes with differing signs [30], which would suggest that we might not be able to rely on our expansion in low-$k$ any longer, although FoG resummation can still help here. From figures we can also see relative contributions to the total monopole and quadrupole power from $\mu^2$ and $\mu^4$ terms. We see that at scales larger than $k \sim 0.15$h/Mpc $\mu^4$ term contributes with 5-10% (depending on the redshift) to the total power of monopole and with 15-30% for the quadrupole. For the quadrupole all the remaining power comes form the $\mu^2$ term while for the monopole the $\mu^2$ term constitutes 25-35% of power and the rest comes from isotropic $P_{00}$ term. To reduce the dynamical range we again divide monopole results by the no-wiggle monopole Kaiser term and the quadrupole results by the no-wiggle quadrupole Kaiser term.

## 5.4 Conclusions

In this paper we use the distribution function approach to redshift space distortions (RSD) that decomposes RSD into moments of distribution function. Our goal is to model the terms

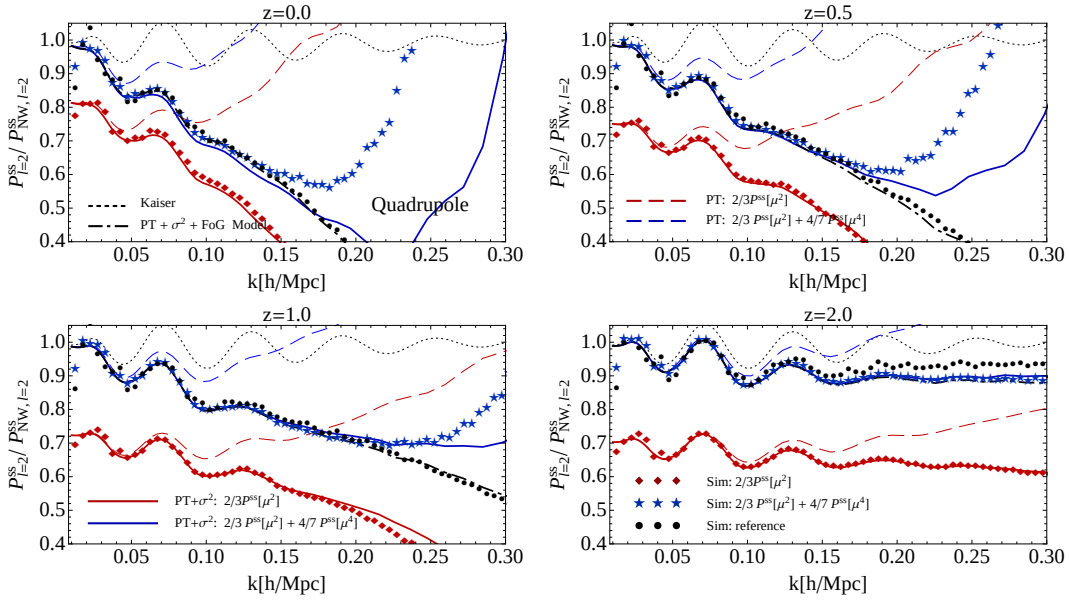


**Figure 5.13:** Quadrupole moment $P_2^{ss}$ is plotted at four redshifts, $z = 0.0,\ 0.5,\ 1.0$ and 2.0. To $\mu^2$ (red) term of $P^{ss}$ expansion we add $\mu^4$ term (blue). We show PT (dashed lines) results, improved velocity dispersion model presented in this paper (solid lines), simulations up to $\mu^4$ contributions (diamonds and stars), and reference simulation results (points). Resummed FoG model from equation 5.90 (black dot-dashed line) and linear Kaiser model (black dotted line) are also shown. All the results shown are divided by quadrupole contributions of the no-wiggle Kaiser model.

that contribute to the redshift space distortions using perturbation theory. We first repeat the derivations presented in [29], explicitly deriving the decomposition of the moments into helicity eigenstates, based on their transformation properties under rotation around the direction of the Fourier mode. We give the explicit forms of correlators of the moments of distribution function and their angular dependencies.

It is worth comparing the phase space approach to the redshift space power spectrum to the alternative perturbative derivations that can be found in the literature, e.g. [22, 11]. The advantage of phase space approach as presented here lies in the decomposition into the hierarchy of terms that contribute to the redshift space power spectrum with an explicit dependence on the expansion parameters. In this way a systematic expansion approach is possible and a physical meaning of each term is revealed that enables effective modeling of each of the contributing correlators in the relation 5.19. This also allows a detailed term-by-term comparison of the simulation results, since one can compare each term to the simulations rather than just the final RSD power spectrum. In this paper we focus on the PT modeling and comparing the results to the simulations we are able to clearly show where the PT modeling preforms well, even at one loop, and where it does less so. The approach also allows us to identify physical reasons for failure of PT in individual terms, which are mostly related to various small scale velocity dispersion effects, and for which other modeling methods may be required. This also enables us to argue that it is more physical to try to model some of the terms in PT going beyond one loop, while remaining at the one loop level for the other terms. We should also mention that if just PT is used to evaluate all the terms at one loop, the results of phase space approach should correspond to [22], although only monopole predictions are presented there (compare e.g. figure 10 in [22] to SPT predictions for monopole in figure 5.12).

The leading order contributions to RSD can be classified in terms of their angular dependence, with the lowest order being $\mu^2$ and $\mu^4$, where $\mu$ is the angle between the Fourier mode and the line of sight. There are three terms contributing to $\mu^2$ and seven terms contributing to $\mu^4$. We evaluate all of these terms using the lowest order PT (one loop) and compare them

to simulation results. For some terms adding two loop contributions proves to be important and we extend our models to include the relevant contributions. Also, for some of these terms standard PT is not sufficient and we propose physically motivated ansatz that goes beyond the loop analysis. These are based on the small scale induced velocity dispersion effects which multiply the long range correlations, such as density-density or density-velocity correlations. Such ansatz has a free parameter, small scale velocity dispersion, which cannot be modeled using PT. We found that a number of these terms have the same value, but also that not all velocity dispersions should be equal. We developed a halo model to describe the hierarchy of these terms and shown that the model can qualitatively explain the simulation results. Our analysis systematically accounts for all of the PT terms at one loop order and the small scale dispersion parameters, while necessary for a good description of RSD, have physically motivated values. In this sense our model goes beyond previous analyses [10, 11], which include some, but not all of the PT terms and which often treat FoG parameters as fitting parameters without a physical meaning.

The dominant term to RSD is the $\mu^2$ term and its dominant contribution is the momentum density correlated with the density. This term can be written in terms of a time derivative of the power spectrum [29] and so can be modeled using dark matter power spectrum emulators. Two other terms contribute to $\mu^2$, the vector part of the momentum density-momentum density correlation, and the scalar part of energy density-density correlation. We find that they affect RSD at a 10% level already at $k \sim 0.05$h/Mpc. The energy density-density correlation term is the dominant nonlinear effect, is negative for all scales and thus reduces the total $\mu^2$ power. It is related to the Fingers-of-God effect. This term contains velocity dispersion term which cannot be modeled in PT and requires a free parameter in the model.

The next angular term has $\mu^4$ dependence and there are seven terms that contribute to the total power spectrum, of which one, scalar part of $P_{11}$, contains a linear contribution that does not vanish on large scales. We evaluate all of these terms in PT. Some of these terms are well modeled by PT, while others also require velocity dispersion type parameters. With these the modeling achieves some level of precision compared to the simulations, but is still limited in the dynamic range, with an error of about 5% at $k \sim 0.2$h/Mpc at $z = 1$.

Our ultimate goal is to develop accurate models of RSD that can be applied to observations. We observe galaxies, not dark matter, and understanding the physical processes that lead to RSD in dark matter is just the first step towards the goal of understanding the RSD in galaxies. The results presented here are only a rough guide for the challenges awaiting us when applying these techniques to the data, but there are some lessons learned that are likely to be valid also for galaxies. One is the importance of velocity dispersion effects, which dominate our model uncertainties on large scales. The good news may be that the velocity dispersion effects, which are the main source of the modeling difficulties in this paper, may be smaller for galaxies than for the dark matter, specially if a sample of central galaxies can be selected. We also expect that the halo model for computing velocity dispersion should be applicable to galaxies as well. However, galaxies also have additional challenges not present for dark matter: galaxy biasing will introduce additional scale dependent effects in redshift space that will need to be modeled, even if there are no such scale dependent biases in real space [29, 44]. The success of modeling the RSD and extracting the cosmological information from it depends on our ability to model these galaxy biasing and velocity dispersion terms. We plan to address some of these issues in the future work.

## Acknowledgments

We would like to thank Nico Hamaus, Darren Reed and Lucas Lombriser for useful discussions and comments. ZV would like to thank the Berkeley Center for Cosmological Physics and the Lawrence Berkeley Laboratory for their hospitality. This work is supported by the DOE, the Swiss National Foundation under contract 200021-116696/1 and WCU grant R32-10130. The simulations were performed on the ZBOX3 supercomputer of the Institute

for Theoretical Physics at the University of Zürich.

## 5.5 Components of moments of distribution function

Starting from equation 5.6 we can chose some basis, for example Cartesian, to express scalar product $\mathbf{h}\cdot\mathbf{q}$. It follows

$$T^L_{\mathbf{h}}(\mathbf{x}) = \frac{ma^{-3}}{\bar{\rho}}\int d^3p f(\mathbf{x},\mathbf{p})\,(h_i p_i/ma)^L, \tag{5.95}$$

where summation over $i=1,2,3$ is implied. Using the multinomial theorem:

$$(x_1+x_2+\ldots+x_m)^n = \sum_{k_1+k_2+\ldots+k_m=n}\frac{n!}{k_1!k_2!\cdots k_m!}x_1^{k_1}x_2^{k_2}\cdots x_m^{k_m}, \tag{5.96}$$

it follows that

$$T^L_{\mathbf{h}}(\mathbf{x}) = \frac{ma^{-3}}{\bar{\rho}}\sum_{k_1+k_2+k_3=L}\frac{L!}{k_1!k_2!k_3!}h_1^{k_1}h_2^{k_2}h_3^{k_3}\int d^3p f(\mathbf{x},\mathbf{p})p_1^{k_1}p_2^{k_2}p_3^{k_3}/(ma)^L. \tag{5.97}$$

Neglecting velocity dispersion and anisotropic stress second rank tensor, and similar higher rank tensors contributions ($\sigma^{ij}=0,\ldots$) we are left with

$$\frac{ma^{-3}}{\bar{\rho}}\int d^3p f(\mathbf{x},\mathbf{q})p_1^{k_1}p_2^{k_2}p_3^{k_3}/(ma)^L = (1+\delta(\mathbf{x}))v_1^{k_1}v_2^{k_2}v_3^{k_3}, \tag{5.98}$$

where $v_i$ is given in equation 5.4. Returning this back into equation 5.97 and using multinomial theorem again we get

$$T^L_{\mathbf{h}}(\mathbf{x}) = (1+\delta(\mathbf{x}))\sum_{k_1+k_2+k_3=L}\frac{L!}{k_1!k_2!k_3!}(h_1v_1)^{k_1}(h_2v_2)^{k_2}(h_3v_3)^{k_3} = (1+\delta(\mathbf{x}))(\mathbf{h}\cdot\mathbf{v}(\mathbf{x}))^L. \tag{5.99}$$

Thus we have retrieved result of equation 5.7, and choosing $\mathbf{h}=\hat{r}$ we get equation 5.13.

## 5.6 Decomposition of $T^L_{\mathbf{h}}$ in spherical tensors

In this section we want to retrieve, starting from equation 5.15, equation 5.16. Let us consider the object $T^L_{\mathbf{h}}(\mathbf{x})$ as defined in 5.6, which can actually be constructed by contracting all the components of rank $L$ of tensor $T^L_{i_1,i_2,\ldots i_L}$ (equation 5.15) with unit $\mathbf{h}$ vectors. Fourier transforming this object gives us simply

$$T^L_{\mathbf{h}}(\mathbf{k}) = \frac{ma^{-3}}{\bar{\rho}}\int d^3p f(\mathbf{k},\mathbf{p})\left(\frac{\mathbf{h}\cdot\mathbf{p}}{am}\right)^L. \tag{5.100}$$

Since we have translation symmetry it follows

$$\langle\mathbf{x}\,|\mathbf{x}+\mathbf{r}\rangle = \xi(\mathbf{r}) \qquad \Rightarrow \qquad \langle\mathbf{k}\,|\mathbf{k}'\rangle = (2\pi)^3P(\mathbf{k})\delta^D(\mathbf{k}-\mathbf{k}'),$$

where it is implied that we take correlation of a general function of similar form like equation 5.6. This enables us to work with each Fourier mode separately, and add them appropriately in the end when we discuss the power spectrum. By symmetry of the problem we may choose a reference frame where $z$-axis is along $\mathbf{h}$ vector. Since spherical harmonics form a complete set of orthonormal functions and thus form an orthonormal basis of the Hilbert space of square-integrable functions, we can expanded $f(\mathbf{k},\mathbf{p})$ in that frame as a linear combination,

$$f(\mathbf{k},p,\theta,\phi) = \sum_{l=0}^{\infty}\sum_{m=-l}^{m=l}f_l^m(\mathbf{k},p)Y_{lm}(\theta,\phi), \tag{5.101}$$

where $p$ is the amplitude of momentum. Let us now consider the transformation properties of $f^m_l(\mathbf{k}, p)$ under rotation around the $z$-axis. We can think of rotation by some angle $\psi$ (i.e. $\phi' = \phi + \psi$) in two ways

$$\begin{aligned} f(\mathbf{k}, p, \theta, \phi') = f(\mathbf{k}, p, \theta, \phi + \psi) &= \sum_{l=0}^{\infty} \sum_{m=-l}^{m=l} f^m_l(\mathbf{k}, p)' Y_{lm}(\theta, \phi) \\ &= \sum_{l=0}^{\infty} \sum_{m=-l}^{m=l} f^m_l(\mathbf{k}, p) Y_{lm}(\theta, \phi'). \end{aligned}$$

From rotation properties of spherical harmonics it follows that $f^m_l(\mathbf{k}, p)$ transform as

$$f^m_l(\mathbf{k}, p)' = e^{im\psi} f^m_l(\mathbf{k}, p), \tag{5.102}$$

so it is an eigenstate of an helicity operator $i\partial/\partial\phi$, with helicity eigenvalue, or simply helicity, $m$. A quantity with helicity 0 is called a scalar, that with helicity $m = 1$ is called a vector and that with $m = 2$ a tensor, but the expansion goes to arbitrary values of $m$. It is possible to do similar considerations for arbitrary rotation and so it can be shown that $f^m_l$ transform as spherical tensors.
In the chosen reference frame, using $(\mathbf{h} \cdot \mathbf{p}) = p_z = p\ \cos\theta$, and inserting equation 5.101 into equation 5.100 we obtain

$$\begin{aligned} T^L_{\mathbf{h}}(\mathbf{k}) &= \frac{ma^{-3}}{\bar{\rho}} \sum_{l,m} \int dp\ p^2 f^m_l(\mathbf{k}, p)(p/am)^L \int d\Omega\ Y_{lm}(\theta, \phi) \cos^L\theta \\ &= \sum_{l,m} T^{L,m}_l(\mathbf{k}) I_{lm} \delta_{m0}, \end{aligned} \tag{5.103}$$

where we have defined helicity eigenstates of moments of the distribution function

$$T^{L,m}_l(\mathbf{k}) = 4\pi \frac{ma^{-3}}{\bar{\rho}} \int dp\ p^2 (p/am)^L f^m_l(\mathbf{k}, p), \tag{5.104}$$

and used abbreviation for the integral

$$I_{lm} = \frac{1}{2} \sqrt{\frac{2l+1}{4\pi} \frac{(l-m)!}{(l+m)!}} \int dx\ x^L P^m_l(x). \tag{5.105}$$

We have used definition of spherical harmonics $Y_{lm}(\theta, \phi) = \sqrt{\frac{2l+1}{4\pi} \frac{(l-m)!}{(l+m)!}} P^m_l(\cos\theta) e^{im\phi}$, and $x = \cos\theta$ abbreviation. Since in equation 5.103 we have Kronecker delta $\delta_{m0}$ it is easy to evaluate integral

$$\begin{aligned} I_{l0} &= \frac{1}{2} \sqrt{\frac{2l+1}{4\pi}} \int_{-1}^{1} dx\ x^L P_l(x) = \frac{(-1)^l L!}{2^{l+1}(l!)^2} \sqrt{\frac{2l+1}{4\pi}} \int_{-1}^{1} dx\ x^{L-l}(x^2-1)^l \\ &= \begin{cases} \sqrt{\frac{2l+1}{4\pi}} \frac{n^L_l}{2} (1 + (-1)^{L-l}) & \text{if } l \leq L, \\ 0 & \text{if } l > L, \end{cases} \end{aligned} \tag{5.106}$$

and here we have used $n^L_l = \frac{1}{2^{l+1}} \binom{L}{l} \frac{\Gamma(l+1)\Gamma\left(\frac{1}{2}(L-l+1)\right)}{\Gamma\left(\frac{1}{2}(L+l+3)\right)}$. Collecting all that, equation 5.103 becomes

$$T^L_{\mathbf{h}}(\mathbf{k}) = \sum_{(l=L, L-2, \ldots)} \sqrt{\frac{2l+1}{4\pi}} n^L_l T^{L,0}_l(\mathbf{k}). \tag{5.107}$$

Since we are working in $\hat{z} \parallel \mathbf{h}$ frame it is apparent that for some arbitrary $\mathbf{k}$, the angular dependence is contained in $T_l^{L,0}(\mathbf{k})$ spherical tensors. The goal now is to disentangle the angular dependence from the radial. The procedure depends on whether one is using active or passive interpretation of rotation transformation. Let us first look at active interpretation. Then the completely contracted tensors, like the one we are dealing with equation 5.107, can be obtained from the same one evaluated in $\mathbf{k}_z = k\hat{z} \parallel \mathbf{h}$ direction by rotating it in general $\mathbf{k}$ direction. Because $T_l^{L,m}$ are spherical tensors it follows

$$\begin{aligned} T_{\mathbf{h}}^L(\mathbf{k}) = \mathcal{D}(R) T_{\mathbf{h}}^L(R^{-1}\mathbf{k}) &= \sum_{(l=L,L-2,\ldots)} \sqrt{\frac{2l+1}{4\pi}} n_l^L \mathcal{D}(R) T_l^{L,0}(k\hat{z}) \\ &= \sum_{(l=L,L-2,\ldots)} \sum_{m=-l}^{m=l} \sqrt{\frac{2l+1}{4\pi}} n_l^L \mathcal{D}_{0m}^{(l)}(R) T_l^{L,m}(k\hat{z}), \end{aligned} \tag{5.108}$$

where $\mathcal{D}(R)$ is the Wigner rotation matrix and $\mathcal{D}_{m'm}^{(l)}(R)$ its matrix elements. Using the well known relations, $\mathcal{D}_{m'm}^{(l)}(R^{-1}) = \mathcal{D}_{mm'}^{(l)*}(R)$ and $\mathcal{D}_{m0}^{(l)}(\phi,\theta,0) = \sqrt{\frac{4\pi}{2l+1}} Y_{lm}^*(\theta,\phi)$, we get

$$T_{\mathbf{h}}^L(\mathbf{k}) = \sum_{(l=L,L-2,\ldots)} \sum_{m=-l}^{m=l} n_l^L T_l^{L,m}(k) Y_{lm}(\theta,\phi), \tag{5.109}$$

where spherical harmonics now describe rotation form direction $\mathbf{k}$ back to $\mathbf{h}$. On the other hand, using the passive interpretation we argue that $T_{\mathbf{h}}^L(\mathbf{k})$ in frame $z \parallel \mathbf{h}$ can be obtained by rotating it from $z' \parallel \mathbf{k}$ frame, which is described by the same equations as before 5.108. Note now that we were able to express result in terms of $T_l^{L,m}(k)$, just a function of amplitude $k$, and all angular dependence is given with spherical harmonics which now describe the angular dependence in $\mathbf{h}$ direction seen from $z' \parallel \mathbf{k}$ frame. Now setting simply $\mathbf{h} = \hat{r}$ along a line of sight direction we get result 5.16, where $\cos\theta = \hat{r} \cdot \mathbf{k}/k = \mu$.
Finally we show that in decomposition form 5.109 we retrieve the same number of independent components $(L+1)(L+2)/2$ as inferred from symmetries of equation 5.15, since for even $L$, i.e. $l = 2n$ we have

$$\sum_{n=0}^{L/2}(2l+1) = \sum_{n=0}^{L/2}(4n+1) = 1 + \frac{L}{2} + 4\frac{\frac{L}{2}(\frac{L}{2}+1)}{2} = \frac{(L+1)(L+2)}{2},$$

and for odd $L$, i.e. $l = 2n+1$, we have

$$\sum_{n=0}^{(L-1)/2}(2l+1) = \sum_{n=0}^{(L-1)/2}(4n+3) = 3 + 3\frac{L-1}{2} + 4\frac{\frac{L-1}{2}(\frac{L-1}{2}+1)}{2} = \frac{(L+1)(L+2)}{2}.$$

## 5.7 Conjugation properties of $P_{LL'}(\mathbf{k})$

In this section we investigate the conjugation properties of $P_{LL'}(\mathbf{k})$ functions. Starting from the condition that overdensity field $\delta(\mathbf{x})$ and velocity field $\mathbf{v}(\mathbf{x})$ are real valued fields, it follows that for Fourier space fields $\delta(\mathbf{k})$, $\theta(\mathbf{k})$ and $v_\parallel(\mathbf{k})$ we have $f^*(\mathbf{k}) = f(-\mathbf{k})$. This is valid also for more complex fields like

$$p_n(\mathbf{k}) = \int \frac{d^3q_1 d^3q_2 \ldots d^3q_n}{(2\pi)^{3n}} f_1(\mathbf{q}_1) f_2(\mathbf{q}_2) \ldots f_n(\mathbf{q}_n) \delta^D(\mathbf{k} - \mathbf{q}_1 - \mathbf{q}_1 - \ldots - \mathbf{q}_n). \tag{5.110}$$

If we compute conjugated field we get

$$p_n^*(\mathbf{k}) = \int \frac{d^3q_1 d^3q_2 \ldots d^3q_n}{(2\pi)^{3n}} f_1^*(\mathbf{q}_1) f_2^*(\mathbf{q}_2) \ldots f_n^*(\mathbf{q}_n) \delta^D(\mathbf{k} - \mathbf{q}_1 - \mathbf{q}_1 - \ldots - \mathbf{q}_n)$$

$$= \int \frac{d^3q_1 d^3q_2 \dots d^3q_n}{(2\pi)^{3n}} f_1(-\mathbf{q}_1) f_2(-\mathbf{q}_2) \dots f_n(-\mathbf{q}_n) \delta^D(\mathbf{k} - \mathbf{q}_1 - \mathbf{q}_1 - \dots - \mathbf{q}_n)$$
$$= p_n(-\mathbf{k}). \tag{5.111}$$

From equation 5.7 it follows that $T_\parallel^{*L}(\mathbf{k}) = T_\parallel^L(-\mathbf{k})$, so for correlator we have

$$\left\langle T_\parallel^L(\mathbf{k}) \left| T_\parallel^{*L'}(\mathbf{k}') \right\rangle = \left\langle T_\parallel^{L'}(-\mathbf{k}) \left| T_\parallel^{*L}(-\mathbf{k}') \right\rangle = \left\langle T_\parallel^{L'}(\mathbf{k}) \left| T_\parallel^{*L}(\mathbf{k}') \right\rangle^* \right. \right. , \tag{5.112}$$

thus we have $P_{LL'}(\mathbf{k}) = P^*_{L'L}(\mathbf{k})$. So, for sum of two correlator we can write

$$\left\langle T_\parallel^L(\mathbf{k}) \left| T_\parallel^{*L'}(\mathbf{k}') \right\rangle + \left\langle T_\parallel^{L'}(\mathbf{k}) \left| T_\parallel^{*L}(\mathbf{k}') \right\rangle = 2\mathrm{Re} \left\langle T_\parallel^L(\mathbf{k}) \left| T_\parallel^{*L'}(\mathbf{k}') \right\rangle \right. \right. . \tag{5.113}$$

## 5.8 Integrals $I(k)$ and $J(k)$

Here we define integrals $I_{nm}(k)$ and $J_{nm}(k)$ used in previous chapters:

$$I_{nm}(k) = \int \frac{d^3q}{(2\pi)^3}\, f_{nm}(\mathbf{k},\mathbf{q}) P_L(q) P_L(|\mathbf{k}-\mathbf{q}|) \qquad \text{and} \qquad J_{nm}(k) = \int \frac{dq^3}{(2\pi)^3}\, g_{nm}\left(\frac{q}{k}\right) \frac{P_L(q)}{q^2}, \tag{5.114}$$

where we define kernels $f_{nm}(\mathbf{k},\mathbf{q})$, and use $r = q/k$ and $x = \mathbf{k}\cdot\mathbf{q}/(kq)$:

$$f_{00}(\mathbf{k},\mathbf{q}) = \left(\tfrac{7x+3r-10rx^2}{14r(1+r^2-2rx)}\right)^2, \qquad f_{01}(\mathbf{k},\mathbf{q}) = \tfrac{\left(7x+3r-10rx^2\right)\left(7x-r-6rx^2\right)}{(14r(1+r^2-2rx))^2},$$
$$f_{10}(\mathbf{k},\mathbf{q}) = \tfrac{x\left(7x+3r-10rx^2\right)}{14r^2(1+r^2-2rx)}, \qquad f_{11}(\mathbf{k},\mathbf{q}) = \left(\tfrac{7x-r-6rx^2}{14r(1+r^2-2rx)}\right)^2,$$
$$f_{02}(\mathbf{k},\mathbf{q}) = \tfrac{(x^2-1)(7x+3r-10rx^2)}{14r(1+r^2-2rx)^2}, \qquad f_{20}(\mathbf{k},\mathbf{q}) = \tfrac{(2x+r-3rx^2)(7x+3r-10rx^2)}{14r^2(1+r^2-2rx)^2},$$
$$f_{12}(\mathbf{k},\mathbf{q}) = \tfrac{(x^2-1)(7x-r-6rx^2)}{14r(1+r^2-2rx)^2}, \qquad f_{21}(\mathbf{k},\mathbf{q}) = \tfrac{\left(2x+r-3rx^2\right)\left(7x-r-6rx^2\right)}{14r^2(1+r^2-2rx)^2},$$
$$f_{22}(\mathbf{k},\mathbf{q}) = \tfrac{x\left(7x-r-6rx^2\right)}{14r^2(1+r^2-2rx)}, \qquad f_{03}(\mathbf{k},\mathbf{q}) = \tfrac{(1-x^2)(3rx-1)}{r^2(1+r^2-2rx)},$$
$$f_{30}(\mathbf{k},\mathbf{q}) = \tfrac{1-3x^2-3rx+5rx^3}{r^2(1+r^2-2rx)}, \qquad f_{31}(\mathbf{k},\mathbf{q}) = \tfrac{(1-2rx)(1-x^2)}{2r^2(1+r^2-2rx)},$$
$$f_{13}(\mathbf{k},\mathbf{q}) = \tfrac{4rx+3x^2-6rx^3-1}{2r^2(1+r^2-2rx)}, \qquad f_{23}(\mathbf{k},\mathbf{q}) = \tfrac{3(1-x^2)^2}{(1+r^2-2rx)^2},$$
$$f_{32}(\mathbf{k},\mathbf{q}) = \tfrac{(1-x^2)(2-12rx-3r^2+15r^2x^2)}{r^2(1+r^2-2rx)^2}, \qquad f_{33}(\mathbf{k},\mathbf{q}) = \tfrac{-4+12x^2+24rx-40rx^3+3r^2-30r^2x^2+35r^2x^4}{r^2(1+r^2-2rx)^2}.$$

Also we have kernels $g_{nm}(r)$:

$$g_{00}(r) = \frac{1}{3024}\left(\frac{12}{r^2} - 158 + 100r^2 - 42r^4 + \frac{3}{r^3}\left(r^2-1\right)^3\left(7r^2+2\right)\ln\left[\frac{r+1}{|r-1|}\right]\right),$$
$$g_{01}(r) = \frac{1}{3024}\left(\frac{24}{r^2} - 202 + 56r^2 - 30r^4 + \frac{3}{r^3}\left(r^2-1\right)^3\left(5r^2+4\right)\ln\left[\frac{r+1}{|r-1|}\right]\right),$$
$$g_{10}(r) = \frac{1}{1008}\left(-38 + 48r^2 - 18r^4 + \frac{9}{r}(r^2-1)^3\ln\left[\frac{r+1}{|r-1|}\right]\right),$$
$$g_{11}(r) = \frac{1}{1008}\left(\frac{12}{r^2} - 82 + 4r^2 - 6r^4 + \frac{3}{r^3}\left(r^2-1\right)^3\left(r^2+2\right)\ln\left[\frac{r+1}{|r-1|}\right]\right),$$
$$g_{02}(r) = \frac{1}{224}\left(\frac{2}{r^2}\left(r^2+1\right)\left(3r^4-14r^2+3\right) - \frac{3}{r^3}\left(r^2-1\right)^4\ln\left[\frac{r+1}{|r-1|}\right]\right),$$
$$g_{20}(r) = \frac{1}{672}\left(\frac{2}{r^2}\left(9-109r^2+63r^4-27r^6\right) + \frac{9}{r^3}\left(r^2-1\right)^3\left(3r^2+1\right)\ln\left[\frac{r+1}{|r-1|}\right]\right), \tag{5.115}$$

and all the rest vanish in next to leading order regime.

# Bibliography


[1] Z. Vlah, U. Seljak, P. McDonald, T. Okumura, and T. Baldauf, **Distribution function approach to redshift space distortions. Part IV: perturbation theory applied to dark matter**, *JCAP* **1211** (2012) 009, [arXiv:1207.0839].

[2] N. Kaiser, **Clustering in real space and in redshift space**, *Mon. Not. Roy. Astron. Soc.* **227** (1987) 1–27.

[3] A. Hamilton, **Linear redshift distortions: A Review**, astro-ph/9708102. Published in The Evolving Universe. Edited by D. Hamilton, Kluwer Academic, 1998, p. 185-275.

[4] S. Cole, K. B. Fisher, and D. H. Weinberg, **Fourier analysis of redshift space distortions and the determination of Omega**, *Mon.Not.Roy.Astron.Soc.* **267** (1994) 785, [astro-ph/9308003].

[5] M. White, Y.-S. Song, and W. J. Percival, **Forecasting Cosmological Constraints from Redshift Surveys**, *Mon.Not.Roy.Astron.Soc.* **397** (2008) 1348–1354, [arXiv:0810.1518].

[6] P. McDonald and U. Seljak, **How to measure redshift-space distortions without sample variance**, *JCAP* **0910** (2009) 007, [arXiv:0810.0323]. * Brief entry *.

[7] G. M. Bernstein and Y.-C. Cai, **Cosmology without cosmic variance**, arXiv:1104.3862.

[8] A. Amara and A. Refregier, **Optimal Surveys for Weak Lensing Tomography**, *Mon.Not.Roy.Astron.Soc.* **381** (2007) 1018–1026, [astro-ph/0610127].

[9] L. Casarini, S. A. Bonometto, S. Borgani, K. Dolag, G. Murante, et al., **Tomographic weak lensing shear spectra from large N-body and hydrodynamical simulations**, arXiv:1203.5251.

[10] R. Scoccimarro, **Redshift-space distortions, pairwise velocities and nonlinearities**, *Phys.Rev.* **D70** (2004) 083007, [astro-ph/0407214].

[11] A. Taruya, T. Nishimichi, and S. Saito, **Baryon Acoustic Oscillations in 2D: Modeling Redshift-space Power Spectrum from Perturbation Theory**, *Phys.Rev.* **D82** (2010) 063522, [arXiv:1006.0699].

[12] E. Jennings, C. M. Baugh, and S. Pascoli, **Modelling redshift space distortions in hierarchical cosmologies**, *Mon.Not.Roy.Astron.Soc.* **410** (2011) 2081, [arXiv:1003.4282].

[13] J. Tang, I. Kayo, and M. Takada, **Likelihood reconstruction method of real-space density and velocity power spectra from a redshift galaxy survey**, arXiv:1103.3614.

[14] J. L. Tinker, **Redshift-Space Distortions with the Halo Occupation Distribution II: Analytic Model**, *Mon.Not.Roy.Astron.Soc.* **374** (2007) 477–492, [astro-ph/0604217].

[15] T. Nishimichi and A. Taruya, **Baryon Acoustic Oscillations in 2D II: Redshift-space halo clustering in N-body simulations**, *Phys.Rev.* **D84** (2011) 043526, [arXiv:1106.4562].

[16] B. A. Reid and M. White, **Towards an accurate model of the redshift space clustering of halos in the quasilinear regime**, arXiv:1105.4165.

[17] M. Sato and T. Matsubara, **Nonlinear Biasing and Redshift-Space Distortions in Lagrangian Resummation Theory and N-body Simulations**, *Phys.Rev.* **D84** (2011) 043501, [arXiv:1105.5007].

[18] F. Bernardeau, S. Colombi, E. Gaztanaga, and R. Scoccimarro, **Large scale structure of the universe and cosmological perturbation theory**, *Phys.Rept.* **367** (2002) 1–248, [astro-ph/0112551].

[19] M. Crocce and R. Scoccimarro, **Renormalized cosmological perturbation theory**, *Phys.Rev.* **D73** (2006) 063519, [astro-ph/0509418].

[20] M. Crocce and R. Scoccimarro, **Memory of initial conditions in gravitational clustering**, *Phys.Rev.* **D73** (2006) 063520, [astro-ph/0509419].

[21] M. Crocce and R. Scoccimarro, **Nonlinear Evolution of Baryon Acoustic Oscillations**, *Phys.Rev.* **D77** (2008) 023533, [arXiv:0704.2783].

[22] T. Matsubara, **Resumming Cosmological Perturbations via the Lagrangian Picture: One-loop Results in Real Space and in Redshift Space**, *Phys.Rev.* **D77** (2008) 063530, [arXiv:0711.2521].

[23] T. Matsubara, **Nonlinear perturbation theory with halo bias and redshift-space distortions via the Lagrangian picture**, *Phys.Rev.* **D78** (2008) 083519, [arXiv:0807.1733].

[24] P. McDonald, **Dark matter clustering: a simple renormalization group approach**, *Phys.Rev.* **D75** (2007) 043514, [astro-ph/0606028].

[25] A. Taruya and T. Hiramatsu, **A Closure Theory for Non-linear Evolution of Cosmological Power Spectra**, arXiv:0708.1367.

[26] M. Pietroni, **Flowing with Time: a New Approach to Nonlinear Cosmological Perturbations**, *JCAP* **0810** (2008) 036, [arXiv:0806.0971].

[27] P. Valageas, **A new approach to gravitational clustering: a path-integral formalism and large-n expansions**, *Astron.Astrophys.* **421** (2004) 23–40, [astro-ph/0307008].

[28] A. Taruya, T. Nishimichi, S. Saito, and T. Hiramatsu, **Non-linear Evolution of Baryon Acoustic Oscillations from Improved Perturbation Theory in Real and Redshift Spaces**, *Phys.Rev.* **D80** (2009) 123503, [arXiv:0906.0507].

[29] U. Seljak and P. McDonald, **Distribution function approach to redshift space distortions**, arXiv:1109.1888.

[30] T. Okumura, U. Seljak, P. McDonald, and V. Desjacques, **Distribution function approach to redshift space distortions: N-body simulations**, arXiv:1109.1609.

[31] P. J. E. Peebles, **Principles of physical cosmology**, . Princeton, USA: Univ. Pr. (1993) 718 p.

[32] V. Desjacques, U. Seljak, and I. Iliev, **Scale-dependent bias induced by local non-Gaussianity: A comparison to N-body simulations**, arXiv:0811.2748.

[33] J. Carlson, M. White, and N. Padmanabhan, **A critical look at cosmological perturbation theory techniques**, *Phys. Rev.* **D80** (2009) 043531, [arXiv:0905.0479].

[34] S. Tassev and M. Zaldarriaga, **The Mildly Non-Linear Regime of Structure Formation**, arXiv:1109.4939.

[35] D. J. Eisenstein and W. Hu, **Baryonic Features in the Matter Transfer Function**, *Astrophys. J.* **496** (1998) 605, [astro-ph/9709112].

[36] P. McDonald, **How to generate a significant effective temperature for cold dark matter, from first principles**, *JCAP* **1104** (2011) 032, [arXiv:0910.1002].

[37] U. Seljak, **Analytic model for galaxy and dark matter clustering**, *Mon.Not.Roy.Astron.Soc.* **318** (2000) 203, [astro-ph/0001493].

[38] J. Peacock and R. Smith, **Halo occupation numbers and galaxy bias**, *Mon.Not.Roy.Astron.Soc.* **318** (2000) 1144, [astro-ph/0005010].

[39] C.-P. Ma and J. N. Fry, **What does it take to stabilize gravitational clustering?**, astro-ph/0005233.

[40] A. A. Berlind, D. H. Weinberg, A. J. Benson, C. M. Baugh, S. Cole, et al., **The Halo occupation distribution and the physics of galaxy formation**, *Astrophys.J.* **593** (2003) 1–25, [astro-ph/0212357].

[41] A. Cooray and R. K. Sheth, **Halo models of large scale structure**, *Phys.Rept.* **372** (2002) 1–129, [astro-ph/0206508].

[42] U. Seljak, **Constraints on galaxy halo profiles from galaxy-galaxy lensing and tully-fisher/fundamental plane relations**, *Mon.Not.Roy.Astron.Soc.* **334** (2002) 797, [astro-ph/0201450].

[43] R. K. Sheth and G. Tormen, **Large scale bias and the peak background split**, *Mon.Not.Roy.Astron.Soc.* **308** (1999) 119, [astro-ph/9901122].

[44] T. Okumura, U. Seljak, and V. Desjacques, **Distribution function approach to redshift space distortions, Part III: halos and galaxies**, arXiv:1206.4070.

# Chapter 6

# Redshift Space Distortions. Part III: Biased Objects [1]

Numerical simulations show that redshift space distortions (RSD) introduce strong scale dependence in the power spectra of halos, with ten percent deviations relative to linear theory predictions even on relatively large scales ($k < 0.1h/Mpc$) and even in the absence of satellites (which induce Fingers-of-God, FoG, effects). If unmodeled these effects prevent one from extracting cosmological information from RSD surveys. In this paper we use Eulerian perturbation theory (PT) and Eulerian halo biasing model and apply it to the distribution function approach to RSD, in which RSD is decomposed into several correlators of density weighted velocity moments. We model each of these correlators using PT and compare the results to simulations over a wide range of halo masses and redshifts. We find that with an introduction of a physically motivated halo biasing, and using dark matter power spectra from simulations, we can reproduce the simulation results at a percent level on scales up to $k \sim 0.15h/Mpc$ at $z = 0$, without the need to have free FoG parameters in the model.

## 6.1 Introduction

Galaxy clustering surveys are one of the most important venues of extracting cosmological information today. The reason is that by measuring the 3 dimensional distribution of galaxies we can in principle relate it to the 3 dimensional distribution of the underlying dark matter, and dark matter distribution is sensitive to many of the cosmological parameters. Growth of dark matter structures in time also provides important constraints on the models, such as the nature and amount of dark energy in the Universe. Since galaxies are not the perfect tracers of dark matter, their clustering is biased relative to the dark matter. This means that galaxy surveys cannot determine the rate of growth of structure unless this biasing is determined. Fortunately, galaxy redshift surveys provide additional information, because the observed redshift is a sum of the radial distance to the galaxy and its peculiar velocity (Doppler shift). Galaxies are expected to follow the same gravitational potential as the dark matter and thus are expected to have the same velocity (in a large-scale average at least). This leads to a clustering strength that depends on the angle between the galaxy pairs and the line of sight, which is referred to as redshift space distortions (RSD). In linear theory this can be easily related to the dark matter clustering [2, 3]. These distortions thus make the galaxy clustering in redshift space more complex, but at the same time provide an opportunity to extract important information on the dark matter clustering directly from the redshift surveys. To what extent this is possible is still a matter of debate: there are significant nonlinear effects that spoil this picture, once one goes beyond the very large

[1] This chapter is based on a paper by Z. Vlah, U. Seljak, T. Okumura, V. Desjacques published in the JCAP, Vol. 1310, [1].

scales. The goal of this paper is to explore these nonlinear effects using analytic modeling.

Velocity induced RSD are usually decomposed into two competing effects: anisotropies along the line of sight due to the large coherent motion, so called Kaiser effect, and random motions in virialized objects, known as the Finger-of-God effect (FoG) [4]. Because of the large coherent motions the RSD anisotropies offer a unique way to measure growth rate of structure formation [5], and also can provide tests of dark energy models and general relativity [6, 7, 8, 9, 10, 11, 12, 13]. If good understanding of the nonlinear effects were achieved, RSD would be the most powerful technique for these studies because of the fact that redshift surveys provide 3-dimensional information, while other methods, such as weak lensing, only provide projected 2-dimensional information (or slightly more if the so-called tomographic information is used [14]).

In the past many studies have been performed investigating these nonlinear effects [15, 16, 17, 18, 19, 20, 21, 22]. Some of these methods use analysis and modelling based on perturbation theory (for overview see [23, 24]), but none attempt to rely entirely on perturbation theory to explain all of the effects. Instead, they use ansatzes with free parameters, so that if the ansatz are accurate one can model the effects accurately. Separately, there have been many approaches trying to improve perturbation methods and to increase their ranges of validity [25, 26, 27, 28, 29, 30, 31, 32, 33, 34, 35, 36, 37]. Going beyond the dark matter modelling to the dark matter halos and galaxies introduces another layer of complication. Dark matter halos are biased relative to the underling dark matter and in order to describe them biasing models have to be introduced. Many models have been introduced in order to describe this relation [38, 39, 40, 41, 42], and some have also been included in RSD studies [43, 44, 45, 46, 47, 48, 49, 50, 51].

Distribution function approach to modelling the RSD has recently been developed [52] as a systematic way to study the nonlinear effects in RSD, by decomposing RSD effects into a series of mass-weighted powers of velocity correlators. This approach has been utilized for the dark matter case using the N-body simulations [53] and each of the constituent terms has been modeled in PT [54]. This model naturally generalizes to the dark matter halos, which have been analyzed using the N-body simulations in [55]. It has been shown that halo clustering in redshift space has a scale dependence relative to linear theory that is stronger than in real space. The goal of this paper is to explain this using Eulerian perturbation theory (PT) modelling applied to the halos. We adopt the local Eulerian biasing model as a tool to connect the underlying dark matter distribution to the halos, but we also explore effects beyond the local biasing model, probing the effects of higher order nonlocal terms [40, 56].

The paper is organized as follows: we begin in Sec.6.2 by generalizing the distribution function approach to RSD for dark matter halo case. We then introduce the biasing model, and applying it to model the velocity moment correlators. In Sec. 6.3 we collect all the modelled terms and investigate the total RSD power spectrum results. We compare the results to the multipoles in Fourier space as well as in configuration space. Results are compared to the N-body simulation measurements presented in [55].

For this work, flat ΛCDM model is assumed $\Omega_{\rm m} = 0.279$, $\Omega_\Lambda = 0.721$, $\Omega_{\rm b}/\Omega_{\rm m} = 0.165$, $h = 0.701$, $n_s = 0.96$, $\sigma_8 = 0.807$. The primordial density field is generated using the matter transfer function by CAMB. The positions and velocities of all the dark matter halos are given at the redshifts $z = 0,\ 0.509,\ 0.989$, and 2.070, which are for simplicity quoted as $z$ =0, 0.5, 1, and 2.

## 6.2 Redshift-space distortions from the distribution function

### 6.2.1 Definitions and starting equations

Following the recent work on phase space approach to redshift space distortions [52, 53, 55, 54], distribution function expansion developed for dark matter can be generalized to the dark matter halos. We can write for halo overdensity field in redshift space

$$\delta_s^h(\mathbf{k}) = \delta^h(\mathbf{k}) + \sum_{j=1} \frac{1}{j!} \left(\frac{ik_\parallel}{\mathcal{H}}\right)^j \mathcal{F}\left[\left(1+\delta^h(\mathbf{x})\right) u_\parallel^j(\mathbf{x})\right](\mathbf{k}), \tag{6.1}$$

where $u_\parallel$ is the halo velocity field projected along the line of sight, and $k_\parallel$ projection of the Fourier mode along the line of sight direction. Also $\mathcal{F}$ stands for the Fourier transformation defined in this paper as;

$$\begin{aligned} \tilde{f}(\mathbf{k}) &= \mathcal{F}\left[f(\mathbf{x})\right](\mathbf{k}) = \int d^3x \, \exp(i\mathbf{k}\cdot\mathbf{x}) f(\mathbf{x}), \\ f(\mathbf{x}) &= \mathcal{F}^{-1}\left[\tilde{f}(\mathbf{k})\right](\mathbf{x}) \int \frac{d^3k}{(2\pi)^3} \exp(-i\mathbf{k}\cdot\mathbf{x}) \tilde{f}(\mathbf{k}). \end{aligned} \tag{6.2}$$

Using the halo filed expression we can define the dark matter halo-halo power spectrum in redshift-space

$$(2\pi)^3 P_s^{(hh)}(\mathbf{k}) \delta^D(\mathbf{k}-\mathbf{k}') = \left\langle \delta_s^h(\mathbf{k}) \delta_s^{*h}(\mathbf{k}') \right\rangle. \tag{6.3}$$

Dark matter halos are considered to be biased tracers of the underlying dark matter. Identifying the correct biasing model has been proven to be a challenging task, and there is still a lot of ongoing work on this subject. In the standard local bias approach the halo field can be considered as a functional of the underlying dark matter density field $\delta^h[\delta]$. In addition to the local relation of the constructed halo field and the underlying matter overdensity field one can also expect nonlocal effects ([39]). For example, in [40, 41, 56] effects of the tidal tensor biasing have been considered. In this paper we adopt the model presented in [56] where the only nonlocal term is due to the second order tidal tensor, which is added to the standard Taylor expansion of local bias, which we expand to 2nd order. We will see that the tidal tensor bias term does not play the crucial role in modeling the two point statistic of biased object as has already been shown in [41], but we will nevertheless keep the term in the following expressions. In addition, the third order nonlocal term may also play an important role in explaining the biasing effects in two point halo statistics studied in this paper. We will include this possibility here in a simplified model, deferring a more detailed analysis to a future paper. In addition to the nonlocal density contributions there are also potential velocity bias effects which, if present, might be important in modelling the halo velocity moments. This is a subject of ongoing studies using initial density peaks [57, 58]. Clear results from these studies are still to be determined and so we will not include this possibility here. Finally, there are also the effects of exclusion which were emphasized recently in [59]. We will include them in a simplified model.
We use Eulerian biasing model

$$\delta^h(\mathbf{x}) = b_1\delta(\mathbf{x}) + \frac{b_2}{2}\left(\delta^2(\mathbf{x}) - \left\langle\delta^2\right\rangle\right) + \frac{b_s}{2}\left(s^2(\mathbf{x}) - \left\langle s^2\right\rangle\right) + \frac{b_3}{6}\delta^3(\mathbf{x}), \tag{6.4}$$

where $\delta$ is underlying dark matter overdensity field, and $b_i$ are the coresponding bias parameters. We also add the nonlocal biasing term $b_s$ presented in [56], and more extensively studied in [40],

$$s^2(\mathbf{k}) = \int \frac{d^3q}{(2\pi)^3} S^{(2)}(\mathbf{q}, \mathbf{k}-\mathbf{q}) \delta(\mathbf{q}) \delta(\mathbf{k}-\mathbf{q}), \qquad S^{(2)}(\mathbf{k},\mathbf{q}) = \frac{(\mathbf{k}\cdot\mathbf{q})^2}{q^2k^2} - \frac{1}{3}. \tag{6.5}$$

From now on we will use the abbreviations for the integrations of the convolution form

$$(U \circ V)_{\mathbf{k}} = \int \frac{d^3q}{(2\pi)^3} U(\mathbf{q}) V(\mathbf{k}-\mathbf{q}) = U_{\mathbf{q}} V_{\mathbf{k}-\mathbf{q}} \tag{6.6}$$

in order to make following expressions shorter. To use this biasing model we need to preform Fourier transformation, which leads to

$$\delta^h_{\mathbf{k}} = b_1 \delta_{\mathbf{k}} + \frac{b_2}{2} \delta_{\mathbf{q}} \delta_{\mathbf{k}-\mathbf{q}} + \frac{b_s}{2} s^2_{\mathbf{k}} + \frac{b_3}{6} \delta_{\mathbf{q}} \delta_{\mathbf{q}'} \delta_{\mathbf{k}-\mathbf{q}-\mathbf{q}'}, \tag{6.7}$$

and for the higher moments of phase space distribution function

$$T^h_L = T^{h,\parallel}_L(\mathbf{k}) \equiv \mathcal{F}\left[1/\bar{\rho} \int d^3q \; f_h(\mathbf{x},\mathbf{q}) q^L_\parallel\right], \tag{6.8}$$

where $f_h$ is the phase space distribution function of halos. This gives

$$\left\langle T^h_L \right| = \Big[ \left(1 - \sigma^2 b_2/2 - \sigma^2_s b_s/2\right) \langle 1| + b_1 \langle \delta| + \frac{b_2}{2} \left\langle \delta^2\right| + \frac{b_s}{2} \left\langle s^2\right| + \frac{b_3}{6} \left\langle \delta^3\right| \Big] | \circ u^L_\parallel |. \tag{6.9}$$

If we have curl free velocity fields we can write $u^\parallel_{\mathbf{k}} = i \frac{k_\parallel}{k^2} \theta_{\mathbf{k}}$.

### 6.2.2 Halo power spectrum expression

Using expressions 6.7 and 6.9 for the halo overdensity and higher moments fields and definition for the halo power spectrum in redshift space, $P^{(hh)}_{ss}$, we get;

$$\begin{aligned} P^{(hh)}_{ss,\mathbf{k}} &= \sum_{L=0} \sum_{L'=0} \frac{(-1)^{L'}}{L!L'!} \left(\frac{ik_\parallel}{\mathcal{H}}\right)^{L+L'} P^{(hh)}_{LL',\mathbf{k}} \\ &= \sum_{L=0} \frac{1}{(L!)^2} \left(\frac{k\mu}{\mathcal{H}}\right)^{L+L'} P^{(hh)}_{LL,\mathbf{k}} + 2Re \sum_{L=0} \sum_{L'>L} \frac{(-1)^{L'}}{L!L'!} \left(\frac{ik\mu}{\mathcal{H}}\right)^{L+L'} P^{(hh)}_{LL',\mathbf{k}}. \end{aligned} \tag{6.10}$$

where $k_\parallel/k = \cos\theta = \mu$ and we define

$$(2\pi)^3 P^{(hh)}_{LL'}(\mathbf{k}) \delta^D(\mathbf{k}-\mathbf{k}') = \left\langle T^h_L(\mathbf{k}) \left| T^{h*}_{L'}(\mathbf{k}') \right\rangle \right. . \tag{6.11}$$

In this paper we will consider terms that contribute up to one loop in Eulerian PT, so we have the contributing terms

$$\begin{aligned} P^{(hh)}_{ss,\mathbf{k}} =& P^{(hh)}_{00,\mathbf{k}} + \left(\frac{k\mu}{\mathcal{H}}\right)^2 P^{(hh)}_{11,\mathbf{k}} + \frac{1}{4}\left(\frac{k\mu}{\mathcal{H}}\right)^4 P^{(hh)}_{22,\mathbf{k}} \\ &+ 2\mathrm{Re}\left[\left(\frac{-ik\mu}{\mathcal{H}} P^{(hh)}_{01,\mathbf{k}}\right) + \left(-\frac{1}{2}\left(\frac{k\mu}{\mathcal{H}}\right)^2 P^{(hh)}_{02,\mathbf{k}}\right) + \left(\frac{i}{6}\left(\frac{k\mu}{\mathcal{H}}\right)^3 P^{(hh)}_{03,\mathbf{k}}\right)\right. \\ &\left. + \left(-\frac{i}{2}\left(\frac{k\mu}{\mathcal{H}}\right)^3 P^{(hh)}_{12,\mathbf{k}}\right) + \left(-\frac{1}{6}\left(\frac{k\mu}{\mathcal{H}}\right)^4 P^{(hh)}_{13,\mathbf{k}}\right) + \left(\frac{1}{24}\left(\frac{k\mu}{\mathcal{H}}\right)^4 P^{(hh)}_{04,\mathbf{k}}\right)\right]. \end{aligned} \tag{6.12}$$

Strictly speaking $P^{(hh)}_{04}$ is of the higher order, but has been proven to be significant [54], so we are including it in the model. As it is discussed in [52, 54], going to higher order in this expression we introduce higher order velocity moments. Since in our biasing model we assume no velocity biasing, at 1-loop level higher order terms will give small difference from the linear biasing model from dark matter halo power spectrum. Terms in which the nonlinear biasing model plays a substantial difference at 1-loop level treatment are $P^{(hh)}_{00}$, $P^{(hh)}_{01}$, $P^{(hh)}_{02}$, $P^{(hh)}_{11}$. In the following part of this section we are considering these terms in more detail.

### 6.2.3 Halo-matter $P_{00}^{(hm)}$ power spectrum

First we consider the $P_{00}^{(h\bar{h})}$ term, the real space power spectrum. Formally we make the distinction between two halo tracers labeling the second bias coefficients with the bar. This term is isotropic and does not have $\mu$ dependence. We will first model the cross-correlation with the matter. For convenience we use the different biasing coefficients for autocorrelation of the halo overdensity field,

$$\begin{aligned}\left\langle \delta^h|\delta^{\bar{h}}\right\rangle &= b_1\bar{b}_1\left\langle\delta|\delta\right\rangle + \frac{1}{4}b_2\bar{b}_2\left\langle\delta^2|\delta^2\right\rangle + \frac{1}{4}b_s\bar{b}_s\left\langle s^2|s^2\right\rangle + \frac{1}{36}b_3\bar{b}_3\left\langle\delta^3|\delta^3\right\rangle \\ &+ \{b_1,b_2\}\left\langle\delta|\delta^2\right\rangle + \frac{1}{3}\{b_1,b_3\}\left\langle\delta|\delta^3\right\rangle + \frac{1}{6}\{b_2,b_3\}\left\langle\delta^2|\delta^3\right\rangle \\ &+ \{b_1,b_s\}\left\langle\delta|s^2\right\rangle + \frac{1}{2}\{b_2,b_s\}\left\langle\delta^2|s^2\right\rangle + \frac{1}{6}\{b_3,b_s\}\left\langle\delta^3|s^2\right\rangle \end{aligned} \tag{6.13}$$

where we have the anticommutator defined as $\{a,b\} = (a\bar{b}+b\bar{a})/2$. Keeping different biasing coefficients enables us to use this result also for the matter-halo cross spectrum $P_{00}^{(hm)}$ by choosing $b_1 = 1$, and $b_2 = b_s = b_3 = 0$ for dark matter. For the matter-halo cross spectrum it follows

$$\left\langle \delta^m|\delta^h\right\rangle = b_1\left\langle\delta|\delta\right\rangle + \frac{1}{2}b_2\left\langle\delta|\delta^2\right\rangle + \frac{1}{2}b_s\left\langle\delta|s^2\right\rangle + \frac{1}{6}b_3\left\langle\delta|\delta^3\right\rangle. \tag{6.14}$$

We restrict our consideration to the 1-loop PT modelling at this level, and use bias renormalization techniques presented in [30]. The same bias renormalization is also used in all the other terms at the 1-loop level. At this order the relevant bias terms are

$$\begin{aligned}&\langle\delta_{\mathbf{k}}|\delta_{\mathbf{k}'}\rangle \sim P_{00,\mathbf{k}}, \\ &\left\langle\delta_{\mathbf{k}}|\delta^2_{\mathbf{k}'}\right\rangle \sim 2F^{(2)}_{\mathbf{q},\mathbf{k}-\mathbf{q}}P^{(L)}_{\mathbf{q}}P^{(L)}_{\mathbf{k}-\mathbf{q}} + 2\frac{34}{21}P^{(L)}_{\mathbf{k}}\sigma^2, \\ &\left\langle\delta_{\mathbf{k}}|\delta^3_{\mathbf{k}'}\right\rangle \sim 3\sigma^2 P_{00,\mathbf{k}}, \\ &\left\langle\delta_{\mathbf{k}}|s^2_{\mathbf{k}'}\right\rangle \sim 2F^{(2)}_{\mathbf{q},\mathbf{k}-\mathbf{q}}S^{(2)}_{\mathbf{q},\mathbf{k}-\mathbf{q}}P^{(L)}_{\mathbf{q}}P^{(L)}_{\mathbf{k}-\mathbf{q}}, \end{aligned} \tag{6.15}$$

where $\sim$ symbol means that we have dropped $(2\pi)^3\delta^D(\mathbf{k}-\mathbf{k}')$ factor from the left hand site of the relations above. From this follows for the cross power spectrum

$$P^{(hm)}_{00,\mathbf{k}} = \left(b_1 + b_2\frac{34}{21}\sigma^2 + \frac{b_3}{2}\sigma^2\right)P_{00,\mathbf{k}} + b_2K_{00,\mathbf{k}} + b_sK^s_{00,\mathbf{k}}, \tag{6.16}$$

where we have

$$\begin{aligned}K_{00,\mathbf{k}} &\equiv P^{(L)}_{\mathbf{q}}P^{(L)}_{\mathbf{k}-\mathbf{q}}F^{(2)}_{\mathbf{q},\mathbf{k}-\mathbf{q}}, \\ K^s_{00,\mathbf{k}} &\equiv P^{(L)}_{\mathbf{q}}P^{(L)}_{\mathbf{k}-\mathbf{q}}F^{(2)}_{\mathbf{q},\mathbf{k}-\mathbf{q}}S^{(2)}_{\mathbf{q},\mathbf{k}-\mathbf{q}}\end{aligned} \tag{6.17}$$

where $F^{(2)}$ is the standard overdensity kernel in Eulerian PT (e.g. [23, 54]) and $S^{(2)}$ kernel is defined in equation 6.5. Using the bias renormalisation

$$\begin{aligned}b_1 \to b_1' &= b_1 + \frac{34}{21}\sigma^2 b_2 + \frac{1}{2}\sigma^2 b_3, \\ b_2 \to b_2' &= b_2, \\ b_s \to b_s' &= b_s,\end{aligned} \tag{6.18}$$

we get

$$P^{(hm)}_{00,\mathbf{k}} = b_1P_{00,\mathbf{k}} + b_2K_{00,\mathbf{k}} + b_sK^s_{00,\mathbf{k}}. \tag{6.19}$$

For halo-halo power spectrum we can take $\bar{b} = b$, and then in addition to the terms in 6.17 we have

$$\left\langle\delta^2_k|\delta^2_{k'}\right\rangle \sim 2P^{(L)}_{\mathbf{q}}P^{(L)}_{\mathbf{k}-\mathbf{q}} \equiv 2K_{01,\mathbf{k}},$$

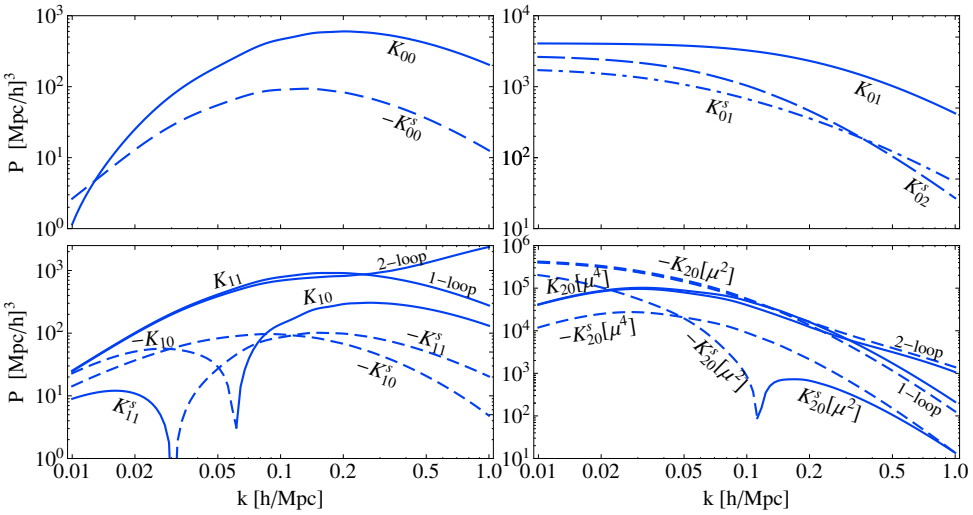


**Figure 6.1:** $K_{ij}$ terms using one loop PT results, and also two loop results for some of these terms. The terms proportional to $b_s$ are denoted with a subscript $s$ and can be compared to the term proportional to $b_2$. Solid lines are for positive values and dashed are for negative.

$$\begin{aligned}\left\langle s_k^2 | s_{k'}^2 \right\rangle &\sim 2\left(S^{(2)}_{\mathbf{q},\mathbf{k}-\mathbf{q}}\right)^2 P^{(L)}_{\mathbf{q}} P^{(L)}_{\mathbf{k}-\mathbf{k}} \equiv 2K^s_{01,\mathbf{k}},\\ \left\langle \delta_k^2 | s_{k'}^2 \right\rangle &\sim 2S^{(2)}_{\mathbf{q},\mathbf{k}-\mathbf{q}} P^{(L)}_{\mathbf{q}} P^{(L)}_{\mathbf{k}-\mathbf{q}} \equiv 2K^s_{02,\mathbf{k}},\end{aligned} \tag{6.20}$$

after the renormalization this gives

$$P^{(hh)}_{00,\mathbf{k}} = b_1^2 P_{00,\mathbf{k}} + 2b_1\left[b_2 K_{00,\mathbf{k}} + b_s K^s_{00,\mathbf{k}}\right] + \frac{1}{2}\left[b_2^2 K_{01,\mathbf{k}} + b_s^2 K^s_{01,\mathbf{k}}\right] + b_2 b_s K^s_{02,\mathbf{k}}. \tag{6.21}$$

This expression still lacks the stochasticity terms coming from the discreteness of the halos, such as the Poisson shot noise or its generalizations, discussed further below.

### Nonlinear bias terms $K_{ij}$

Modelling the biasing of dark matter halos beyond the linear bias $b_1$ introduces additional 1-loop terms in perturbative approach. These terms are labeled here with $K_{ij}$ and will show up in the first few moment power spectra $P^{hh}_{00}, P^{hh}_{01}, P^{hh}_{02}$, where $b_2$, $b_s$ and $b_{3,nl}$ (the nonlocal third order bias [39, 41, 60]) appear at 1-loop level. In figure 6.1 we show the k-dependence of $K_{ij}$ terms. The relative contribution of these terms depends on the amplitudes of $b_2$, $b_s$ and $b_{3,nl}$. For example, one can use the values of $b_2$, $b_s$ from bispectrum [56, 41], where $b_s$ terms are small relative to the $b_2$. Taking into account also the $k$-dependence of these terms we can see that effectively $b_s$ effects can be absorbed in the renormalized $b_2$ value. For $b_{3,nl}$ the corresponding trispectrum analysis has not been performed yet, but a power spectrum analysis together with the coevolution values [60] suggests that it can be important relative to $b_2$.

Over a limited range of interest where these terms matter and we are not too deeply into nonlinear regime, $0.05h/Mpc < k < 0.2h/Mpc$, these terms can be organised (considering the $k$-dependences and relative amplitudes) in a way that for each statistics we can define a single effective nonlinear bias parameter. In case of $P_{00}$ we will denote it $b_2^{00}$, and in case of $P_{01}$, $b_2^{01}$.

### Effective model for halo-halo power spectrum $P^{(hh)}_{00}$

Following the arguments from previous section we will absorb $b_s$ and $b_{3,nl}$ terms into $b_2$ and omit them from the analysis of $P^{hh}_{00}$ in this section. For a complete model of $P^{hh}_{00}$ from $P^{hm}_{00}$

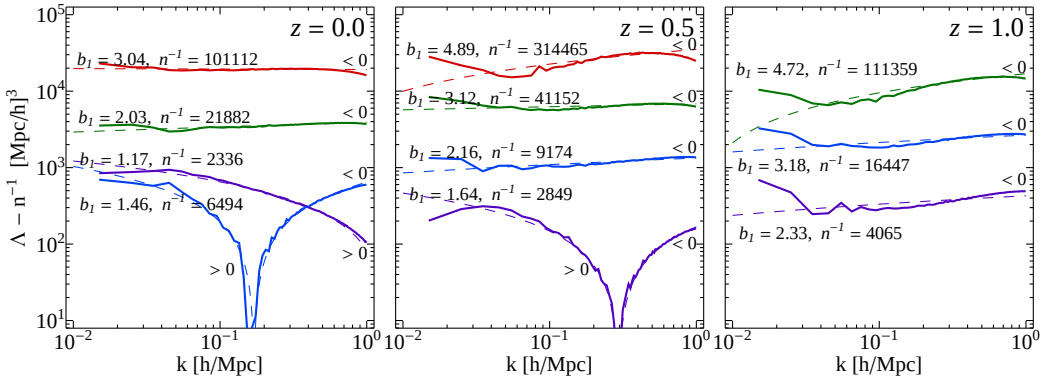


**Figure 6.2:** The stochasticity as measured from the simulations, once the Poisson shot noise is subtracted (full lines). Four different mass bins are shown at the redshift $z = 0.0$ and $z = 0.5$ and three at the redshift $z = 1.0$. Most of the plotted lines are negative, i.e. stochasticity is sub-Poissonian, except for the lowest mass bins at redshift $z = 0.0$ and $z = 0.5$ which are positive on large scales. Simple model from equation 6.23 is also shown (dashed lines).

we need to model the stochasticity term,

$$\Lambda(k) = P^{(hh)}_{00,\mathbf{k}} - 2b_1 P^{(hm)}_{00,\mathbf{k}} + b_1^2 P^{(mm)}_{00,\mathbf{k}}. \tag{6.22}$$

This term has recently been studied extensively in [59], where it is denoted as the diagonal term of the stochasticity matrix $C_{ij}$. In the simplest models the stochasticity is given by the Poisson shot noise $\bar{n}^{-1}$, where $\bar{n}$ is the halo number density. As discussed in [59], there are deviations from this prediction sourced by both the halo exclusion and the nonlinear clustering of halos relative to dark matter: the latter can be seen from upper right panel of figure 6.1, where we see that all the terms are constant at low $k$, suggesting a white noise contribution at low $k$. Similarly, imposing a finite radius on halos lowers the stochasticity in the low $k$ limit below the Poisson $\bar{n}^{-1}$ value. In the $k \to 0$ limit one can determine from the clustering of halos in initial conditions: the dominant positive contribution comes from local biasing of initial halos and the negative contribution comes from exclusion. This limit does not change when evolving halos from initial to final redshift. The scale dependence of this term however changes from initial to final redshift and the theoretical modeling is still poorly understood. In this paper we add this model for the stochastic noise to our PT model of RSD and compare the result to the simulations. These shot noise effects are isotropic so the term does not have $\mu$ dependence. It affects only the modelling of $P^{(hh)}_{00}$ term, while all the higher order velocity moments contributions to RSD power spectra are independent of it. To determine it we use the N-body simulation measurements presented in [53, 55]. In figure 6.2 we show the results for $\Lambda(k)$ as measured from simulations, subtracting out the Poisson shot noise $\bar{n}^{-1}$ (which are given in [55]). From the figure we see that deviations from Poisson model are of order 10-20% at low $k$ and thus cannot be neglected. Most of the plotted lines are negative, i.e. the measured stochasticity is sub-Poissonian, except for the lowest mass bins at redshift $z = 0.0$ and $z = 0.5$, where it is positive on large scales. As discussed in [61, 59] this is because exclusion dominates over nonlinear biasing for higher mass halos, while the opposite is true at low masses.

To model this $k$ dependence on the scales of interest we propose a simple model

$$\Lambda - \bar{n}^{-1} = \lambda + p \log k, \tag{6.23}$$

where we fit for the values of $\lambda$ and $p$ and show the results in the same figure 6.2 as dashed lines. We see that this reproduces the measurements over a broad range of $k$ values, specially around $k \sim 0.1h/Mpc$, where its effects are most important.

In figure 6.3 we show the scale dependence of the halo-matter cross power spectrum $P^{(hm)}_{00}$ for several mass bins, at redshifts $z = 0.0$, $z = 0.5$ and $z = 1.0$. We fit for an effective

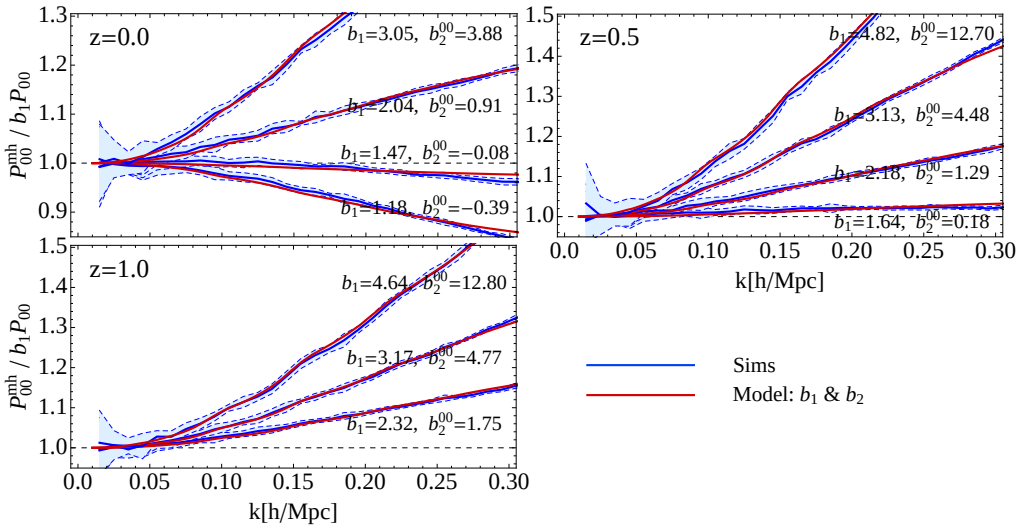


**Figure 6.3:** Scale dependence of halo-matter cross power spectrum $P_{00}^{(hm)}$ is shown for several mass bins, at reshifts $z = 0.0$, $z = 0.5$ and $z = 1.0$. Simulation measurements (blue solid line) are shown, as well as the results of the model presented in the text. We have fitted for $b_2$ that reproduces best simulation measurements. All the lines are divided by $b_1$ times the dark matter power spectrum from simulations.

$b_2^{00}$ parameter to reproduce simulation measurements on the scales of interest and use these values then to model $P_{00}^{(hh)}$. In figure 6.4 we show the scale dependence of halo-halo auto power spectrum $P_{00}^{(hh)}$ for the same mass bins as before, at reshifts $z = 0.0$, $z = 0.5$ and $z = 1.0$. Using the stochasticity model presented above we evaluate it from

$$P_{00,\mathbf{k}}^{(hh)} = 2b_1 P_{00,\mathbf{k}}^{(hm)} - b_1^2 P_{00,\mathbf{k}}^{(mm)} + \Lambda(k). \tag{6.24}$$

In this model we also use simulation predictions for dark matter $P_{00}^{(mm)}$ term at each of the redshifts.

### 6.2.4 $P_{01}^{(hh)}$

Next we consider a correlation of the halo field and the halo momentum field. This term has only a scalar contribution and is the leading term in the $\mu^2$ dependence of the total redshift power spectrum, as was shown in [52, 54]. Here we generalize this terms to halos. Using definitions of the halo density 6.7 and momentum fields 6.9 we get

$$\begin{aligned}\left\langle \delta^h | T_1^{\bar{h}} \right\rangle = b_1 \left\langle \delta | (1+\bar{b}_1\delta) u_\parallel \right\rangle + \frac{1}{2}\Big[ b_2 \left\langle \delta^2 | u_\parallel \right\rangle + b_s \left\langle s^2 | u_\parallel \right\rangle \Big] + \frac{1}{2} b_1 \bar{b}_2 \left\langle \delta | \delta^2 v_\parallel \right\rangle_c \\ + \frac{1}{2}\bar{b}_1 \Big[ b_2 \left\langle \delta^2 | \delta u_\parallel \right\rangle + b_s \left\langle s^2 | \delta u_\parallel \right\rangle \Big] + \frac{1}{4} b_2 \bar{b_2} \left\langle \delta^2 | \delta^2 v_\parallel \right\rangle_c + \frac{1}{6} b_3 \left\langle \delta^3 | u_\parallel \right\rangle_c ,\end{aligned} \tag{6.25}$$

where we have used the same renormalization scheme as for $P_{00}^{(hh)}$ term. Subscript $c$ stands for the connected part of the correlator, while the disconnected parts get renormalized. Keeping the terms at one loop order we get for the power spectrum,

$$P_{01,\mathbf{k}}^{(h\bar{h})} = b_1 \bar{b}_1 P_{01,\mathbf{k}} + b_1(1-\bar{b}_1)\alpha P_{\delta\theta,\mathbf{k}} + \alpha \Big[ b_2 K_{10,\mathbf{k}} + b_s K_{10,\mathbf{k}}^s \Big] + \alpha \bar{b}_1 \Big[ b_2 K_{11,\mathbf{k}} + b_s K_{11,\mathbf{k}}^s \Big], \tag{6.26}$$

where we have $\alpha = -i\mu/k$. Using the PT to evaluate the contributions of nonlinear biasing terms we get

$$K_{10,\mathbf{k}} \equiv P_{\mathbf{q}}^{(L)} P_{\mathbf{k}-\mathbf{q}}^{(L)} G_{\mathbf{q},\mathbf{k}-\mathbf{q}}^{(2)},$$

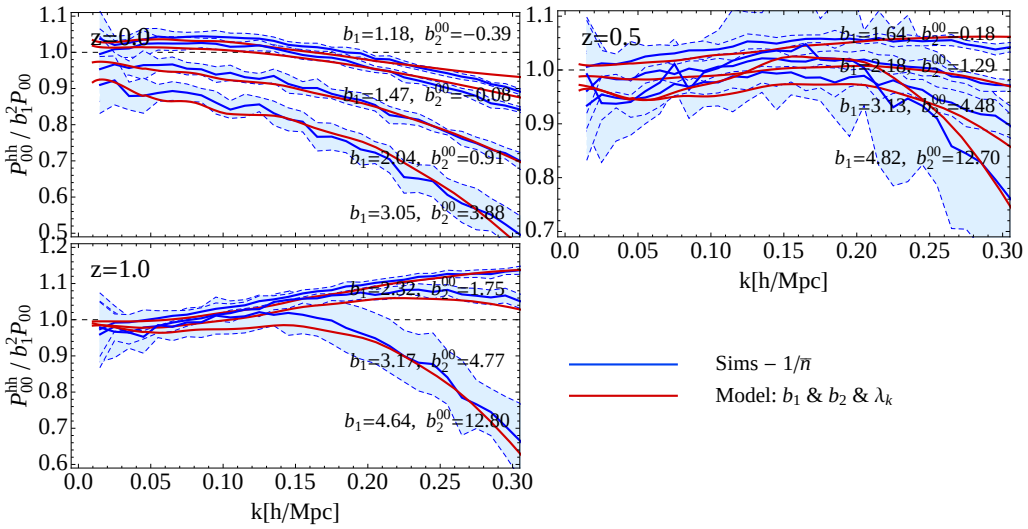


**Figure 6.4:** Scale dependence of halo-halo auto power spectrum $P_{00}^{(hh)}$ shown for several mass bins, at reshifts $z = 0.0$, $z = 0.5$ and $z = 1.0$. Simulation measurements (blue solid line) are shown, as well as the results of the model presented in the text. All the lines are divided by the $b_1^2$ times the dark matter power spectrum from the simulations.

$$
\begin{aligned}
K^s_{10,\mathbf{k}} &\equiv P^{(L)}_{\mathbf{q}} P^{(L)}_{\mathbf{k-q}} G^{(2)}_{\mathbf{q},\mathbf{k-q}} S^{(2)}_{\mathbf{q},\mathbf{k-q}}, \\
K_{11,\mathbf{k}} &\equiv \frac{kx}{q} P^{(L)}_{\mathbf{q}} P^{(L)}_{\mathbf{k-q}}, \\
K^s_{11,\mathbf{k}} &\equiv \frac{kx}{q} P^{(L)}_{\mathbf{q}} P^{(L)}_{\mathbf{k-q}} S^{(2)}_{\mathbf{q},\mathbf{k-q}},
\end{aligned}
\tag{6.27}
$$

where again the integration over $q$ variable is implied and $G^{(2)}$ is the standard kernel of velocity divergence in Eulerian PT (e.g. [23, 54]). In figure 6.5 we show the results for halo-halo $P_{01}$ modelling, and comparison to the N-body simulation results. The model presented in 6.26 contains dark matter parts, $P_{01}$ and $P_{\delta\theta}$ that were already extensively discussed in [54]. These two contributions we actually measure from the simulations in order to focus on the bias modelling and reduce potential degeneracy with PT modelling. It is also good to note that on the scales of interest, using $P_{\delta\theta}$ either measured from simulations or predicted by PT has only a slight impact on best fit value of $b_2^{01}$. We use the $b_1$ values determined from the matter-halo power spectra $P_{00}^{(hm)}$ from previous section. Note that the relative contributions from $b_2$ and $b_{3,nl}$ terms in $P^{(h\bar{h})}_{01,\mathbf{k}}$ differ from those in $P^{(h\bar{h})}_{00,\mathbf{k}}$, but the scale dependence of these terms is similar over the limited range of scale of interest here ($0.05h/Mpc < k < 0.2h/Mpc$). This again suggests we can replace all the nonlinear bias terms with a single effective $b_2^{01}$, which however can take a different numerical value from $b_2^{00}$. We thus fit for a new set of $b_2^{01}$ values in order to achieve better correspondence with the halo simulation results. In the same figure we also show the results using just the linear biasing $b_1$.

### On the different $b_2$ values for $P_{00}^{(hm)}$ and $P_{01}^{(hh)}$

As was mentioned above two different sets of $b_2$ parameters are used: one set to model matter halo-cross power spectrum $P_{00}^{(hm)}$ and, consequently, halo-halo auto power spectra $P_{00}^{(hh)}$, and the second set to model the predictions for $P_{01}^{(hh)}$. We have argued that this is necessary because there are several free bias parameters that enter the power spectra at 1-loop level, all of which have a similar scale dependence, which means we cannot determine them individually and we have replaced them with a single effective $b_2$ parameter instead.

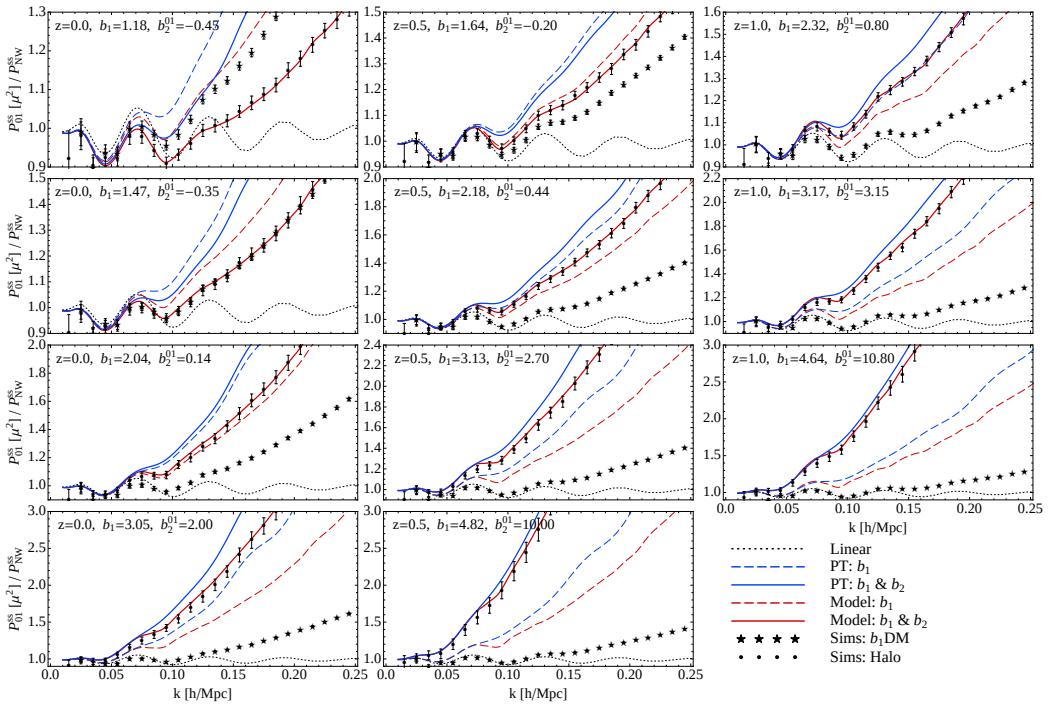


**Figure 6.5:** Halo-halo density-momentum power spectrum $P_{01}$ for four mass bins, at reshifts $z = 0.0$, $z = 0.5$ and $z = 1.0$. We show SPT results (blue lines) and, because SPT does not reproduce DM simulations well, we also show results using the model where we use DM simulations for linear biasing terms (red lines) to isolate the biasing effects in RSD. For comparison we also show linear biasing (dashed lines) and nonlinear biasing (solid lines) models. Halo (black points) simulation data and $b_1$ times the dark matter data (black stars) are also shown. All the spectra are divided by the no wiggle linear prediction [62] for $b_1 P_{01}$ term.

However, while for each statistic we can replace them all with a single effective parameter, the relative contributions from each physical nonlinear bias to different statistics changes, so the values of the effective parameters can change as well.

One wishes to have a biasing model valid for all the statistics of interest and thus for all the correlators used in our RSD model. Ideally this would also include the higher order correlations, as well as all correlations with the dark matter. It is important to realize that this difference in $b_2$ bias stays at the level of $P_{00}$ and $P_{01}$ correlators, since all the higher order correlators come only through these two terms, at least at one loop level we work here. So one can ask whether one can explain the difference using a physically motivated model of nonlinear biasing. We find that $b_s$ does not seem to matter much assuming its values from the bispectrum analysis [56, 40], or its values from the coevolution model assuming it is zero in initial conditions, and so can be ignored. In contrast, $b_2$ and $b_{3,nl}$ appear to be equally important [39, 60]. For the terms we are discussing, this gives

$$\begin{aligned} P^{(hh)}_{00,\mathbf{k}} =& b_1^2 P_{00,\mathbf{k}} + 2b_1\left[b_2 K_{00,\mathbf{k}} + b_s K^s_{00,\mathbf{k}}\right] + \frac{1}{2}\left[b_2^2 K_{01,\mathbf{k}} + b_s^2 K^s_{01,\mathbf{k}}\right] \\ &+ b_2 b_s K^s_{02,\mathbf{k}} + 2b_{3,nl}\sigma^2_{3,k} P^{(L)}_k, \end{aligned} \tag{6.28}$$

and also

$$\begin{aligned} P^{(hh)}_{01,\mathbf{k}} =& b_1^2 P_{01,\mathbf{k}} + b_1(1-b_1)\alpha P_{\delta\theta,\mathbf{k}} + \alpha\left[b_2 K_{10,\mathbf{k}} + b_s K^s_{10,\mathbf{k}}\right] \\ &+ \alpha b_1\left[b_2 K_{11,\mathbf{k}} + b_s K^s_{11,\mathbf{k}}\right] + \alpha b_{3,nl}\sigma^2_{3,k} P^{(L)}_k, \end{aligned} \tag{6.29}$$

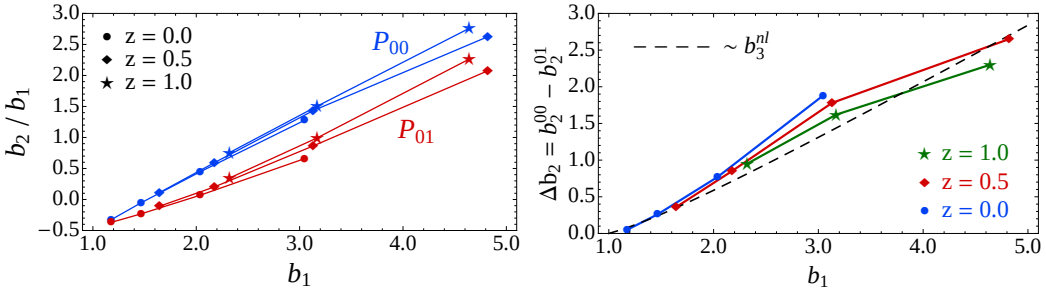


**Figure 6.6:** Comparison of $b_2^{00}$ and $b_2^{01}$ used in modelling of $P_{00}$ and $P_{01}$ terms. In the left panel we show redshift dependence of $b_2/b_1$ values for $P_{00}$ term (blue) and $P_{01}$ (red) term. In the right panel we show the dependence of the difference $\Delta b_2 = b_2^{00} - b_2^{01}$ on the values of $b_1$. We show results for redshift $z = 0.0$ (blue), $z = 0.5$ (red) and $z = 1.0$ (green).

where $\sigma_{3,k}$ is defined in [39] and for detailed discussion of these terms we refer to [60]. The coevolution model predicts a specific value for $b_{3,nl}$ today assuming it is zero initially [40]. Using these predicted values we can predict the difference between the two effective $b_2$ values: we find that this model indeed predicts that $b_2^{00}$ is larger than $b_2^{01}$ and that the amplitude of the difference increases with halo bias $b_1$. The prediction of this model is shown in figure 6.6, together with the results from the fits. We show the redshift dependence of $b_2$ on $b_1$ and the difference $\Delta b_2 = b_2^{00} - b_2^{01}$.
Even having these three nonlocal bias models may not be all that is required for a complete model: in the peak model one expects to have $k^2$ corrections to linear bias both in the halo density and in the halo velocity in the initial conditions [63, 58]. If shown to be significant at later times of evolution, this could play an important role in modelling of all velocity correlators.

### 6.2.5 $P_{02}^{(hh)}$

Next term we are considering is the correlation of the halo field with the halo kinetic energy density field. This term has the only scalar part but these give the contributions to both $\mu^2$ and $\mu^4$ parts of the total redshift power spectrum. We have

$$\begin{aligned}\left\langle \delta^h | T_2^{\bar{h}} \right\rangle = b_1 \left\langle \delta | u_\parallel^2 \right\rangle + b_1 \bar{b}_1 \left\langle \delta | \delta u_\parallel^2 \right\rangle + \frac{1}{2} b_2 \left\langle \delta^2 | u_\parallel^2 \right\rangle + \frac{1}{2} b_s \left\langle s^2 | u_\parallel^2 \right\rangle \\ + \frac{1}{2} \bar{b}_1 b_2 \left\langle \delta^2 | \delta u_\parallel^2 \right\rangle + \frac{1}{2} b_1 \bar{b}_2 \left\langle \delta | \delta^2 u_\parallel^2 \right\rangle_c + \frac{1}{4} b_2 \bar{b}_2 \left\langle \delta^2 | \delta^2 u_\parallel^2 \right\rangle_c \end{aligned} \tag{6.30}$$

where we have used the same renormalization scheme as for $P_{00}^{(hh)}$ term. Subscript $c$ stands for the connected part of the correlator, while the disconnected parts of this terms get renormalized. We get for the power spectrum of this term

$$P_{02,\mathbf{k}}^{(h\bar{h})} = b_1 \bar{P}_{02,\mathbf{k}} + P_{00,\mathbf{k}}^{hh} \sigma_v^2 - \Big[ b_2 K_{20,\mathbf{k}} + b_s K_{20,\mathbf{k}}^s \Big], \tag{6.31}$$

where the first term is the reduced dark matter contribution $\propto \left\langle \delta | v_\parallel \right\rangle_c$ as defined in [54]. Nonlinear bias comes in through the biasing in $P_{00}^{hh}$ term and we also have the contributions of two additional terms

$$\begin{aligned} K_{20,\mathbf{k}} &\equiv \frac{q_\parallel}{q^2} \frac{(\mathbf{k}-\mathbf{q})_\parallel}{(\mathbf{k}-\mathbf{q})^2} P_{\mathbf{q}}^{(L)} P_{\mathbf{k}-\mathbf{q}}^{(L)}, \\ K_{20,\mathbf{k}}^s &\equiv \frac{q_\parallel}{q^2} \frac{(\mathbf{k}-\mathbf{q})_\parallel}{(\mathbf{k}-\mathbf{q})^2} P_{\mathbf{q}}^{(L)} P_{\mathbf{k}-\mathbf{q}}^{(L)} S_{\mathbf{q},\mathbf{k}-\mathbf{q}}^{(2)}. \end{aligned} \tag{6.32}$$

These terms have contributions to both $\mu^2$ and $\mu^4$. As was shown in [54], the term that is proportional to the velocity dispersion will appear in the $\mu^2$ part. Since for DM it is

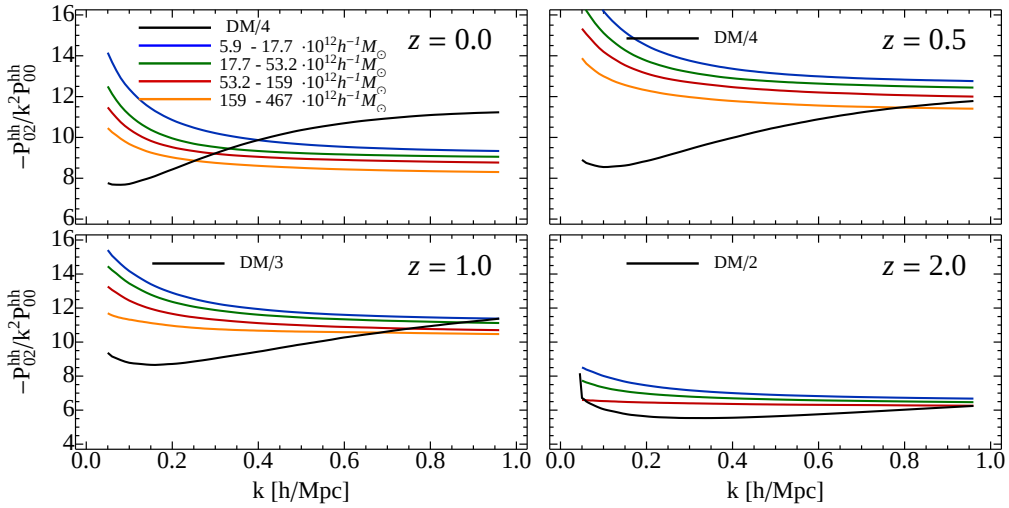


**Figure 6.7:** $P_{02}/P_{00}$ for halos and dark matter. Results are presented for dark matter halos (color coding for respective bias values) and for the dark matter (in black). Values of velocity dispersion can be estimated at the smaller scale regions (higher $k$), where the ratio tends approach the constant values. We show the ratio for four different halo mass bins and for four different redshifts.

not possible to evaluate the total velocity dispersion using PT we had to model small scale contributions adding a part which was motivated by the velocity dispersion in a halo using the halo model. For halos the situation is simpler in that we do not expect such a term to be present, as there is no small scale velocity dispersion contribution, and hence no FoG. Most of the contribution comes from the large scale velocities which can at least in principle be described using PT.

### Velocity dispersion predictions and simulation measurements

In order to test the velocity dispersion behaviour in more detail let us consider more closely the contribution of $\mu^2$ part of $P_{02}^{hh}$. From previous work on dark matter [54], we have seen that on quasi-nonlinear scales most of the contributions to the $P_{02}$ term came from the part proportional to the factor corresponding to the dark matter velocity dispersion multiplied with $P_{00}$ term. For halos this will be generalized to the $\sigma_v^2 P_{00}^{hh}$, where we have the halo velocity dispersion instead. In order to test the behaviour on the halo velocity dispersion in simulations, in figure 6.7 we show the $k$ dependence of $P_{02}^{hh}/P_{00}^{hh}$. From the figure it can be seen that at smaller scales this ratio tends to a constant for all mass bins and redshifts. This constant values can be interpreted as the halo velocity dispersion $\sigma_v^2$. Note that for this figure we include the shot noise $\bar{n}^{-1}$ in $P_{00}^{hh}$, and we expect there is also the shot noise $\sigma_v^2/\bar{n}$ in $P_{02}$.
In figure 6.8 we show the redshift dependence of the halo velocity dispersion $\sigma_v$ as obtained from simulations (high-k regime in figure 6.7). We see the trend of the velocity dispersion values increasing and then decreasing with redshift, as predicted by the linear theory prediction of the velocity dispersion

$$\sigma_{v,\mathrm{lin}}^2(\tau) = \frac{1}{3}\int \frac{d^3q}{(2\pi)^3}\frac{P_{\theta\theta}(q,\tau)}{q^2}. \tag{6.33}$$

We see that velocity dispersions weakly depend on the masses of the halos, at all the redshifts, and are in a good agreement with linear theory predictions. In contrast, the dark matter velocity dispersion is significantly higher than the linear theory prediction. Slight dependence of halo velocity dispersion on halo mass, noticeable in figures 6.7 and 6.8 can be explained by the terms in equation 6.31 that do not depend on $\sigma_v$. Higher order terms

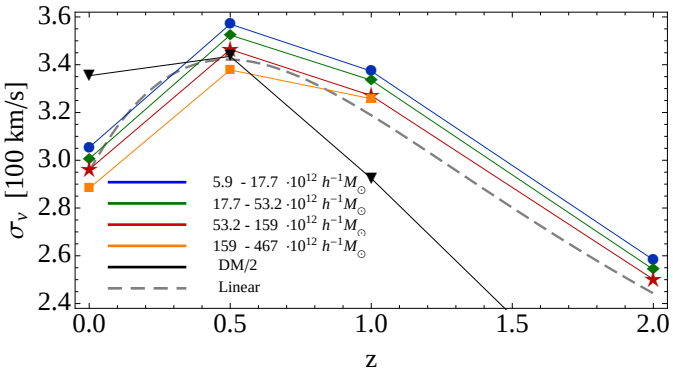


**Figure 6.8:** Redshift dependence of the halo velocity dispersion measurements obtained from simulations. Four different mass bins values are shown (in different color coding respectively). We also show the velocity dispersion measurements for dark matter case (in Black). Also shown are the linear theory prediction for velocity dispersion values (gray dashed line). Notice that the values of measured velocity dispersion have a weak dependence on mass of the halo bins.

can also play a role in modelling both $\left\langle \delta^h | u_\parallel^2 \right\rangle$ and also connected term $\left\langle \delta^h | \delta^h u_\parallel^2 \right\rangle$.
In figure 6.9 we show the $\mu^2$ part of $P_{02}^{(hh)} + P_{11}^{(hh)}$ and $\mu^4$ part of $P_{02}^{(hh)}$ as contributions to the total redshift power spectrum. The sum of $P_{02}^{(hh)}$ and $P_{11}^{(hh)}$ terms is chosen since both of these terms have isotropic shot noise contributions $\sigma^2/\bar{n}$, and which can be large for rare tracers such as halos. Since these two contributions come with opposite signs and exactly cancel in the sum, they give no residual shot noise contribution to the total RSD power spectrum . From equation 6.31 we see that $P_{02}^{hh}$ term also contains contributions from $P_{00}^{hh}$ term which contains nonlinear $b_2$ bias. Thus for modelling the $P_{02}^{hh}$ term we use the same $b_2$ values as for $P_{00}^{hh}$ term.

### 6.2.6 $P_{11}^{(hh)}$

Next term to consider is the autocorrelation of the halo momentum field $P_{11}^{(hh)}$. This term will give the contributions to both $\mu^2$ (which has only contributions from the vector part) and $\mu^4$ angular dependence (which has dominantly contributions from the scalar part on large scales, as it is present already in linear theory, while the vector part becomes important on small scales). Leading term on the large scales has $\mu^4$ angular dependence and in the limit of small $k$ consists only of the third Kaiser term. Correlating the two halo momentum fields using the biasing model (equation 6.9) we get

$$\begin{aligned}\left\langle T_1^h | T_1^{\bar{h}} \right\rangle = &\left\langle u_\parallel | u_\parallel \right\rangle + (b_1 + \bar{b}_1) \left\langle u_\parallel | \delta u_\parallel \right\rangle + b_1 \bar{b}_1 \left\langle \delta u_\parallel | \delta u_\parallel \right\rangle \\ &+ \frac{1}{2}(b_2 + \bar{b}_2) \left\langle u_\parallel | \delta^2 u_\parallel \right\rangle_c + \{b_1, b_2\} \left\langle \delta u_\parallel | \delta^2 u_\parallel \right\rangle_c + \frac{1}{4} b_2 \bar{b}_2 \left\langle \delta^2 u_\parallel | \delta^2 u_\parallel \right\rangle_c \end{aligned} \tag{6.34}$$

where we can again use the same renormalization scheme as for $P_{00}^{(hh)}$ term. Subscript $c$ again represents connected part of the correlator, while the disconnected parts gets renormalized. Keeping the terms at one loop order we get for the power spectrum,

$$P_{11,\mathbf{k}}^{(h_1 h_2)} = P_{11,\mathbf{k}} + \left[(b_1 - 1) + (\bar{b}_1 - 1)\right] \frac{\mu}{k} B_{11,\mathbf{k}} + (b_1 \bar{b}_1 - 1) C_{11,\mathbf{k}}, \tag{6.35}$$

where the dark matter terms $P_{11}$, $B_{11}$ and $C_{11}$ used here have been computed in [54]. At the one loop level of PT modelling, there are no contributions of $b_2$ bias terms, as can be seen from 6.34 where all $b_2$ terms appear only at the 2-loop level. The same is true for higher order local and nonlocal bias contributions.

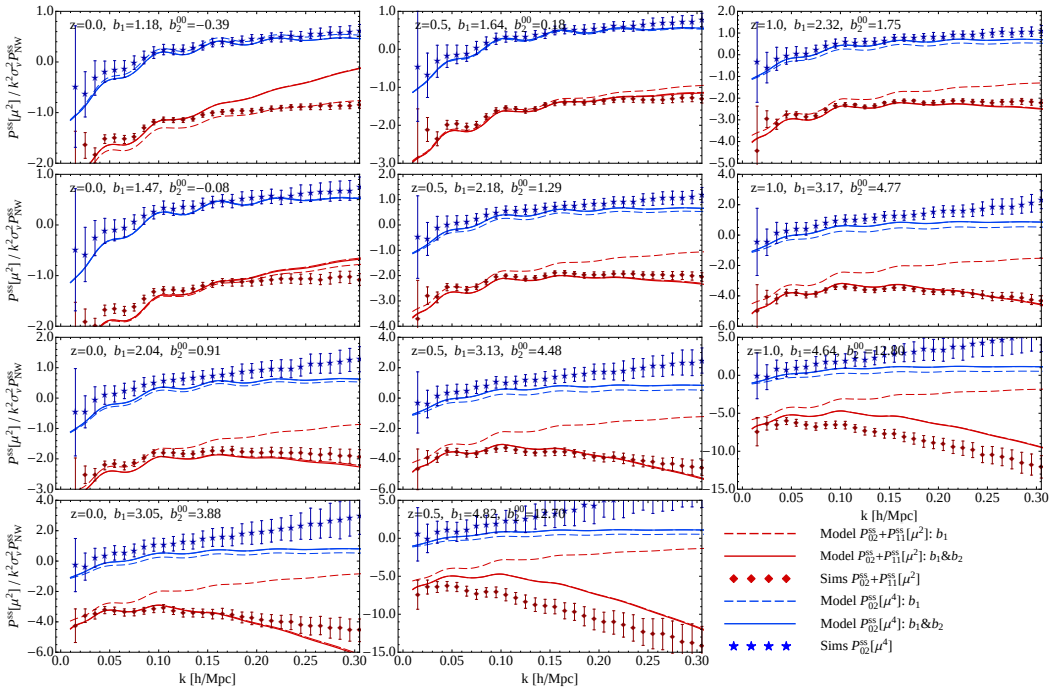


**Figure 6.9:** $\mu^2$ part of $P_{02} + P_{11}$ (red color) and $\mu^4$ part of $P_{02}$ (blue color) is shown at three different redsifts, for several mass bins. Simulation measurements (points) of these two terms are compared to the model 6.31 using linear (dashed lines) and non-linear (solid lines) biasing. All the plots are divided by the linear predictions $k^2\sigma_v^2 P_{NW}$ with no BAO wiggles.

In figure 6.10 we show the scalar part of velocity moment halo power spectra $P_{11}^{(hh)}$. To improve the precision we use simulations for the scalar part of $P_{11}$ for dark matter. For a more extensive discussion about how to model this in PT and consistency of this procedure we refer to [54]. We also investigate the two loop contributions and show terms proportional to $b_2$ in equation 6.34. Notice that these contributions are suppressed by the $f^2D^6$ factor so the contribution at higher redshifts quickly becomes less important. Overall we see that the model qualitatively reproduces simulations well, but not quantitatively for all halos. Notice the very strong scale dependence of the term, specially for the highly biased halos. The scale dependence is induced already at the linear biasing level. As mentioned in previous section, vector part of $P_{11}^{(hh)}$ is shown in figure 6.9 where it is combined with $\mu^2$ part of the $P_{02}^{(hh)}$ term. Overall we conclude that our model reproduces all the trends seen in simulations without any additional free parameters (except the $b_1$ and $b_2$ bias parameters that have been fitted to measurement of $P_{00}^{(hh)}$ and $P_{01}^{(hh)}$), but is not sufficient to achieve high precision predictions down to very small scales.

### 6.2.7 $P_{12}^{(hh)}$ and $P_{03}^{(hh)}$

In this subsection we look at higher order moment terms $P_{12}^{(hh)}$ and $P_{03}^{(hh)}$ which have the lowest angular contribution at $\mu^4$ level. We will only model the lowest order $\mu^4$ terms, which give the nonlinear corrections to the last Kaiser term. Nonlinear $b_2$ bias enter in these terms indirectly through the terms $P_{00}^{(hh)}$, $P_{01}^{(hh)}$ and consequently $P_{11}^{(hh)}$. For the correlation of first and second order momentum fields $P_{12}^{(h\bar{h})}$ we have

$$\begin{aligned}\left\langle T_1^h | T_2^{\bar{h}} \right\rangle &= \left\langle (1+\delta^h)u_\parallel | (1+\delta^{\bar{h}})u_\parallel^2 \right\rangle \\ &= \left\langle (1+\delta^h)u_\parallel | u_\parallel^2 \right\rangle + \left\langle (1+\delta^h)u_\parallel | \delta^{\bar{h}} u_\parallel^2 \right\rangle . \end{aligned} \tag{6.36}$$

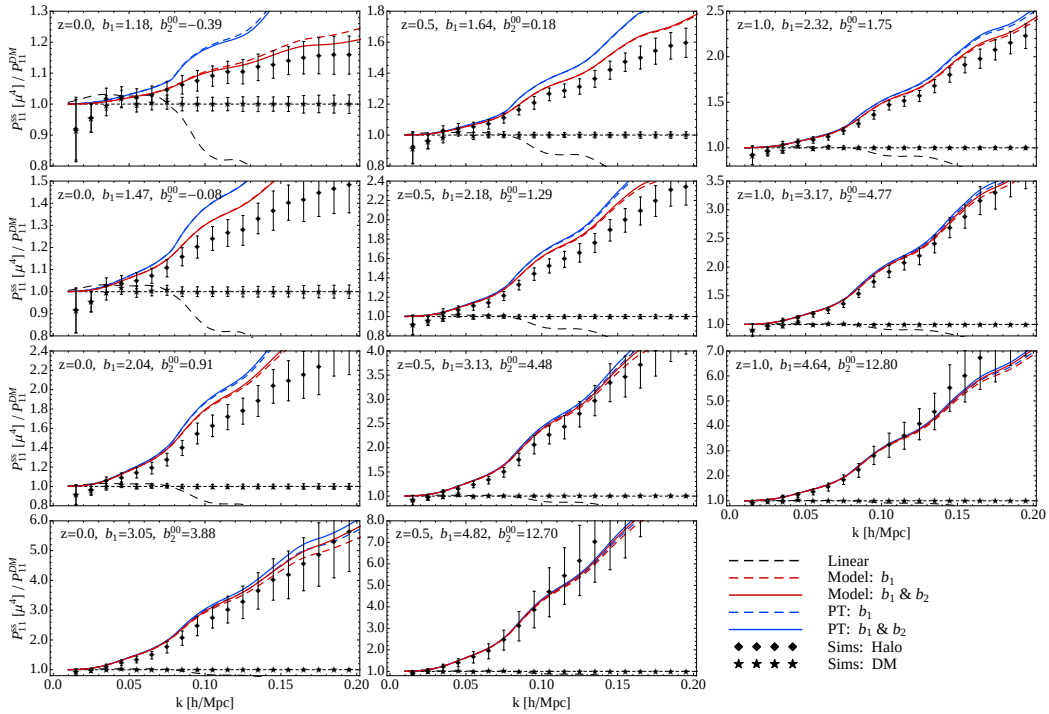


**Figure 6.10:** $\mu^4$ part of the halo momentum power spectrum $P_{11}^{(hh)}$ relative to $P_{11}$ for dark matter. Results are shown for halos for several mass bins at redshifts $z = 0.0,\ 0.5,\ 1.0$. We show the full SPT result (blue line) and the model (red line) where simulations are used for the DM part of $P_{11}$. Both the linear biasing model (dashed lines) and the nonlinear biasing model with $b_2$ terms is shown (solid line). Here we emphasize that the $b_2$ parameters are not free, but have been fixed by the $P_{00}$ and $P_{01}$ analyses. We also show the halo simulation measurements (black dots) and $b_1$ times DM simulations (black stars). Kaiser linear result with $b_1$ bias is also shown (lond-dashed black line).

By decomposing these two terms further we get

$$\begin{aligned}
\left\langle (1+\delta^h)u_\parallel|u_\parallel^2\right\rangle &= \left\langle (1+\delta)u_\parallel|u_\parallel^2\right\rangle + \left\langle (\delta^h-\delta)u_\parallel|u_\parallel^2\right\rangle \\
&= \left\langle (1+\delta)u_\parallel|(1+\delta)u_\parallel^2\right\rangle + (b_1-1)\left\langle \delta u_\parallel|u_\parallel^2\right\rangle - \left\langle (1+\delta)u_\parallel|\delta\right\rangle \left\langle u_\parallel^2\right\rangle + \dots \\
&= (2\pi)^3\left(P_{12,\mathbf{k}} - i(b_1-1)B_{12,\mathbf{k}} + P_{01,\mathbf{k}}\sigma_v^2 + \dots\right)\delta^D(\mathbf{k}-\mathbf{k}'), \\
\left\langle (1+\delta^h)u_\parallel|\delta^{\bar h}u_\parallel^2\right\rangle &= \left\langle (1+\delta^h)u_\parallel|\delta^{\bar h}u_\parallel^2\right\rangle_c + \left\langle (1+\delta^h)u_\parallel|\delta^{\bar h}\right\rangle \left\langle u_\parallel^2\right\rangle \\
&= (2\pi)^3\left(-P_{01,\mathbf{k}}^{(h\bar h)}\sigma_v^2\right)\delta^D(\mathbf{k}-\mathbf{k}'),
\end{aligned} \tag{6.37}$$

where we again refer to [54] for detailed expressions for dark matter terms $P_{12}$ and $B_{12}$, and we use the property of high order momentum correlators $P_{LL'} = P_{L'L}^*$. Connected part will have contributions at the level higher than one loop so will not be considered here. Combining these results above we get

$$P_{12,\mathbf{k}}^{(h\bar h)} = P_{12,\mathbf{k}} - i(b_1-1)B_{12,\mathbf{k}} - \left(P_{01,\mathbf{k}}^{(h\bar h)} - P_{01,\mathbf{k}}\right)\sigma_v^2. \tag{6.38}$$

Similarly for the $P_{03}^{(h\bar h)}$ term we have,

$$\begin{aligned}
\left\langle \delta^h|T_3^{\bar h}\right\rangle &= \left\langle \delta^h|(1+\delta^{\bar h})u_\parallel^3\right\rangle \\
&= b_1\left\langle \delta|u_\parallel^3\right\rangle + b_1\bar b_1\left\langle \delta|\delta u_\parallel^3\right\rangle + \dots,
\end{aligned} \tag{6.39}$$

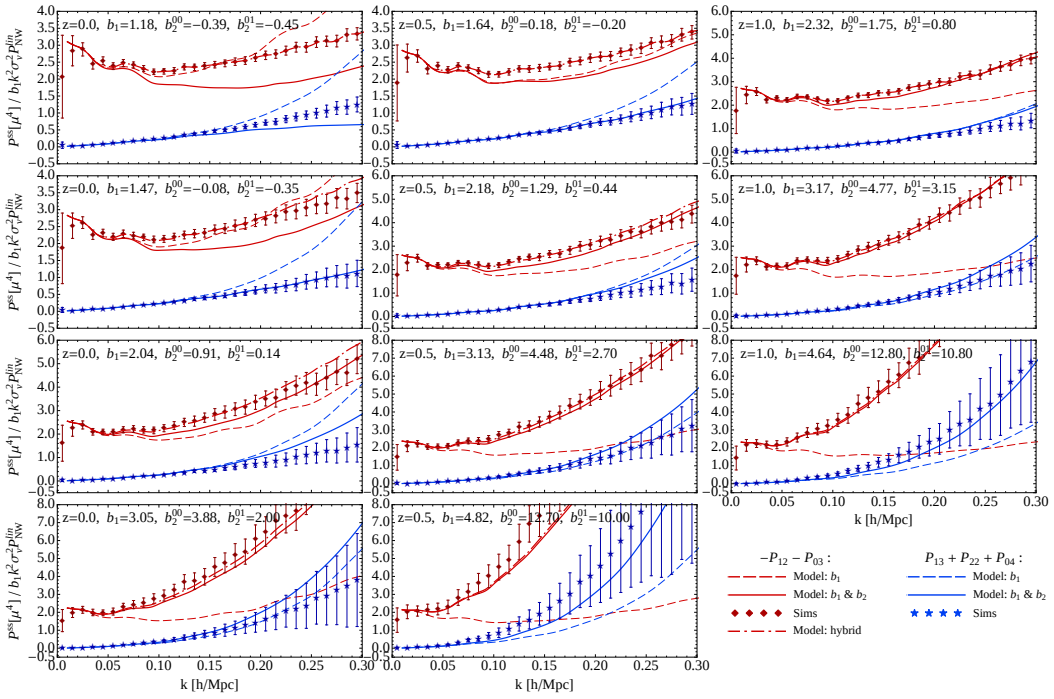


**Figure 6.11:** $\mu^4$ parts of the $P_{12}+P_{03}$ (red) term and $P_{13}+P_{22}+P_{04}$ (blue) for several mass bins at redshifts $z = 0.0,\ 0.5,\ 1.0$. We take the specific combinations for which the shot noise contributions cancel out. We show results for the linear biasing model (dashed) and for the nonlinear biasing (solid). Note the large effect of nonlinear biasing. Here again we emphasize that the $b_2$ parameters are not free, but have been fixed by the $P_{00}$ and $P_{01}$ analyses. For $P_{12}+P_{03}$ term we also present a hybrid result (red dot-dashed line) where we fit for the correction in the lowest mass bin at each redshift and apply it to higher mass bins. All the plots are divided by the linear predictions $b_1 k^2 \sigma_v^2 P_{NW}$ with no BAO wiggles.

which can be generalized to the following form

$$P^{(h\bar{h})}_{03,\mathbf{k}} = 3P^{(h\bar{h})}_{01,\mathbf{k}}\sigma_v^2, \tag{6.40}$$

where we have again omitted the connected part since it gives only contributions at the higher level than one loop.
It is again convenient to combine some of these terms, such as $P_{12}$ and $P_{03}$ to eliminate the shot noise contributions. These two terms together give the contribution to the total redshift power spectrum

$$\frac{i}{3}\left(\frac{k\mu}{\mathcal{H}}\right)^3 P^{(h\bar{h})}_{03,\mathbf{k}} - i\left(\frac{k\mu}{\mathcal{H}}\right)^3 P^{(h\bar{h})}_{12,\mathbf{k}} = i\left(\frac{k\mu}{\mathcal{H}}\right)^3 \left(2\sigma_v^2 P^{(hh)}_{01,\mathbf{k}} + ib_1 B_{12,\mathbf{k}} - (P_{12,\mathbf{k}} + iB_{12,\mathbf{k}} + \sigma_v^2 P_{01,\mathbf{k}})\right). \tag{6.41}$$

In figure 6.11 we show the result of this model for sum of two terms. We show contribution from both linear biasing and nonlinear $b_2$ contributions that come through the $P^{(hh)}_{01}$ term and compare it to the simulation measurements. We find that nonlinear biasing terms in most cases improve the agreement. Note that the $b_2$ terms are not fitted, but have been fixed by the lower order analyses. We also present the result of so called hybrid model where we first fit for the correction to our PT model relative to the simulations in the lowest mass bins at each redshift. This correction is applied then to the higher mass bins at the given redshift. We see that this procedure gives an improvement for all mass bins we consider. This suggests that improving the modelling of dark matter rather then biasing might be more important in order to improve the result for $P_{12}+P_{03}$.

### 6.2.8 $P_{13}^{(hh)}$, $P_{22}^{(hh)}$ and $P_{04}^{(hh)}$

The remaining terms to consider at the $\mu^4$ level to the total RSD power spectrum are $P_{13}^{(hh)}$, $P_{22}^{(hh)}$ and $P_{04}^{(hh)}$. First we look at the $P_{13}^{(h\bar{h})}$ term,

$$\begin{aligned}\left\langle T_1^h | T_3^{\bar{h}} \right\rangle &= \left\langle (1+\delta^h) u_\parallel | (1+\delta^{\bar{h}}) u_\parallel^3 \right\rangle \\ &= \left\langle u_\parallel | u_\parallel^3 \right\rangle + b_1 \left\langle \delta u_\parallel | u_\parallel^3 \right\rangle + \bar{b}_1 \left\langle u_\parallel | \delta u_\parallel^3 \right\rangle + b_1 \bar{b}_1 \left\langle \delta u_\parallel | \delta u_\parallel^3 \right\rangle + \dots ,\end{aligned} \tag{6.42}$$

which can be collected to give

$$\begin{aligned}P_{13,\mathbf{k}}^{(h\bar{h})} =& 3\sigma_v^2 \Big[ P_{11,\mathbf{k}} - \big[(b_1 - 1) + (\bar{b}_1 - 1)\big] \frac{\mu}{k} B_{11,\mathbf{k}} + (b_1 \bar{b}_1 - 1) C_{11,\mathbf{k}} + \dots \Big] \\ =& 3 P_{11,\mathbf{k}}^{(h\bar{h})} \sigma_v^2 .\end{aligned} \tag{6.43}$$

The obtained result is given in terms of previous $P_{11}^{hh}$ term, and velocity dispersion.
Next we look at the $P_{22}^{(h\bar{h})}$ term,

$$\begin{aligned}\left\langle T_2^h | T_2^{\bar{h}} \right\rangle &= \left\langle u_\parallel^2 | (1+\delta^{\bar{h}}) u_\parallel^2 \right\rangle + \left\langle \delta^h u_\parallel^2 | (1+\delta^{\bar{h}}) u_\parallel^2 \right\rangle \\ &= \left\langle u_\parallel^2 | u_\parallel^2 \right\rangle + (b_1 + \bar{b}_1) \left\langle u_\parallel^2 | \delta u_\parallel^2 \right\rangle + b_1 \bar{b}_1 \left\langle \delta u_\parallel^2 | \delta u_\parallel^2 \right\rangle + \dots\end{aligned} \tag{6.44}$$

which can be collected to give,

$$\begin{aligned}P_{22,\mathbf{k}}^{(h\bar{h})} &= \bar{P}_{22,\mathbf{k}} + (b_1 + \bar{b}_1) \bar{P}_{02,\mathbf{k}} \sigma_v^2 + P_{00,\mathbf{k}}^{(h\bar{h})} \sigma_v^4 + \big( P_{00}^{(h\bar{h})} \circ \bar{P}_{22} \big)_{\mathbf{k}} + \dots \\ &= \bar{P}_{22,\mathbf{k}} + b_1 \bar{P}_{02,\mathbf{k}} \sigma_v^2 + P_{02,\mathbf{k}}^{(h\bar{h})} \sigma_v^2 + \big( P_{00}^{(h\bar{h})} \circ \bar{P}_{22} \big)_{\mathbf{k}} .\end{aligned} \tag{6.45}$$

Here we again refer to [54] where the dark matter terms $\bar{P}_{22}$ and $\bar{P}_{02}$ have been computed using the PT.
Lastly we turn to the $P_{04}^{(h\bar{h})}$ term which is formally of the two loop order but it turns up to be significant contribution to the $\mu^4$ part of the total redshift space power spectrum,

$$\left\langle \delta^h | T_4^{\bar{h}} \right\rangle = b_1 \left\langle \delta | u_\parallel^4 \right\rangle + b_1 \bar{b}_1 \left\langle \delta | \delta u_\parallel^4 \right\rangle + \dots . \tag{6.46}$$

which in terms of power spectrum gives

$$P_{04,\mathbf{k}}^{(h\bar{h})} = 6 b_1 \bar{P}_{02,\mathbf{k}} \sigma_v^2 + b_1 \bar{b}_1 P_{00,\mathbf{k}}^{(h\bar{h})} \Big( 3\sigma_v^4 + \left\langle u_\parallel^4 \right\rangle_c \Big) . \tag{6.47}$$

In figure 6.11 we show the result of modelling the sum of these three terms. We show contribution from both linear biasing and nonlinear $b_2$ contributions that come through the $P_{00}^{(hh)}$, $P_{01}^{(hh)}$ and $P_{11}^{(hh)}$ terms. For comparison we show simulation measurements of these terms. Once again nonlinear biasing dramatically improves the accuracy of the model.

## 6.3 Putting it all together: angular dependence and multipole moments

In this section we collect all the contributions to the $\mu^2$ and $\mu^4$ angular dependence in the redshift space power spectrum. First we collect all of the terms that contribute to the halo redshift space power spectrum up to $\mu^4$ angular dependence. We write the power spectrum in the form of powers of $\mu^2$,

$$P_{ss,\mathbf{k}} = A_k + B_k \mu^2 + C_k \mu^4 + D_k \mu^6 + \dots , \tag{6.48}$$

where the isotropic factor terms are

$$
\begin{aligned}
A_k &= P_{00,k}\left[\mu^0\right], \\
B_k &= P^{ss}_{01,k}\left[\mu^2\right] + P^{ss}_{02,k}\left[\mu^2\right] + P^{ss}_{11,k}\left[\mu^2\right], \\
C_k &= P^{ss}_{11,k}\left[\mu^4\right] + P^{ss}_{02,k}\left[\mu^4\right] + P^{ss}_{12,k}\left[\mu^4\right] + P^{ss}_{03,k}\left[\mu^4\right] + P^{ss}_{13,k}\left[\mu^4\right] + P^{ss}_{22,k}\left[\mu^4\right] + P^{ss}_{04,k}\left[\mu^4\right], \\
D_k &= P^{ss}_{12,k}\left[\mu^6\right] + P^{ss}_{13,k}\left[\mu^6\right] + P^{ss}_{22,k}\left[\mu^6\right] + \dots .
\end{aligned}
\tag{6.49}
$$

Each of these terms has been modelled separately in previous chapters. For $\mu^6$ part we write down only the terms that contribute at one loop level. In figure 6.12 we show the performance of the model on $\mu^2$, and in figure 6.13 on $\mu^4$. We see that the model performs reasonably well on $\mu^2$ term up to $k \approx 0.15$ for most of the halo masses and redshifts. To achieve this we had to use the dark matter simulations for the dominant terms ($P_{00}$, $P_{01}$, $P_{11}$ and $P_{\delta\theta}$), include nonlinear biasing with 2 nonlinear bias parameters, and take into account the effect of halo exclusion in the the stochasticity parameter $\Lambda$. Main remaining source of discrepancy here is the $P_{02} + P_{11}$ contribution, so improving this term would lead to a further overall improvement of the $\mu^2$ part. On the other hand, our model is less successful for $\mu^4$ part since these terms show stronger scale dependence, for which our adopted biasing model is less successful. Also, note that $\mu^4$ term has seven constituent terms and since the total error on the final result is cumulative, the final discrepancy from simulations tends to be larger than that for $\mu^2$. Nevertheless, it appears that the main culprit is our modeling of $P_{03} + P_{12}$, which is the analog of $P_{02} + P_{11}$ as it has very similar correlators. In figure 6.14 we also show the leading, one loop contributions to $\mu^6$. Terms that contribute to $\mu^6$ at one loop level are $P_{12}$, $P_{03}$, $P_{13}$ and $P_{22}$. From the figure we see that we can give some quantitative prediction of simulation results, but higher order modelling is required in order to archive better agreement. Also note that the prediction that we show is strictly one loop SPT with no additional parameters.

In [54] we resummed our model 6.48 to allow a continuation to higher powers of $\mu^2$. In the dark matter case this procedure was not possible because of the small scale velocity dispersion, and because these small scale velocity dispersions appear with different amplitudes in contributing terms. This is because dark matter is distributed into halos of widely varying mass and different terms pick up different mass weightings: for example, some are additionally weighted by bias, some by higher powers of mass etc. (see [54] for details). In the case of halos we concluded above that our modeling gives a fairly good estimate of the velocity dispersion for all correlators, meaning that the small scale velocity dispersion is small and the velocity correlators are dominated by large scale velocity flows. However, in case of halos this procedure might be formally justified, but this only partially resums the series, leaving all of the other terms that do not contain velocity correlators untouched. Since velocity dispersion is much smaller in case of halos than it is for dark matter, terms that do not contain velocity dispersion are more relevant for halos in a relative sense. Since resummation is effecting only velocity dispersion terms one should not expect that this will then dramatically improve the overall performance of RSD model.

It is customary to expand the redshift-space power spectrum in terms of Legendre multipole moments

$$
P^{ss}(k,\mu) = \sum_{l=0,2,4,\cdots} P^{ss}_l(k)\mathcal{P}_l(\mu),
\tag{6.50}
$$

where $\mathcal{P}_l(\mu)$ are ordinary Legendre polynomials and multipole moments, $P^{ss}_l$, are given by

$$
P^{ss}_l(k) = (2l+1)\int_0^1 P^{ss}(k,\mu)\mathcal{P}_l(\mu)d\mu \ .
\tag{6.51}
$$

In the RSD analysis it is common to model the monopole ($l = 0$) and quadrupole ($l = 2$) terms, since these contain most of the information on the angular structure of the correlations, although some information is also contained in the hexadecapole term ($l = 4$), which

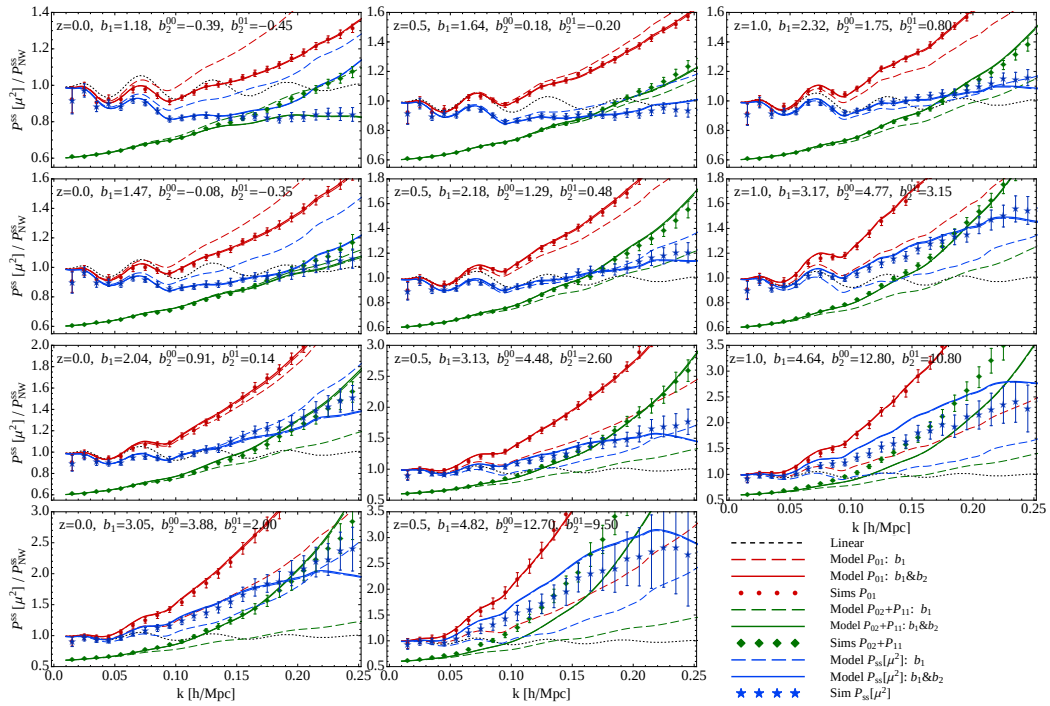


**Figure 6.12:** Contribution of all the terms to $\mu^2$ part of redshift space power spectrum, for several mass bins at redshifts $z = 0.0$, $z = 0.5$ and $z = 1.0$. We also show the contribution of $P_{01}$ term (red) and $P_{02} + P_{11}$ term (green) to the total model (blue). $P_{02} + P_{11}$ term has been shifted up by 0.6. We compare the model results (solid lines) to the simulation measurements (points). Model where only linear $b_1$ is used is also shown (dashed lines) for comparison. All the lines are divided by no-wiggle Kaiser $\mu^2$ term.

we will not include here since it is dominated by $\mu^6$ terms that we do not explicitly model (although is present in our model through the resummation term).

In figures 6.15 and 6.16 we show monopole and quadrupole power spectra predictions. We show contributions to the multipoles as powers of $\mu$ and compare all the results to the reference multipole data obtained from full simulation redshift space power spectra. We also show simulation results where only terms up to $\mu^4$ are considered. In the case of monopole we see that these two simulation results agree on scales larger than $k \sim (0.10 - 0.15)$h/Mpc (depending on redshift and bias), but then start to deviate one from the other. These is especially apparent the case of the quadrupole, where we clearly see the difference in power when terms up to $\mu^4$ are considered, and the power when higher powers of $\mu$ are also taken into account, i.e. terms proportional to $\mu^6$ and higher. We also show the result where one loop SPT prediction of $\mu^6$ term is added to the model. We see that better modelling of also these $\mu^6$ terms is necessary to achieve more precise results in total.

In figure 6.17 we show the angular dependence of model versus simulations for five angular bins, also known in the literature as clustering wedges. Similar techniques have recently been used in analysis of the correlation function (e.g. [64]). We show the model up to $\mu^4$, with and without the correction on $P_{03} + P_{12}$ model and compare the results to the simulation measurements. We see that, as expected, the model is better for the case of low $\mu$ since the expansion parameter of the distribution function approach is $k_\parallel v$ and by construction we have a very good model for real space power spectrum.

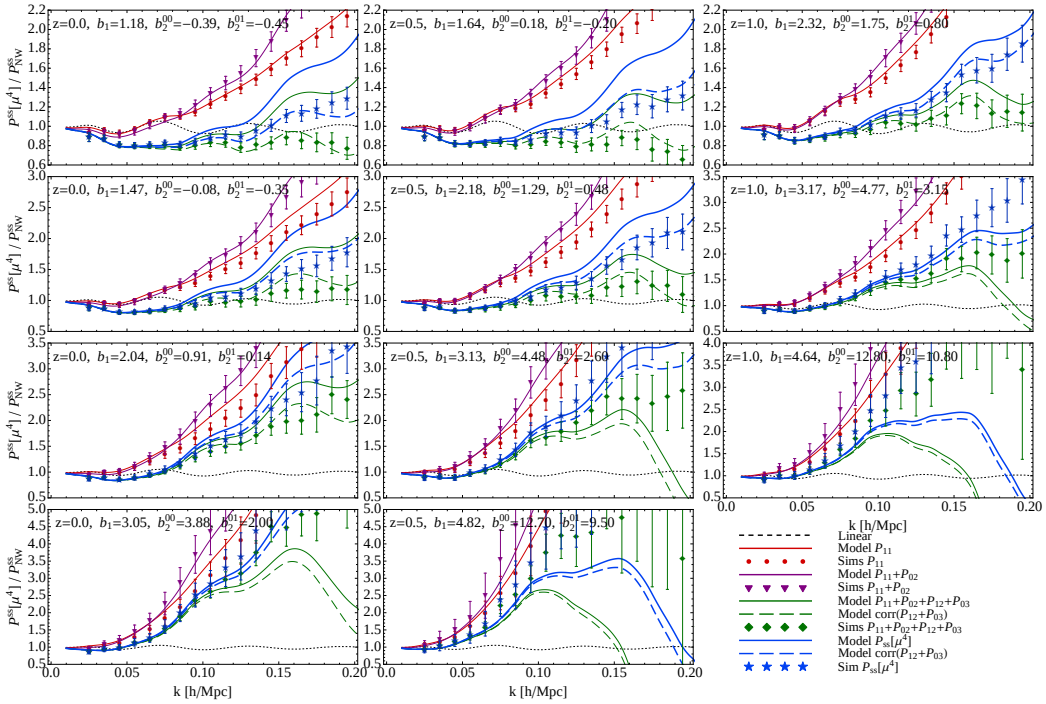


**Figure 6.13:** Contribution of all the terms to $\mu^4$ part of redshift space power spectrum, for several mass bins at redshifts $z = 0.0$, $z = 0.5$ and $z = 1.0$. We also show the contribution of $P_{11}$ term (red), $P_{02}$ term (purple), $P_{12} + P_{03}$ term (green) to the total model (blue). We compare the model results (solid lines) to the simulation measurements (points). We also show the results when the correction to $P_{12} + P_{03}$ term is added to the model (dashed lines), as discussed in section 6.2.7. All the lines are divided by no-wiggle Kaiser $\mu^4$ terms.

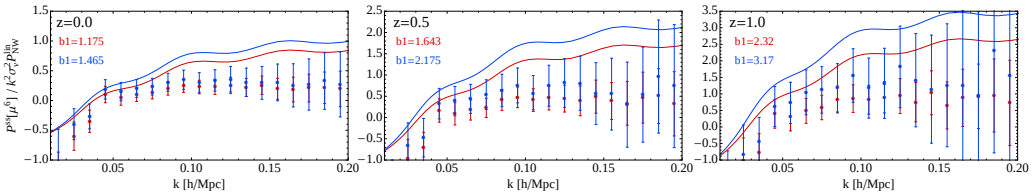


**Figure 6.14:** Contribution to $\mu^6$ part of redshift space power spectrum, for two mass bins at redshifts $z = 0.0$, $z = 0.5$ and $z = 1.0$. We show one loop PT result (solid lines) and compare to the simulation measurements (points). All the plots are divided by the linear predictions $k^2\sigma_v^2 P_{NW}$ with no BAO wiggles.

## 6.4 Correlation function

Our model was built in Fourier space, but we can also look at its performance in configuration space. To get the correlation function we Fourier transform the redshift space power spectra

$$\begin{aligned}\xi^{ss}(\mathbf{s}) &= \int \frac{d^3q}{(2\pi)^3}\, P^{ss}(\mathbf{q}) e^{-i\mathbf{q}\cdot\mathbf{s}} \\ &= \xi_0(s)\mathcal{P}_0(\nu) + \xi_2(s)\mathcal{P}_2(\nu) + \xi_4(s)\mathcal{P}_4(\nu) \end{aligned} \tag{6.52}$$

where we used first four ordinary Legendre polynomials, $\mathcal{P}_0(\nu) = 1$, $\mathcal{P}_2(\nu) = (3\nu^2 - 1)/2$ and $\mathcal{P}_4(\nu) = (35\nu^4 - 30\nu^2 + 3)/8$, and $\nu$ is the cosine of the angle between $\mathbf{s}$ and line of sight. Expansion coefficients are given by spherical Bessel function $j_l$ moments of the power

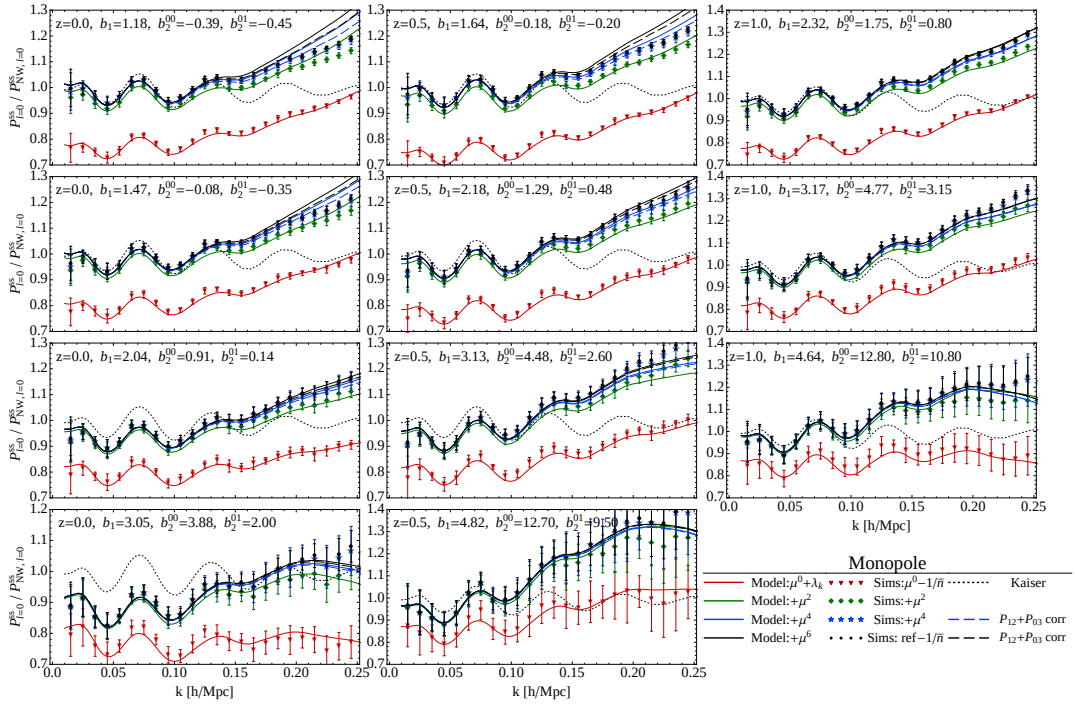


**Figure 6.15:** Monopole ($l = 0$) shown for several mass bins at redshifts $z = 0.0$, $z = 0.5$ and $z = 1.0$. First the isotropic $P_{00}$ part (in red) is shown and then we add the contributions of $\mu^2$ (green), $\mu^4$ (blue) and $\mu^6$ (black) part. Solid lines show the model presented in this paper and corresponding point marks simulation measurements of the same quantities. We also show the model (dashed lines) when the correction to $P_{12} + P_{03}$ term is added to the $\mu^4$ term, as discussed in section 6.2.7. Direct simulation measurements of monopole (black points) is also shown. All the lines and data are divided by the Kaiser no-wiggle monopole prediction.

spectra

$$\xi_l(s) = i^l \int \frac{q^2 dq}{2\pi^2} W_R(q) P_l^{ss}(q) j_l(qs). \tag{6.53}$$

However, many of our PT model predictions strongly diverge from simulations at high $k$, a well known problem of PT. To cure this we introduce the window function $W(qR)$ with smoothing radius $R$, which reduces the importance of high $k$ contributions to the correlation function. For the smoothing $W(qR)$ function we use the simple Gaussian filter. This suppresses the amplitude of the correlation function, and the effect is stronger as we approach smaller scales. We choose the value for which the filter effects on scales larger than $s = 5Mpc/h$ are small and are not noticeable in the figures 6.18 and 6.19 presented bellow. In principle stricter criteria could be implemented here to quantify these effects, but for our purposes this is not of the crucial importance. We find the value to be $R = 1.0h/Mpc$ for both monopole and quadrupole case. In figures 6.18 and 6.19 we show monopole and quadrupole predictions in configuration space, obtained by Fourier transforming the model presented in this work. We show the results for several mass bins and redshifts and compare them to the N-body simulation measurements. We note that the model is not supposed to be compared against simulations below $s = 10Mpc/h$ because of the artificial smoothing of the model against simulations. In principle we could have inserted the smoothing also into the simulations, but for this procedure a broad range of scales of the correlation function measurements is needed.

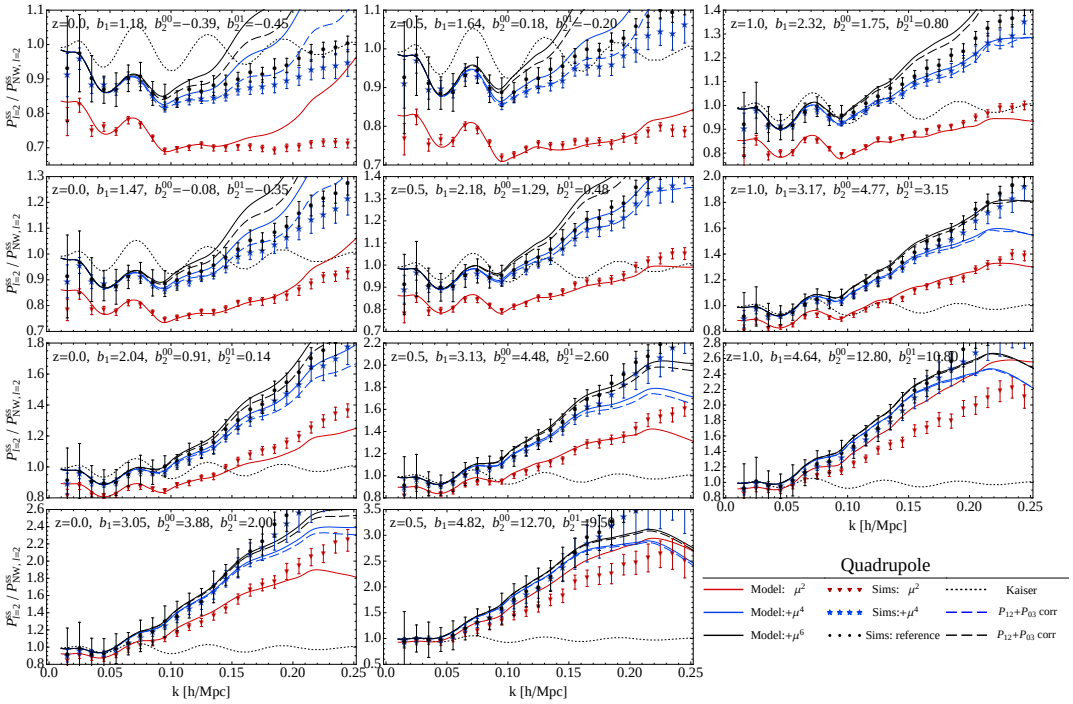


**Figure 6.16:** Quadrupole ($l = 2$) shown for several mass bins at redshifts $z = 0.0$, $z = 0.5$ and $z = 1.0$. We show $\mu^2$ part (in red) and then add the contributions of $\mu^4$ (blue) and $\mu^6$ (black) part. Solid lines show the model presented in this paper and corresponding point marks simulation measurements of the same quantities. We also show the model (dashed lines) when the correction to $P_{12}+P_{03}$ term is added to the $\mu^4$ term, as discussed in section 6.2.7. Direct simulation measurements of monopole (black points) is also shown. All the lines and data are divided by the Kaiser no-wiggle quadrupole prediction.

## 6.5 Conclusions

In this paper we continue the studies of distribution function approach to redshift space distortions (RSD), applying Eulerian perturbation theory (PT) to the case of dark matter halos. In this formalism the RSD power spectrum is decomposed into moments of distribution function and our goal is to model these contributing terms using the perturbation theory and Eulerian biasing model. We work at 1-loop level in PT, requiring us to introduce 3 additional biasing parameters, of which we find that one, the tidal tensor bias $b_s$, turns out not to be important if one assumes its amplitude is given by the bispectrum analysis [56, 40]. The remaining two nonlinear bias parameters are the local quadratic bias $b_2$ and the non-local 3rd order bias $b_{3,nl}$. These two have similar scale dependence with $k$, at least over a limited range of $k < 0.15h/Mpc$, but have different amplitudes in the density-density correlator $P_{00}^{hm}$ relative to the density-momentum correlator $P_{01}^{(hh)}$. One can thus parametrize these nonlinear biases with 2 independent effective 2nd order bias terms. Simple coevolution theory predicts that the nonlinear biasing should be weaker in density-momentum relative to density-density [60], and our results confirm this prediction.

We require that our biasing scheme is consistent with other statistics, in particular the halo-dark matter density cross-correlation $P_{00}^{hm}$ [60]. We also assume that the tidal tensor bias $b_s$ is consistent with the bispectrum [41, 56]. We thus start by modelling the halo matter cross correlation term $P_{00}^{(hm)}$ where we fit for effective $b_2^{00}$ values, combining all the nonlinear bias terms into one. However, since the statistic that enters the RSD is the halo-halo density correlator $P_{00}^{hh}$, this means we also need to describe the stochasticity $\Lambda(k) = P_{00}^{hh} - 2b_1P_{00}^{hm} + b_1^2P_{00}^{mm}$. Detailed modeling of this term is complicated, and is

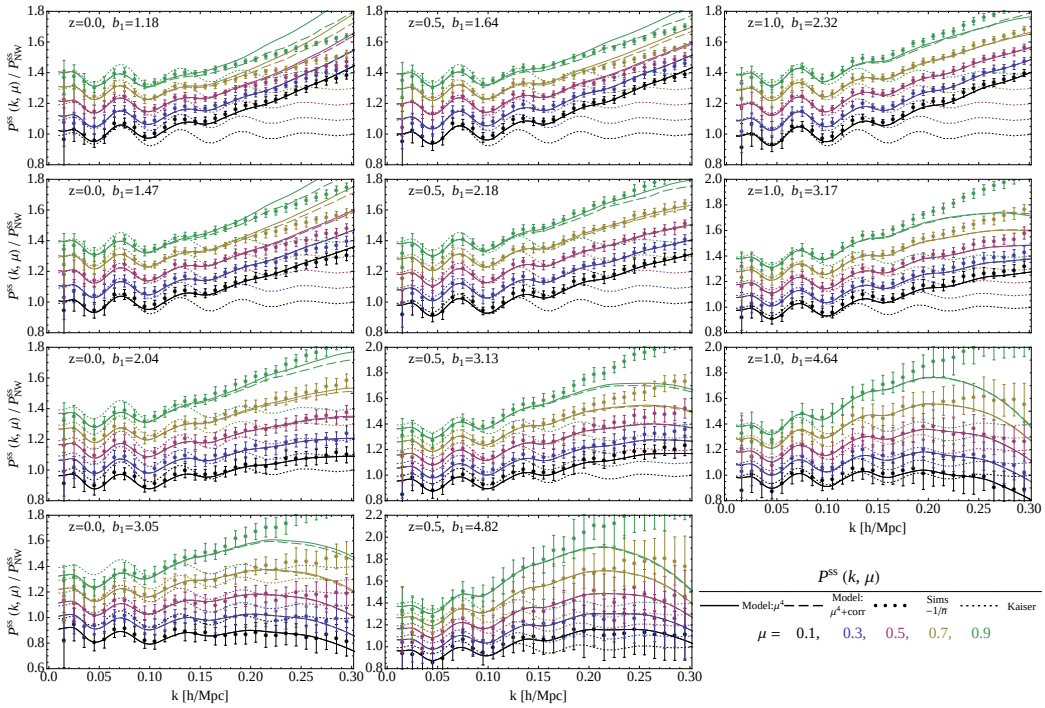


**Figure 6.17:** Angular dependence of the RSD model for several mass bins at redshifts $z = 0.0$, $z = 0.5$ and $z = 1.0$. We show the RSD model up to $\mu^4$ (solid lines), and $\mu^6$ (dashed lines). Simulation measurements (points) are also shown for each $\mu$ bin. We also show the model when the correction to $P_{12} + P_{03}$ term is added to the $\mu^4$ term (dashed line), as discussed in section 6.2.7. All the lines and data are divided by the Kaiser no-wiggle predictions. Results for each angle bin are offset for a constant value for a better overview.

related to halo exclusion and nonlinear biasing [59]. Since our goal is to study RSD we do not attempt to develop a more detailed model of this term and instead we simply parametrize it with a simple power law expression. For the most of the mass bins that were considered we encounter sub-Poissonian stochasticity. We next turn to the modelling of higher momentum correlations, for which the nonlinear contributions of bias at one loop level enter explicitly only in the $P_{01}^{(hh)}$ term. We find the values of effective $b_2^{01}$ that reproduce the simulation measurements. We have argued that at the level of 1-loop calculations this approach is consistent, as we have both quadratic local bias $b_2$ and cubic non-local bias $b_{3,nl}$ entering at the same order, but with differing coefficients in $P_{00}^{hh}$ versus $P_{01}^{hh}$.

In addition to biasing PT approach also computes dark matter clustering. However, in previous work [54] we found that PT does not do a good job in predicting the dark matter correlators: this is a well known property of PT for density-density and density-velocity correlations (e.g. [24]), which also holds for higher order density weighted velocity moment correlators. As a result we use the dark matter correlators as presented in [54], which were a combination of simulation measurements and perturbation theory calculations. We divide the halo correlators into the dark matter part and the remaining part, which depends on linear and nonlinear bias parameters. We use PT to compute both linear and nonlinear biasing contributions to the halo correlators. For the dark matter part, we use $P_{00}$, $P_{01}$, $P_{11}$ and $P_{\delta\theta}$ as given by the dark matter simulations. Ideally this part will also be eventually replaced by PT, but since our goal here is not the dark matter modeling but the halo modeling we do not investigate it further.

The dominant term to RSD is the $\mu^2$ term and its dominant contribution is the halo momentum density correlated with the halo density. Two other terms contribute to $\mu^2$, the vector part of the halo momentum density- halo momentum density correlation $P_{11}^{hh}$, and

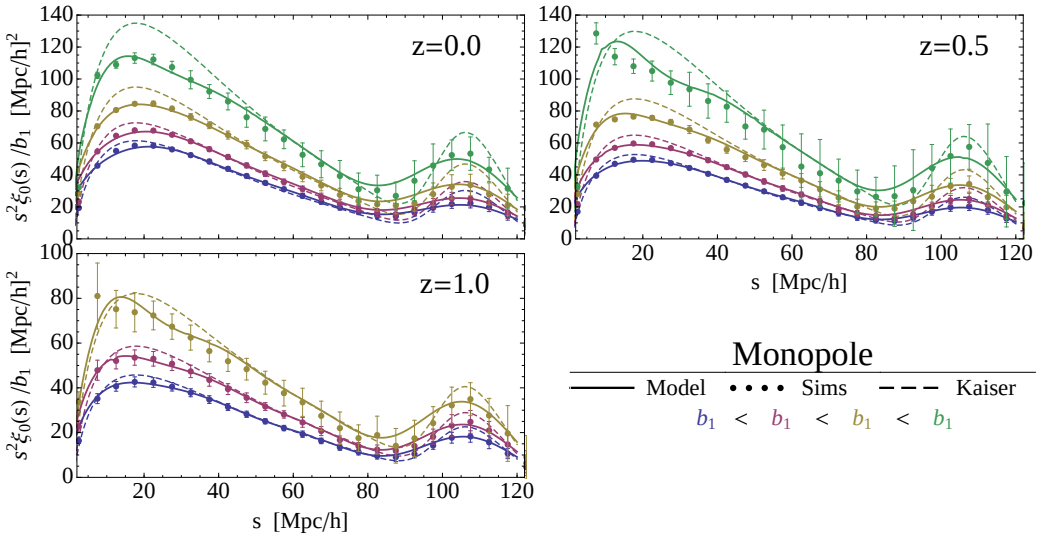


**Figure 6.18:** Monopole of redshift-space correlation function for several mass bins at redshifts $z = 0.0$, $z = 0.5$ and $z = 1.0$. We show the results of model presented in this work (solid lines) linear theory predictions (dashed lines) and halo simulation measurements (points). Results are shown for the same mass bins as in previous plots (upper line represents the highest bias and lower line represents the lowest bias, respectively).

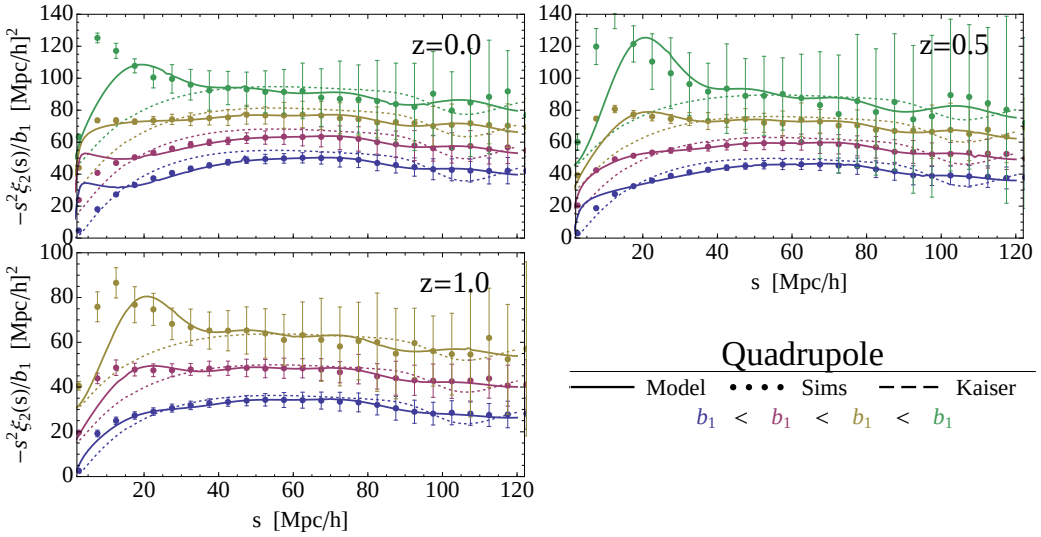


**Figure 6.19:** Same as figure 6.18 but for quadrupole moment of redshift-space correlation function. Results for each mass bin are offset by a constant value (15 (Mpc/h)$^2$) relative to the lowest (blue) bias.

the scalar part of halo kinetic energy density - halo density correlation $P_{02}^{hh}$. We find that they affect RSD at a 10% level already at $k \sim 0.05$h/Mpc for most of the mass bins we consider. The halo kinetic energy density- halo density correlation term $P_{02}$ is the dominant nonlinear effect, and is negative at all $k$ and thus reduces the total $\mu^2$ power. It is related to the Fingers-of-God (FoG) effect, since this term contains velocity dispersion term. However, unlike the velocity dispersion inside the halos, which dominates FoG for dark matter, this effect is generated by the large scale velocity flows which cancel out with $P_{11}$ term on small scales. As a result there are no velocity dispersion effects on small scales.

The next angular term has $\mu^4$ dependence and there are seven terms that contribute to the

total power spectrum, of which one, scalar part of $P_{11}^{(hh)}$, contains a linear order contribution that does not vanish on large scales. Modelling these terms has proven to be even more difficult than lower order terms, but certain level of success has been achieved compared to the simulations over a limited dynamic range, with errors of about 10% at $k \sim 0.1$h/Mpc at $z = 0$. All these terms exhibit very strong scale dependence, which we can reproduce in our model, which should be viewed as a success since there are no free parameters used. Nevertheless, some of the terms also have a considerable error, specially in $P_{03}^{hh} + P_{12}^{hh}$, and as a result we do not succeed in modeling accurately the modes above $k \sim 0.15h/Mpc$.
Our ultimate goal is to develop an accurate RSD model that can be applied to observations, but this was not the primary focus of this work. Instead, here we focused on asking whether we can model all the diferent halo density weighted powers of velocity using a consistent halo biasing model at 1-loop level. We emphasize that all of our biasing parameters are physically motivated: indeed, in most cases they can be predicted from a biasing model [56, 40, 60] and all of the bias parameters exhibit a simple halo mass dependence that can be used as a prior when applying these models to the real data. We introduced no arbitrary velocity dispersion parameters, like those needed in models of most previous work on the subject [15, 21]. This is because when it comes to halos there is no small scale velocity dispersion, as the halos centers are at rest with respect to the local center of mass. All velocity dispersion effects come from large scale velocities which are fully modeled in our approach using PT. We do not compute higher order velocity effects beyond $\mu^4$ and instead we propose a simple resummation ansatz that should approximately capture these terms. We have achieved some level of accuracy with our modeling, but a 1% precision, needed for current and future RSD surveys, can only be achieved up to $k \sim 0.15h/Mpc$. We have seen that the nonlinear effects at that $k$ are at 10-20% level or larger and rapidly growing towards higher $k$, making it difficult to significantly improve the model beyond what was achieved here. Performance of the presented RSD model in determining the cosmological parameter and comparison to some of the other models will be studied in [65].
Successful modeling of halo velocity statistics is just one ingredient of the complete RSD model. We observe galaxies, not dark matter halos, and our analysis remains to be extended to galaxies. We saw previously that for dark matter we had to introduce small scale velocity dispersion to model FoG effects in RSD and we expect the same to be true for galaxies. Nevertheless, separating halo biasing effects, the focus of this work, from FoG effects is an important step towards the complete RSD model. The treatment of FoG we used for dark matter, based on the halo model for computing velocity dispersion, should also be applicable to galaxies. We plan to address this in the future work.

## Acknowledgments

We would like to thank Patrick McDonald, Shun Saito, Tobias Baldauf, Jonathan Blazek, Masanori Sato, Jaiyul Yoo and Nico Hamaus for useful discussions and comments. ZV would like to thank the Berkeley Center for Cosmological Physics and the Lawrence Berkeley Laboratory for their hospitality. This work is supported by the DOE, the Swiss National Foundation under contract 200021-116696/1 and WCU grant R32-10130. V.D. acknowledges support by the Swiss National Science Foundation. The simulations were performed on the ZBOX3 supercomputer of the Institute for Theoretical Physics at the University of Zürich. For making some of the plots in this paper LevelScheme package [66] has been used.

## 6.6 Connecting the correlation function and power spectrum

In this section we give a short derivation of correlation function multipoles from the power spectrum multipoles. We start by expanding the redshift-space power spectrum in terms of

Legendre multipole moments. Using ordinary Legendre polynomials $\mathcal{P}_l(\mu)$, we have

$$P^{ss}(k,\mu) = \sum_{l=0,2,4,...} P_l^{ss}(k)\mathcal{P}_l(\mu), \tag{6.54}$$

where multipole moments, $P_l^{ss}$, are given by

$$P_l^{ss}(k) = (2l+1)\int_0^1 P^{ss}(k,\mu)\mathcal{P}_l(\mu)d\mu \ . \tag{6.55}$$

where $\mathcal{P}_l(\mu)$ are the ordinary Legendre polynomials. In the RSD analyses we are usually limited to modelling the monopole ($l = 0$) and quadrupole ($l = 2$) terms, although some information is also contained in hexadecapole term ($l = 4$).
Correlation function is given as a Fourier transform of the power spectrum

$$\begin{aligned}\xi^{ss}(\mathbf{s}) &= \int \frac{d^3q}{(2\pi)^3}\ P^{ss}(\mathbf{q})e^{-i\mathbf{q}\cdot\mathbf{s}} \\ &= \sum_l \int q^2dq\ P_l^{ss}(q)\int \frac{d\Omega}{(2\pi)^3}\ \mathcal{P}_l(\mu)e^{-i\mathbf{q}\cdot\mathbf{s}}\end{aligned} \tag{6.56}$$

We can use the spherical harmonics expansion of the plane wave

$$e^{i\mathbf{k}\cdot\mathbf{r}} = 4\pi\sum_{lm} i^l j_l(kr)Y_{lm}(\hat{r})Y^*_{lm}(\hat{k}),$$

and the properties of spherical harmonics on parity transformation $P : \{\theta,\phi\} \to \{\pi-\theta,\pi+\phi\}$,

$$PY_{lm}(\hat{r}) = Y_{lm}(-\hat{r}) = (-)^l Y_{lm}(\hat{r}).$$

Combining all this we get for the angular integral in correlation function

$$\int \frac{d\Omega}{(2\pi)^3}\ \mathcal{P}_l(\mu)e^{-i\mathbf{q}\cdot\mathbf{s}} = \frac{1}{2\pi^2}(-i)^l j_l(qs)\mathcal{P}_l(\nu), \tag{6.57}$$

where $\nu$ is the cosine of the angle between $\mathbf{s}$ and line of sight $\hat{z}$, $\nu = \mathbf{s}\cdot\hat{z}/s$. Here we have also used the orthogonality relation for spherical harmonics. The expansion of the redshift space correlation function into multipoles

$$\xi^{ss}(\mathbf{s}) = \sum_{l=0,2,4,...} \xi_l(s)\mathcal{P}_l(\nu) \tag{6.58}$$

gives the expansion coefficients, which are given by spherical Bessel function moments of the power spectra

$$\xi_l(s) = i^l\int \frac{q^2dq}{2\pi^2}\ P_l^{ss}(q)j_l(qs). \tag{6.59}$$

## 6.7 Smoothing of the correlation function and power spectrum

In section 6.4 we introduce the Gaussian function in order to smooth the model prediction of the RSD power spectrum. Primary motivation for this is better control of the Fourier transform. In this way we get a well behaved predictions of the smoothed correlation function

$$\xi_W^{ss}(\mathbf{s}) = \int \frac{d^3q}{(2\pi)^3}\ W_R(q)P^{ss}(\mathbf{q})e^{-i\mathbf{q}\cdot\mathbf{s}}, \tag{6.60}$$

where $W_R(q)$ is the Gaussian smoothing filter. In order to be consistent in comparing the agreement of the modelling results with the direct measurements of correlation function in N-body simulations we also have to evaluate the effects of smoothing on the simulation data. Using the definition above we can connect the smoothed correlation function with the unsmoothed one

$$\xi^{ss}_W(\mathbf{r}) = \int d^3r' \; \tilde{W}_R(|\mathbf{r}' - \mathbf{r}|)\xi^{ss}(\mathbf{r}'), \tag{6.61}$$

where $\tilde{W}_R(\mathbf{r})$ is a Fourier transform of window function $W_R(\mathbf{k})$. In Gaussian case this gives:

$$W_R(\mathbf{k}) = \exp\left(-1/4 \; k^2R^2\right) \implies \tilde{W}_R(\mathbf{r}) = \frac{1}{\pi^{3/2}R^3}\exp(-r^2/R^2). \tag{6.62}$$

Finally expanding the unsmoothed correlation function in multipoles 6.58 we find the multipole expansion of smoothed correlation function

$$\xi^{ss}_W(\mathbf{s}) = \sum_{l=0,2,4,\ldots} \xi^{(l)}_W(s)\mathcal{P}_l(\nu), \tag{6.63}$$

where the multipoles are given by:

$$\xi^{(l)}_W(r) = 4\pi(-i)^l \exp(-r^2/R^2) \int dr' \; r'^2 \tilde{W}_R(r')\xi^{ss}_l(r')j_l\left(i\frac{2rr'}{R^2}\right). \tag{6.64}$$

In general the smoothing filter dose not have to be Gaussian function. If the filter is still a spherically symmetric function we have for the multipoles:

$$\xi^{(l)}_W(r) = \int dr' \; r'^2\xi^{ss}_l(r') \; \frac{2}{\pi}\int dq \; q^2 W_R(q) j_l\left(qr'\right) j_l\left(qr\right). \tag{6.65}$$

Note also that when we choose a filter to be spherical in either configuration or momentum space, it follows that its Fourier transform is also spherical.

# Bibliography


[1] Z. Vlah, U. Seljak, T. Okumura, and V. Desjacques, **Distribution function approach to redshift space distortions. Part V: perturbation theory applied to dark matter halos**, *JCAP* **1310** (2013) 053, [arXiv:1308.6294].

[2] N. Kaiser, **Clustering in real space and in redshift space**, *Mon. Not. Roy. Astron. Soc.* **227** (1987) 1–27.

[3] A. Hamilton, **Linear redshift distortions: A Review**, astro-ph/9708102. Published in The Evolving Universe. Edited by D. Hamilton, Kluwer Academic, 1998, p. 185-275.

[4] J. Jackson, **Fingers of God**, *Mon.Not.Roy.Astron.Soc.* **156** (1972) 1, [arXiv:0810.3908].

[5] S. Cole, K. B. Fisher, and D. H. Weinberg, **Fourier analysis of redshift space distortions and the determination of Omega**, *Mon.Not.Roy.Astron.Soc.* **267** (1994) 785, [astro-ph/9308003].

[6] M. White, Y.-S. Song, and W. J. Percival, **Forecasting Cosmological Constraints from Redshift Surveys**, *Mon.Not.Roy.Astron.Soc.* **397** (2008) 1348–1354, [arXiv:0810.1518].

[7] P. McDonald and U. Seljak, **How to measure redshift-space distortions without sample variance**, *JCAP* **0910** (2009) 007, [arXiv:0810.0323].

[8] K. Yamamoto, T. Sato, and G. Huetsi, **Testing general relativity with the multipole spectra of the SDSS luminous red galaxies**, *Prog.Theor.Phys.* **120** (2008) 609–614, [arXiv:0805.4789].

[9] B. A. Reid, W. J. Percival, D. J. Eisenstein, L. Verde, D. N. Spergel, et al., **Cosmological Constraints from the Clustering of the Sloan Digital Sky Survey DR7 Luminous Red Galaxies**, *Mon.Not.Roy.Astron.Soc.* **404** (2010) 60–85, [arXiv:0907.1659].

[10] **S**DSS Collaboration Collaboration, W. J. Percival et al., **Baryon Acoustic Oscillations in the Sloan Digital Sky Survey Data Release 7 Galaxy Sample**, *Mon.Not.Roy.Astron.Soc.* **401** (2010) 2148–2168, [arXiv:0907.1660].

[11] E. A. Kazin, M. R. Blanton, R. Scoccimarro, C. K. McBride, and A. A. Berlind, **Regarding the Line-of-Sight Baryonic Acoustic Feature in the Sloan Digital Sky Survey and Baryon Oscillation Spectroscopic Survey Luminous Red Galaxy Samples**, *Astrophys.J.* **719** (2010) 1032–1044, [arXiv:1004.2244].

[12] G. M. Bernstein and Y.-C. Cai, **Cosmology without cosmic variance**, arXiv:1104.3862.

[13] B. A. Reid, L. Samushia, M. White, W. J. Percival, M. Manera, et al., **The clustering of galaxies in the SDSS-III Baryon Oscillation Spectroscopic Survey: measurements of the growth of structure and expansion rate at z=0.57 from anisotropic clustering**, arXiv:1203.6641.

[14] L. Casarini, S. A. Bonometto, S. Borgani, K. Dolag, G. Murante, et al., **Tomographic weak lensing shear spectra from large N-body and hydrodynamical simulations**, arXiv:1203.5251.

[15] R. Scoccimarro, **Redshift-space distortions, pairwise velocities and nonlinearities**, *Phys.Rev.* **D70** (2004) 083007, [astro-ph/0407214].

[16] J. R. Shaw and A. Lewis, **Non-linear Redshift-Space Power Spectra**, *Phys.Rev.* **D78** (2008) 103512, [arXiv:0808.1724].

[17] T. Okumura and Y. Jing, **Systematic Effects on Determination of the Growth Factor from Redshift-space Distortions**, *Astrophys.J.* **726** (2011) 5, [arXiv:1004.3548].

[18] A. Taruya, T. Nishimichi, and S. Saito, **Baryon Acoustic Oscillations in 2D: Modeling Redshift-space Power Spectrum from Perturbation Theory**, *Phys.Rev.* **D82** (2010) 063522, [arXiv:1006.0699].

[19] E. Jennings, C. M. Baugh, and S. Pascoli, **Modelling redshift space distortions in hierarchical cosmologies**, *Mon.Not.Roy.Astron.Soc.* **410** (2011) 2081, [arXiv:1003.4282].

[20] J. Tang, I. Kayo, and M. Takada, **Likelihood reconstruction method of real-space density and velocity power spectra from a redshift galaxy survey**, arXiv:1103.3614.

[21] A. Taruya, T. Nishimichi, and F. Bernardeau, **Precision modeling of redshift-space distortions from multi-point propagator expansion**, arXiv:1301.3624.

[22] A. Vallinotto and E. V. Linder, **Redshift Space Distortion Reconstruction**, arXiv:1307.2906.

[23] F. Bernardeau, S. Colombi, E. Gaztanaga, and R. Scoccimarro, **Large scale structure of the universe and cosmological perturbation theory**, *Phys.Rept.* **367** (2002) 1–248, [astro-ph/0112551].

[24] J. Carlson, M. White, and N. Padmanabhan, **A critical look at cosmological perturbation theory techniques**, *Phys. Rev.* **D80** (2009) 043531, [arXiv:0905.0479].

[25] M. Crocce and R. Scoccimarro, **Renormalized cosmological perturbation theory**, *Phys.Rev.* **D73** (2006) 063519, [astro-ph/0509418].

[26] M. Crocce and R. Scoccimarro, **Memory of initial conditions in gravitational clustering**, *Phys.Rev.* **D73** (2006) 063520, [astro-ph/0509419].

[27] M. Crocce and R. Scoccimarro, **Nonlinear Evolution of Baryon Acoustic Oscillations**, *Phys.Rev.* **D77** (2008) 023533, [arXiv:0704.2783].

[28] T. Matsubara, **Resumming Cosmological Perturbations via the Lagrangian Picture: One-loop Results in Real Space and in Redshift Space**, *Phys.Rev.* **D77** (2008) 063530, [arXiv:0711.2521].

[29] T. Matsubara, **Nonlinear perturbation theory with halo bias and redshift-space distortions via the Lagrangian picture**, *Phys.Rev.* **D78** (2008) 083519, [arXiv:0807.1733].

[30] P. McDonald, **Dark matter clustering: a simple renormalization group approach**, *Phys.Rev.* **D75** (2007) 043514, [astro-ph/0606028].

[31] A. Taruya and T. Hiramatsu, **A Closure Theory for Non-linear Evolution of Cosmological Power Spectra**, arXiv:0708.1367.

[32] M. Pietroni, **Flowing with Time: a New Approach to Nonlinear Cosmological Perturbations**, *JCAP* **0810** (2008) 036, [arXiv:0806.0971].

[33] P. Valageas, **A new approach to gravitational clustering: a path-integral formalism and large-n expansions**, *Astron.Astrophys.* **421** (2004) 23–40, [astro-ph/0307008].

[34] A. Taruya, T. Nishimichi, S. Saito, and T. Hiramatsu, **Non-linear Evolution of Baryon Acoustic Oscillations from Improved Perturbation Theory in Real and Redshift Spaces**, *Phys.Rev.* **D80** (2009) 123503, [arXiv:0906.0507].

[35] A. Taruya, F. Bernardeau, T. Nishimichi, and S. Codis, **RegPT: Direct and fast calculation of regularized cosmological power spectrum at two-loop order**, *Phys.Rev.* **D86** (2012) 103528, [arXiv:1208.1191].

[36] S. Anselmi and M. Pietroni, **Nonlinear Power Spectrum from Resummed Perturbation Theory: a Leap Beyond the BAO Scale**, *JCAP* **1212** (2012) 013, [arXiv:1205.2235].

[37] M. Crocce, R. Scoccimarro, and F. Bernardeau, **MPTbreeze: A fast renormalized perturbative scheme**, arXiv:1207.1465.

[38] P. McDonald, **Clustering of dark matter tracers: Renormalizing the bias parameters**, *Phys.Rev.* **D74** (2006) 103512, [astro-ph/0609413].

[39] P. McDonald and A. Roy, **Clustering of dark matter tracers: generalizing bias for the coming era of precision LSS**, *JCAP* **0908** (2009) 020, [arXiv:0902.0991].

[40] K. C. Chan, R. Scoccimarro, and R. K. Sheth, **Gravity and Large-Scale Non-local Bias**, *Phys.Rev.* **D85** (2012) 083509, [arXiv:1201.3614].

[41] K. C. Chan and R. Scoccimarro, **Halo Sampling, Local Bias and Loop Corrections**, arXiv:1204.5770.

[42] A. J. Nishizawa, M. Takada, and T. Nishimichi, **Perturbation theory for nonlinear halo power spectrum: the renormalized bias and halo bias**, arXiv:1212.4025.

[43] J. L. Tinker, **Redshift-Space Distortions with the Halo Occupation Distribution II: Analytic Model**, *Mon.Not.Roy.Astron.Soc.* **374** (2007) 477–492, [astro-ph/0604217].

[44] T. Nishimichi and A. Taruya, **Baryon Acoustic Oscillations in 2D II: Redshift-space halo clustering in N-body simulations**, *Phys.Rev.* **D84** (2011) 043526, [arXiv:1106.4562].

[45] T. Matsubara, **Nonlinear Perturbation Theory Integrated with Nonlocal Bias, Redshift-space Distortions, and Primordial Non-Gaussianity**, *Phys.Rev.* **D83** (2011) 083518, [arXiv:1102.4619].

[46] T. Matsubara, **Deriving an Accurate Formula of Scale-dependent Bias with Primordial Non-Gaussianity: An Application of the Integrated Perturbation Theory**, *Phys.Rev.* **D86** (2012) 063518, [arXiv:1206.0562].

[47] B. A. Reid and M. White, **Towards an accurate model of the redshift space clustering of halos in the quasilinear regime**, arXiv:1105.4165.

[48] M. Sato and T. Matsubara, **Nonlinear Biasing and Redshift-Space Distortions in Lagrangian Resummation Theory and N-body Simulations**, *Phys.Rev.* **D84** (2011) 043501, [arXiv:1105.5007].

[49] H. Gil-Marin, C. Wagner, L. Verde, C. Porciani, and R. Jimenez, **Perturbation theory approach for the power spectrum: from dark matter in real space to haloes in redshift space**, *JCAP* **1211** (2012) 029, [arXiv:1209.3771].

[50] J. Carlson, B. Reid, and M. White, **Convolution Lagrangian perturbation theory for biased tracers**, arXiv:1209.0780.

[51] L. Wang, B. Reid, and M. White, **An analytic model for redshift-space distortions**, *Mon. Not. R. Astron. Soc.* (2013) [arXiv:1306.1804].

[52] U. Seljak and P. McDonald, **Distribution function approach to redshift space distortions**, arXiv:1109.1888.

[53] T. Okumura, U. Seljak, P. McDonald, and V. Desjacques, **Distribution function approach to redshift space distortions: N-body simulations**, arXiv:1109.1609.

[54] Z. Vlah, U. Seljak, P. McDonald, T. Okumura, and T. Baldauf, **Distribution function approach to redshift space distortions. Part IV: perturbation theory applied to dark matter**, arXiv:1207.0839.

[55] T. Okumura, U. Seljak, and V. Desjacques, **Distribution function approach to redshift space distortions, Part III: halos and galaxies**, arXiv:1206.4070.

[56] T. Baldauf, U. Seljak, V. Desjacques, and P. McDonald, **Evidence for Quadratic Tidal Tensor Bias from the Halo Bispectrum**, arXiv:1201.4827.

[57] V. Desjacques and R. K. Sheth, **Redshift space correlations and scale-dependent stochastic biasing of density peaks**, *Phys.Rev.* **D81** (2010) 023526, [arXiv:0909.4544].

[58] V. Desjacques, M. Crocce, R. Scoccimarro, and R. K. Sheth, **Modeling scale-dependent bias on the baryonic acoustic scale with the statistics of peaks of Gaussian random fields**, *Phys.Rev.* **D82** (2010) 103529, [arXiv:1009.3449].

[59] T. Baldauf, U. Seljak, R. E. Smith, N. Hamaus, and V. Desjacques, **Halo Stochasticity from Exclusion and non-linear Clustering**, arXiv:1305.2917.

[60] S. Saito, **et. al., In preparation**, .

[61] N. Hamaus, U. Seljak, V. Desjacques, R. E. Smith, and T. Baldauf, **Minimizing the Stochasticity of Halos in Large-Scale Structure Surveys**, *Phys.Rev.* **D82** (2010) 043515, [arXiv:1004.5377].

[62] D. J. Eisenstein and W. Hu, **Baryonic Features in the Matter Transfer Function**, *Astrophys. J.* **496** (1998) 605, [astro-ph/9709112].

[63] V. Desjacques, **Baryon acoustic signature in the clustering of density maxima**, *Phys.Rev.* **D78** (2008) 103503, [arXiv:0806.0007].

[64] E. A. Kazin, A. G. Sanchez, A. J. Cuesta, F. Beutler, C.-H. Chuang, et al., **The Clustering of Galaxies in the SDSS-III Baryon Oscillation Spectroscopic Survey: Measuring H(z) and D(z) at z = 0.57 with Clustering Wedges**, arXiv:1303.4391.

[65] J. Blazek et al., **In preparation**, .

[66] M. Caprio, **LevelScheme: A level scheme drawing and scientific figure preparation system for Mathematica**, *Computer Physics Communications* **171** (Sept., 2005) 107–118, [physics/0].

# Chapter 7

# Lagrangian Perturbation Theory: Power Spectrum at 1-loop Order [1]

We explore Lagrangian perturbation theory (LPT) approach, in which one can express the matter density power spectrum in terms of integrals over a function of cumulants of the displacement field, allowing for a resummation of the terms. We evaluate the full one loop power spectrum in LPT keeping the cumulants up to third order, extending the Zel'dovich approximation and providing the power spectrum analogous to the calculations recently performed for correlation function. We compare the results to the N-body simulations and to the LPT simulations up to the second order. We find that the analytic calculations are in a good agreement with the LPT simulations, thus justifying a truncation of cumulant hierarchy in this case. While one loop calculations improve upon the Zel'dovich approximation, the resulting power spectrum is still significantly below the N-body simulations. We argue that the problem, in large extent, can be traced to the zero lag rms displacement field, which is in one loop calculations significantly over predicted. We also show the results for the correlation function and compare it to the N-body correlation function measurements.
In the latter part of this chapter we decompose the power spectra and correlation function in tree additive parts: Zel'dovich part, residual BAO wiggle part, and residual broad band part. Motivation for such decomposition comes from the fact that the correlation function in Zel'dovich approximation gives far better prediction in comparison to N-body simulation than does the linear theory. Residual wiggle contribution is treated using LPT based approach, where good agreement is found both in power spectrum and correlation function. For the residual broad band contribution we propose simple two parameter formula. We compare the results to the N-body simulations in both, Fourier and configuration space.

## 7.1 Introduction

Clustering of dark matter particles under the gravity represents one of the building blocs in the study of large scale structure (LSS). Understanding the non-linear effects of dark matter clustering is crucial for improving the theoretical modelling for many current cosmological probes like galaxy surveys, weak lensing etc. Current paradigm is that large-scale structure grows through a process of gravitational instability, starting from a nearly scale-invariant spectrum of Gaussian fluctuations at early times. Since dark matter particles are assumed to be non-relativistic, at scales smaller than the Hubble scale general relativistic description of gravity can be reduced to Newtonian description. On large scales (but inside the Hubble horizon) the matter distribution is well modelled by linear perturbation theory. Conversely, on small scales, or Fourier modes with $k > 0.1$ Mpc$/h$, the dynamics starts to be non-linear.

[1] This chapter is based on a paper by Z. Vlah, U. Seljak and T. Baldauf that has been submitted to the Physical Review D.

One way to address this are the numerical simulations of the N-body type which offer a reliable way to understand the nonlinear clustering of matter.

An alternative approach to the non-linear scales (at least in quasi linear regime) is to extend the perturbation theory beyond the linear order. Main advantages of this approach are twofold. From the practical side perturbation theory offers a faster way of evaluating the observables for a given set of cosmological parameters. These observables are then used for comparison with the measurements in order to put the constraints on cosmological parameters. From a theoretical perspective perturbation theory offers an additional and/or complementary physical insight into the effects of non-linear clustering. A better physical understanding would also be useful to model higher order correlations, such as modelling the covariance matrix of dark matter two-point correlations etc.

Consequently, numerous approaches have been introduced for computing statistical properties of the matter distribution. The standard perturbation theory (SPT) in Eulerian framework has been extensively studied and has achieved some success (see for example [1, 2, 3, 4]). Various resummation schemes have been proposed [5, 6, 7, 8, 9, 10, 11, 12, 13] in order to extend the validity of the perturbative expansion. Numerical implementations of some of these methods have become available [14, 15]. Also, a number of alternative methods have been suggested (e.g. [16, 17, 18, 19, 20]) that use different levels of approximation. Alternatively, one can also consider Lagrangian picture as starting point of perturbation theory (LPT), e.g. [21, 22, 23, 24, 25, 26, 27, 28], where the focus is on perturbing the displacement field rather than overdensity and velocity fields itself. Recent work has emphasized the fundamental failure of ab initio perturbation theory on small scales, where effects are non-perturbative (e.g. [29, 30, 31, 32, 33, 34, 35, 36]), forcing one to adopt a more modest goal of integrating out the small scales and introduce effective description with free parameters.

In this paper we first follow the recent work done in studying the Lagrangian picture [21, 24, 28], extending the analytic calculation methods, and exploring the accuracy and performance of this approach for the matter power spectrum and correlation function. We test the performance of one loop analytical calculations against the N-body simulations in both Fourier and configuration space. We then connect these calculations to the standard perturbation theory and show the connection between the two. We identify the main shortcomings of the approach and propose the decomposition of the powers spectra in tree additive parts; Zel'dovich part, residual contribution to the baryon acoustic oscillation (BAO) wiggles and residual contribution to broad band power. We show that LPT based approach is well suited for analysing the residual wiggle contribution. We show how the corrections of the displacement field of two point function (see [37]) effect the residual contributions to the BAO wiggles. For the residual broad band part we propose the simple, two parameter, formula. Finely, we show the relative effects of these contributions and comparison to the N-body simulations in both, Fourier and configuration space.

This paper is organised as follows: in section 7.2 we present the framework for the dark matter power spectrum and review the Lagrangian perturbation theory for the displacement field. We present the methods to compute the one loop power spectrum and show the corresponding low k limit result. In section 7.3 we look at various cross-power spectra at 2LPT level and compare it to to the grid 2LPT numerical results. In section 7.4 the correlation function results are presented and compared to the N-body measurements. In section 7.5 we study the improvement of the LPT results by decomposing it into tree additive parts and we show the extent of agreement of these results with N-body simulations on the power spectrum and the correlation function. Finally, we conclude our findings in section 7.6. In Appendices 7.7, 7.8, 7.9, 7.10 we show some details of the calculations and write explicit forms of the terms contributing to the power spectra.

For this work, flat $\Lambda$CDM model is assumed $\Omega_{\rm m} = 0.272$, $\Omega_\Lambda = 0.728$, $\Omega_{\rm b}/\Omega_{\rm m} = 0.167$, $h = 0.704$, $n_s = 0.967$, $\sigma_8 = 0.81$. The primordial density field is generated using the matter transfer function by CAMB. The positions and velocities of all the dark matter particles are given at the redshifts $z = 0.0$, 0.5, 1.0, and 2.0.

## 7.2 Clustering in Lagrangian picture

### 7.2.1 Overdensity field evolution and power spectrum

A central quantity in Lagrangian picture is the displacement field $\Psi(\mathbf{q}, \tau)$. It represents the mapping of a particle from its initial position $\mathbf{q}$, to the Eulerian-space coordinate at a given moment in time $\mathbf{r}$

$$\mathbf{r}(\mathbf{q}, \tau) = \mathbf{q} + \Psi(\mathbf{q}, \tau). \tag{7.1}$$

From this we see that $\Psi(\mathbf{q}, \tau)$ can also be understood as the velocity field integral along the world-line of the particle, starting from the origin

$$\Psi(\mathbf{q}, \tau) = \int^{\tau} d\tau' \mathbf{v}\left(\mathbf{r}(\mathbf{q}, \tau'), \tau'\right). \tag{7.2}$$

We are interested in the density field of dark matter particles and how it evolves with time. Continuity equation and the assumption that we have uniform initial density field give the relation of overdensity field in the volume element $d^3r$ at the position $\mathbf{r}$ with initial conditions

$$(1 + \delta(\mathbf{r}))\, d^3r = d^3q \quad \rightarrow \quad 1 + \delta(\mathbf{r}) = \int d^3q\ \delta^D\left(\mathbf{r} - \mathbf{q} - \Psi(\mathbf{q})\right).$$

In Fourier space this relation gives

$$(2\pi)^3 \delta^D(\mathbf{k}) + \delta(\mathbf{k}) = \int d^3q\ e^{i\mathbf{k}\cdot\mathbf{q}}\ \exp\left(i\mathbf{k}\cdot\Psi\right), \tag{7.3}$$

where we are following the Fourier conventions:

$$\tilde{f}(\mathbf{k}) = \mathcal{F}\left[f(\mathbf{x})\right](\mathbf{k}) = \int d^3x\ \exp(i\mathbf{k}\cdot\mathbf{x}) f(\mathbf{x}),$$
$$f(\mathbf{x}) = \mathcal{F}^{-1}\left[\tilde{f}(\mathbf{k})\right](\mathbf{x}) = \int \frac{d^3k}{(2\pi)^3}\ \exp(-i\mathbf{k}\cdot\mathbf{x})\tilde{f}(\mathbf{k}).$$

The simplest and thus the most interesting statistical quantity that can be constructed from this field is the two point correlation function, or its Fourier space analog, the power spectrum. Since we assume a homogeneity and isotropy of the dark matter distribution we can define the power spectrum

$$(2\pi)^3 P(k) \delta^D(\mathbf{k} + \mathbf{k}') = \left\langle \delta(\mathbf{k})\delta(\mathbf{k}') \right\rangle. \tag{7.4}$$

Using equation 7.3 it follows that the power spectrum in terms of displacement field is given by

$$(2\pi)^3 \delta^D(k) + P(k) = \int d^3q\ e^{-i\mathbf{q}\cdot\mathbf{k}} \left\langle \exp(-i\mathbf{k}\cdot\Delta) \right\rangle, \tag{7.5}$$

where we have introduced the differential displacement vector field

$$\Delta = \Psi(\mathbf{q}_2) - \Psi(\mathbf{q}_1) \tag{7.6}$$

and define the separation vector $\mathbf{q} = \mathbf{q}_2 - \mathbf{q}_1$. Following the notation from [24] we can introduce the generating function of the differential displacement vector field

$$K(\mathbf{q}) = \left\langle \exp(-i\mathbf{k}\cdot\Delta) \right\rangle, \tag{7.7}$$

As a consequence of spatial homogeneity and isotropy, generating function $K$ is a function of separation vector $\mathbf{q}$ only, rather than $\mathbf{q}_2$ and $\mathbf{q}_1$. In this way the translational invariance remains manifestly imposed at every step of this approach.

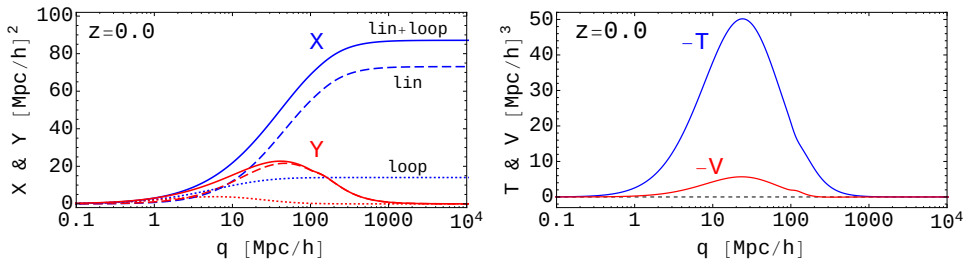


**Figure 7.1:** Scale dependence of two and tree point functions of displacement field, equations 7.12, that contribute to the cumulant expansion, shown at redshift $z = 0.0$. Linear (dotted) and one loop (dashed) contributions to the $X$ (blue) and $Y$ (red) terms (solid line is linear + one loop) are shown on the left panel. On the right panel we show tree level contribution to the $V$ (red) and $T$ (blue) terms (solid lines).

### 7.2.2 Cumulant expansion and the hierarchy

The cumulant expansion theorem allows expansion of the expected value of exponential function

$$K = \left\langle e^{-i\mathbf{k}\cdot\Delta} \right\rangle = \exp\left[ \sum_{N=1}^{\infty} \frac{(-i)^N}{N!} \left\langle (\mathbf{k}\cdot\Delta)^N \right\rangle_c \right], \tag{7.8}$$

where $\left\langle (\mathbf{k}\cdot\Delta)^N \right\rangle_c$ stands for $N$th cumulant of random variable X. In diagrammatic representation this means that only connected terms contribute to the correlation. We can write [24],

$$\begin{aligned} \log K &= \sum_{N=1}^{\infty} \frac{(-i)^N}{N!} \left\langle (\mathbf{k}\cdot\Delta)^N \right\rangle_c \\ &= \sum_{N=1}^{\infty} \frac{(-i)^N}{N!} k_{i_1} \dots k_{i_N} \left\langle \Delta_{k_1} \dots \Delta_{k_N} \right\rangle_c . \end{aligned} \tag{7.9}$$

In order to get the full power spectrum an infinite sum of these terms should be computed. However, since this is an expansion in powers of $k$, the series is convergent for sufficiently small values of $k$, in which case we can truncate the sum at a given order that meets our required accuracy. By isotropy we have that $N = 1$ term vanishes. At the first order the displacement field is Gaussian and this gives the Zel'dovich approximation, for which only the $N = 2$ cumulant is non-vanishing. In his paper we expand the displacement field to third order and keep only one loop terms, which means the fourth cumulant vanishes, hence we evaluate the summation to the third cumulant of $\Delta$ field, which leaves two cumulants to evaluate

$$\begin{aligned} A_{ij}(\mathbf{q}) &= \left\langle \Delta_i \Delta_j \right\rangle_c , \\ W_{ijk}(\mathbf{q}) &= \left\langle \Delta_i \Delta_j \Delta_k \right\rangle_c . \end{aligned} \tag{7.10}$$

This gives

$$\log K = -\frac{1}{2} k_i k_j A_{ij}(\mathbf{q}) + \frac{i}{6} k_i k_j k_l W_{ijl}(\mathbf{q}).$$

Using this we have for the expression for the power spectrum given up to the third cumulant

$$(2\pi)^3 \delta^D(k) + P(k) = \int d^3q \; e^{-i\mathbf{q}\cdot\mathbf{k}} \exp\left[ -\frac{1}{2} k_i k_j A_{ij}(\mathbf{q}) + \frac{i}{6} k_i k_j k_l W_{ijl}(\mathbf{q}) \right]. \tag{7.11}$$

Next step is to evaluate the contributing cumulants in LPT. The displacement cumulants $A_{ij}(\mathbf{q})$ and $W_{ijk}(\mathbf{q})$ can be decomposed into irreducible components relative to the pair separation vector $\mathbf{q}$:

$$\begin{aligned} A_{ij}(\mathbf{q}) &= X(q)\delta^K_{ij} + Y(q)\hat{q}_i\hat{q}_j, \\ W_{ijk}(\mathbf{q}) &= V(q)\hat{q}_{\{i}\,\delta^K_{jk\}} + T(q)\hat{q}_i\hat{q}_j\hat{q}_k, \end{aligned} \tag{7.12}$$

here, we have introduced the four scalar functions $X(q)$, $Y(q)$, $V(q)$ and $T(q)$ which depend on the amplitude of separation $q$. Angular brackets on the summation indexes imply that the summation is to be taken over all of the cyclic permutations. This follows from the fact that $W_{ijk}$ cumulant is symmetric under a permutation of its indexes. Contracting indexes on these tensors and solving the system we get

$$\left.\begin{aligned} A_0 \equiv \delta^K_{ij}A_{ij} = 3X + Y \\ \bar{A} \equiv \hat{q}_i\hat{q}_jA_{ij} = X + Y \end{aligned}\right\} \rightarrow \begin{aligned} X &= \tfrac{1}{2}(A_0 - \bar{A}) \\ Y &= \tfrac{1}{2}(3\bar{A} - A_0), \end{aligned} \tag{7.13}$$

for the second cumulant, and similarly

$$\left.\begin{aligned} W_0 \equiv \hat{q}_i\delta^K_{jk}W_{ijk} = 5V + T \\ \overline{W} \equiv \hat{q}_i\hat{q}_j\hat{q}_kW_{ijk} = 3V + T \end{aligned}\right\} \rightarrow \begin{aligned} V &= \tfrac{1}{2}(W_0 - \overline{W}) \\ T &= \tfrac{1}{2}(5\overline{W} - 3W_0). \end{aligned} \tag{7.14}$$

for the third cumulant. Using this we can rewrite the power spectrum into the form

$$(2\pi)^3\delta^D(k) + P(k) = \int d^3q\; e^{i\mu k\left(q - \frac{1}{2}k^2V\right)} \exp\left[-\frac{1}{2}k^2(X + \mu^2Y) - \frac{i}{6}\mu^3k^3T\right], \tag{7.15}$$

where we have introduced the angle between the given $k$-mode and separation vector $\mu = \hat{q}\cdot\hat{k}$. It is worth keeping in mind that $A_{ij}$ is the two point correlator of the difference of displacement field and so contains a zero lag component: one can write

$$A_{ij}(\mathbf{q}) = \langle\Delta_i\Delta_j\rangle_c = 2\left(\sigma^2\delta^K_{ij} - \langle\Psi_i(\mathbf{q}_1)\Psi_j(\mathbf{q}_2)\rangle_{\mathbf{q}_2-\mathbf{q}_1=\mathbf{q}}\right), \tag{7.16}$$

where $\sigma^2\delta^K_{ij} = \langle\Psi_i(\mathbf{q})\Psi_j(\mathbf{q})\rangle = \frac{1}{2}X(q \rightarrow \infty)$ is the squared zero lag rms displacement. Because it is a zero lag quantity it is susceptible to nonlinear effects down to very small scales, where perturbation theory is unlikely to be reliable. Since this quantity does not depend on $\mathbf{q}$ its Fourier transform is zero except for $k = 0$. Because of this we will see below that it does not enter the final density power spectrum at the lowest order in $A_{ij}$, but it does enter at the quadratic order in $A_{ij}$ even in the low $k$ limit. In fact, due to its large value it dominates the nonlinear effects in this limit and is responsible for the smoothing of the BAO, among other effects. We will return to this discussion below.

### 7.2.3 Perturbation theory of the displacement fields

We use Lagrangian perturbation theory (LPT) up to one loop to compute the contributions to scalar functions $X$, $Y$, $V$ and $T$. This has in most parts been derived in [24] and we summarize it here for completeness, and in order to set up the framework for the later section 7.3, when we look at the cross power spectra of 2LPT. Detailed derivation of the $X$, $Y$, $V$ and $T$ terms is also given in appendix 7.7, and 7.8, respectively.
We start from the ansatz for the displacement field in Fourier space (see e.g. [21] )

$$\begin{aligned} \Psi_i(\mathbf{p},\tau) &= \sum_{n=1}^{\infty}\Psi_i^{(n)}(\mathbf{p},\tau) \\ &= -i\sum_{n=1}^{\infty}\frac{D^{(n)}(\tau)}{n!}\int\prod_{l=1}^{n}\left[\frac{d^3p_l}{(2\pi)^3}\delta_L(\mathbf{p}_l)\right](2\pi)^3\delta^3\Big(\sum_{j=1}^{n}\mathbf{p}_j - \mathbf{p}\Big)L_i^{(n)}(\mathbf{p}_1,\ldots,\mathbf{p}_n). \end{aligned} \tag{7.17}$$

where $\delta_L$ is the linear dark matter density field. Plugging this ansatz into the equation of motion and consistently solving order by order one gets the solution for the vector displacement kernels $\mathbf{L}^{(n)}(\mathbf{p}_l)$. This gives (see e.g. [38, 39, 2, 21, 40]

$$
\begin{aligned}
L_i^{(1)} &= \frac{k_i}{k^2}, \\
L_i^{(2)}(\mathbf{p}_1, \mathbf{p}_2) &= \frac{3}{7}\frac{k_i}{k^2}\left[1 - \left(\frac{\mathbf{p}_1 \cdot \mathbf{p}_2}{p_1 p_2}\right)^2\right], \\
L_i^{(3)}(\mathbf{p}_1, \mathbf{p}_2, \mathbf{p}_3) &= \frac{5}{7}\frac{k_i}{k^2}\left[1 - \left(\frac{\mathbf{p}_2 \cdot \mathbf{p}_3}{p_2 p_3}\right)^2\right] \\
&\quad \times \left\{1 - \left[\frac{\mathbf{p}_1 \cdot (\mathbf{p}_2 + \mathbf{p}_3)}{p_1 |\mathbf{p}_1 + \mathbf{p}_2|}\right]^2\right\} - \frac{1}{3}\frac{k_i}{k^2}\left[1 - 3\left(\frac{\mathbf{p}_1 \cdot \mathbf{p}_2}{p_1 p_2}\right)^2\right. \\
&\quad \left. + 2\frac{(\mathbf{p}_1 \cdot \mathbf{p}_2)(\mathbf{p}_2 \cdot \mathbf{p}_3)(\mathbf{p}_3 \cdot \mathbf{p}_1)}{p_1^2 p_2^2 p_3^2}\right] + \epsilon_{ijl} k_j K_l(\mathbf{p}_1, \mathbf{p}_2, \mathbf{p}_3),
\end{aligned}
\tag{7.18}
$$

where $\mathbf{k} = \mathbf{p}_1 + \ldots + \mathbf{p}_n$ for $\mathbf{L}^{(n)}$, and $K_l$ is the transverse part which does not enter at the lowest order. For the last $\mathbf{L}^{(3)}$ kernel it is useful to make it fully symmetrical in all the $\mathbf{p}_i$ variables. In general we can also solve for time evolution of these kernels, i.e. solve the second order differential equation for each $D^{(n)}(\tau)$ (see e.g. [2]), but for simplicity we assume the logarithmic growth rate to be $f(\tau) = d\ln D/d\ln a = \Omega_m^{1/2}(\tau)$. This simplifies the situation so the growth rate at each order in perturbations can be written as powers of linear growth rate $D^{(n)}(\tau) = D_L^n(\tau)$.
As done in [21] it is useful to define multispectra of the displacement field

$$
\langle \Psi_{i_1}(\mathbf{p}_1) \ldots \Psi_{i_N}(\mathbf{p}_1) \rangle_c = (2\pi)^3 \delta^D(\mathbf{p}_1 + \ldots + \mathbf{p}_N)\; i^{N-2} C_{i_1 \ldots i_N}(\mathbf{p}_1, \ldots, \mathbf{p}_N),
\tag{7.19}
$$

where $\Psi_i(\mathbf{p})$ are the Fourier transforms of the displacement fields.
Using this we can compute the $X$, $Y$ $V$ and $T$ terms up to one loop. Details of this calculation are presented in appendix 7.7 and 7.8, and can also be found in e.g. [24]. In figure 7.1 we show the result of up to one loop prediction of these terms at redshift $z = 0.0$. We see that going beyond the Zel'dovich calculation introduces the corrections to the $X$ and $Y$ terms where for $Y$ term we see that corrections are restricted to the scales below $\sim 100$ Mpc$/h$, while for the $X$ term on the other hand we have a correction on very large scales, which means that the 1 loop calculation gives a considerable contribution to the zero lag rms displacement. $V$ and $T$ terms are pure one loop terms which are zero in linear approximation. Both terms asymptote to zero at large and small scales. For $Y$, $V$, and $T$ terms we see that they have a peak at the scales of around $\sim 30$ Mpc$/h$.

### 7.2.4 Expansion in the angular moments

It is known that evaluating the matter power spectrum even in the Zel'dovich approximation is not as straightforward as doing the direct two dimensional integral. Direct numerical integration is not the optimal approach since the integral function can be highly oscillatory. In [43] the method is proposed to solve the Zel'dovich approximation power spectrum. Here we generalise this method to evaluate the higher order power spectrum.
We can express the power spectrum in the spherical frame where $\mathbf{k}$ is along the $\hat{z}$ direction:

$$
P(k) = 2\pi \int_0^\infty q^2 dq \int_{-1}^1 d\mu\; e^{i\mu k q} \left\{ e^{-\frac{1}{2}k^2 X} e^{-\frac{i}{2}\mu k^3 V} \exp\left[-\frac{1}{2}\mu^2 k^2 Y - \frac{i}{6}\mu^3 k^3 T\right] - e^{-\frac{1}{2}k^2\sigma^2} \right\},
\tag{7.20}
$$

where in the last term we added the zero lag term, which is an extra contribution that is a constant, hence vanishes for all $k$ except $\mathbf{k} = 0$. It is introduced to cure the oscillatory

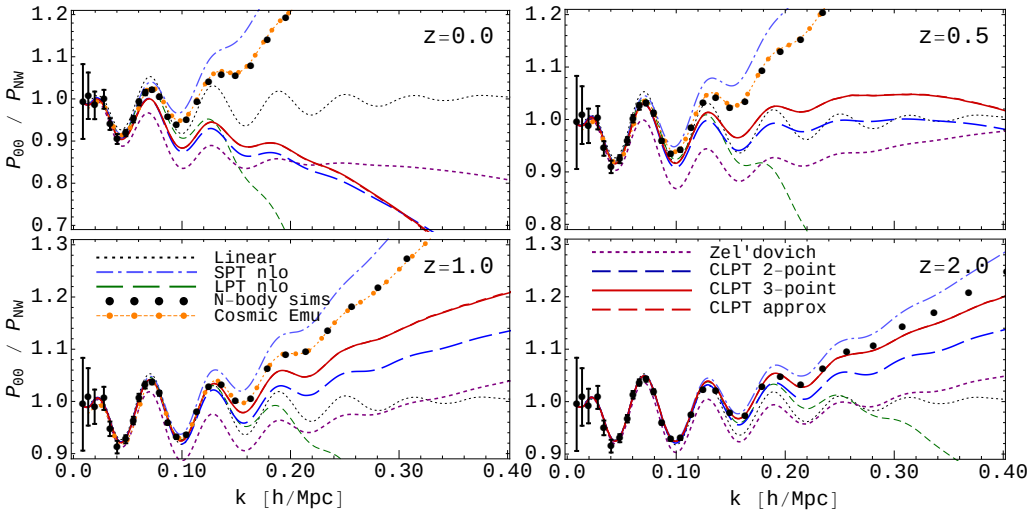


**Figure 7.2:** Power spectrum result obtained by several methods at redshift $z = 0.0,\ 0.5,\ 1.0$ and 2.0. Full result of equation 7.15 at one loop is shown (solid red line) together with the approximations where tree point contribution of $V$ and $T$ terms are dropped and two point terms $X$ and $Y$ remain at one loop (long-dashed blue line). Shown is also the corresponding result presented in [24] (long-dashed red line), where the exponent with three point term $W_{ijk}$ is expanded and only the first term is kept. This turns out to be a good approximation on scales shown here, and the difference is hardly noticeable. We also show the Zel'dovich result (short-dashed purple line), usual one loop SPT (dot-dashed light-blue line), one loop LPT (dashed green line) as presented in [21] as well as linear theory (dotted black line). For comparison we show the N-body simulation results (black dots) and cosmic emulator results [41] (orange connected-dots). All the spectra is divided by the no-wiggle linear power spectra [42] in order to reduce the range of scales.

integration problems. It depends on $\sigma^2$, the squared rms displacement, which can be evaluated in high $q$ limit of $X(q)$ (figure 7.1). We will return to this in the next section where we will focus on the low $k$ limit of the power spectrum. Direct evaluation of equation 7.20 is difficult because of fast oscillating terms. Instead we first rewrite equation 7.15 in more convenient form for evaluation

$$P(k) = \mathcal{Z}(k) + \mathcal{V}(k) + \mathcal{T}(k) \tag{7.21}$$

where we have

$$\begin{aligned}
\mathcal{Z}(k) &= \int d^3q\ e^{i\mu kq}\left(e^{-\frac{1}{2}k^2(X+\mu^2Y)} - e^{-\frac{1}{2}k^2\sigma^2}\right),\\
\mathcal{V}(k) &= \int d^3q\ e^{i\mu kq}e^{-\frac{1}{2}k^2(X+\mu^2Y)}\left(e^{-\frac{1}{2}\mu k^3V} - 1\right),\\
\mathcal{T}(k) &= \int d^3q\ e^{i\mu k\left(q-\frac{1}{2}k^2V\right)}e^{-\frac{1}{2}k^2(X+\mu^2Y)}\left(e^{-\frac{i}{6}\mu^3k^3T} - 1\right)
\end{aligned} \tag{7.22}$$

Note that the first contribution $\mathcal{Z}$ is the nonlinear Zel'dovich case where only the two point contribution in cumulant expansion is considered. To evaluate these terms we can use the expansion formula presented in Appendix 7.9. For the first two terms above, $\mathcal{Z}$ and $\mathcal{V}$ we can use the expansion

$$\int_{-1}^{1} d\mu\ e^{iA\mu}\ \exp(B\mu^2) = 2e^B\sum_{n=0}^{\infty}\left(-\frac{2B}{A}\right)^n j_n(A), \tag{7.23}$$

and for the third term we use the generalized equation 7.58

$$\int_{-1}^{1} d\mu\ e^{iA\mu}\ \exp(B\mu^2 + i\epsilon\mu^3) = 2e^B\sum_{n=0}^{\infty}\left(-\frac{2B}{A}\right)^n J_n(A,\epsilon), \tag{7.24}$$

where we $J_n(A,\epsilon)$ is the generalization for the spherical Bessel function $j_n(A)$ which we had in previous case. Explicit form for $J_n$ is given by equation 7.63. Note that in the limit of $\epsilon \to 0$ we retrieve the result above, i.e. $J_n(A,\epsilon) \to j_n(A)$. We see that integrals in equation 7.22 can be expressed in terms of these expansions using

$$A(k,q) = k\left(q - \frac{1}{2}k^2 V(q)\right), \quad B(k,q) = -\frac{1}{2}k^2 Y(q), \quad \epsilon(k,q) = -\frac{1}{6}k^3 T(q). \tag{7.25}$$

Doing so we have reduced the equation 7.22 integrals from three dimensional integrals to a quickly converging sum of one dimensional integrals. Typically the sum over $n$ can be truncated at $n < 15$ for $k < 1h/\text{Mpc}$ (in [43] it was argued $n = 3$ is good enough for $k < 0.3h/\text{Mpc}$). Since one dimensional integration over $q$ for a given $k$ is fast we use a conservative value of $n = 25$. We also developed an alternative expansion in spherical harmonics, which is presented in Appendix 7.10. This gives equivalent numerical results and will not be discussed here in more detail.
In figure 7.2 we show the results of the one loop LPT power spectrum up to four different redshifts, $z = 0.0$, 0.5, 1.0 and 2.0. Also shown are the results when three point function $W_{ijk}$ in equation 7.10 is neglected and only $A_{ij}$ term remains. We compare these to the N-body results as well as one loop SPT results. We see that LPT at low redshifts is significantly below the N-body results. We also show the corresponding result presented in [24], where the exponent with three point term $W_{ijk}$ is expanded and only the first term is kept. On the mildly-nonlinear scales that we are showing this is a very good approximation and it can hardly be distinguished from the full results presented in the same figure 7.2. Adding the three point function helps in the sense that it adds power, but the effect is relatively small. We also see that the effect of adding 1 loop corrections to Zeldovich leads to an increase in power at higher redshifts and also at lower redshifts for low $k$, as desired, but actually reduces power at higher $k$ for lower redshifts. This is a sign that there is something going wrong in the approach: we will argue below this is a sign of rms displacement in 1 loop calculations being too large.

### 7.2.5 Low $k$ limit and cosmic propagator

In this section we expand our result in equation 7.15 in $k$ powers to get the $k^2$ corrections to the linear theory. Expanding equation 7.11 it follows

$$\begin{aligned}(2\pi)^3\delta^D(k) + P(k) = (2\pi)^3\delta^D(k) &- \frac{1}{2}k_i k_j \int d^3q\; e^{i\mathbf{q}\cdot\mathbf{k}} A_{ij} \\ &- \frac{i}{6}k_i k_j k_l \int d^3q\; e^{i\mathbf{q}\cdot\mathbf{k}} W_{ijl} \\ &+ \frac{1}{8}k_i k_j k_l k_m \int d^3q\; e^{i\mathbf{q}\cdot\mathbf{k}} A_{ij} A_{lm} + \ldots\end{aligned} \tag{7.26}$$

Evaluating each of these terms using equations 7.50, 7.57 and the standard identities for spherical Bessel functions (e.g. [44, 45]) gives

$$\begin{aligned}-\frac{1}{2}k_i k_j \int d^3q\; e^{i\mathbf{q}\cdot\mathbf{k}} A_{ij} &= p(k) \\ -\frac{i}{6}k_i k_j k_l \int d^3q\; e^{i\mathbf{q}\cdot\mathbf{k}} W_{ijl} &= \frac{3}{7}\Big(Q_2(k) + 2R_2(k)\Big) \\ \frac{1}{8}k_i k_j k_l k_m \int d^3q\; e^{i\mathbf{q}\cdot\mathbf{k}} A_{ij} A_{lm} &= \frac{1}{2}Q_3(k) - k^2\sigma^2 p(k),\end{aligned} \tag{7.27}$$

where we use

$$p(k) = P_L(k) + \frac{9}{98}Q_1(k) + \frac{10}{21}R_1(k). \tag{7.28}$$

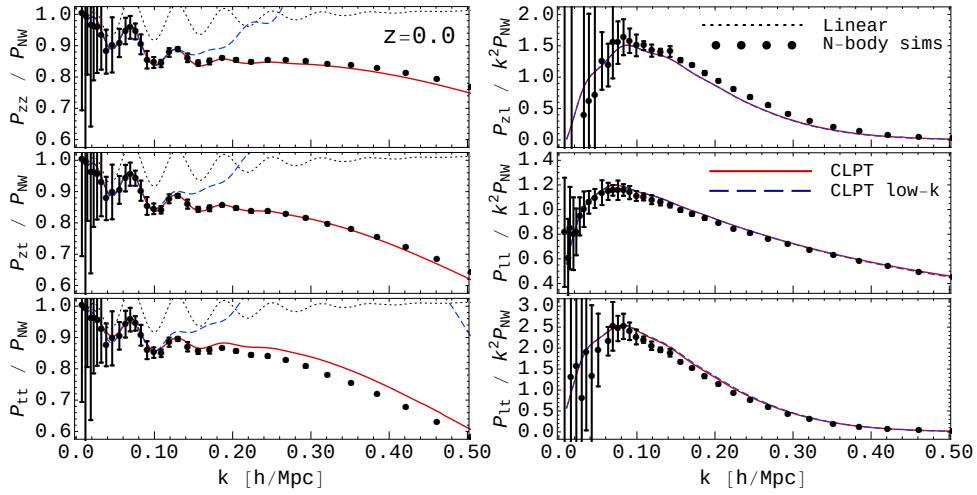


**Figure 7.3:** Cross and auto power spectrum results from table 7.1 using up to the 2LPT displacement at redshift $z = 0.0$. Result of equation 7.15 up to the 2LPT is shown (solid red lines) together with the low-$k$ limit results (dashed blue lines). For comparison we show the measured LPT simulation power spectra (black dots) obtained by displacing particle on the grid with the initial condition codes [46]. All the spectra are divided by the no-wiggle linear power spectra [42] in order to reduce the range in the plots.

Here all $Q_i$ and $R_i$ are as defined in [21]. For example, we have

$$\bar{Q}_3(k) = \int \frac{d^3p}{(2\pi)^3} \frac{(\mathbf{k}\cdot\mathbf{p})^2}{p^4} \frac{(\mathbf{k}\cdot(\mathbf{k}-\mathbf{p}))^2}{(\mathbf{k}-\mathbf{p})^4} p(k)p(|\mathbf{k}-\mathbf{p}|). \tag{7.29}$$

It is useful to define the projector operator $\mathbb{P}$ which acts on the function by projecting the full one loop result to its perturbation components: linear part $\mathbb{P}_L$, convolution part $\mathbb{P}_Q$ and the propagator part $\mathbb{P}_R$. As an example, the result of applying the $\mathbb{P}_Q$ to the full one loop result of bispectrum term $T$ given in equation 7.57 is

$$\mathbb{P}_Q T(k) = 3 \int \frac{dk}{2\pi^2 k} \left(-\frac{3}{7}\right) \Big(Q_1(k) + 2Q_2(k)\Big) j_3(qk), \tag{7.30}$$

Note that summing the three different operators gives identity operation, i.e. $\mathbb{P}_L + \mathbb{P}_Q + \mathbb{P}_R = \mathbb{I}$. With this one has

$$\sigma^2 = \sigma_L^2 + \sigma_{1\text{loop}}^2 = \frac{1}{3} \int \frac{d^3k}{(2\pi)^3} \frac{p(k)}{k^2}. \tag{7.31}$$

Here we have used the labels for the dispersion contributions $\sigma_L^2 = \mathbb{P}_L\sigma^2$ and $\sigma_{1\text{loop}}^2 = (\mathbb{P}_Q + \mathbb{P}_R)\sigma^2$. If we also define the new contributions

$$Q_{3Q,L}(k) = \int \frac{d^3p}{(2\pi)^3} \frac{(\mathbf{k}\cdot\mathbf{p})^2}{p^4} \frac{(\mathbf{k}\cdot(\mathbf{k}-\mathbf{p}))^2}{(\mathbf{k}-\mathbf{p})^4} \mathbb{P}_{Q,L}p(q)\mathbb{P}_{Q,L}p(|\mathbf{k}-\mathbf{p}|) \tag{7.32}$$

This gives the correction to the 1 loop SPT power spectrum

$$P(k) = P_{1\text{loop}}^{\text{SPT}}(k) + \frac{1}{2}\left(Q_3(k) - Q_{3L}(k)\right) - k^2 P_L(k)\sigma_{1\text{loop}}^2. \tag{7.33}$$

The last part here gives the correction to the $k^2$ SPT propagator which suppresses the power. In the high $k$ limit this term is cancelled by the second term due to the fact that relative displacement field vanishes in the limit of small separation (the so called galilean invariance), but in the low $k$ limit the last term dominates. At $z = 0$ the linear theory value of $\sigma_L^2 = 36.55$ (Mpc/$h$)$^2$, and $\sigma_{1\text{loop}}^2 = 7.00$ (Mpc/$h$)$^2$, so the 1 loop correction is quite large.

**Table 7.1:** Cross and auto power spectra up to 2LPT.

| | $P^{zz}$ | $P^{zl}$ | $P^{zt}$ | $P^{ll}$ | $P^{lt}$ | $P^{tt}$ |
|---|---|---|---|---|---|---|
| $X^{\alpha\beta}$ | $\mathbb{P}_L X$ | $(\mathbb{P}_L + \mathbb{P}_Q)\sigma^2$ | $\mathbb{P}_L X + \mathbb{P}_Q \sigma^2$ | $\mathbb{P}_Q X$ | $\mathbb{P}_Q X + \mathbb{P}_L \sigma^2$ | $(\mathbb{P}_L + \mathbb{P}_Q)X$ |
| $Y^{\alpha\beta}$ | $\mathbb{P}_L Y$ | 0 | $\mathbb{P}_L Y$ | $\mathbb{P}_Q Y$ | $\mathbb{P}_Q Y$ | $(\mathbb{P}_L + \mathbb{P}_Q)Y$ |
| $V^{\alpha\beta}$ | 0 | $\frac{1}{2}\mathbb{P}_Q V$ | $\frac{1}{2}V$ | 0 | $\frac{1}{2}\mathbb{P}_Q V$ | $V$ |
| $T^{\alpha\beta}$ | 0 | $\frac{1}{2}\mathbb{P}_Q T$ | $\frac{1}{2}T$ | 0 | $\frac{1}{2}\mathbb{P}_Q T$ | $T$ |

In this paper we argue that zero lag quantities are difficult to evaluate perturbatively because they receive contributions from all scales, including very small scales not amenable to the perturbation theory. Both the linear Zel'dovich and its 1 loop generalization suffer from the adhesion problem: while in simulations particles stop its displacement streaming because they are trapped inside the dark matter halos, in Zeldovich approximation and its higher order LPT extensions this does not happen and the particles keep streaming along their paths. Because of this the displacement field will be filtered out on small scales, which is the regime where 1 loop calculation predicts a large contribution. As a consequence, 1 loop LPT is unreliable in its rms displacement prediction, results from N-body simulations (see e.g. [37, 47] suggest that the full nonlinear value should be just slightly higher than the linear prediction $\sigma_L^2$. This is because most of the linear Zel'dovich contribution comes from rather large scales, where the predictions are reliable. If we erase both of the last two terms in equation 7.33 we obtain precisely the 1 loop SPT result in this limit. If, instead, we neglect the second term and allow a free $\sigma^2$ in the last term of equation 7.33 we obtain the one loop effective field theory correction to the SPT (e.g. [31]).

We can also considered modification of the LPT approach in which one would seek to reduce the negative effect of 1 loop contribution to the rms displacement. As we discussed above, in the low $k$ limit, at a quadratic order in $A_{ij}$, last term in 7.33 dominates over the mode coupling term and leads to a reduction in power, thus ruining the success of LPT. One approach in correcting this reduction would be to modify the two point correlator of the displacement field, which then changes both $X$ and $Y$ terms in equation 7.15. This still gives a lot of freedom since we have a whole function to modify. For example in [37] Lorentzian smoothing ansatz for the 1 loop LPT result of displacement field power spectra is suggested, with parameters calibrated on the N-body simulation results. This helps in bring the LPT density spectra up, but not sufficiently and still does not cure the problem. One might also be tempted to modify just the zero lag part of the displacement field $\sigma^2$ and replace it with the e.g. linear prediction or treat it as free parameter. This turns out to be an ill defined and inconsistent procedure since the correction would not preserve Galilean invariance because the relative displacement does not vanish in the small scale limit. Additionally, in this procedure the correlation function result would yield a imaginary values. The reason is that $X + Y$ has to be positive-definite on whole $q$ domain, and lowering the $\sigma^2$ corresponds to negative values of $X$ in low $q$ regime. Finely we would like to emphasize that even though these particular approximations do not give physically satisfactory results more detailed analysis based on the numerical simulation of displacement field correlators can give us valuable insight and will be explored elsewhere.

## 7.3 Cross and auto power at 2LPT

Using LPT we can test the performance of the analytical solution of the integral in equation 7.11, comparing it to the cross and auto power spectra obtained from 'initial condition' code [46] at redshift $z = 0$, where the nonlinear effects are most apparent. For this purpose let us first introduce labelling that we will use in analysing all of the cross and auto spectra. Let us identify the set of indexes $\{z, l, t\} = \{\text{zel}, \text{2lpt}, \text{zel} + \text{2lpt}\}$, where in the first case we use the Zel'dovich result, followed by the sole 2LPT result and finally a sum of the two. Using

the same formalism as when deriving equation 7.11, we can write

$$(2\pi)^3\delta^D(k) + P^{\alpha\beta}(k) = \int d^3q\; e^{-i\mathbf{q}\cdot\mathbf{k}} \exp\left[-\frac{1}{2}k_ik_jA_{ij}^{\alpha\beta}(\mathbf{q}) + \frac{i}{6}k_ik_jk_lW_{ijl}^{\alpha\beta}(\mathbf{q})\right]. \quad (7.34)$$

Both, $\alpha$ and $\beta$, indexes can take the values from the set $\{z, l, t\}$ in representing the Zel'dovich, 2LPT or combined result. Note that the $P^{zz}$ result is the standard Zel'dovich power spectrum, using the linear displacement. In table 7.1 we show the result for all the combinations of cross and auto spectra up to the 2LPT. We show the results in terms of how the decomposition coefficients of $X$, $Y$, $V$ and $T$ change when using different combination of PT approximation levels. Using equations 7.26 and result of the table 7.1 we also can find the low $k$ limit for each of the cross power spectra. We have

$$\begin{aligned}
P^{zz} &= (1-k^2\sigma_L^2)P_L + \frac{1}{2}Q_3,\\
P^{zl} &= e^{-\frac{1}{2}k^2(\sigma_L^2+\sigma_Q^2)}\frac{3}{14}Q_2,\\
P^{zt} &= e^{-\frac{1}{2}k^2\sigma_Q^2}\Big((1-k^2\sigma_L^2)P_L + \frac{3}{14}(Q_2+2R_2) + \frac{1}{2}Q_3\Big),\\
P^{ll} &= (1-k^2\sigma_Q^2)\frac{9}{98}Q_1 + \frac{1}{2}Q_{3Q},\\
P^{lt} &= e^{-\frac{1}{2}k^2\sigma_L^2}\Big((1-k^2\sigma_Q^2)\frac{9}{98}Q_1 + \frac{3}{14}Q_2 + \frac{1}{2}Q_{3Q}\Big),\\
P^{tt} &= \big(1-k^2(\sigma_L^2+\sigma_Q^2)\big)\left(P_L + \frac{9}{98}Q_1\right) + \frac{3}{7}(Q_2+2R_2) + \frac{1}{2}Q_3.
\end{aligned} \quad (7.35)$$

In figure 7.3 we show the results of 6 different cross and auto spectra up to the 2LPT approximations. We compare these results with numerical results obtained from measuring the power spectra on the grid from initial condition code [46]. For N-body grid results we use 1000 Mpc/$h$ box size with $1024^3$ particles. Since we are dealing with the finite box size there are some residual effects. For example there will be effects coming from Nyquist frequency cut off in N-body result which we do not account for in analytical calculations. Up to these numerical effects we see that overall, for all of the cross spectra we are considering, the analytical calculations and numerical measurements agree well with each other. In addition to the numerical effects mentioned above in some of the spectra like $P_{ll}$, $P_{lt}$ and $P_{tt}$ the contribution of 2LPT bispectrum term $\left\langle\Psi^{(2)}\Psi^{(2)}\Psi^{(2)}\right\rangle$ can be considered. Since this is formally a two loop term it does not enter into our analytic result but it is present in the numerical N-body result.

## 7.4 Correlation function

Correlation function is defined as the two point correlation of density field in configuration space and it is a Fourier transform of the power spectrum

$$\xi(r) = \int \frac{d^3k}{(2\pi)^3}\,\exp(-i\mathbf{k}\cdot\mathbf{r})P(k) = \int \frac{k^2dk}{2\pi^2}\,P(k)j_0(kr) \quad (7.36)$$

We Fourier transform the main results shown in figure 7.2. In figure 7.4 we show the results for the correlation function at redshifts $z = 0.0$, $z = 0.5$, $z = 1.0$ and $z = 2.0$. We show the results of the equation 7.15 at one loop together with the approximations where tree point contribution of $V$ and $T$ terms are dropped and two point terms $X$ and $Y$ remain at one loop. For comparison we also show one loop LPT from [21]. As mentioned before, formally the result in this paper differs from the one presented in [24] in respect that there the exponent with three point function is expanded and only the leading term (linear in $V$ and $T$) is kept, and in this work we keep all the terms in the exponent. In practice though

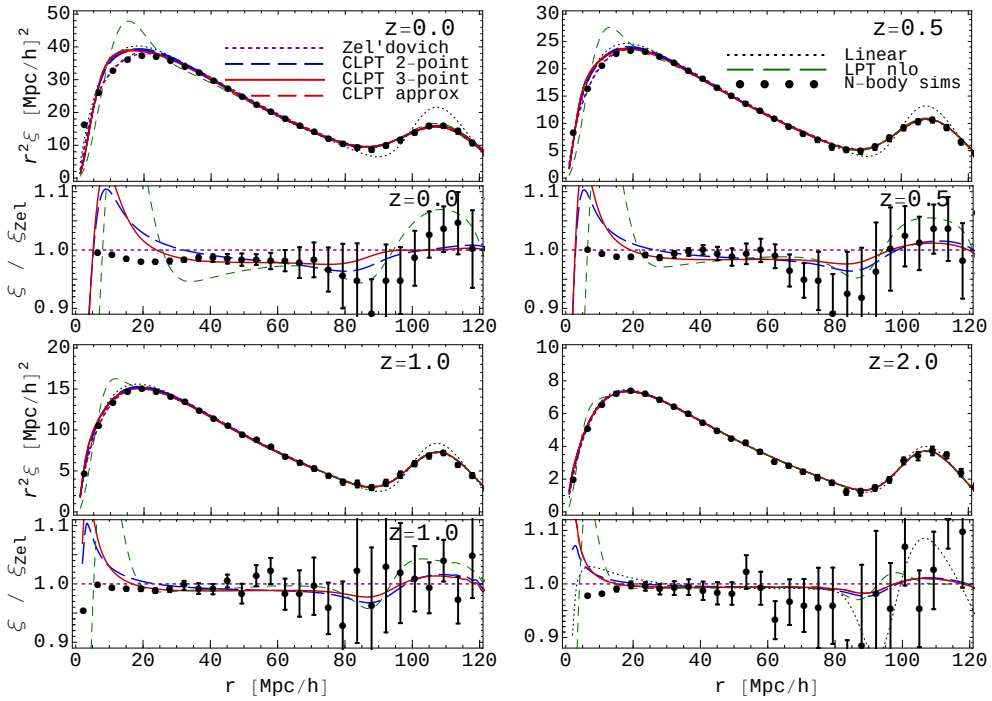


**Figure 7.4:** Correlation function obtained by numerically Fourier transforming the results from figure 7.2 at redshift $z = 0.0,\ 0.5,\ 1.0$ and 2.0. In the upper panel we show the correlation function and in the lower panel the same result is divided by the Zel'dovich result (short-dashed purple line in upper panel). Full result of equation 7.15 at one loop is shown (solid red line) together with the approximations where tree point contribution of $V$ and $T$ terms are dropped and two point terms $X$ and $Y$ remain at one loop (long-dashed blue line). For compareison we also show one loop LPT (short-dashed green line) as presented in [21] as well as linear theory (dotted black line). For comparison we also show the N-body simulation results (black dots).

these two methods give very similar results since the corrections coming from the expansion terms above the leading one are small on scales shown in the plots, and thus the results agree. From figure 7.4 we note that nonlinear results improve the comparison with N-body simulation results on scales less $40 - 50$ Mpc$/h$.

## 7.5 Decomposition of power spectrum and correlation function

From correlation function results shown in figure 7.4 we can see that the Zel'dovich approximations goes beyond the linear theory and much better agreement with the N-body simulations is achieved (in configuration space). This manifest itself particularly on the BAO smoothing where little excess power remains in the N-body simulation data. We also see that one loop result helps in describing these excess BAO features. On the other hand, both Zel'docivh and one loop power spectrum results show significant dampening in the broad band power spectrum. This clearly shows that in process of Fourier transforming, the features like BAO peak and excess nonlinear power, that are to a given extent separated in scales in configuration space, get much more intertwined and mixed to a grater extent in the Fourier space.

We suggest the decomposition of the total power spectrum in the Zel'dovich contribution plus the residual BAO wiggle and broad band contributions. We can write

$$P(k) = P_{\rm Zel}(k) + P_W(k) + P_{BB}(k), \tag{7.37}$$

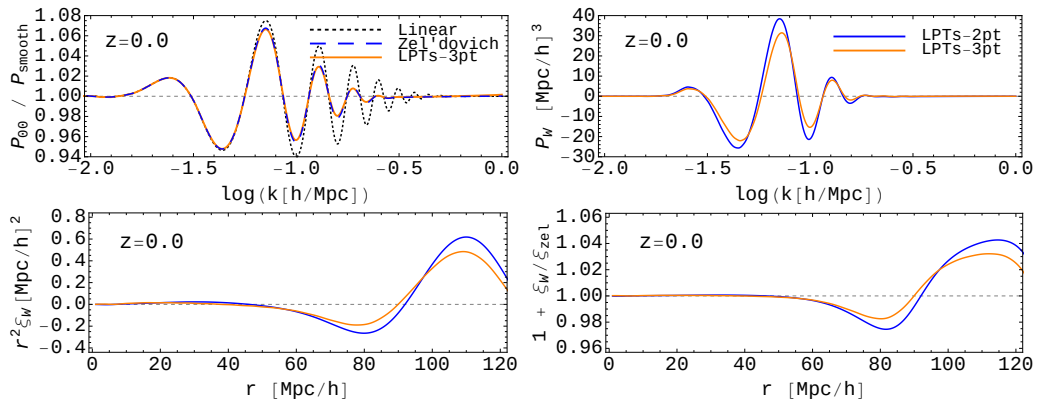


**Figure 7.5:** (*Upper panels:*) On the left panel we show the linear (black dotted line), Zel'dovich (blue dashed line) and one loop LPTs (orange solid line) power spectra divided by the smooth versions of the same. On the right we show the residual wiggle spectra $P_W$: one loop LPTs-2pt result (blue solid line) does not including the bispecta terms $V$ and $T$, and one loop LPTs-3pt result (orange solid line) including the $V$ and $T$ terms. (*Bottom panels:*) On the left panel we show the residual wiggles in configuration space $r^2\xi_W$ and on the right site the same thing is shown relative to the Zel'dovich correlation function. Colour coding is the same as in the upper panels.

where first therm is the Zel'dovich power spectrum, second $P_W$ is the BAO wiggle residual contribution, i.e. the BAO wiggle smoothing and shifting beyond the Zel'dovich theory results. Last part, $P_{BB}$ is the residual broad band power that does not contain any BAO wiggles.

Let us focus first on the residual wiggle part, $P_W$, for which we can use the LPT results discussed earlier. The key in extracting just the wiggle information lies in the construction of reliable no-wiggle power spectrum results. In order to achieve this we use the b-spline smoothing methods similar to the once used in [48]. The procedure we adapt is as follows; we first obtain the smooth version of the linear power spectra and then use these smoothed linear power spectra as input to compute Zel'dovich and one loop LPT result. Since there is no unique way in obtaining the smoothed line we construct the family of smooth approximations and construct the final result as a linear composition of those. Further on we impose two integral constraint requirements, i.e. we want $\sigma_8$ and $\sigma_v$ to be the same in the cases of smoothed spectra and the one with BAO wiggles. This guarantees that any no-wiggle nonlinear power spectra obtained in this way will agree well with the spectra containing wiggles even for high k values. Using this smoothing on Zel'dovich and one loop LPT result we extract the residual wiggle spectra

$$P_W(k) = (P_{LPT} - P_{Zel}) - (P_{LPT} - P_{Zel})_{nw}, \tag{7.38}$$

where $P_{LPT}$ is the one loop LPT power spectra and $P_{Zel}$ is the Zel'dovich one. Subscript "$nw$" stands for the no-wiggle spectra, i.e. the one with smoothed BAO wiggles.

The wiggle result obtained by this procedure does not change the BAO correlation function feature from the one loop LPT result presented in figure 7.4. From the comparison of power spectrum results with N-body simulation results found in [37, 49] we have learned that one loop LPT overestimates the rms displacement dispersion value which leads to damping of the total power spectra as well as oversmoothing of the wiggles. Thus we can adopt the Lorentzian correction to the displacement field power spectra suggested in [37] (parameters are also given). This in turn corrects $X$ and $Y$ and boosts the power of the total power spectra, as well as the BAO wiggles. Following the [37] we label this result LPTs. In section 7.2.5 we have argued that this does not solve all problems in correcting the total power spectrum result, but here we are interested only in the consequences on the wiggles spectra $P_W$, which justifies the procedure. The residual wiggle $P_W$ spectra results using the LPTs,

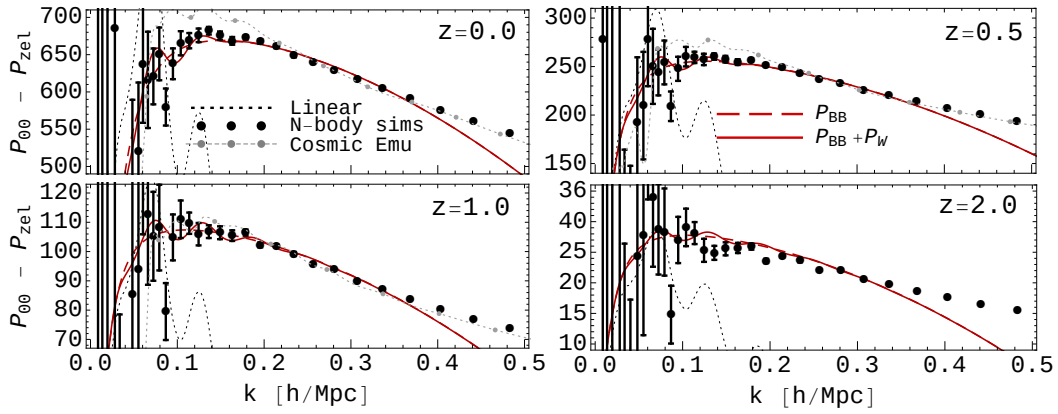


**Figure 7.6:** $P_{BB}$ model is show and compared to the N-body simulations at redshifts $z = 0.0$, $z = 0.5$, $z = 1.0$ and $z = 2.0$. We show the full power spectra minus the Zel'dovich contribution. We show the N-body simulation result (black points), cosmic emulator (gray dots and dotted line) $P_{BB}$ model from the equation 7.39 (red dashed line) and finely the sum of the residual wiggles and broad bend part, i.e. $P_{BB} + P_W$ (red solid line). For the reference we also show the linear theory (black dotted line).

as well as its Fourier transform $\xi_W$ are shown in figure 7.5. We use the LPTs corrections for the displacement field spectra in order to correct the $X$ and $Y$, but not the $V$ and $T$ terms (since there is no consistent procedure to apply the same correction). This results in boosting the power of residual wiggles since it reduces the overall dampening effects in one loop LPT spectra, especially the effects of the rms displacement dispersion. We also show the difference between the results where $V$ and $T$ terms are neglected.
We move onto the modelling of the last term in equation 7.38, a broad band part, $P_{BB}$. As discussed in previous chapters LPT turns out to be ill suited in addressing the broad band part of the power spectra. For this reason we resort to the simple phenomenological ansatz:

$$P_{BB}(k) = \left(1 - \frac{1}{1 + R^2k^2}\right)\left(A_0 + A_1k^2\right). \tag{7.39}$$

First part in the brackets ensures that the model vanishes in the limit $k \to 0$ and thus we retrieve the linear theory result on largest of scales. Using this model we fit the N-body simulations and so determine the $R, A_0$ and $A_1$ parameters. Best fit parameters are given in the table 7.2. In figure 7.6 we show the best fit model $P_{BB}$ together with the N-body simulations. We find that this ansatz can fit the data very well up to the scales $k \sim 0.35h$Mpc/. Parameter $R$ ensures the low k behaviour of the model, while $A_0$ sets the peak amplitude of $P_{BB}$ which is at around $k \sim 0.12h$/Mpc for all redshifts. Additional $A_1$ parameter sets the slope of the $P_{BB}$ spectra at higher k (beyond the peak). As we will see below this $A_1$ parameter turns out to have a negligible impact on correlation function results.
Nice advantage of such a simple ansatz is the existence of the analytical Fourier transform:

$$\xi_{BB}(r) = -\frac{e^{-\frac{r}{R}}}{4\pi r R^2}\left(A_0 - \frac{A_1}{R^2}\right), \tag{7.40}$$

where we have dropped the terms contributing only to the $r = 0$ limit. To evaluate the $\xi_{BB}$ we use the same parameters as in the the table 7.2 above. As mentioned, from the values presented in the table we see that contributions of $A_1$ term can be neglected since $A_0 \gg A_1/R^2$ for every given redshift. This effectively reduces the tree parameter model that we started with in Fourier space to the two parameter model in the configuration space. Since the decomposition of the power spectra 7.37 is additive in all the contributions discusses

**Table 7.2:** Best fit parameter of the residual broad-band spectra $P_{BB}$.

| z | R | $A_0$ | $A_1$ |
|---|---|---|---|
| 0.0 | 37.9 | 709.8 | -890.4 |
| 0.5 | 47.5 | 269.5 | -436.0 |
| 1.0 | 56.9 | 112.9 | -229.0 |
| 2.0 | 50.9 | 29.8 | -96.0 |

above, it follows for the total correlation function:

$$\xi(r) = \xi_{\rm Zel}(r) + \xi_W(r) + \xi_{BB}(r), \tag{7.41}$$

where each of the constituents is respectively the Fourier transform of the terms in 7.37. In figure 7.7 we show the results of the full model in configuration space, as well as the performance of the full model in Fourier space. In both cases the same parameters from table 7.2 have been used. Shown results nicely convey the consistency of the result in both spaces. It is important to stress that in the past this has usually been neglected, and analytical and phenomenological models have mostly focused on modelling either the correlation functions or the power spectra. The model we construct gives very clear insight into the interplay of broad band and wiggle effects and the way they manifest themselves in the power spectrum and correlation function. Even thought the model at present consists of free parameters we conceder it a valuable toy model for understanding the dark matter clustering effects, as well as an outpost for future analysis.

## 7.6 Conclusions

In this paper we use the Lagrangian perturbation theory for evaluation of the displacement fields in order to compute up to one loop contributions to the cumulants in the resulting power spectrum. We start by reviewing the Lagrangian framework of describing the overdesity of dark matter particles and present the framework of computing the two point function in Fourier space, i.e. the power spectra. In this framework (first suggested in [24] for the correlation function) power spectrum is given as a sum of n-point cumulants of the difference of displacement field in two points $\Delta = \Psi_2 - \Psi_1$. In this form the translation invariance is given explicitly in each of the cumulants. A similar result to this part of the paper, has been presented in [28] which appeared in the meanwhile as this paper has been written: wherever it is comparable, the results agree.

Only the first two cumulants (two-point and three-point) have contributions at one loop and we show that scale dependence of each of these. Computationally difficult part of integrating a highly oscillatory integrand is overcome by angular moment expansion. This yields the result expressed as the sum of integrals with spherical Bassel functions, which ensure the quick convergence rate of the sum. Alternative scheme of solving these equations by expanding the integrand into spherical harmonics gives identical results. We note that the convergence rate of the first expansion method is somewhat better since it involves partial resummation of some of the terms. We compare the final result to the N-body simulations. For low redshifts our results do not agree well with the N-body simulations and one of the main reasons is that perturbation theory for the displacement field overpredicts the rms displacement at zero lag.

We note that simple fixes like modifications of the zero lag displacement to the linear order while keeping all the other terms at one loop level leads to the inconsistencies and has fatal consequences in the configuration space. Alternative approach presented in e.g. [37] is to implement the dampening of the displacement field power spectra, called LPTs. This offers

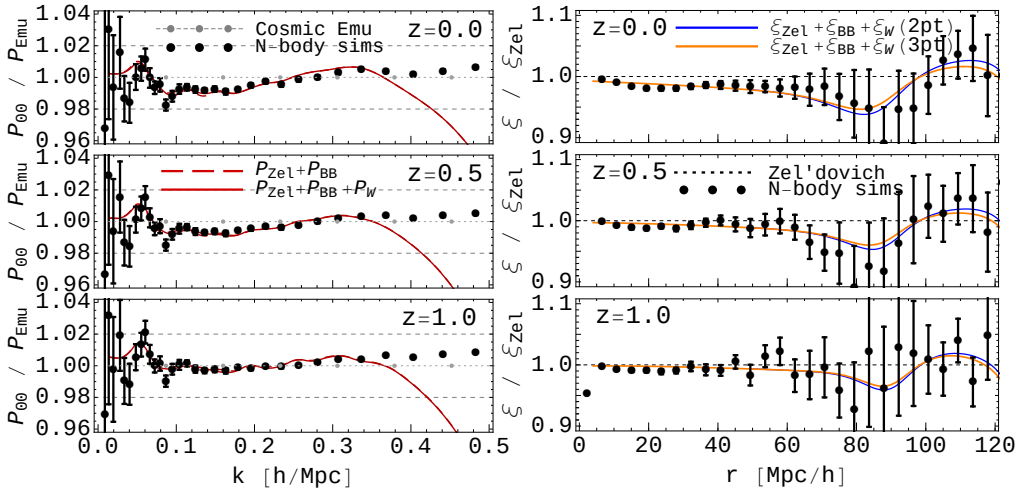


**Figure 7.7:** (*Left panels:*) In the left panel we show the relative agreement of the decomposition model $P_{Zel} + P_{BB} + P_W$ (red solid lines) and the N-body simulation results (black points). In addition we show the case where the residual wiggle term is dropped, i.e. $P_{Zel} + P_{BB}$ (red dashed lines). The effect of $P_W$ is difficult to distinguish here since it is supressed by the large broad band power and one might rather refer to the figure 7.6. In order to reduce the dynamical range all the lines are divided by the cosmic emulator spectra (gray points and dotted line). (*Right panels:*) Correlation function $\xi_{zel} + \xi_{BB} + \xi_W$ model is shown. Results using the LPTs, including the bispectrum terms $V$ and $T$, for $\xi_W$ are shown (solid orange line), as well as the case where $V$ and $T$ terms have been dropped (solid blue line). In the latter case only two point terms $X$ and $Y$ contribute. For comparison, N-boady simulation results (black points) are shown as well. In order to reduce the dynamical range all the lines are divided by the Zel'dovich result (dotted black line).

a more consistent treatment of the two point displacement functions $X$ and $Y$ but not the tree point functions $V$ and $T$. The result of this procedure improves the overall broad band behaviour of the power spectra in the right direction, but still fails to reproduce the final N-body simulations result.

Next we look at the cross and auto spectra at 2LPT level, i.e. up to the second order expansion of displacement field. In this way we can directly compare the performance of our analytic solution with the measurements of the spectra on the grid obtained by displacing the particles using initial conditions code [46]. We compare six different power spectra: three auto spectra, Zel'dovich, 2LPT (second order only) and Zeldovich+2LPT, and similarly three cross spectra. We find a very good agreement of the analytic and measured predictions in all of the spectra. Differences that are noticeable as we approach higher scales ($k \sim 0.4$) are due to resolution effects of grid measurements which start to affect the results. In addition, even though both calculations are of the same perturbative order in the displacement field, in our analytic approach we truncate the cumulant expansion at one loop order, while grid measurements in principle have contributions from higher orders of cumulant expansion for some of the spectra.

We Fourier transform our result for the one loop power spectra to obtain the correlation function predictions. We compare the results to the N-body measurements of the correlation function. We conclude that the one loop LPT results found in this paper when Fourier transformed agree nicely with those found in [24]. We also show the difference of the performance of one loop LPT result and the Zel'dovich results.

Finely we construct the simple model where we decompose the total power spectrum into the Zel'dovich part plus the residual BAO wiggle $P_W$ and the broad band $P_{BB}$ contribution. We show the effects of the residual wiggles using the LPTs on both the power spectra and the correlation function. We propose the simple phenomenological model for the broad band part where the parameters are fitted to the N-body simulations. A nice feature of the broad

band model is the analytical Fourier transform. We show that this model reproduces well the amplitude and shape or the total power spectra down to the $k \sim 0.35h$/Mpc and correlation function down to 10Mpc/$h$ for redshifts $z = 0.0,\ 0.5\ , 1.0$ and $z = 2.0$. The model also shows in a very clear way how the broad band and BAO features, smeared and intertwined in Fourier space, decouple and populate different scales in the configuration space.

## Acknowledgments

We would like to thank Raul Angulo, Teppei Okumura and Leonardo Senatore, Marcel Schmittfull, Martin White and Jaiyul Yoo for useful discussions and comments. ZV would like to thank the Berkeley Center for Cosmological Physics and the Lawrence Berkeley Laboratory for their hospitality. ZV would also like to thank Thomas Gehrmann and Nenad Smontara for stimulating discussion related to technical aspects of this work. This work is supported by the DOE, the Swiss National Foundation under contract 200021-116696/1 and WCU grant R32-10130. We use CUBA libery [50] for numerical integration, and FFTLog [51] for the integrals involving sperical Bessel funcitons. The simulations were performed on the ZBOX4 supercomputer of the Institute for Computational Science at the University of Zürich.

## 7.7 PT computation for $A_{ij}$ term

In this section we show the one loop LPT calculation of the $A_{ij} = \langle \Delta_i \Delta_j \rangle_c$, a similar result can be found in [24]. From the definition of $\Delta$ we have

$$\Delta_i = \Psi_i(\mathbf{q}_2) - \Psi_i(\mathbf{q}_1) = \int \frac{d^3p}{(2\pi)^3} \left(e^{-i\mathbf{p}\cdot\mathbf{q}_2} - e^{-i\mathbf{p}\cdot\mathbf{q}_1}\right) \Psi_i(\mathbf{p}). \tag{7.42}$$

From equation 7.19 the two point function is given by

$$\left\langle \tilde{\Psi}_i(\mathbf{p}_1)\tilde{\Psi}_j(\mathbf{p}_2) \right\rangle_c = (2\pi)^3 \delta^D(\mathbf{p}_1 + \mathbf{p}_2) C_{ij}(\mathbf{p}_1), \tag{7.43}$$

where the $C_{ij}(\mathbf{k})$ are the two point displacement spectra. One loop LPT prediction for these spectra gives the contributions

$$C_{ij}^{(11)}(\mathbf{k}) = \frac{k_i k_j}{k^4} P_L(k) \tag{7.44}$$

$$C_{ij}^{(22)}(\mathbf{k}) = \frac{9}{98} \frac{k_i k_j}{k^4} Q_1(k) \tag{7.45}$$

$$C_{ij}^{(13)}(\mathbf{k}) = C_{ij}^{(31)}(\mathbf{k}) = \frac{5}{21} \frac{k_i k_j}{k^4} R_1(k). \tag{7.46}$$

where $R_n$ and $Q_n$ terms are defined as in [21, 24]. We can simplify this result by writing $C_{ij} = (k_i k_j / k^4) p(k)$, where $p(k)$ is the one loop displacement spectra defined in equation 7.28. We have

$$A_{ij} = 2 \int \frac{d^3k}{(2\pi)^3} \left(1 - \cos\left(\mathbf{k}\cdot\mathbf{q}\right)\right) \frac{k_i k_j}{k^4} \left( P_L(k) + \frac{9}{98} Q_1(k) + \frac{10}{21} R_1(k) \right). \tag{7.47}$$

Contracting this quantity first by $\delta_{ij}$ and then by $\hat{q}_i \hat{q}_j$, we obtain the system of equations

$$\left.\begin{array}{l} A_0 \equiv \delta^K_{ij} A_{ij} = 3X + Y \\ \bar{A} \equiv \hat{q}_i \hat{q}_j A_{ij} = X + Y \end{array}\right\} \rightarrow \begin{array}{ll} X & = \frac{1}{2}(A_0 - \bar{A}) \\ Y & = \frac{1}{2}(3\bar{A} - A_0), \end{array} \tag{7.48}$$

Defining the $\mu = \hat{k} \cdot \hat{q}$ and by perform the angular integrations, we get

$$X(q) = \int_0^\infty \frac{dk}{\pi^2} \left( P_L(k) + \frac{9}{98} Q_1(k) + \frac{10}{21} R_1(k) \right) \left( \frac{1}{3} - \frac{j_1(kq)}{kq} \right), \tag{7.49}$$

$$Y(q) = \int_0^\infty \frac{dk}{\pi^2}\left(P_L(k) + \frac{9}{98}Q_1(k) + \frac{10}{21}R_1(k)\right) j_2(kq). \tag{7.50}$$

In small $q$ limit $X$ and $Y$ vanish while in the large $q$ limit $Y \to 0$ and $X \to \sigma^2$, where $\sigma$ is defined in equation 7.32. Full $q$ dependence of $X$ and $Y$ terms at $z = 0$ is shown in the left panel of figure 7.1.

## 7.8 PT computation for $W_{ijk}$ term

As in the previous section using the Fourier transform of the field $\Psi(\mathbf{q})$ we have

$$\begin{aligned} W_{ijk}(\mathbf{q}) =& \int \prod_{n=1}^{3} \frac{d^3p_n}{(2\pi)^3} \left(e^{-i\mathbf{q}_2\cdot\mathbf{p}_n} - e^{-i\mathbf{q}_1\cdot\mathbf{p}_n}\right) \langle \Psi_i(\mathbf{p}_1)\Psi_j(\mathbf{p}_2)\Psi_k(\mathbf{p}_3)\rangle \\ =& i(2\pi)^3 \int \prod_{n=1}^{3} \frac{d^3p_n}{(2\pi)^3} \left(e^{-i\mathbf{q}_2\cdot\mathbf{p}_n} - e^{-i\mathbf{q}_1\cdot\mathbf{p}_n}\right) \delta^D_{123} C_{ijk}(\mathbf{p}_1,\mathbf{p}_2,\mathbf{p}_3) \\ =& i(2\pi)^3 \delta\binom{ijk}{nmr} \int \prod_{n=1}^{3} \frac{d^3p_n}{(2\pi)^3} \left(e^{-i\mathbf{q}_2\cdot\mathbf{p}_n} - e^{-i\mathbf{q}_1\cdot\mathbf{p}_n}\right) \delta^D_{123} C^{(112)}_{nmr}(\mathbf{p}_1,\mathbf{p}_2,\mathbf{p}_3), \end{aligned} \tag{7.51}$$

where in the last line we have expanded $C_{ijk}$ in terms of the one loop contributions and symmetrised the indexes. We use the abbreviation for the Dirac delta function $\delta^D_{123} = \delta^D(\mathbf{p}_1 + \mathbf{p}_2 + \mathbf{p}_3)$, as well as for the symmetrized sum of Kronecker deltas

$$\delta\binom{ijk}{nmr} = \delta^K_{in}\delta^K_{jm}\delta^K_{kr} + \delta^K_{kn}\delta^K_{im}\delta^K_{jr} + \delta^K_{jn}\delta^K_{km}\delta^K_{ir}. \tag{7.52}$$

Contracting the tensor we get

$$\begin{aligned} \overline{W}(q) =& 3i(2\pi)^3 \int \prod_{n=1}^{3} \frac{d^3p_n}{(2\pi)^3} \left(e^{-i\mathbf{q}_2\cdot\mathbf{p}_n} - e^{-i\mathbf{q}_1\cdot\mathbf{p}_n}\right) \delta^D_{123} \hat{q}_i\hat{q}_j\hat{q}_k C^{(112)}_{ijk}(\mathbf{p}_1,\mathbf{p}_2,\mathbf{p}_3), \\ W_0(q) =& i(2\pi)^3 \int \prod_{n=1}^{3} \frac{d^3p_n}{(2\pi)^3} \left(e^{-i\mathbf{q}_2\cdot\mathbf{p}_n} - e^{i\mathbf{q}_1\cdot\mathbf{p}_n}\right) \delta^D_{123} \Big(2\hat{q}_i C^{(112)}_{ijj}(\mathbf{p}_1,\mathbf{p}_2,\mathbf{p}_3) \\ & + \hat{q}_i C^{(112)}_{jji}(\mathbf{p}_1,\mathbf{p}_2,\mathbf{p}_3)\Big). \end{aligned} \tag{7.53}$$

Before we evaluate these integrals one by one let us first do some general simplifications. First we use the delta function to integrate out the $\mathbf{p}_3$ momentum which gives

$$\begin{aligned} & i(2\pi)^3 \int \prod_{n=1}^{3} \frac{d^3p_n}{(2\pi)^3} \left(e^{-i\mathbf{q}_2\cdot\mathbf{p}_n} - e^{-i\mathbf{q}_1\cdot\mathbf{p}_n}\right) \delta^D_{123} C_{ijk}(\mathbf{p}_1,\mathbf{p}_2,\mathbf{p}_3) = \\ & \quad 2\int \frac{d^3p_1}{(2\pi)^3}\frac{d^3p_2}{(2\pi)^3} \Big(\sin(\mathbf{q}\cdot\mathbf{p}_1) + \sin(\mathbf{q}\cdot\mathbf{p}_2) - \sin\big(\mathbf{q}\cdot(\mathbf{p}_1+\mathbf{p}_2)\big)\Big) C_{ijk}(\mathbf{p}_1,\mathbf{p}_2,\mathbf{p}_3). \end{aligned} \tag{7.54}$$

After some straight forward computation these integrals can be written in the form

$$\begin{aligned} \overline{W}(q) =& \frac{6}{5}\int \frac{dk}{2\pi^2 k}\left(-\frac{3}{7}\right)\Big(Q_1(k) - 3Q_2(k) + 2R_1(k) - 6R_2(k)\Big) j_1(qk) \\ & + \frac{6}{5}\int \frac{dk}{2\pi^2 k}\left(-\frac{3}{7}\right)\Big(Q_1(k) + 2Q_2(k) + 2R_1(k) + 4R_2(k)\Big) j_3(qk), \end{aligned} \tag{7.55}$$

and

$$W_0(q) = 2\int \frac{dk}{2\pi^2 k}\left(-\frac{3}{7}\right)\big(Q_1(k) - 3Q_2(k) + 2R_1(k) - 6R_2(k)\big) j_1(qk), \tag{7.56}$$

where $R_n$ and $Q_n$ terms are defined as in [21, 24]. Using the transformations from equation 7.14 we get the final one loop estimate of the displacement bispectrum contribution to the density power spectrum

$$T(q) = 3\int \frac{dk}{2\pi^2 k}\left(-\frac{3}{7}\right)\Big(Q_1(k) + 2Q_2(k) + 2R_1(k) + 4R_2(k)\Big)j_3(qk),$$
$$V(q) = \frac{1}{5}\big(W_0(q) - T(q)\big). \tag{7.57}$$

Note that each of these quantities approaches 0 as $q \to 0$ as well as in $q \to \infty$ limit. Full $q$ dependence of $V$ and $T$ terms at $z = 0$ is shown in the right panel in figure 7.1.

## 7.9 Angular integration

As shown in [43] the angular integral that appears in Zel'dovich limit can be expressed as

$$\int_{-1}^{1} d\mu\ e^{iA\mu}\ \exp(B\mu^2) = 2e^B \sum_{n=0}^{\infty}\left(-\frac{2B}{A}\right)^n j_n(A), \tag{7.58}$$

where $j_n$ are the spherical Bessel functions. We can define the $k-$th moment of the integral function $M_k$ as

$$M_k(A,B) = \int_{-1}^{1} d\mu\ \mu^k\ e^{iA\mu}\ \exp(B\mu^2). \tag{7.59}$$

If we take the $k$-derivative of this integral with respect to $A$ we get the expression for the $k-$th moment

$$M_k(A,B) = 2\ (-i)^k e^B \sum_{n=0}^{\infty}(-2B)^n\left(\frac{d}{dA}\right)^k A^{-n} j_n(A), \tag{7.60}$$

where we can use the relation for the spherical Bessel functions

$$\left(\frac{1}{\nu}\frac{d}{d\nu}\right)^k\big(\nu^{-n} j_n(\nu)\big) = (-1)^k \nu^{-n-k} j_{n+k}. \tag{7.61}$$

Finally, we are interested in the case where we have $i\epsilon\mu^3$ term in the exponent. Expanding the left hand side in $\epsilon$ we get

$$\int_{-1}^{1} d\mu\ e^{iA\mu}\ \exp(B\mu^2 + i\epsilon\mu^3) = \sum_{l=0}^{\infty}\frac{(i\epsilon)^l}{l!}M_{3l}(A,B) = 2e^B\sum_{n=0}^{\infty}\left(-\frac{2B}{A}\right)^n J_n(A,\epsilon), \tag{7.62}$$

where we have defined the new function $J_n$ which deviates from the spherical Bessel function $j_n$ depending on the values of parameter $\epsilon$, and is given in the form of a series

$$J_n(A,\epsilon) = \sum_{l=0}^{\infty}(-1)^l\frac{\epsilon^{2l}}{(2A)^{3l}}\Big[F_1^{(n,l)}(A) - 3(3l+1)(6l+1)\frac{\epsilon}{A}F_2^{(n,l)}(A)\Big], \tag{7.63}$$

with the additional auxiliary functions defined as

$$F_1^{(n,l)}(A) = \frac{(6l)!}{(2l)!}\sum_{p=0}^{3l}\frac{(-2A)^p}{(2p)!(3l-p)!}j_{n+3l+p}(A),$$
$$F_2^{(n,l)}(A) = \frac{(6l)!}{(2l)!}\sum_{p=0}^{3l+1}\frac{(-2A)^p}{(2p+1)!(3l-p+1)!}j_{n+3l+p+2}(A). \tag{7.64}$$

We can approximate the result at a first order in $\epsilon$, which would correspond to the solution presented in [24] for the correlation function. We have

$$\begin{aligned}\int_{-1}^{1} d\mu\; e^{iA\mu+B\mu^2}(1+i\epsilon\mu^3) &= 2e^B \sum_{n=0}^{\infty}\left(\frac{-2B}{A}\right)^n \left[F_1^{(n,0)}(A) - 3\frac{\epsilon}{A}F_2^{(n,0)}(A)\right] \\ &= 2e^B \sum_{n=0}^{\infty}\left(\frac{-2B}{A}\right)^n \Big(j_n(A) - \frac{\epsilon}{A}\big[3j_{n+2}(A) - Aj_{n+3}(A)\big]\Big).\end{aligned} \tag{7.65}$$

In the limit $\epsilon \to 0$ it is clear that we regain the old result in equation 7.58. If we compare our full integral 7.15 to the equation 7.62 we get the correspondence

$$A(k,q) = k\left(q - \frac{1}{2}k^2V(q)\right), \quad B(k,q) = -\frac{1}{2}k^2Y(q), \quad \epsilon(k,q) = -\frac{1}{6}k^3T(q). \tag{7.66}$$

From equation 7.62 and 7.58 we see that the expansion parameters of the series are $-2B/A$, $-\epsilon^2$, and $-\epsilon/A$. We find that the bispectrum terms $V$ and $T$ start to be relevant for higher $k$ as one would expect, as we see from low-$k$ calculation in section 7.2.5.

## 7.10 Angular integration: alternative approach

In this section we present an alternative derivation of the solution of the equation 7.62 integral. The idea is to generalize the plane wave expansion (for review see e.g. [52]) in order to obtain the solution of the integral. We start from the well known formula of the plane wave expansion

$$e^{i\mathbf{k}\cdot\mathbf{r}} = \sum_{l=0}^{\infty} i^l(2l+1)P_l(\cos\theta)j_l(kr), \tag{7.67}$$

where $\theta$ is the angle between $\mathbf{k}$ and $\mathbf{r}$. Expanding this, it follows that for the powers of the plane wave variable we have

$$(ix)^n = \left(\frac{d^n}{d\alpha^n}e^{i\alpha x}\right)_{\alpha=0} = \sum_{l=0}^{\infty} i^l(2l+1)P_l(x)\left(\frac{d^n j_l(\alpha)}{d\alpha^n}\right)_{\alpha=0}. \tag{7.68}$$

This gives us the Taylor expansion of the spherical Bessel function around the zero

$$j_l(\alpha) = \sum_{n=0}^{\infty}\frac{\alpha^n}{n!}\left(\frac{d^n j_l(\alpha)}{d\alpha^n}\right)_{\alpha=0}. \tag{7.69}$$

We can compare this expansion to the well known form of the series representation of spherical Bessel functions (for reference see e.g. [44, 45])

$$j_l(\alpha) = \alpha^l \sum_{k=0}^{\infty}\frac{(-)^k}{2^k k!}\frac{\alpha^{2k}}{(2l+2k+1)!!}, \tag{7.70}$$

which gives the coefficients of the Taylor expression above

$$b_n^l = \left(\frac{d^n j_l(\alpha)}{d\alpha^n}\right)_{\alpha=0} = \begin{cases} \frac{i^{n-l}n!}{\sqrt{2}^{n-l}\left(\frac{1}{2}(n-l)\right)!(n+l+1)!!}, & \text{if } n \geq l \;\&\; n \text{ and} \\ & l \text{ both even or odd,} \\ 0, & \text{otherwise.} \end{cases} \tag{7.71}$$

Using these coefficients we have

$$(ix)^n = \sum_{l=0}^{\infty} i^l (2l+1) P_l(x) b_n^l, \tag{7.72}$$

from which follows

$$\begin{aligned} e^{Bx^2} &= \sum_{l=0}^{\infty} i^l (2l+1) P_l(x) \sum_{n=0}^{\infty} \frac{(-B)^n}{n!} b_{2n}^l, \\ e^{i\epsilon x^3} &= \sum_{l=0}^{\infty} i^l (2l+1) P_l(x) \sum_{n=0}^{\infty} \frac{(-\epsilon)^n}{n!} b_{3n}^l. \end{aligned} \tag{7.73}$$

After some calculation we have the solution of the integral 7.58 in form of the series

$$\int_{-1}^{1} d\mu \; e^{iA\mu} \; \exp(B\mu^2) = 2 \sum_{n=0}^{\infty} \frac{(2n)!}{2^n n!} B^n \sum_{p=0}^{n} (-2)^p \frac{4p+1}{(n-p)!(2n+2p+1)!!} j_{2p}(A), \tag{7.74}$$

where we have used the properties of $b_n^l$ coefficients and orthogonality of Legendre polynomials

$$\int_{-1}^{1} d\mu \; P_{l_1}(\mu) P_{l_2}(\mu) = \frac{2}{2l_1+1} \delta^D_{l_1 l_2}. \tag{7.75}$$

Finally for the integral in equation 7.62 it follows

$$\begin{aligned} \int_{-1}^{1} d\mu \; e^{iA\mu} \; \exp(B\mu^2 + i\epsilon\mu^3) = 2 \sum_{p_1=0}^{\infty} (-)^{p_1} \Big( & (4p_1+1) F_1(p1, B, \epsilon) j_{2p_1}(A) \\ & + (4p_1+3) F_2(p1, B, \epsilon) j_{2p_1+1}(A) \Big) \end{aligned} \tag{7.76}$$

where we define the functions

$$\begin{aligned} F_1(p1, B, \epsilon) &= \sum_{n=0}^{\infty} \sum_{r=0}^{\infty} c_1(p_1, n, r) B^n \epsilon^{2r}, \\ F_2(p1, B, \epsilon) &= \sum_{n=0}^{\infty} \sum_{r=0}^{\infty} c_2(p_1, n, r) B^n \epsilon^{2r+1}, \end{aligned} \tag{7.77}$$

and the coefficients are given by

$$\begin{aligned} c_1(p_1, n, r) = \frac{(-)^r}{2^{n+3r}} \frac{(2n)!(6r)!}{n!(2r)!} & \sum_{p_2=0}^{n} \frac{2^{p_2}(4p_2+1)}{(n-p_2)!(2n+2p_2+1)!!} \\ & \times \sum_{p_3=|p_1-p_2|}^{\min\{p_1+p_2, 3r\}} \frac{2^{p_3} \langle 2p_1, 0, 2p_2, 0 | 2p_3, 0 \rangle^2}{(3r-p_3)!(6r+2p_3+1)!!}, \\ c_2(p_1, n, r) = \frac{(-)^{r+1}}{2^{n+3r+1}} \frac{(2n)!(6r+3)!}{n!(2r+1)!} & \sum_{p_2=0}^{n} \frac{2^{p_2}(4p_2+1)}{(n-p_2)!(2n+2p_2+1)!!} \\ & \times \sum_{p_3=\frac{1}{2}(|2(p_1-p_2)+1|-1)}^{\min\{p_1+p_2, 3r+1\}} \frac{2^{p_3} \langle 2p_1+1, 0, 2p_2, 0 | 2p_3+1, 0 \rangle^2}{(3r-p_3+1)!(6r+2p_3+5)!!}. \end{aligned} \tag{7.78}$$

Here we have used the properties of $b_n^l$ coefficients, and introduced the Clebsch-Gordan coefficients $\langle l_1, m_1, l_2, m_2 | L, M \rangle$, which appeared as a solution of the integral over three Legendre polynomial

$$\int_{-1}^{1} d\mu \; P_{l_1}(\mu) P_{l_2}(\mu) P_{l_3}(\mu) = \frac{2}{2l_3+1} \langle l_1, 0, l_2, 0 | l_3, 0 \rangle^2. \tag{7.79}$$

We stress that $c_1$ and $c_2$ are coefficients and do not depend on the values of $A$, $B$ or $\epsilon$. Moreover, the sums that they contain are finite, thus these coefficients are finite number themselves and can be precomputed. In this way they do not pose any computational obstacle, even though the expressions look somewhat formidable. Note also that in this expansion $A$ term appears only as an argument of the spherical Bessel functions and the rest of the expansion is in powers of $B$ nad $\epsilon$.

# Bibliography


[1] F. Bouchet, **Introductory overview of Eulerian and Lagrangian perturbation theories**, astro-ph/9603013.

[2] F. Bernardeau, S. Colombi, E. Gaztanaga, and R. Scoccimarro, **Large scale structure of the universe and cosmological perturbation theory**, *Phys.Rept.* **367** (2002) 1–248, [astro-ph/0112551].

[3] J. Carlson, M. White, and N. Padmanabhan, **A critical look at cosmological perturbation theory techniques**, *Phys. Rev.* **D80** (2009) 043531, [arXiv:0905.0479].

[4] F. Bernardeau, **The evolution of the large-scale structure of the universe: beyond the linear regime**, arXiv:1311.2724.

[5] M. Crocce and R. Scoccimarro, **Renormalized cosmological perturbation theory**, *Phys.Rev.* **D73** (2006) 063519, [astro-ph/0509418].

[6] M. Crocce and R. Scoccimarro, **Memory of initial conditions in gravitational clustering**, *Phys.Rev.* **D73** (2006) 063520, [astro-ph/0509419].

[7] A. Taruya and T. Hiramatsu, **A Closure Theory for Non-linear Evolution of Cosmological Power Spectra**, arXiv:0708.1367.

[8] S. Matarrese and M. Pietroni, **Resumming Cosmic Perturbations**, *JCAP* **0706** (2007) 026, [astro-ph/0703563].

[9] F. Bernardeau, M. Crocce, and R. Scoccimarro, **Multi-Point Propagators in Cosmological Gravitational Instability**, *Phys.Rev.* **D78** (2008) 103521, [arXiv:0806.2334].

[10] F. Bernardeau, M. Crocce, and R. Scoccimarro, **Constructing Regularized Cosmic Propagators**, *Phys.Rev.* **D85** (2012) 123519, [arXiv:1112.3895].

[11] F. Bernardeau, A. Taruya, and T. Nishimichi, **Cosmic propagators at two-loop order**, arXiv:1211.1571.

[12] S. Anselmi and M. Pietroni, **Nonlinear Power Spectrum from Resummed Perturbation Theory: a Leap Beyond the BAO Scale**, *JCAP* **1212** (2012) 013, [arXiv:1205.2235].

[13] N. S. Sugiyama and T. Futamase, **Relation between standard perturbation theory and regularized multi-point propagator method**, *Astrophys.J.* **769** (2013) 106, [arXiv:1303.2748].

[14] M. Crocce, R. Scoccimarro, and F. Bernardeau, **MPTbreeze: A fast renormalized perturbative scheme**, arXiv:1207.1465.

[15] A. Taruya, F. Bernardeau, T. Nishimichi, and S. Codis, **RegPT: Direct and fast calculation of regularized cosmological power spectrum at two-loop order**, *Phys.Rev.* **D86** (2012) 103528, [arXiv:1208.1191].

[16] P. McDonald, **Dark matter clustering: a simple renormalization group approach**, *Phys.Rev.* **D75** (2007) 043514, [astro-ph/0606028].

[17] M. Pietroni, **Flowing with Time: a New Approach to Nonlinear Cosmological Perturbations**, *JCAP* **0810** (2008) 036, [arXiv:0806.0971].

[18] P. Valageas, **Large-N expansions applied to gravitational clustering**, *Astron.Astrophys.* (2006) [astro-ph/0611849].

[19] N. S. Sugiyama and T. Futamase, **An Application of Wiener Hermite Expansion to Non-linear Evolution of Dark Matter**, *Astrophys.J.* **760** (2012) 114, [arXiv:1210.1663].

[20] D. Blas, M. Garny, and T. Konstandin, **Cosmological perturbation theory at three-loop order**, arXiv:1309.3308.

[21] T. Matsubara, **Resumming Cosmological Perturbations via the Lagrangian Picture: One-loop Results in Real Space and in Redshift Space**, *Phys.Rev.* **D77** (2008) 063530, [arXiv:0711.2521].

[22] T. Matsubara, **Nonlinear perturbation theory with halo bias and redshift-space distortions via the Lagrangian picture**, *Phys.Rev.* **D78** (2008) 083519, [arXiv:0807.1733].

[23] T. Okamura, A. Taruya, and T. Matsubara, **Next-to-leading resummation of cosmological perturbations via the Lagrangian picture: 2-loop correction in real and redshift spaces**, *JCAP* **1108** (2011) 012, [arXiv:1105.1491].

[24] J. Carlson, B. Reid, and M. White, **Convolution Lagrangian perturbation theory for biased tracers**, arXiv:1209.0780.

[25] P. Valageas, T. Nishimichi, and A. Taruya, **Matter power spectrum from a Lagrangian-space regularization of perturbation theory**, *Phys.Rev.* **D87** (2013) 083522, [arXiv:1302.4533].

[26] L. Wang, B. Reid, and M. White, **An analytic model for redshift-space distortions**, *Mon. Not. R. Astron. Soc.* (2013) [arXiv:1306.1804].

[27] P. Valageas, **Accuracy of analytical models of the large-scale matter distribution**, arXiv:1308.6755.

[28] N. S. Sugiyama, **Using Lagrangian perturbation theory for precision cosmology**, arXiv:1311.0725.

[29] J. J. M. Carrasco, M. P. Hertzberg, and L. Senatore, **The Effective Field Theory of Cosmological Large Scale Structures**, *JHEP* **1209** (2012) 082, [arXiv:1206.2926].

[30] J. J. M. Carrasco, S. Foreman, D. Green, and L. Senatore, **The 2-loop matter power spectrum and the IR-safe integrand**, arXiv:1304.4946.

[31] J. J. M. Carrasco, S. Foreman, D. Green, and L. Senatore, **The Effective Field Theory of Large Scale Structures at Two Loops**, arXiv:1310.0464.

[32] E. Pajer and M. Zaldarriaga, **On the Renormalization of the Effective Field Theory of Large Scale Structures**, *JCAP* **1308** (2013) 037, [arXiv:1301.7182].

[33] L. Mercolli and E. Pajer, **On the velocity in the Effective Field Theory of Large Scale Structures**, *JCAP* **1403** (2014) 006, [arXiv:1307.3220].

[34] S. M. Carroll, S. Leichenauer, and J. Pollack, **A Consistent Effective Theory of Long-Wavelength Cosmological Perturbations**, arXiv:1310.2920.

[35] R. A. Porto, L. Senatore, and M. Zaldarriaga, **The Lagrangian-space Effective Field Theory of Large Scale Structures**, arXiv:1311.2168.

[36] L. Senatore and M. Zaldarriaga, **The IR-resummed Effective Field Theory of Large Scale Structures**, arXiv:1404.5954.

[37] K. C. Chan, **Helmholtz Decomposition of the Lagrangian Displacement**, *Phys.Rev.* **D89** (2014) 083515, [arXiv:1309.2243].

[38] P. Catelan, **Lagrangian dynamics in nonflat universes and nonlinear gravitational evolution**, *Mon.Not.Roy.Astron.Soc.* **276** (1995) 115, [astro-ph/9406016].

[39] P. Catelan and T. Theuns, **Nonlinear evolution of the angular momentum of protostructures from tidal torques**, astro-ph/9604078.

[40] C. Rampf and T. Buchert, **Lagrangian perturbations and the matter bispectrum I: fourth-order model for non-linear clustering**, *JCAP* **1206** (2012) 021, [arXiv:1203.4260].

[41] E. Lawrence, K. Heitmann, M. White, D. Higdon, C. Wagner, et al., **The Coyote Universe III: Simulation Suite and Precision Emulator for the Nonlinear Matter Power Spectrum**, *Astrophys.J.* **713** (2010) 1322–1331, [arXiv:0912.4490].

[42] D. J. Eisenstein and W. Hu, **Baryonic Features in the Matter Transfer Function**, *Astrophys. J.* **496** (1998) 605, [astro-ph/9709112].

[43] P. Schneider and M. Bartelmann, **The power spectrum of density fluctuations in the Zel'dovich approximation**, *Mon. Not. Roy. Astron. Soc.* **273** (1995).

[44] "NIST Digital Library of Mathematical Functions." http://dlmf.nist.gov/, Release 1.0.5 of 2012-10-01. Online companion to [45].

[45] F. W. J. Olver, D. W. Lozier, R. F. Boisvert, and C. W. Clark, eds., *NIST Handbook of Mathematical Functions*. Cambridge University Press, New York, NY, 2010. Print companion to [44].

[46] M. Crocce, S. Pueblas, and R. Scoccimarro, **Transients from Initial Conditions in Cosmological Simulations**, *Mon.Not.Roy.Astron.Soc.* **373** (2006) 369–381, [astro-ph/0606505].

[47] S. Tassev, **Lagrangian or Eulerian; Real or Fourier? Not All Approaches to Large-Scale Structure Are Created Equal**, arXiv:1311.4884.

[48] B. A. Reid, W. J. Percival, D. J. Eisenstein, L. Verde, D. N. Spergel, et al., **Cosmological Constraints from the Clustering of the Sloan Digital Sky Survey DR7 Luminous Red Galaxies**, *Mon.Not.Roy.Astron.Soc.* **404** (2010) 60–85, [arXiv:0907.1659].

[49] S. Tassev, M. Zaldarriaga, and D. Eisenstein, **Solving Large Scale Structure in Ten Easy Steps with COLA**, *JCAP* **1306** (2013) 036, [arXiv:1301.0322].

[50] T. Hahn, **CUBA: A Library for multidimensional numerical integration**, *Comput.Phys.Commun.* **168** (2005) 78–95, [hep-ph/0404043].

[51] A. Hamilton, **Uncorrelated modes of the nonlinear power spectrum**, *Mon.Not.Roy.Astron.Soc.* **312** (2000) 257–284, [astro-ph/9905191].

[52] R. Mehrem, **The Plane Wave Expansion, Infinite Integrals and Identities involving Spherical Bessel Functions**, astro-ph/0909.0494.

# Chapter 8

# Summary & Conclusions

## 8.1 Overview

Amongst all the observational probes of large scale structure (LSS) formation galaxy clustering surveys are one of the most important for extracting cosmological information. The reason for this lies in the fact that by measuring the three dimensional distribution of galaxies we can in principle extract the information of the three dimensional distribution of the underlying dark matter which is itself sensitive to many of the cosmological parameters. The growth of dark matter structures in time also provides important constraints on the models of the origins of structure in the universe (e.g. inflation and alternative theories), the composition of the universe (the nature and amount of the dark matter and dark energy) e.g. [1, 2], its equation of state and the linear growth rate as a function of redshift e.g. [3, 4]. It also addresses the question of the neutrino mass, modifications to gravity e.g. [5, 6], as well as the cosmological signatures of string physics.

In recent years there have been many ongoing and planned galaxy redshift surveys such as the Baryon Oscillation Spectroscopic Survey (BOSS) which is part of Sloan Digital Sky Survey III (SDSS-III) [7], Hobby-Eberly Telescope Dark Energy Experiment (HETDEX) [8], EUCLID [9] and others. The aim of these surveys is the precise measurement of the anisotropic power spectrum and two-point correlation function in the redshift space. Thus, from the observational perspective there is a great wealth of information offering an opportunity to constrain these cosmological models.

In this thesis the main focus has been in developing physically robust model for redshift space distortions (RSD) of galaxies. In the galaxy surveys one measures redshift instead of actual position, so in the redshift space the position of an object is distorted by its peculiar velocity through the Doppler shift. We have developed a new approach in order to model these distortions on the level of phase space distribution function. This model contains many advantageous characteristics like well controlled expansion. It is constructed from physically well defined momentum moments which makes it applicable for arbitrary tracers. Further on, the model can also be easily generalized and applied on any n-point statistics of either density or momentum fields.

In chapter 5 we present a perturbative approach to redshift space distortions using the phase space distribution function approach and apply it to the dark matter redshift space power spectrum and its moments. RSD can be written as a sum over density weighted velocity moment correlators. The lowest order of these moments are density, momentum density and stress energy density. We use standard and extended perturbation theory to determine their auto and cross correlators, comparing them to N-body simulations. We show which of the terms can be modeled well with the standard PT and which need additional terms that include higher order corrections which cannot be modeled in PT. Most of these additional terms are related to the small scale velocity dispersion effects, so called finger of god (FoG) effects, which affect some, but not all, of the terms in this expansion, and which

can be approximately modelled using a simple physically motivated ansatz such as the halo model. We point out that there are several velocity dispersions that enter into the detailed RSD analysis with very different amplitudes, which can be approximately predicted by the halo model. In contrast to the previous models our approach systematically includes all of the terms at a given order in PT and provides a physical interpretation for the small scale dispersion values. We investigate RSD power spectrum as a function of $\mu$, the cosine of the angle between the Fourier mode and line of sight, focusing on the lowest order powers of $\mu$ and multipole moments which dominate the observable RSD power spectrum. Overall we find considerable success in modeling many, but not all, of the terms in this expansion. This is similar to the situation in real space, but predicting power spectrum in redshift space is more difficult because of the explicit influence of small scale dispersion type effects in RSD, which extend to very large scales.

In chapter 6 we continue the investigation of phase space distribution function RSD model, applying it to the dark matter halos, looking at the halo velocity moments and the halo redshift space power spectrum. Halo spectrum is similarly as before written as a sum over the halo velocity moment correlators. We use PT methods to determine auto and cross correlators of these halo velocity moments. We adopt the nonlocal biasing model and use the renormalization methods presented in [10] to connect the dark matter halos with the underlying dark matter overdensity field. We compare our PT results at every stage with the N-body simulation measurements presented in [11]. We show which of these terms can be modeled well with the PT methods and which need more sophisticated nonlinear treatment (as resummation etc.). Since halos are objects of finite size, when computing the statistics like power spectrum we also encounter the shot noise effects. We studied the features of the shot noise which effects the angular independent part of RSD halo power spectrum. We found that simple Poisson description of the shut noise is insufficient, and that we have to allow for some scale dependence in the shot noise amplitude, which we eventually model with the power law. We also investigate the role of velocity dispersion effects which appear in the higher order velocity moment correlators. Since halos do not have the velocity contributions from the small scales as dark matter does, we find that the halo velocity dispersion values are smaller. In fact it turns out that linear theory describes it sufficiently well. Finally, our power spectrum model gives robust results and achieves 1% accuracy up to wave scales of $k \sim 0.15h/\mathrm{Mpc}$ for a range of halo masses, which is currently state of the art in the field.

In chapter 7 we explore the Lagrangian perturbation theory (LPT) approach to dark matter clustering. We evaluate the full one loop power spectrum in LPT keeping the cumulants up to third order, extending the Zel'dovich approximation and providing the power spectrum analogous to the calculations recently performed for correlation function. We compare the results to the N-body simulations and to the LPT simulations up to the second order. We find that the analytic calculations are in a good agreement with the LPT simulations, thus justifying a truncation of cumulant hierarchy in this case. While one loop calculations improve upon the Zel'dovich approximation, the resulting power spectrum is still significantly below the N-body simulations. We also explore the decomposition of the power spectra and correlation function in tree additive parts: Zel'dovich part, residual BAO wiggle part, and residual broadband part. Motivation for such decomposition comes from the fact that the correlation function in Zel'dovich approximation gives far better prediction in comparison to N-body simulation than does the linear theory. Residual wiggle contribution is treated using LPT based approach, where good agreement is found both in power spectrum and correlation function. For the residual broadband contribution we propose simple two parameter formula.

## 8.2 Current Outlook

In figure 8.1 we show the schematic template of the galaxy clustering. Components contributing to this scheme are dark matter clustering, redshift space distortions, galaxy biasing and contributions from satellites. In this thesis we have addressed most of these compo-

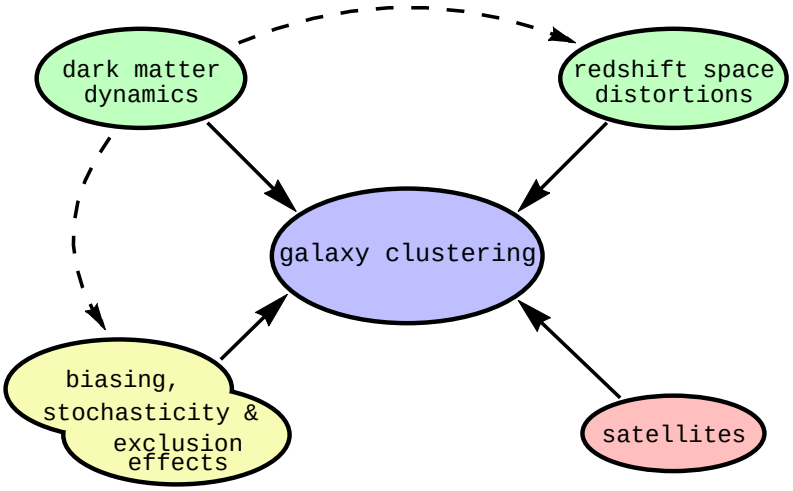


**Figure 8.1:** Galaxy clustering scheme: physical components contributing to the understanding and modeling of galaxy clustering on large scales. Dynamics of dark matter clustering and redshift space distortions are the basic elements in this composition and in chapter 5 we have studied their connection in detail. Additional component arises from the fact that galaxies reside in dark matter halos, which leads to the biasing and associated effects like halo exclusion. In chapter 6 we have added the biasing effects to the nonlinear clustering and redshift space distortions, but the details of modeling the exclusion effects and its impact on the scale dependence of power spectra still remain to be understood in detail. In addition to these components we need to take into account also the fact that more than one galaxy can populate single dark matter halo. This constitutes so called satellite contribution to the galaxy clustering scheme.

nents and modeled their connections and cumulative effects. We note that two details in this scheme have been beyond the scope of the thesis. First one concerns the details of the halo exclusion effects, due to its finite size, which contributes to the scale dependence of the galaxy power spectra and higher order statistics as well. Second is related to the fact that several galaxies can populate the same dark matter halo and so we need to take these effects also into account. This can be done by dividing galaxies into two categories, so called centrals and satellites, and modeling the contribution of each of these components. Modeling and adding this satellite contribution to the total galaxy power spectrum, as well as exclusion effects of halos mentioned above, is going to be addressed in the future work.

In order to improve the current understanding of formation of clusters of galaxies on large scales we should focus on improving and finally combining several aspects of underlying physical phenomena:

- Developing robust analytical and semi-analytical models for nonlinear evolution of dark matter under gravity.
- Understanding of biasing and stochastic nature of dark matter halos and galaxies.
- Addressing the problem of existence of satellite galaxies and including them in the final RSD models.
- Developing RSD models for statistics beyond the power spectra and correlation function.
- Writing the publicly available codes that incorporate all these mentioned components.

### 8.2.1 Perturbative Approaches to Gravitational Clustering

Recently a lot of work has been done in extending the validity range of PT techniques (e.g. renormalization theory [12] and EFT [13]). In order to model the RSD these techniques have to be applied on statistics that contains different velocity moments as well as statistics higher than two-point. Multi-point propagator methods [14] enable this and offer a way to proceed. In addition, the performance of these perturbative schemes is usually compared to the N-body simulation results. Fairness of this treatment has to be reexamined and convergence of PT techniques studied independently of simulation. In EFT approach physical interpretation of Wilson coefficients and the role and evolution of nonlinear scales is a interesting topic that should be explored in more depth. The importance of understanding these issues also transcends the boundaries of cosmological structure formation and also underlines topics in the field of fluid dynamics, statistical mechanics etc.

### 8.2.2 Halo Biasing as a Step Towards Describing the Galaxies

Modelling of bias in the sense of parametrized prescription that would relate dark matter halos to dark matter, for different statistics is still an unsolved problem. Standard paradigm says that the reasons for this lie in overly simplistic biasing schemes and thus approaches following the ideas of [15] have been suggested, incorporating also the methods from effective field theories. These would imply thorough consideration of all the terms allowed by the given symmetries of the problem and investigations of physical scales appearing in the problem, e.g. virialization scales. Combining these with the models that include the dynamical effects of halo evolution, like evolution of density peaks (e.g.[16]) and peak-bacground split (e.g.[17]) offers an potentially interesting way to proceed. Expectation is that this would yield more constraints on the number of effective parameters and thus enable more predictive power. Considerations of biasing of halo velocities are also a natural part of this framework. The latter would particularly effect the models of RSD since these depend on higher order momentum correlations.

Since halos are finite size objects they exhibit exclusion effects which lead to nontrivial scale dependencies in halo statistics [18]. Currently these effects have been studied in N-body simulations [19] and in order to incorporate them in final RSD models they have to be understood at the level of analytic or semi-analytic models. In addition, in order to model realistic galaxy samples, biased objects have to be divided into samples of central galaxies and satellites. This extension would also have to include a halo occupation distribution modeling which populates the dark matter halos with galaxies according to the halo mass e.g [20, 21]. N-body simulations analysis for such samples has already been presented in [11], and here developed theoretical models can be applied in order to describe this results.

### 8.2.3 Modelling the Redshift Space Distortion Effects

Phase space distribution function formalism [22] to RSD is also convenient for studying statistics beyond the density power spectrum, as e.g. bispectrum as well as momentum statistics. In addition to the theoretical developments, there is also a practical side of creating a fast and efficient tool/code for galaxy survey statistics. The purpose of such a tool/code lies in its applicability and usage in the analysis of observational data.

# Bibliography


[1] S. Cole, K. B. Fisher, and D. H. Weinberg, **Fourier analysis of redshift space distortions and the determination of Omega**, *MNRAS* **267** (1994) 785, [astro-ph/9308003].

[2] L. Guzzo, M. Pierleoni, B. Meneux, E. Branchini, O. L. Fevre, et al., **A test of the nature of cosmic acceleration using galaxy redshift distortions**, *Nature* **451** (2008) 541–545, [arXiv:0802.1944].

[3] Y.-S. Song and W. J. Percival, **Reconstructing the history of structure formation using Redshift Distortions**, *JCAP* **0910** (2009) 004, [arXiv:0807.0810].

[4] M. White, Y.-S. Song, and W. Percival, **Forecasting Cosmological Constraints from Redshift Surveys**, *MNRAS* **397** (2008) 1348–1354, [arXiv:0810.1518].

[5] P. McDonald and U. Seljak, **How to measure redshift-space distortions without sample variance**, *JCAP* **0910** (2009) 007, [arXiv:0810.0323]. * Brief entry *.

[6] G. M. Bernstein and Y.-C. Cai, **Cosmology without cosmic variance**, arXiv:1104.3862.

[7] **S**DSS-III Collaboration Collaboration, D. Schlegel, M. White, and D. Eisenstein, **The Baryon Oscillation Spectroscopic Survey: Precision measurements of the absolute cosmic distance scale**, arXiv:0902.4680.

[8] G. Hill, K. Gebhardt, E. Komatsu, N. Drory, P. MacQueen, et al., **The Hobby-Eberly Telescope Dark Energy Experiment (HETDEX): Description and Early Pilot Survey Results**, *ASP Conf.Ser.* **399** (2008) 115–118, [arXiv:0806.0183].

[9] J. Beaulieu, D. Bennett, V. Batista, A. Cassan, D. Kubas, et al., **EUCLID : Dark Universe Probe and Microlensing planet Hunter**, arXiv:1001.3349.

[10] P. McDonald, **Clustering of dark matter tracers: Renormalizing the bias parameters**, *Phys.Rev.* **D74** (2006) 103512, [astro-ph/0609413].

[11] T. Okumura, U. Seljak, and V. Desjacques, **Distribution function approach to redshift space distortions, Part III: halos and galaxies**, arXiv:1206.4070.

[12] M. Crocce and R. Scoccimarro, **Renormalized cosmological perturbation theory**, *Phys.Rev.* **D73** (2006) 063519, [astro-ph/0509418].

[13] J. J. M. Carrasco, M. P. Hertzberg, and L. Senatore, **The Effective Field Theory of Cosmological Large Scale Structures**, *JHEP* **1209** (2012) 082, [arXiv:1206.2926].

[14] F. Bernardeau, M. Crocce, and R. Scoccimarro, **Multi-Point Propagators in Cosmological Gravitational Instability**, *Phys.Rev.* **D78** (2008) 103521, [arXiv:0806.2334].

[15] P. McDonald, **How to generate a significant effective temperature for cold dark matter, from first principles**, *JCAP* **1104** (2011) 032, [arXiv:0910.1002].

[16] V. Desjacques, M. Crocce, R. Scoccimarro, and R. K. Sheth, **Modeling scale-dependent bias on the baryonic acoustic scale with the statistics of peaks of Gaussian random fields**, *Phys.Rev.* **D82** (2010) 103529, [arXiv:1009.3449].

[17] F. Schmidt, D. Jeong, and V. Desjacques, **Peak-Background Split, Renormalization, and Galaxy Clustering**, *Phys.Rev.* **D88** (2013) 023515, [arXiv:1212.0868].

[18] N. Hamaus, U. Seljak, V. Desjacques, R. E. Smith, and T. Baldauf, **Minimizing the Stochasticity of Halos in Large-Scale Structure Surveys**, *Phys.Rev.* **D82** (2010) 043515, [arXiv:1004.5377].

[19] T. Baldauf, U. Seljak, R. E. Smith, N. Hamaus, and V. Desjacques, **Halo Stochasticity from Exclusion and non-linear Clustering**, arXiv:1305.2917.

[20] U. Seljak, **Analytic model for galaxy and dark matter clustering**, *Mon.Not.Roy.Astron.Soc.* **318** (2000) 203, [astro-ph/0001493].

[21] R. Scoccimarro, R. K. Sheth, L. Hui, and B. Jain, **How many galaxies fit in a halo? Constraints on galaxy formation efficiency from spatial clustering**, *Astrophys.J.* **546** (2001) 20–34, [astro-ph/0006319].

[22] U. Seljak and P. McDonald, **Distribution function approach to redshift space distortions**, arXiv:1109.1888.